UNIVERSITY OF SOUTHAMPTON

FACULTY OF ENGINEERING AND THE ENVIRONMENT

Institute of Sound and Vibration Research

Time-Domain DGM for Turbofan Exhaust Noise Predictions

by

Michael Williamschen

Thesis for the degree of Doctor of Philosophy

August 2018

UNIVERSITY OF SOUTHAMPTON

ABSTRACT

FACULTY OF ENGINEERING AND THE ENVIRONMENT
Institute of Sound and Vibration Research

Doctor of Philosophy

TIME-DOMAIN DGM FOR TURBOFAN EXHAUST NOISE PREDICTIONS

by Michael Williamschen

Over the past fifty years, large strides have been made in reducing aircraft noise pollution. To continue on this trend, and to meet more aggressive noise regulations, higher-fidelity numerical models must be used early in the design process to accurately characterize the noise signature of prospective aircraft and engine designs. Predicting turbofan exhaust noise propagation requires a numerical scheme that can model a highly non-uniform flow-field, has low dispersion and dissipation error, has high computational efficiency, and can handle complex geometries. Time-domain nodal discontinuous Galerkin methods (DGM) have shown success in applications requiring high spatial accuracy, computational efficiency, and complex geometry representation. This thesis further develops the DGM for turbofan exhaust noise applications using a hybrid approach and solving the three-dimensional (3D) linearized Euler equations (LEE) in the time-domain. A parallel, 3D implementation of the above scheme is outlined and the accuracy and efficiency are verified. Challenges in applying the scheme to engineering applications are addressed. The relationship between accuracy and computational cost is investigated using a dispersion analysis of the scheme. Complications involving modeling of the highly non-uniform exhaust flow-field are addressed, including developing a new dispersion analysis of the LEE to study the formation and growth of aliasing-driven instabilities in shear layers, and the impact of the mean flow representation accuracy on the acoustic solution. A mapping procedure used to interface the mean flow solver with the aeroacoustic solver is discussed, and extended to the treatment of mean-flow boundary-layers that are unresolved on the acoustic mesh. Addressing the robustness and efficiency of the method, compact analytical source terms are developed that exploit the numerical flux between elements and band-limited source terms are investigated to reduce the number of computations required for an analysis. The numerical scheme is applied to the problem of scattering of fan tonal noise by noise-reducing chevrons on the bypass duct, considering a realistic geometry and flow-field.

Contents

Declaration of Authorship

I, Michael Williamschen, declare that the thesis entitled *Time-Domain DGM for Turbofan Exhaust Noise Predictions* and the work presented in the thesis are both my own, and have been generated by me as the result of my own original research. I confirm that:

- this work was done wholly or mainly while in candidature for a research degree at this University;
- where any part of this thesis has previously been submitted for a degree or any other qualification at this University or any other institution, this has been clearly stated;
- where I have consulted the published work of others, this is always clearly attributed;
- where I have quoted from the work of others, the source is always given. With the exception of such quotations, this thesis is entirely my own work;
- I have acknowledged all main sources of help;
- where the thesis is based on work done by myself jointly with others, I have made clear exactly what was done by others and what I have contributed myself;
- parts of this work have been published as:
  - M. Williamschen, G. Gabard, and H. Bériot, "Performance of the DGM for the Linearized Euler Equations With Non-Uniform Mean-Flow," in 21st AIAA/CEAS Aeroacoustics Conference, p. 3277, 2015.
  - M. Williamschen, G. Gabard, and H. Bériot,"A study of aliasing error in DGM solutions to turbofan exhaust noise problems," in ICSV 22, 2015.
  - Bériot, Hadrien & Gabard, Gwénaël & Hamiche, Karim & Williamschen, Michael. "High-order unstructured methods for computational aero-acoustics," 2015.

- M. Williamschen, G. Gabard, and H. Bériot, "Impact of the Mean Flow Representation on DGM Simulations of Flow Acoustics," in 22nd AIAA/CEAS Aeroacoustics Conference, 2016.
- M. Williamschen, G. Gabard, and H. Bériot, "Diffraction of Tonal Noise by Chevrons in a Turbofan Exhaust," in 23rd AIAA/CEAS Aeroacoustics Conference, 2017.

Date: March 1, 2018

Acknowledgements

I am very grateful to my supervisors, Dr. Gwénaël Gabard and Dr. Hadrien Bériot for their guidance and support over the course of this project. I am thankful for the support of this research from the European Commission under the 7th Framework Programme People 2013 through the CRANE Marie Curie Initial Training Network (606844). I would also like to thank Siemens Industry Software for hosting me during my secondment at the latter half of my project. Additionally, I owe great thanks to the University of Southampton IRIDIS High Performance Computing Facility which provided the computational support for this work.

Nomenclature

h	characteristic element size
Δt	time-step
p	polynomial order
Ω	volume region
Γ	surface region
$\rho, \rho', \rho_\circ$	density, fluctuating density, and mean density
$\vec{v} = u\hat{\imath} + v\hat{\jmath} + w\hat{k}$	velocity
$\vec{v}' = u'\hat{\imath} + v'\hat{\jmath} + w'\hat{k}$	fluctuating velocity
$\vec{v}_\circ = u_\circ\hat{\imath} + v_\circ\hat{\jmath} + w_\circ\hat{k}$	mean velocity
$(\rho u)', (\rho v)', (\rho w)'$	fluctuating x, y, and z momentum
$p, p', p_\circ$	pressure, fluctuating pressure, mean pressure
$\pi, \pi', \pi_\circ$	pressure ratio, fluctuating pressure ratio, mean pressure ratio
$c, c_\circ$	sound speed, mean sound speed
$\mathbf{q}$	vector of conserved, fluctuating variables
$\mathbf{q}_\circ$	vector of conserved, mean variables
$\mathbf{s}$	source term vector
$\mathbf{F}_\circ, \mathbf{G}_\circ, \mathbf{H}_\circ$	x, y, and z flux matrices
$\mathbf{W}$	right eigenvector matrix of the LEE
$\mathbf{\Lambda}$	eigenvalue matrix of the LEE
$\vec{\mathbf{f}}, \mathbf{f}_i$	LEE flux tensor
$\tilde{\mathbf{f}}$	numerical flux vector
$\mathbf{\Psi}, \psi_n$	nodal basis functions, nth nodal basis function
$\mathbf{\Phi}$	test functions
$\bar{\mathbf{q}}$	nodal LEE solution values
$\hat{\mathbf{q}}$	modal LEE solution coefficients
$\bar{\mathbf{f}}_i$	nodal values of the LEE flux tensor
$\bar{\mathbf{s}}$	nodal values of the LEE source term
$\hat{\mathbf{f}}^b$	nodal values of the numerical flux on face b
Γ_e^b	face b of the computational element, e
N_p	number of interpolation points in the nodal expansion

N_v	number of conserved variables
N_e	number of elements
N_s	number of sides of the element
N_st	number of time-integration stages
$\vec{k}, k$	wavenumber vector, wavenumber magnitude
ω	angular frequency
t_p	period
$\Delta x, \Delta y$	element spacing in x and y

Chapter 1

Introduction

Over the past several decades, aircraft noise reduction has become a significant part of the design process of new aircraft and airports. Superficially, aircraft noise is an annoyance for people living in and around areas of high aircraft traffic. However, recent studies into the effects of aircraft noise on people's mental and physical health have found links between living near high air-traffic regions and increased risk of disorders [1], including potential for cardiovascular and sleep problems [2, 3], and cognitive impairment [4, 5]. Furthermore, there are economic impacts associated with airport planning and operation costs, flight re-routing, noise-abatement, aircraft design [6], and property value [7].

Problems associated with aircraft noise are only expected to increase in the coming years with higher demand for air transportation expected [8]. Over the next twenty years, airline passenger traffic is expected to grow at 4.8% each year, exposing more of the population to aircraft noise [8]. Therefore, aircraft currently in design will operate in a stricter noise environment by the time they are in operation, motivating research into novel noise-reduction strategies to meet aggressive noise reduction targets.

1.1 Sources of aircraft noise

On modern transport aircraft, noise sources come from two broad categories, airframe noise and engine noise. Airframe noise is generated by the unsteady flow of air over the exterior geometry of the aircraft. Interactions of the unsteady flow with the wings and high-lift devices, landing gear, or even with fuselage surface protuberances or cavities, can generate noise. Airframe noise is predominantly heard on landing and approach to airports, when the aircraft is at low altitude over populated areas, and the landing gear and high-lift devices are deployed.

Turbofan engine noise is generated by both the mechanics of the engine and the air flowing through it. The periodic pressure field caused by the rotating fan blades as well as their unsteady wake impinging on static or moving surfaces, can generate tonal noise which exits the engine through the front and rear. Additionally, at a takeoff thrust condition, shock waves may form at the blade tips and propagate forward. Broadband noise is also present at the fan and is caused by the stochastic fluctuations associated with turbulence. In the core of the engine, the compressor generates tonal and broadband noise which propagates through the front of the engine. The combustion chamber generates mainly broadband noise caused by turbulent mixing and entropy production associated with combustion, which exits through the rear of the engine. Tonal noise is again generated by the turbine stages and exits into the exhaust nozzle. The interaction of the bypass stream and the core streams in the exhaust, generate mainly broadband noise, caused by the breakdown of vortical flow structures and turbulence. Furthermore, the presence of shear layers in the exhaust streams cause the propagating sound waves to refract into the far-field.

The propagation of acoustic waves from the aft of the engine is particularly challenging to study due to the strong flow and thermodynamic state gradients, and the often complex geometry in this region. This work is focused on predicting aircraft noise associated with aft-propagating engine noise. Specifically, detailed understanding of the engine exhaust noise requires a prediction method that can take into account the many sources outlined above, as well as the complicated interactions of the sound with strongly nonuniform flow, and the engine and aircraft geometry.

1.2 Aeroacoustics and motivation

Reducing aircraft noise requires multi-disciplinary collaboration between researchers studying the driving physics behind noise production and propagation, and researchers studying aircraft and engine design. This partnership is challenged by the fact that increasing the performance of the aircraft, *e.g.* range and fuel efficiency, can in some ways be in opposition to noise reduction. Therefore care must be taken to fully analyze both the noise impact and performance impact of new design modifications.

Traditionally, the analysis of aircraft noise is studied theoretically, experimentally, and computationally. Theoretical predictions of noise can involve analytical or empirical models which include knowledge of the main physical processes involved in the problems. These theoretical models are typically used to gain an understanding of the driving physical features present in a particular problem. As these methods are analytical or empirical, they offer a fast first-step in the aircraft conceptual design

process. Unfortunately, the detail incorporated into these models is low, and therefore not sufficiently accurate for the prediction of noise required later in the design stages.

Experimental studies of aircraft noise seek to record the actual production and effects of noise by studying the true physical processes. These can include both small-scale studies of representative models or even full-scale studies, evaluating the noise of real aircraft. These studies are limited however, by the accuracy and detail of the measurements and the high cost of experiments, in terms of both time and money. Therefore experiments must be chosen carefully so as to minimize the cost, which limits their effectiveness as a design tool.

The rapid advances in computing power over the past few decades has been a driving force behind the research into, and practical use of, computational tools for aircraft noise prediction. Computational tools for aeroacoustics have the benefit of being quite general, such that they may be used to study many different types of problems without redevelopment of the models. As a design tool, they are comparatively inexpensive to experiments and can typically produce results faster. In addition, numerical studies are not limited by the number or choice of physical quantities to measure. While computational tools for aeroacoustics are widely used, they require deep knowledge of the algorithms and assumptions used in their development and it can also be difficult to validate their accuracy in predicting real-world aeroacoustic effects.

While drawbacks can be seen for any of the above prediction tools, it is important to consider all of them for an aeroacoustic analysis. While computational tools are rapidly increasing in fidelity with advances in computing power, they must still be compared with experimental results to ensure that they can reproduce actual physical phenomena. Additionally, theoretical models are useful to verify that the computational tools can identify the driving physics of a problem and can be used when experimental results are not available.

1.3 Computational aeroacoustics

Computational aeroacoustics (CAA) emerged from the well-established computational fluid dynamics (CFD) community in the early 1990's due to the very specific needs required for solving aeroacoustic problems [9]. Aeroacoustic problems typically feature *i*) time-dependency, *ii*) disparate spatial scales, *iii*) disparate temporal scales, *iv*) disparate amplitude scales, and *v*) complex geometries [10].

Time-dependency of aeroacoustic problems is a natural consequence of the underlying physics. Acoustic waves can propagate with a wide range of frequencies, from fast

fluctuations to very slow fluctuations of state variables. To capture the full physics of a problem, long time-integration can be necessary, leading to high computational cost and strict accuracy requirements. Therefore the computational efficiency and accuracy of the numerical method are extremely important.

Far-field propagation of sound leads to strict requirements on numerical accuracy. The domain of interest is large compared to the acoustic wavelength, which may be multiple orders of magnitude smaller than the propagation distance, especially at high frequencies. High accuracy requirements for the acoustic waves dictates a fine computational mesh on a large domain, leading to high computational cost. Additionally, acoustic waves are often orders of magnitude smaller in amplitude than the fluid convective amplitudes and therefore high accuracy is necessary to distinguish the acoustic waves.

Generally, the effect of a geometry on sound generation or propagation is desired. However, when considering the accuracy requirements of the numerical scheme, introducing a complicated geometry is not straightforward. It is important that the representation of the geometry is detailed enough such that high accuracy of the scheme is not negatively impacted. For these reasons, the specific traits of a numerical method for CAA should include high spatial and temporal accuracy, computational efficiency, and complex geometry representation.

1.3.1 Computational aeroacoustics approaches

Approaches for CAA can be classified into two broad categories, direct and hybrid approaches. A direct approach seeks to solve the full compressible Navier-Stokes equations directly, with the solution containing the base flow and the perturbations combined. A Direct Numerical Simulation (DNS) considers all scales of the problem, from the smallest turbulent fluctuations to the largest convective features [11, 12, 13]. Since the ratio between the largest and smallest length scales can be nearly $\mathrm{Re}^{9/4}$, where Re is the Reynolds number, typically in the tens of millions for commercial aircraft, a DNS of a typical commercial airliner would require prohibitive computational resources to discretize. An alternative to computing all scales of the problem is to perform a Large Eddy Simulation (LES), which requires only computing the largest turbulent scales of a problem, while modeling the rest [14, 15]. Even with an LES approach, for aeroacoustics applications involving far-field propagation and large Reynolds numbers, it is still prohibitively expensive for all but the most simple problems. Modeling sources of sound generated by rotating turbo-machinery is yet even more computationally expensive. Lattice-Boltzmann [16, 17] approaches use a Lagrangian description of the flow physics, and can solve for the flow and acoustics efficiently with low dissipation and dispersion error, and are well-suited to complex geometries. While these methods

offer an improvement in computational cost over traditional LES, they are still too expensive to use as an early-stage design tool.

It is therefore apparent that computing the sound sources and propagation together is too computationally expensive. A hybrid approach seeks to reduce the computational cost by decoupling the sound propagation from the sound generation. To compute the sound generation, DNS or LES can be used in a small source region [18] and then an acoustic analogy, such as Lighthill's [19], or a simplified form of the Navier-Stokes equations can be used to propagate the acoustic waves to the far-field [20]. For engineering applications, where parameter trade studies are performed, DNS and LES are still too computationally costly for practical problems.

Recognizing that the scale of the acoustic fluctuations are often very small relative to the convective scales, a linearization of the Navier-Stokes equations about a mean state can be derived [21]. This linearized form results in a separation of the mean convective scales from the small perturbations, allowing them to be solved for separately with numerical schemes optimized for each case [10]. This hybrid approach involves computing a steady-state mean flow field, typically using the Reynolds Averaged Navier-Stokes (RANS) equations, and either analytically prescribing the acoustic sources, or using a stochastic method [22] to construct them from the RANS solution. The linearized Euler equations (LEE)[23], linearized Navier-Stokes equations (LNSE)[24], acoustic perturbation equations (APE)[25], or linearized potential equations (LPE), can then be used to propagate the source fluctuations. The LNSE are generally important for the modeling of viscous dissipation of acoustic energy at small scales, such as by the small orifices in sound-dampening liners. The APE are a simplified form of the LEE, permitting no entropy or vorticity solutions. While they are computationally less expensive to solve than the LEE, their locally-uniform mean flow assumption makes them unable to model the advection of temperature non-uniformities and vortices, which are important generators of noise in the exhaust of turbofan engines. The LPE rely on a potential flow assumption, which is a poor assumption of the rotational flow in the exhaust.

Solutions to the LEE are in the form of acoustic, entropy, and vorticity modes [26] and have the advantage of being able to model scattering of entropy and vorticity fluctuations into acoustic fluctuations. Aside from the disadvantage of being more computationally expensive to solve than the APE or LPE, the LEE has the potential for unstable solutions caused by growing undamped vortical modes in shear layers [9], that can lead to pollution of the acoustic solution. However, these instabilities, which are dependent on the frequency and shear layer thickness, tend to remain finite in the exhaust shear layers due to their quickly growing thickness with downstream position [27].

Time-domain and frequency-domain

If one is only interested in the response of the aeroacoustic system to time-harmonic sources, a great deal of simplification can be afforded by solving the problem in the frequency domain. Frequency domain approaches represent the perturbation variables, $\mathbf{q}(\vec{x}, t)$, as Fourier modes,

$$\mathbf{q}(\vec{x}, t) = \hat{\mathbf{q}}(\vec{x}, \omega) e^{i\omega t}, \tag{1.1}$$

where $\hat{\mathbf{q}}(\vec{x}, \omega)$ is the complex amplitude of the solution at angular frequency, ω, varying in space only. Inserting the above expression into the governing equations, results in a system that can be solved directly for the solution amplitudes at the desired source frequency, without having to consider a transient solution. In addition, shear layer instabilities can be avoided by solving the problem in the frequency domain at frequencies that will not excite the shear layer [28]. The practicality of frequency domain approaches are somewhat reduced as the frequency and computational domain size increases, due to the increasing size of the linear system and its storage in memory. Furthermore, direct solvers, which are imperative to use for avoiding shear instabilities, have difficultly scaling well with increased distributed computing power. For these reasons, frequency domain approaches are not often used to solve the LEE, especially in three dimensions.

Time-domain approaches are required when the aeroacoustic solution is not time-harmonic, for example with broadband sources or advection dominated problems. In these approaches, the fully transient response of the aeroacoustic system must be solved for by discretizing the solution in both space and time. For this reason, when applied to time-harmonic problems, time-domain methods are generally more computationally costly than frequency-domain methods. However, distributed explicit schemes for time-domain problems generally scale well, making them more practical for the solution of high degree of freedom (DOF) problems [29]. Turbofan exhaust noise applications in three dimensions typically require a large number of DOF, making a time-domain approach practical. However, choosing discretization parameters for minimizing error and computational cost can be more difficult for a time-domain approach due to the addition of time-discretization error and stability considerations. The time-step must be small enough to ensure sufficient accuracy of the far-field solution and stability, and yet as large as possible, since the overall computation time scales linearly with the number of time-steps. For the above reasons, the time-domain LEE are selected to model the propagation of turbofan exhaust noise in this work.

1.3.2 Numerical schemes for the solution of the LEE

Many solution strategies are available to solve the LEE, but following the criteria defined at the beginning of Section 1.3, the numerical solution scheme must be highly accurate, to propagate acoustic and hydrodynamic waves from the source to the mid- or far-field; efficient and scalable, to allow for the propagation of high-frequency waves in large domains; and permit complex geometries, to model realistic engines. The following sections outline various solution schemes that can solve the LEE and their potential for meeting the above criteria.

Finite difference methods

Historically, finite-difference methods have had the widest popularity in CAA. One of the first schemes developed specifically to address many of the difficulties outlined above, was the Dispersion-Relation-Preserving (DRP) scheme by Tam and Webb [26]. The DRP scheme is optimized specifically such that the dispersion relation of the numerical scheme, the relation between the angular frequency and wavenumber for time-harmonic solutions, closely approximates the true dispersion relation of the governing equations. The DRP scheme exhibits high order spatial accuracy and due to its structured grid and point-wise spatial operators, the method can achieve high computational efficiency. The finite-difference method has since been applied to the solution of many problems in aeroacoustics [30, 31, 32, 33, 34, 35]. However, a major disadvantage of standard finite-difference approaches, is being confined to using structured meshes. For simplistic problems, structured mesh generation is straightforward, but for complex, 3D geometries, generating high-quality meshes must be done with mostly manual input.

Finite volume methods

A popular method in the CFD community is the Finite-volume method (FVM) [36]. This approach directly discretizes the integral form of the conservation laws, and the solution takes a piecewise-constant form in each element. On the boundaries of the elements, where the solution is doubly-defined, a Riemann solver [36] is used to find a unique solution state and couple the solutions in adjacent elements. Since the discrete equations satisfy the integral form of the conservation laws, they are conservative. Due to the piecewise-constant solution, the local solution in each element can be updated with explicit time-integration approaches and unstructured meshes can be readily used.

While the piecewise-constant solution leads to a flexible and robust scheme, the downside is that the error for the standard Godunov scheme [36] converges only at $\mathcal{O}(h)$, where h is the spacing between elements. The accuracy can be improved by using a high-resolution scheme, computing a more accurate estimate of the solution at the element boundaries by fitting a polynomial to the solutions over the adjacent elements. However, this solution reconstruction leads to a less local scheme as the degree of the polynomial increases, since more surrounding elements are necessary to compute the fit. In three-dimensions and with an unstructured mesh, this reconstruction procedure makes high-order accuracy costly. Nevertheless, the FVM has been applied to aeroacoustic problems [37, 38, 39].

Finite element methods

The finite element approach discretizes the solution using globally continuous basis functions on an unstructured mesh. Due to the global continuity of the basis functions, explicit integration approaches cannot be used, and implicit approaches must be used instead. Finite element methods (FEM) have been successful in solving frequency-domain problems, especially for the Helmholtz or convected Helmholtz equations, with reviews given by Thompson [40] and Astley [9]. Some have applied finite-element methods to the solution of the LEE in two-dimensions [41, 42, 43], although its use for the LEE is less popular than time-domain methods, due to the high memory requirements for construction of the linear system. Polynomial finite-element (pFEM) methods can achieve high-order accuracy for smooth solutions [44].

A disadvantage of using the finite element method is that solutions to a problem involve solving and constructing a large system of equations. For three-dimensional problems with millions of degrees of freedom (DOF), solving the system may be prohibitively expensive. Recently however, the efficiency of pFEM approaches has been improved through adaptive pFEM, which locally adapts the polynomial order in each element based on local element size [45]. This approach has the effect of equidistributing the computational effort over the domain at a fixed accuracy level. Another advantage of this approach is that the same mesh can be used for computing solutions over a wide range of source frequencies.

Spectral methods are similar to FEM, using global Fourier or Chebyshev series instead of decomposing the domain into elements with local basis functions [46]. Such methods achieve spectral decay of the error, $\mathcal{O}(1/N)^N$, where $1/N$ is the normalized grid spacing, and are highly efficient [46]. A disadvantage of the spectral method is that complex geometries are difficult to incorporate into the scheme without the order of

accuracy deteriorating. The spectral element method, using high degree polynomials [47, 48], can achieve spectral accuracy on unstructured meshes.

Boundary element methods

Boundary element methods (BEM) are commonly used for the solution of wave equations in the frequency domain [40]. Unlike other methods which require discretization of both the surfaces and volume of the domain, the BEM requires only a surface mesh, using analytical Green's functions to relate the geometry and boundary surfaces and the solution inside the volume. This approach greatly simplifies 3D problems and offers a way to compute fast solutions to acoustic scattering problems. A strong disadvantage however, is the requirement of a uniform mean-flow field, and it is therefore not of use for this work.

Discontinuous Galerkin methods

Over the past 15 years, the discontinuous Galerkin method (DGM) has emerged as a scheme well-suited for the solution of aeroacoustic problems [49, 50, 51, 52, 53, 24, 29, 54], where high wave-propagation accuracy is critical. Unlike the finite element method where the approximation space is globally continuous, the DGM uses piecewise-continuous basis functions, coupling the solutions in adjacent elements with a numerical flux. The DGM retains the geometrical flexibility of the FEM and the high-order accuracy of pFEM, but with the advantage of using explicit integration and being suitable for advection-dominated problems without any additional stabilization. Due to the duplicated DOF on the boundaries of elements, more DOF are generally required for DGM to achieve a fixed accuracy level than the FEM. However, for nodal DGM, the local element solution is only coupled to the neighboring elements through the DOF on the element boundaries, allowing relatively easy domain decomposition and parallelization for solving larger problems.

For polynomial basis functions, there are two different ways of expressing the solution polynomials, a modal expansion, where the solution DOF are the polynomial coefficients, and a nodal expansion, where the DOF are the solution values at a set of interpolation nodes on each element [55]. Nodal DGM offers a lower operation count, since the fluxes can be evaluated by directly using the solution DOF.

For meshes composed of straight-sided simplices, the local element matrices can be expressed in terms of scaled, reference element matrices, substantially reducing the memory footprint and allowing efficient, cache-optimized residual updates [56, 57, 54]. For quadrilateral or hexahedral elements, Gauss-Legendre interpolation points result

in the discontinuous Galerkin (DG) spectral element method (DGSEM) [13, 58, 12, 59], which can exploit the tensor structure of the discrete equations to reduce the number of operations.

While the DGM is a highly efficient scheme for time-domain governing equations, it has also been used in the frequency domain for avoiding Kelvin-Helmholtz instabilities [41, 28], and with physical plane-wave basis functions [60]. A DG approach based on the Arbitrary high order schemes using derivatives (ADER) approach was developed by Dumbser and Munz [61]. This method can achieve arbitrarily high order accuracy in space and time, avoiding the use of high order accurate explicit integration schemes that require the storage of multiple previous solutions.

Flux reconstruction methods

Over the past decade, flux-reconstruction (FR) methods [62] have seen rapid increases in development and application. Flux-reconstruction methods discretize the solution with piecewise-discontinuous basis functions. Using a Riemann solver, a common flux at element interfaces is found, then polynomial correction functions are added to the flux to make a C^0 continuous flux. Unlike the DGM, the FR method discretizes the differential form of the governing equations directly. An important feature of flux-reconstruction methods is their ability recover other schemes such as nodal DGM, spectral-difference method, spectral-volume method, and correction procedure via reconstruction (CPR) method [63], through different specifications of the correction functions. By optimizing the correction functions for desired attributes, such as dispersion-relation accuracy or stability, entirely new schemes can be formulated. In this sense, nodal DGM is a specific case of a flux-reconstruction method.

1.4 Current state of the DGM

1.4.1 Applications to aeroacoustics

Over the past two decades, the DGM has seen significant development for aeroacoustic applications. The development of Quadrature-free DGM [56] led to significant reductions in computational cost, allowing the solution of larger aeroacoustic problems. Atkins and Lockard [49] then demonstrated the ability of the DGM to solve realistic two- and three-dimensional acoustic scattering problems involving complex geometries with nonuniform mean flow. Stanescu *et al.* [50] used the DGM to study the effects of scattering from an aircraft wing and fuselage. Reymen [53] applied the DGM to aeroacoustic propagation through a 3D aircraft inlet with acoustic liners.

More recently, Manera *et al.* [64] studied broadband and tonal noise propagation through a turbofan exhaust using a 2.5D formulation of the DGM. Rinaldi *et al.* [29] developed an adaptive order DGM for the solution of the linearized Euler equations (LEE) and the acoustic perturbation equations (APE). Rarata [65] applied time-domain DGM to turbofan intake aeroacoustics and considered non-axisymmetric inlet geometries with mean flow distortion on the acoustic propagation. Flad *et al.* [13] recently used the DGM to study the generation of airfoil trailing edge noise, by performing a direct numerical simulation of the turbulent scales.

1.4.2 Accuracy and stability

Interpolation error of the method for a polynomial basis was found by Richter [66] to converge at a rate of $\mathcal{O}(h^{p+1})$, where h is the size of the element and p is the polynomial order. Accuracy for model wave propagation problems in one and two dimensions has been studied in detail by Hu *et al.* [67]. They used a dispersion analysis technique in which wave-like solutions are sought and their numerical dispersion relations were compared to the exact dispersion relation. Dissipation error was found to dominate for the use of an upwind numerical flux. Hu and Atkins [68] extended their dispersion analysis approach to nonuniform grids and quantified the spectral accuracy of scheme. They calculated that the dissipation error decays at a rate of $\mathcal{O}(h^{2p+2})$ and the dispersion error decays at $\mathcal{O}(h^{2p+3})$. Later, Ainsworth studied the spectral properties more rigorously for the scalar advection equation [69] for $kh \ll 1$ and for large kh, where k is the wavenumber. Increasing the polynomial order was found to be more beneficial in terms of accuracy than decreasing the mesh size. In addition, an exponential decay rate of the error was found for $2p + 1 \approx \kappa hk$ for some constant, κ. Chevaugeon *et al.* [70] applied a similar one-dimensional dispersion analysis technique to the solution of aeroacoustics problems.

The stability restriction of the DGM for Runge-Kutta time-integration was found by Cockburn *et al.* [71] to be

$$\Delta t \leq \frac{h}{f(p)|c|} \tag{1.2}$$

where Δt is the time-step, f is some increasing function of the polynomial order and c is the maximum wave-speed. Kubatko *et al.* [72] derived a Courant-Friedrichs-Lewy (CFL) condition for polynomial orders up to 3 for the strong stability preserving (SSP) Runge-Kutta scheme. Measures of triangle size and anisotropy were studied. Toulorge and Desmet [73] studied the linear stability of several Runge-Kutta DGM schemes for a range of element shapes and sizes. They found that the upwind flux allows larger time-steps than the Lax-Friedrichs flux and that CFL conditions for local stability are generally too restrictive.

1.4.3 Efficiency

While the DGM has been in use since the mid-1970's, its practicality was greatly improved in the mid-1990's after the development of the quadrature-free DGM by Atkins and Shu [56]. The quadrature-free DGM significantly reduces the computational cost associated with the storage of local element matrices for problems using straight-sided triangles and tetrahedra. This improvement makes the DGM more competitive with other methods. The DGM has also been shown to achieve high parallel scaling [54]. Graphics processing units (GPUs) have also been shown to perform well for DG applications [74, 75, 76].

The overall computational effort required for a time-domain calculation scales linearly with the number of time-steps. It is therefore of great interest to maximize the time-step while obeying stability restrictions. Owing to the high flexibility of the DGM, several methods have been developed in an attempt to increase the effective time-step and are discussed below.

Multi-rate time-stepping

The stability condition, Equation 1.2, shows that the time-step size is dictated by the smallest element and the highest wave speed. One way to circumvent this restriction is to use a different time-step in every element, to better distribute computational effort over the domain. However, to maintain time-accuracy of the scheme, the time-level of all elements must be synchronized. This constraint poses a load balancing and communication problem that can require a complex implementation. Liu [77] created a multi-rate coupling procedure that minimizes dissipation and dispersion errors at interfaces of differing time-levels and also performed a stability and accuracy analysis of the method. A parallel multi-rate scheme developed by Seny *et al.* [78] maximized the workload of individual processors by appropriately partitioning elements into groups. Parallel scalability studies showed that the multi-rate scheme has a lower scalability than the single-rate scheme but offers improved performance for lower numbers of processors. Dawson *et al.* [79] applied a parallel multi-rate scheme to the solution of ocean modeling problems and achieved a 1.5 times speedup compared to a single-rate scheme. Gödel *et al.* [74] created an optimal two time-level partitioning method that was solved on GPUs. In addition to the GPU speedup, Gödel achieved a 1.2 times speedup with the multi-rate scheme applied to a three-dimensional electromagnetic simulation.

Implicit time-marching schemes

As an alternative to the stability-restricted time-step in explicit schemes, implicit time integration strategies may offer improved performance since the time-step is not limited by stability restrictions. Wang and Mavriplis [80] compared several implicit time-integration strategies for the unsteady Euler equations. They determined that the choice of the implicit scheme depends on the desired accuracy versus the desired efficiency. Kanevsky *et al.* [81] used an implicit-explicit Runge-Kutta scheme to solve nonlinear problems. Where the element size was small, an implicit scheme was used and where the element size was large, explicit time-marching was used. Recently, Hochbruck *et al.* [82] evaluated the performance of several implicit schemes for solving unsteady, linear equations and found that polynomial Krylov methods offer the largest speedup. Both Kanevsky and Hochbruck suggest that the development of efficient preconditioners will be required to achieve the largest benefit.

Variable order elements

The maximum stable time-step can be increased by changing the time-integration scheme, increasing the mesh size, or by decreasing the polynomial order. If the polynomial order is chosen non-uniformly, based on the local accuracy requirements in each element, the global time-step may be reduced. For example, the smallest elements may only need a low-order polynomial to achieve the same accuracy level as a larger element. Houston and Süli [83] created a fully-adaptive DGM for hyperbolic problems which locally alters the element size and order based on *a posteriori* error bound. Remacle *et al.* [84] also created an h–p adaptive DGM. A disadvantage of such approaches is the considerable complexity introduced when sharing solution information at the interface between elements of differing order [55]. To solve this problem, Chevaugeon [70] assumed that the mesh is known *a priori* and the polynomial order in each element is fixed at a maximum level based on accuracy requirements in the largest elements. To adapt the polynomial order, Chevaugeon applied a filter to the smaller elements, projecting the high-order solution onto an optimal lower-order basis which allowed the use of a larger global time-step, without having to significantly change the implementation.

1.5 Research direction

The DGM offers high-order accuracy, a simple implementation, and the ability to use unstructured meshes, making it well-suited for the solution of aeroacoustic problems.

Furthermore, using the time-domain DGM to solve the LEE has seen widespread popularity for aeroacoustic applications involving aircraft [49, 50, 51, 52, 53, 24, 29]. This work will focus on further developing the time-domain discontinuous Galerkin method for turbofan exhaust noise applications.

The final outcome of this work is to efficiently apply the DGM to the solution of a realistic, three-dimensional, exhaust noise prediction problem involving a complex geometry and realistic mean flow field. To limit the computational complexity, a hybrid method, solving the LEE in a nonuniform flow, is used. While the DGM has been applied to turbofan exhaust noise propagation previously [64, 29, 28], demonstrating that this can be done efficiently and accurately in 3D has yet to be accomplished to the best of the author's knowledge. To reach that goal, several developments must be made to address the efficiency and accuracy of the DGM as well as ensure that the method is robust.

The computational cost of the method depends on the time-step, mesh size, or polynomial order to reach a certain accuracy. Therefore, *a priori* estimates of the time-step, mesh size, and polynomial order for aeroacoustic problems are required to achieve maximum efficiency. Furthermore, it is important that the relationship between the choice of parameters, the accuracy, and the computational cost is identified such that optimal parameters may be chosen for a particular problem.

Applying the hybrid method to exhaust noise problems requires an accurate description of the exhaust mean flow field to be used as the propagation medium for the acoustic waves. In this work, the RANS are solved to predict the mean turbulent flow field expected in the exhaust. Once computed, the RANS flow field must be incorporated into the LEE model with sufficient accuracy to resolve shear layers and other high-gradient regions that will refract or scatter the acoustic waves. However, representing the mean flow at the RANS mesh resolution would lead to excessive computational cost of the LEE solution, so a compromise between accuracy and cost must be determined.

Nonuniform propagation media also present numerical challenges, such as aliasing error which can lead to numerical instabilities in marginally resolved computations [55]. Aliasing results from transfer of the energy in unresolved, high wavenumber modes in the flux, into low wavenumber modes, leading to instability. Aliasing-driven instabilities are especially problematic in solutions to turbofan exhaust noise problems where shear layer instabilities are present. While aliasing errors have been studied extensively, the focus has been predominantly on nonlinear governing equations. Aliasing errors in solutions to linear, non-constant coefficient governing equations, have received less attention, but are important for this work. Therefore, a goal of this work is to gain insight into the aliasing problem for LEE-governed sound propagation in nonuniform mean flows and to determine the effect of the discretization parameters on the stability.

For the LEE, source terms are used to model the effect on the system by external forces, mass injections, and temperature or vortical disturbances. Such sources are responsible for the generation of sound and can be described empirically, analytically, or can come from separate simulations. For analytically-described sound sources, such as using simple solutions to the LEE in an axially-infinite duct to describe tonal noise in the bypass duct of a turbofan, their numerical implementation presents challenges. Often these are implemented through absorbing regions at the extents of the computational domain, requiring that these regions be both good at absorbing outgoing waves and good at generating the analytical acoustic modes. A goal of this work is to exploit the upwind numerical flux to accurately generate the desired sources at user-defined, internal surfaces in the computational domain. Additionally, these analytical sound sources are often described at a single frequency. While time-domain methods can be used, obtaining results over a range of source frequencies requires many computations to be performed. It is advantageous to build the desired frequency range into the source term and perform a single computation [85]. This work further develops these sources to be used efficiently for turbofan exhaust noise applications.

Addressing the difficulties identified above is critical for obtaining accurate and efficient solutions. Therefore the main goals for this project are summarized as:

- Analyze the accuracy and computational cost of the DGM for solutions to the LEE.
- Identify the behavior of aliasing-driven instabilities in DGM solutions to the LEE.
- Understand the relationship between mean flow representation accuracy and the acoustic solution.
- Develop new source terms to make the specification of acoustic and hydrodynamic disturbances more straightforward than existing methods.
- Apply the DGM to a realistic turbofan exhaust noise problem using the methods developed in this work.

To address the above challenges, this thesis is structured as outlined below. Beginning from first principles, the linearized Euler equations, governing the physics in this work, are derived and the assumptions leading to their simplification are discussed. The nodal DGM is applied to the LEE and the boundary conditions, temporal discretization, and efficient implementation on parallel architectures is outlined. The numerical solution scheme, and its computational efficiency, are then verified by solving benchmark problems in two- and three-dimensions, in **Chapter 2**. The remainder of the

thesis can be divided into two parts, one focused on the numerics of the scheme, and the other on application considerations.

Included in part one, in an effort to better understand parameter choices and their impact on the accuracy and computational cost of the scheme, a dispersion analysis of the full two-dimensional LEE is performed in **Chapter 3**. Targeting aliasing-driven instabilities in solutions to the LEE, a dispersion analysis technique is developed, permitting a nonuniform mean flow-field, and used to provide insight into the development of numerical instabilities and the effect of the discretization, in **Chapter 4**.

In part two, difficulties in applying the time-domain DGM to aeroacoustics applications are addressed, by first investigating the relationship between the accuracy of the mean flow representation to the acoustic solution accuracy and then developing a procedure to effectively map CFD data to the acoustic mesh in **Chapter 5**. Source terms are developed in **Chapter 6** that provide an efficient and accurate way to impose common aeroacoustic sources when a complex geometry and flow-field is present. All of the developments in parts one and two of this thesis are applied to the problem of scattering of tonal noise by nacelle chevrons in **Chapter 7**. First, a parameter study is performed to characterize the scattering for a simplified turbofan model, and then a detailed engine geometry and mean flow-field are considered.

1.5.1 Three-dimensional time-domain DGM implementation

The above research goals rely on having a three-dimensional implementation of the nodal DGM for solving the linearized Euler equations. The implementation in this work extends a two-dimensional nodal DGM code developed by Gwénaël Gabard at the University of Southampton. Written in C++ and parallelized using OpenMPI [86], the two-dimensional implementation offers a solid foundation over which to develop the three-dimensional code. In addition to implementing the 3D numerical scheme, to allow the solution of complex engineering problems, other functionalities are implemented, including,

- curved elements to accurately discretize complex geometries, including the evaluation of surface fluxes using cubature rules and load-balancing of the more computationally costly curved elements,
- buffer regions to absorb out-going acoustic, entropy, and vorticity waves while minimizing unphysical reflections,
- periodic solution filtering to damp unphysical solutions,

- procedures to map from structured or unstructured CFD data to the interpolation points on the acoustic mesh,
- pre-processing utilities to import acoustic meshes, define boundary conditions, set solver parameters,
- source terms for describing sources of sound for realistic aeroacoustic applications, and,
- periodic exporting of solution data in parallel applications.

The above components can be considered here as the minimum required for the solution of engineering applications.

Chapter 2

Governing equations and the nodal discontinuous Galerkin method

In this chapter, the physical model describing the propagation of sound in non-uniform flows is discussed, including the assumptions leading to the governing equations for the problems considered in this work. The discussion begins from the integral conservation laws for a general, fluid continuum, and derives the linearized form of the Euler equations that will represent the basis of the numerical model. An analysis of the eigenstructure of the linearized Euler equations (LEE) is used to illustrate the space-time behavior of simple solutions. A nodal discontinuous Galerkin discretization is applied to the LEE and the parallel implementation is discussed. Following the definition of the numerical solution scheme, several benchmark problems are solved to verify the implementation and its performance for both serial and parallel applications.

2.1 Integral form of the conservation laws

Consider the fluid element in a continuum shown in Figure 2.1, occupying a volume, Ω, enclosed by the surface, Γ. As the fluid element moves, it is subject to normal and shear stresses acting on the surface and body forces acting on the volume, which distort the element. By applying the principles of conservation of mass, momentum, and energy, the effect on the fluid can be described mathematically. For an element contained in a fluid with a velocity of $\vec{v}$, and a density of ρ, applying the conservation

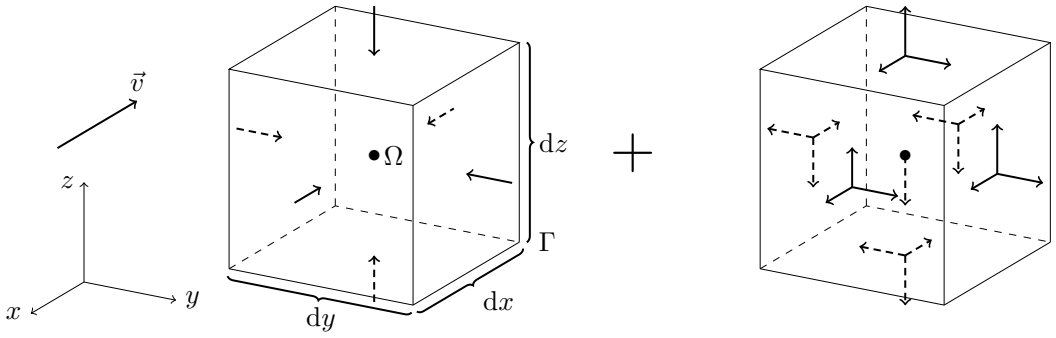

Figure 2.1: Left: fluid element with resultant pressure forces acting on it. Right: Viscous and body forces acting on the element.

of mass to the element [87] gives,

$$\frac{\partial}{\partial t}\int_{\Omega}\rho\,\mathrm{d}\Omega+\int_{\Gamma}\rho\vec{v}\cdot\mathrm{d}\vec{\Gamma}=0, \tag{2.1}$$

assuming there are no sources or sinks of mass. This equation establishes that the time rate of change of the fluid element's mass results from the flow of mass into or out of the volume through the bounding surface. Considering again the stresses acting on the fluid element in Figure 2.1, in addition to the pressure, p, there are body forces, $\vec{f}$, such as gravity or electromagnetic forces, and viscous shear stresses, caused by the fluid viscosity. Applying the conservation of momentum to the fluid element [87] gives,

$$\frac{\partial}{\partial t}\int_{\Omega}\rho\vec{v}\,\mathrm{d}\Omega+\int_{\Gamma}\vec{v}(\rho\vec{v}\cdot\mathrm{d}\Gamma)=-\int_{\Gamma}p\,\mathrm{d}\vec{\Gamma}+\int_{\Omega}\rho\vec{f}\,\mathrm{d}\Omega+\text{viscous term}, \tag{2.2}$$

which states that the forces acting on the fluid must be balanced by the time rate of change of the fluid momentum and its flux through the bounding surface. A third and final conservation equation can be found through application of the first law of thermodynamics to the fluid element [87], resulting in,

$$\frac{\partial}{\partial t}\int_{\Omega}E\,\mathrm{d}\Omega+\int_{\Gamma}E\,\vec{v}\cdot\mathrm{d}\vec{\Gamma}=\int_{\Omega}\rho\dot{q}\,\mathrm{d}\Omega-\int_{\Gamma}p\vec{v}\cdot\,\mathrm{d}\vec{\Gamma}+\int_{\Omega}\rho(\vec{f}\cdot\vec{v})\,\mathrm{d}\Omega \tag{2.3}$$

$$+\text{viscous heat transfer}+\text{work by viscosity}, \tag{2.4}$$

where $E=\rho e+\frac{1}{2}\rho\|\vec{v}\|$, is the total energy in the fluid, composed of specific internal energy, e, and kinetic energy, $\frac{1}{2}\rho\|\vec{v}\|$. The first term on the right hand side of 2.3 is the volumetric heat addition, where $\dot{q}$ is the specific heat transfer rate, and the second and third terms are the work done on the volume by pressure and body forces, respectively. These integral equations describe the physical laws governing the fluid in a very general form. The next step is to simplify the equations for the physical applications considered in this work and obtain a differential form of the governing

equations which will be discretized and form the basis of the numerical model.

2.1.1 Modeling assumptions

Since this work focuses mainly on the propagation of small disturbances in the exhaust of turbofan engines, the governing equations can be simplified to reduce the computational effort. The inclusion of viscosity adds complexity to the model, namely nine additional forces acting on the fluid element plus the addition of terms in the energy balance associated with heating and work due to friction. This imposes stricter mesh requirements to resolve fine-scale flow structures resulting from the viscous effects. Viscosity can often be neglected for acoustic propagation applications, since the propagation distances are short, and high frequency effects are not desired, *e.g.* above the threshold for human hearing. Additionally, the flow regime is such that an ideal, calorically perfect gas can be assumed, so that dissociation effects and phase change are not important. Since the acoustic disturbances are small and occur rapidly without heat transfer, the flow is assumed to be isentropic and adiabatic, $\mathrm{d}S = 0$ and $\dot{q} = 0$. Gravitational effects on the air are also negligible such that they too can be neglected.

All of the work in this thesis relies on the important assumption that these acoustic disturbances behave linearly. Generally, this assumption is justifiable since the disturbances are very small relative to the free-stream values and the velocity of the fluctuations is much smaller than the propagation speed [21]. For example, assume that the threshold of pain is around 130 dB [88] and consider a plane wave in quiescent air at standard atmospheric conditions. Even for this high sound level example, the maximum pressure amplitude of the acoustic wave and the particle velocity are only $p_{\max} \approx 90\,\mathrm{Pa}$ and $u_{\max} \approx 200\,\mathrm{mm/s}$, respectively. These are far smaller than the standard atmospheric pressure, $p_\infty = 101,325\,\mathrm{Pa}$ and sound speed, $c_\infty = 343\,\mathrm{m/s}$. However, the linear approximation may not hold for supersonic flows, such as in the exhaust jet of a military engine or the intake of a large turbofan with supersonic fan-tip speeds; very high amplitudes, such as those found in explosions; for long distances over which wave-steepening is possible; or for flows transitioning to instability. The assumption of linearity will be applied when deriving the linearized Euler equations in Section 2.3.

2.2 The Euler equations

Applying the model simplifications defined above results in the conservative Euler equations, which can be expressed in differential form by application of the divergence

theorem, resulting in,

$$\frac{\partial \mathbf{U}}{\partial t} + \frac{\partial \mathbf{F}}{\partial x} + \frac{\partial \mathbf{G}}{\partial y} + \frac{\partial \mathbf{H}}{\partial z} = \mathbf{s}, \tag{2.5}$$

where,

$$\mathbf{U} = \begin{bmatrix} \rho \\ \rho u \\ \rho v \\ \rho w \\ E \end{bmatrix}, \ \mathbf{F} = \begin{bmatrix} \rho u \\ \rho u^2 + p \\ \rho uv \\ \rho uw \\ (E+p)u \end{bmatrix}, \ \mathbf{G} = \begin{bmatrix} \rho v \\ \rho uv \\ \rho v^2 + p \\ \rho vw \\ (E+p)v \end{bmatrix}, \ \mathbf{H} = \begin{bmatrix} \rho w \\ \rho uw \\ \rho vw \\ \rho w^2 + p \\ (E+p)w \end{bmatrix}, \tag{2.6}$$

and $\mathbf{s}$ represents any sources or sinks in the problem.

The system of equations is closed by the assumption of an ideal, calorically perfect gas, with the internal specific energy defined as,

$$e = c_v T, \tag{2.7}$$

where c_v is the specific heat of the gas at constant volume, and T is the temperature, related to density and pressure through the ideal gas law,

$$p = \rho R T, \tag{2.8}$$

where R is the specific gas constant. The Euler equations can also be expressed in terms of the primitive variables, ρ, u, v, w, and p, in the form,

$$\frac{\mathbf{D}\rho}{\mathbf{D}t} + \nabla\rho = 0, \tag{2.9}$$

$$\rho\frac{\mathbf{D}u}{\mathbf{D}t} + \frac{\partial p}{\partial x} = 0, \tag{2.10}$$

$$\rho\frac{\mathbf{D}v}{\mathbf{D}t} + \frac{\partial p}{\partial y} = 0, \tag{2.11}$$

$$\rho\frac{\mathbf{D}w}{\mathbf{D}t} + \frac{\partial p}{\partial z} = 0, \tag{2.12}$$

$$\frac{\mathbf{D}p}{\mathbf{D}t} + \rho c^2 \vec{\nabla} \cdot \vec{v} = 0, \tag{2.13}$$

where the substantial derivative is defined as,

$$\frac{\mathbf{D}}{\mathbf{D}t} = \frac{\partial}{\partial t} + \vec{v} \cdot \vec{\nabla}. \tag{2.14}$$

2.2.1 Alternative formulations of the energy equation

It is possible to express the energy equation in alternate forms which may be more convenient when implementing it in the numerical scheme. One form replaces the energy equations with the conservation of entropy and the other is in the form of a conservation equation for a pressure ratio variable. Both of the forms rely on the assumption of isentropy and will only apply to smooth solutions.

2.2.1.1 Entropy conservation equation

One such replacement for the energy equation can be obtained as a conservation law for entropy. Replacing the total energy by the expression, $E = \rho e + \frac{1}{2}\rho\|\vec{v}\|$, and then applying the continuity and momentum equations in conservation and primitive form, the conservation equation for total energy can be replaced by a non-conservative equation in terms of specific internal energy,

$$\rho\frac{\mathbf{D}e}{\mathbf{D}t} + p\vec{\nabla}\cdot\vec{v} = 0. \tag{2.15}$$

From the first and second laws of thermodynamics, the specific internal energy can be related to specific entropy, s, with no heat addition as,

$$T\mathrm{d}s = \mathrm{d}e + p\,\mathrm{d}\left(\frac{1}{\rho}\right), \tag{2.16}$$

which may also be written in terms of the substantial derivative,

$$\rho\frac{\mathbf{D}e}{\mathbf{D}t} = \rho T\frac{\mathbf{D}s}{\mathbf{D}t} + \frac{p}{\rho}\frac{\mathbf{D}\rho}{\mathbf{D}t}. \tag{2.17}$$

Substituting the above expression into 2.15 and applying the continuity equation, the conservation equation for total entropy, $S = \rho s$,

$$\frac{\partial S}{\partial t} + \vec{\nabla}\cdot(S\,\vec{v}) = 0, \tag{2.18}$$

is obtained. This is valid only for smooth solutions to the Euler equations.

2.2.1.2 Conserved pressure ratio equation

Another form of the energy equation can be found starting from the primitive equation for pressure 2.13,

$$\frac{\mathbf{D}p}{\mathbf{D}t} + \rho c^2\vec{\nabla}\cdot\vec{v} = 0, \tag{2.19}$$

and looking for a conserved quantity, π, such that,

$$\frac{\partial \pi}{\partial t}\frac{\partial p}{\partial \pi} + (\vec{v}\cdot\vec{\nabla}\pi)\frac{\partial p}{\partial \pi} + \rho c^2 \vec{\nabla}\cdot\vec{v} = 0, \tag{2.20}$$

or,

$$\frac{\mathbf{D}\pi}{\mathbf{D}t} + \frac{\partial \pi}{\partial p}\rho c^2 \vec{\nabla}\cdot\vec{v} = 0. \tag{2.21}$$

For π to satisfy a conservation equation, it is required that,

$$\frac{\partial \pi}{\partial p}\rho c^2 = \pi, \tag{2.22}$$

or,

$$\frac{\mathrm{d}\pi}{\pi} = \frac{\mathrm{d}p}{\gamma p}. \tag{2.23}$$

After integrating both sides, the above expression becomes,

$$\ln\left(\frac{\pi}{\pi_\infty}\right) = \frac{1}{\gamma}\ln\left(\frac{p}{p_\infty}\right), \tag{2.24}$$

where π_∞ and p_∞ are constants. Therefore the conserved variable becomes,

$$\pi = \pi_\infty \left(\frac{p}{p_\infty}\right)^{1/\gamma}, \tag{2.25}$$

which gives the conservation equation,

$$\frac{\partial \pi}{\partial t} + \vec{\nabla}\cdot(\pi\vec{v}) = 0. \tag{2.26}$$

This alternative to the conserved total energy equation is attractive for its simplified form after linearization. Therefore this replacement of the energy equation will be used in the numerical implementation. Note that this variable is similar to the variable defined by Goldstein [89].

2.3 The linearized Euler equations

Now that the form of the nonlinear governing equations is defined, a linearization of the conservative equations is introduced. A change of variables is made, replacing the density, momentum, pressure, and the new variable, π, by a mean value around which

the equations are linearized, plus a fluctuating value,

$$\begin{aligned}
\rho &= \rho_\circ + \rho' \\
\rho u &= \rho_\circ u_\circ + (\rho u)' \\
\rho v &= \rho_\circ v_\circ + (\rho v)' \\
\rho w &= \rho_\circ w_\circ + (\rho w)' \\
\pi &= \pi_\circ + \pi' \\
p &= p_\circ + p',
\end{aligned} \tag{2.27}$$

where, $\{\cdot\}_\circ$, indicates a mean-flow quantity, and $\{\cdot\}'$, indicates a fluctuating quantity. It is assumed that the fluctuating variables are much smaller than the mean variables so that any products of fluctuating variables can be neglected. The fluctuating conserved variables are related to the primitive variables by,

$$\begin{aligned}
(\rho u)' &= \rho' u_\circ + \rho_\circ u' \\
(\rho v)' &= \rho' v_\circ + \rho_\circ v' \\
(\rho w)' &= \rho' w_\circ + \rho_\circ w' \\
\pi' &= p' \frac{\pi_\circ}{\gamma\, p_\circ} = p' \frac{\pi_\circ}{\rho_\circ c_\circ^2}.
\end{aligned} \tag{2.28}$$

Substituting the change of variables into the Euler equations and setting to zero any products of the fluctuating variables, results in the system of equations,

$$\frac{\partial \mathbf{q}}{\partial t} + \frac{\partial \mathbf{F}_\circ \mathbf{q}}{\partial x} + \frac{\partial \mathbf{G}_\circ \mathbf{q}}{\partial y} + \frac{\partial \mathbf{H}_\circ \mathbf{q}}{\partial z} = \mathbf{s}, \tag{2.29}$$

where $\mathbf{q} = [\rho', (\rho u)', (\rho v)', (\rho w)', \pi']^\intercal$ is the vector of conserved variables, and $\mathbf{F}_\circ$, $\mathbf{G}_\circ$, and $\mathbf{H}_\circ$ are the flux matrices in the x, y, and z directions, given by,

$$\mathbf{F}_\circ = \begin{bmatrix} 0 & 1 & 0 & 0 & 0 \\ -u_\circ^2 & 2u_\circ & 0 & 0 & \frac{c_\circ^2 \rho_\circ}{\pi_\circ} \\ -u_\circ v_\circ & v_\circ & u_\circ & 0 & 0 \\ -u_\circ w_\circ & w_\circ & 0 & u_\circ & 0 \\ -\pi_\circ u_\circ / \rho_\circ & \pi_\circ / \rho_\circ & 0 & 0 & u_\circ \end{bmatrix}, \quad \mathbf{G}_\circ = \begin{bmatrix} 0 & 0 & 1 & 0 & 0 \\ -u_\circ v_\circ & v_\circ & u_\circ & 0 & 0 \\ -v_\circ^2 & 0 & 2v_\circ & 0 & \frac{c_\circ^2 \rho_\circ}{\pi_\circ} \\ -v_\circ w_\circ & 0 & w_\circ & v_\circ & 0 \\ -\pi_\circ v_\circ / \rho_\circ & 0 & \pi_\circ / \rho_\circ & 0 & v_\circ \end{bmatrix},$$

$$\mathbf{H}_\circ = \begin{bmatrix} 0 & 0 & 0 & 1 & 0 \\ -u_\circ w_\circ & w_\circ & 0 & u_\circ & 0 \\ -v_\circ w_\circ & 0 & w_\circ & v_\circ & 0 \\ -w_\circ^2 & 0 & 0 & 2w_\circ & \frac{c_\circ^2 \rho_\circ}{\pi_\circ} \\ -\pi_\circ w_\circ / \rho_\circ & 0 & 0 & \pi_\circ / \rho_\circ & w_\circ \end{bmatrix}, \tag{2.30}$$

respectively. A vector, $\mathbf{s}$, is added to the right hand side of Equation 2.29 to represent any sources present in the problem.

2.3.1 Eigenstructure of the LEE

While the above system of equations models the propagation of small disturbances over a mean flow-field, the structure of the solutions is not immediately apparent. Since Equation 2.29 is a hyperbolic system, perturbations to the solution variables travel along characteristic curves at specific propagation speeds. By performing an eigenstructure analysis of the equations, these wave speeds and characteristics can be determined, giving insight into how a given set of initial conditions evolves in time and space. The following discussion follows directly from the theory of hyperbolic systems.

Defining an arbitrary unit normal direction, $\hat{n} = n_x\hat{\imath} + n_y\hat{\jmath} + n_z\hat{k}$, where $\hat{\imath}$, $\hat{\jmath}$, $\hat{k}$, are the unit vectors associated with the x, y, and z directions, the normal flux matrix is,

$$\mathbf{F}_{\circ,n} = \mathbf{F}_\circ n_x + \mathbf{G}_\circ n_y + \mathbf{H}_\circ n_z. \tag{2.31}$$

Along the normal direction, the LEE become,

$$\frac{\partial \mathbf{q}}{\partial t} + \frac{\partial \mathbf{F}_{\circ,n}\mathbf{q}}{\partial x_n} = \mathbf{0}, \tag{2.32}$$

which can be written in advection form as,

$$\frac{\partial \mathbf{q}}{\partial t} + \frac{\partial \mathbf{F}_{\circ,n}\mathbf{q}}{\partial \mathbf{q}}\frac{\partial \mathbf{q}}{\partial x_n} = \frac{\partial \mathbf{q}}{\partial t} + \mathbf{F}_{\circ,n}\frac{\partial \mathbf{q}}{\partial x_n} = \mathbf{0}. \tag{2.33}$$

The flux Jacobian can be decomposed into eigenvalues and eigenvectors,

$$\mathbf{F}_{\circ,n} = \mathbf{W}\mathbf{\Lambda}\mathbf{W}^{-1}, \tag{2.34}$$

where the right eigenvectors are given as the columns of,

$$\mathbf{W} = \begin{bmatrix} 1 & 0 & 0 & 1 & 1 \\ n_x v_{\circ,n} & 0 & -n_z & u_\circ - n_x c_\circ & u_\circ + n_x c_\circ \\ n_y v_{\circ,n} & -n_z & 0 & v_\circ - n_y c_\circ & v_\circ + n_y c_\circ \\ n_z v_{\circ,n} & n_y & n_x & w_\circ - n_z c_\circ & w_\circ + n_z c_\circ \\ 0 & 0 & 0 & \pi_\circ/\rho_\circ & \pi_\circ/\rho_\circ \end{bmatrix}, \tag{2.35}$$

and the eigenvalues are the diagonal values of,

$$\mathbf{\Lambda} = \begin{bmatrix} v_{\circ,n} & 0 & 0 & 0 & 0 \\ 0 & v_{\circ,n} & 0 & 0 & 0 \\ 0 & 0 & v_{\circ,n} & 0 & 0 \\ 0 & 0 & 0 & v_{\circ,n} - c_\circ & 0 \\ 0 & 0 & 0 & 0 & v_{\circ,n} + c_\circ \end{bmatrix}, \tag{2.36}$$

for a normal mean flow velocity of $v_{\circ,n} = u_\circ n_x + v_\circ n_y + w_\circ n_z$. Defining characteristic variables as $\mathbf{w} = \mathbf{W}^{-1}\mathbf{q}$, the normal LEE can be written in terms of these variables, resulting in,

$$\frac{\partial \mathbf{w}}{\partial t} + \mathbf{\Lambda}\frac{\partial \mathbf{w}}{\partial x_n} = \mathbf{0}, \tag{2.37}$$

which is a set of uncoupled advection equations for the characteristic variables. This equation is useful in a number of ways, for instance, it describes the solution of the LEE, $\mathbf{q} = \mathbf{W}\mathbf{w}$, as a linear combination of waves, given as the columns of $\mathbf{W}$, with strengths defined as the characteristic variables, $\mathbf{w}$, and wave speeds defined as the diagonal values of $\mathbf{\Lambda}$. Inspecting the advection equations, the characteristic variables will evolve in time and space as,

$$\mathbf{w}(x_n, t) = \mathbf{w}(x_n - \mathbf{\Lambda}t, t_0) = \mathbf{w}_0(x_n - \mathbf{\Lambda}t). \tag{2.38}$$

The solution to the LEE at any time $t > t_0$ can then be expressed as,

$$\mathbf{q}(x_n, t) = \mathbf{W}\mathbf{w}_0(x_n - \mathbf{\Lambda}t). \tag{2.39}$$

Therefore the solution at any time is simply a summation of waves defined by $\mathbf{W}$, each multiplied by the amplitude of the waves, $\mathbf{w}_0$, advecting at speeds, $\mathbf{\Lambda}$. The fourth and fifth columns of $\mathbf{W}$ represent acoustic waves propagating with speeds $v_{\circ,n} - c_\circ$ and $v_{\circ,n} + c_\circ$, against and with the mean flow, respectively. Waves associated with the transport of entropy and vorticity are defined by the first three columns, and propagate in the direction of the mean flow at the mean flow velocity, $v_{\circ,n}$. This simple analysis shows how simple solutions to the LEE behave in a uniform flow-field and this information will be used in future sections to formulate aspects of the numerical solution scheme and the boundary conditions.

2.4 The discontinuous Galerkin formulation

As described in Chapter 1, the discontinuous Galerkin method is an attractive scheme for solving time-domain aeroacoustics problems, in part due to its ability to achieve

high-order accuracy on unstructured meshes, and its scalability for the solution of large problems. The following sections outline the DG scheme used in this work, its application to the LEE, and its efficient parallel implementation.

To make the notation more compact, the linearized Euler equations, Equation 2.29 are written here as,

$$\frac{\partial \mathbf{q}}{\partial t} + \frac{\partial \mathbf{f}_i(\mathbf{q})}{\partial x_i} = \mathbf{s} \,, \tag{2.40}$$

where $\mathbf{q}$ is the vector of conserved variables, and an index summation convention over i is used for the divergence of the flux, *i.e.*,

$$\frac{\partial \mathbf{f}_i(\mathbf{q})}{\partial x_i} = \vec{\nabla} \cdot \vec{\mathbf{f}}, \tag{2.41}$$

with the tensor, $\vec{\mathbf{f}} = \mathbf{F}_\circ \mathbf{q}\, \hat{\imath} + \mathbf{G}_\circ \mathbf{q}\, \hat{\jmath} + \mathbf{H}_\circ \mathbf{q}\, \hat{k}$. The computational domain, Ω, is partitioned into a set of non-overlapping elements, $\Omega_e \in \Omega$, with no restrictions placed on the element shape thus far. Defining the approximated solution on element, e, as $\mathbf{q}_e$, a standard weighted residual approach is applied to each element, Ω_e, giving,

$$\int_{\Omega_e} \mathbf{\Phi}_e^\intercal \left(\frac{\partial \mathbf{q}_e}{\partial t} + \frac{\partial \mathbf{f}_i(\mathbf{q}_e)}{\partial x_i} - \mathbf{s} \right) \mathrm{d}\Omega_e = 0, \tag{2.42}$$

where $\mathbf{\Phi}_e$ are the piecewise test functions, discontinuous across the element boundaries. The term involving the flux divergence can then be integrated by parts, to obtain,

$$\int_{\Omega_e} \mathbf{\Phi}_e^\intercal \frac{\partial \mathbf{q}_e}{\partial t} - \frac{\partial \mathbf{\Phi}_e^\intercal}{\partial x_i} \mathbf{f}_i(\mathbf{q}_e) - \mathbf{\Phi}_e^\intercal \, \mathbf{s} \, \mathrm{d}\Omega_e + \int_{\Gamma_e} \mathbf{\Phi}_e^\intercal \, \mathbf{f}_i(\mathbf{q}_e) \, n_i \, \mathrm{d}\Gamma_e = 0 \,, \tag{2.43}$$

where n_i is the normal to the element edge, Γ_e. Due to the discontinuity of the test functions the solution, $\mathbf{q}_e$, at the element boundary, Γ_e, is doubly defined, making the evaluation of the flux at the boundary uncertain. To ensure conservation, continuity of the flux is imposed such that,

$$\mathbf{f}_i(\mathbf{q}_e) n_i|_{\Gamma_e} = \mathbf{f}_i(\mathbf{q}_{e+}) n_i|_{\Gamma_{e+}}, \tag{2.44}$$

or that there is some unique flux on the boundary which is evaluated with a combination of the two solutions on either side of the interface, $\mathbf{q}_e$, and $\mathbf{q}_{e+}$, with Γ_{e+} as the interface for element $e+$. This unique normal flux, $\tilde{\mathbf{f}}(\mathbf{q}_e, \mathbf{q}_{e+})$, is denoted as the numerical flux which replaces $\mathbf{f}_i(\mathbf{q})\, n_i$ in Equation 2.43 resulting in the weak formulation,

$$\int_{\Omega_e} \mathbf{\Phi}_e^\intercal \frac{\partial \mathbf{q}_e}{\partial t} - \frac{\partial \mathbf{\Phi}_e^\intercal}{\partial x_i} \mathbf{f}_i(\mathbf{q}_e) - \mathbf{\Phi}_e^\intercal \, \mathbf{s} \, \mathrm{d}\Omega_e + \int_{\Gamma_e} \mathbf{\Phi}_e^\intercal \, \tilde{\mathbf{f}}(\mathbf{q}_e, \mathbf{q}_{e+}) \, \mathrm{d}\Gamma_e = 0 \,. \tag{2.45}$$

The specific choice of the numerical flux function is described in more detail in the following section.

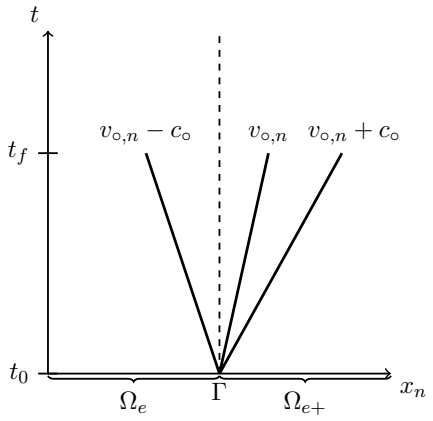

Figure 2.2: Evolution of a discontinuous solution state at $x_n = \Gamma$ from time, $t = t_0$ to $t = t_f$. The wave speeds are indicated by $v_{\circ,n} - c_\circ$, $v_{\circ,n}$, and $v_{\circ,n} + c_\circ$, where the normal mean flow velocity and sound speed are $v_{\circ,n}$ and $c_\circ$, respectively.

The flux divergence term in the weak formulation above can be integrated by parts once more to obtain the strong formulation,

$$\int_{\Omega_e} \boldsymbol{\Phi}_e^\intercal \left[\frac{\partial \mathbf{q}_e}{\partial t} + \frac{\partial \mathbf{f}_i(\mathbf{q}_e)}{\partial x_i} - \mathbf{s} \right] \mathrm{d}\Omega_e - \int_{\Gamma_e} \boldsymbol{\Phi}_e^\intercal \left[\mathbf{f}_i(\mathbf{q}_e)\, n_i - \tilde{\mathbf{f}}(\mathbf{q}_e, \mathbf{q}_{e+}) \right] \mathrm{d}\Gamma_e = 0 \,. \quad (2.46)$$

The strong formulation permits the use of non-smooth test functions, such as Delta functions [55]. In Section 2.5.1, an appropriate set of basis functions are defined and the variables are discretized to allow for numerical solutions.

2.4.1 Numerical flux functions for the LEE

The difficulty in formulating a numerical flux lies in how to combine the discontinuous solution states on adjacent sides of element interfaces, such that it forms a unique solution state at the interface that is consistent with the governing physics. This is recognized as the well-known Riemann problem, where knowledge about the temporal evolution of a piecewise-constant initial condition is used to determine the unique interface state. Most of the development of flux functions can be attributed to the finite volume community [36]. The two flux functions used in this work, the upwind flux, and the Lax-Friedrichs flux, are defined in this section.

To formulate the upwind flux it is beneficial to refer back to the eigenstructure analysis of the LEE presented in Section 2.3.1. Along a normal direction, pointing from element Ω_e into element Ω_{e+}, the LEE solution can be decomposed into a summation of waves, each with a strength and a wave speed. This is illustrated in Figure 2.2 for a mean flow velocity $v_{\circ,n} > 0$, where at the interface between two elements, Γ, the solution along the normal direction evolves in time and space as a superposition of acoustic waves with

speeds $v_{\circ,n} - c_\circ$ and $v_{\circ,n} + c_\circ$, and entropy and vorticity waves with speed $v_{\circ,n}$. Notice that the entropy, vorticity, and the right-moving acoustic wave are traveling from Ω_e into Ω_{e+} and only the left-moving acoustic wave is traveling into Ω_e. Therefore, it is logical that the contribution to the flux associated with the right-moving waves should be computed using $\mathbf{q}_e$, and the contribution to the flux associated with the left-moving waves should be computed using $\mathbf{q}_{e+}$. This is known as upwinding, and it can be described mathematically by,

$$\tilde{\mathbf{f}}(\mathbf{q}_e, \mathbf{q}_{e+}) = \frac{1}{2}\left[\mathbf{F}_{\circ,n}\,\mathbf{q}_e + \mathbf{F}_{\circ,n}\,\mathbf{q}_{e+} + \theta\,\mathbf{W}\,|\mathbf{\Lambda}|\,\mathbf{W}^{-1}\,(\mathbf{q}_e - \mathbf{q}_{e+})\right] , \tag{2.47}$$

where the matrices, $\mathbf{F}_{\circ,n}$, $\mathbf{W}$, and $\mathbf{\Lambda}$ are defined in Section 2.3.1. The upwinding parameter, θ, is a scalar between zero and one which defines the level of upwinding. For $\theta = 1$, this gives the exact upwind flux function for the LEE in one dimension and for $\theta = 0$, the central flux is recovered, which is simply the arithmetic average of the fluxes computed on either side of the interface. The choice of an upwind or central flux will influence both the stability and the accuracy of the scheme. In this work, the fully upwind flux is used unless otherwise noted.

Another choice of flux function is the Lax-Friedrichs flux,

$$\tilde{\mathbf{f}}(\mathbf{q}_e, \mathbf{q}_{e+}) = \frac{1}{2}\left[\mathbf{F}_{\circ,n}\,\mathbf{q}_e + \mathbf{F}_{\circ,n}\,\mathbf{q}_{e+} + \max\left(|\mathbf{\Lambda}|\right)\,(\mathbf{q}_e - \mathbf{q}_{e+})\right] , \tag{2.48}$$

which can be thought of as a central flux with an added dissipation term proportional to the maximum wave speed at the interface. In some cases, the simpler expression for the numerical flux and its additional dissipation can be useful, especially concerning stability in non-uniform flows, examined in Chapter 4.

2.4.2 Boundary conditions

Enforcement of boundary conditions can be done simply by specifying an appropriate numerical flux at the boundaries of the domain. In this section, two common boundary conditions, the hard wall, and the non-reflecting surface are defined based on the characteristics of the governing equations.

At the boundary of the computational domain, two solution states can be defined, the internal solution, $\mathbf{q}_{\text{int}}$, associated with an element on the boundary, and a fictitious, "external" state, $\mathbf{q}_{\text{ext}}$, which can be specified to introduce boundary conditions. This external solution can be thought of as the value the solution would take in the neighboring element if a neighboring element existed outside of the computational domain. Since the upwind numerical flux is computed as a function of the two solution states

on either side of the interface, Γ, no modifications to the scheme need to happen at the boundaries.

Hard wall

A hard-wall boundary condition for the LEE is defined such that any incident waves are completely reflected normal to the boundary surface and there are no out-going waves. For a non-porous wall, it is required that the flow is not allowed to penetrate the hard surface, therefore, $v_{\circ,n}$ is assumed to be zero.

To ensure that the incoming waves are reflected, the momentum vector should be reflected across the boundary interface. This restriction results in the following expression for the solution state vector external to the boundary interface,

$$\mathbf{q}_{\text{ext}} = \begin{bmatrix} \rho' \\ -(\rho u)' \\ -(\rho v)' \\ -(\rho w)' \\ \pi' \end{bmatrix}_{\text{int}}, \tag{2.49}$$

where the subscript, ext, refers to the solution state *external* to the boundary interface, and the subscript, int, refers to the use of solution state variables *internal* to the domain.

Non-reflecting condition

For a non-reflecting boundary condition, the opposite behavior to the condition above is desired. Instead of completely reflecting any incident waves, a non-reflecting boundary condition allows outgoing waves to pass freely out of the domain and requires that no waves pass back into the domain. In terms of characteristics of the governing equations, this boundary condition sets the strength of any incoming waves to zero. Similar to the hard wall case above, the non-reflecting boundary condition can be defined through the external solution state vector. To force the strength of any incoming waves to zero, this condition is implemented as simply,

$$\mathbf{q}_{\text{ext}} = \mathbf{0}. \tag{2.50}$$

It is important to note that this boundary condition is only completely non-reflecting for incident wave fronts parallel to the boundary surface. For waves with high angles of incidence, spurious reflections will occur. Generally, alternative absorbing boundary

conditions are used when spurious outflow reflections can pollute the solution. The next section outlines a buffer region which damps out-going waves through application of a volume source term.

2.4.3 Buffer zone for damping outflow disturbances

An alternative way of damping out-going disturbances while generating less reflections than characteristic boundary conditions, is to apply a buffer zone. Buffer zones are regions at the outflow of the computational volume, that progressively damp the nodal solution values as the disturbances approach the outflow boundary. An explicit buffer zone in similar form to the ones evaluated by Richards *et al.* [90] and Fattah *et al.* [91], is used in this work. In the buffer zone, following each time-step, the solution is modified through application of the damping function,

$$\mathbf{q}(\vec{x}) \leftarrow \mathbf{q}(\vec{x})(1 - \sigma(\vec{x})), \tag{2.51}$$

where $\sigma(\vec{x})$ is the damping factor, evaluated at the buffer zone coordinate, $\vec{x}$. The damping factor can be evaluated with the expression,

$$\sigma(\vec{x}) = \sigma_{\max}\phi(\vec{x})^{\beta}, \tag{2.52}$$

where β adjusts the transition rate from the interior of the domain to the outflow boundary, $\sigma_{\max}$ is a coefficient defining the amount of damping, and $\phi(\vec{x})$ varies smoothly from zero at the beginning of the zone to one at the outflow boundary. An important parameter of the buffer zone is its thickness. Generally, the thickness should be at least as much as the maximum wavelength [90].

The function $\phi(\vec{x})$ is typically defined manually, based on simplistic buffer shapes, such as rectangular or spherical regions. Arbitrarily-shaped outflow regions make $\phi(\vec{x})$ difficult to define manually, particularly in three-dimensional applications such as when a curved CAD geometry intersects with the outflow region. In this work, $\phi(\vec{x})$ is defined automatically through the solution of the Laplace equation in the buffer zone,

$$\frac{\partial^2 \phi}{\partial x_i^2} = 0, \tag{2.53}$$

with boundary conditions, $\phi = 0$ at the beginning of the buffer zone, and $\phi = 1$ at the end. Figure 2.3 shows the solution of Equation 2.53 in the buffer zone of an irregularly-shaped, two-dimensional, computational domain. Notice that the solution handles both sharp corners and curved regions well.

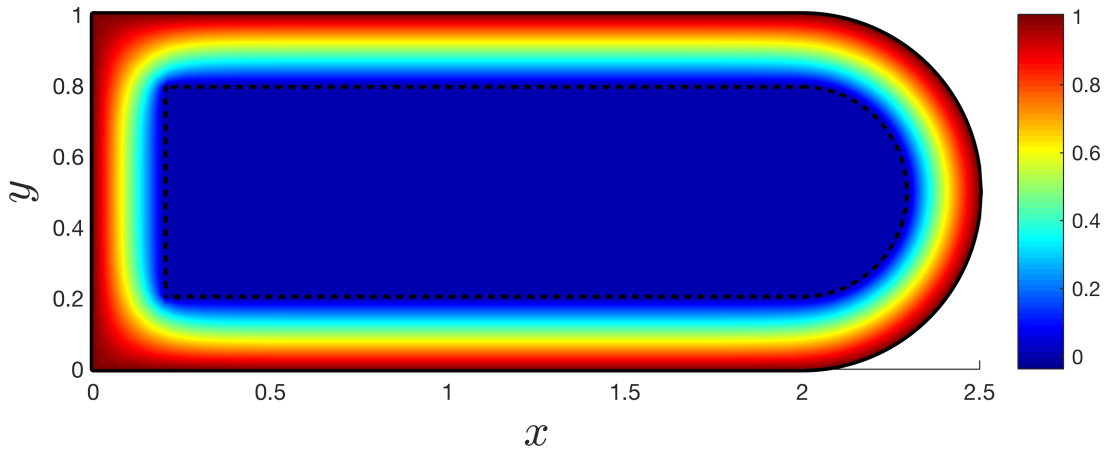

Figure 2.3: Buffer zone variable, ϕ, in an irregular-shaped, two-dimensional, domain. The start of the buffer zone, is outlined in dashed lines, and the end, in solid lines.

2.5 The nodal discontinuous Galerkin method

This section introduces the discretization of the solution variables, allowing the solution of the LEE to be computed numerically.

2.5.1 Spatial discretization

The discretization of the solution, $\mathbf{q}_e$, has thus far been left undefined. Using a polynomial basis, the solution in element, Ω_e, at spatial location, $\vec{x}$, and at time, t, can be expressed as the expansion,

$$\mathbf{q}_e(\vec{x},t) \approx \sum_{n=1}^{N} P_n(\vec{x}) \left\{\hat{\mathbf{q}}_e\right\}_n (t), \tag{2.54}$$

where $P_n(\vec{x})$ is the n-th term of N polynomial basis functions evaluated at $\vec{x}$, and $\left\{\hat{\mathbf{q}}_e\right\}_n (t)$ is the n-th coefficient of the polynomial. This is known as a *modal* expansion of the solution, in which the polynomial coefficients are the unknowns. In this work, the orthonormal Jacobi polynomials are chosen to ensure good conditioning at high orders [55]. An alternative way to represent the solution is through a *nodal* expansion where,

$$\mathbf{q}_e(\vec{x},t) \approx \sum_{n=1}^{N_p} \psi_n(\vec{x})\, \mathbf{q}_e(\vec{x}_n,t). \tag{2.55}$$

In the nodal expansion, the N_p interpolating Lagrange polynomials, ψ_n, are the basis functions, and the unknowns are now the interpolated values of the solution, $\mathbf{q}_e(\vec{x}_n,t)$, at specific nodes on the element, $\vec{x}_n$. It is important that the nodes be chosen to ensure a well-behaved interpolation. For example, choosing equidistant interpolation

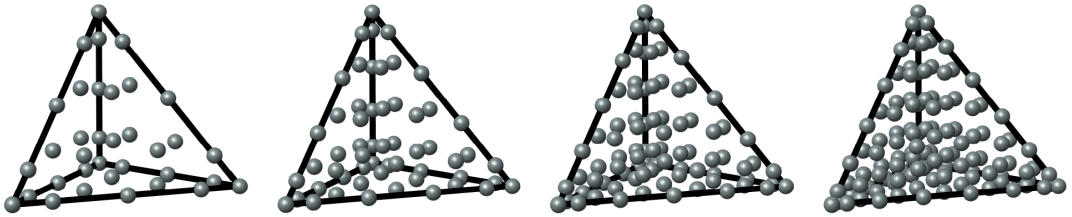

Figure 2.4: Optimized interpolation nodes on a regular tetrahedron, for polynomial orders 4–7.

nodes can lead to the classic Runge's phenomenon with spurious oscillations in the interpolated values. The Legendre-Gauss-Lobatto interpolation nodes are a typical choice, optimized for a minimal Lebesgue constant. Further information on constructing these nodal sets is given by Hesthaven and Warburton [55]. Examples of these nodes on tetrahedral elements for a range of polynomial orders are shown in Figure 2.4.

The nodal basis functions are not known explicitly, but can be instead related to the modal basis through a Vandermonde matrix, $\boldsymbol{\mathcal{V}}$, such that,

$$\bar{\mathbf{q}}_{e,v}(t) = \boldsymbol{\mathcal{V}} \hat{\mathbf{q}}_{e,v}(t), \tag{2.56}$$

where $\hat{\mathbf{q}}_{e,v}(t)$ indicates the vector of N_p coefficients for the variable, v, in element, e. The entries, $\{\boldsymbol{\mathcal{V}}\}_{nj} = P_j(\vec{x}_n)$, are the polynomials evaluated at the optimized interpolation nodes. Values of the solution variable, v, at the interpolation nodes in element, e, are given by the vector, $\bar{\mathbf{q}}_{e,v}$. One has the choice between a modal or nodal representation of the solution. The nodal form has the advantage that flux evaluations are less computationally expensive since they can be computed readily with the nodal values of the solution, while the modal form requires an interpolation first. The modal form may have advantages for some nonlinear problems [55]. In this work, the nodal form is used exclusively.

Similarly to the solution, the flux can be expressed as a nodal expansion,

$$\mathbf{f}_i \approx \sum_{n=1}^{N_p} \psi_n(\vec{x})\, \mathbf{f}_i(\mathbf{q}_e(\vec{x}_n, t)). \tag{2.57}$$

The above expansion is identical to the expansion of the solution, but it is only accurate for constant flux matrices. For spatially-varying flux matrices, *i.e.* a nonuniform mean flow, the above expression is a collocation projection of the flux onto the nodal basis. For problems in which the product of the solution and the mean flow terms in the flux matrices are poorly resolved by the interpolation, aliasing error will occur and

can have a significant impact on the solution accuracy and stability. This problem is discussed in detail in Chapter 4. It is also possible to evaluate the flux integrals using a sufficiently high degree quadrature rule to reduce aliasing, however, the additional computational cost associated with the evaluation can be prohibitive and therefore is not considered in this work.

2.5.2 Semi-discrete formulation

In Section 2.4, the test functions, $\mathbf{\Phi}_e$, were left undefined. To complete the semi-discrete scheme, the test functions are taken as the same polynomial basis functions as the solution is approximated with, and therefore $\mathbf{\Phi}_e = \mathbf{\Psi}_e$, where $\mathbf{\Psi}_e$ are the nodal basis functions. Now that the test functions and the solution approximation are defined, they can be substituted into the weak and strong formulations. The vector of nodal solution values is denoted by, $\bar{\mathbf{q}}_e$, with $N_p N_v$ degrees of freedom (DOF). Similarly, the solution vector, flux, and the source term at location $\vec{x}$ can be written as an interpolation,

$$\begin{aligned}
\mathbf{q}_e(\vec{x},t) &= \mathbf{\Psi}_e(\vec{x})\,\bar{\mathbf{q}}_e(t) \\
\mathbf{f}_i(\vec{x},t) &= \mathbf{\Psi}_e(\vec{x})\,\bar{\mathbf{f}}_{i,e}(t) \\
\mathbf{s}(\vec{x},t) &= \mathbf{\Psi}_e(\vec{x})\,\bar{\mathbf{s}}_e(t) \\
\tilde{\mathbf{f}}^b(\vec{x},t) &= \mathbf{\Psi}_e(\vec{x})\,\hat{\mathbf{f}}^b_e(t),
\end{aligned} \tag{2.58}$$

where $\bar{\mathbf{q}}_e$, $\bar{\mathbf{f}}_{i,e}$, $\bar{\mathbf{s}}_e$, and $\hat{\mathbf{f}}^b_e$ are the nodal values of the solution, flux, source term, and the numerical flux in element, e. Substituting the above interpolation of the solution for $\mathbf{q}_e$ in Equations 2.45 and 2.46, leads to,

$$\int_{\Omega_e} \mathbf{\Psi}_e^\intercal \mathbf{\Psi}_e \frac{\mathrm{d}\bar{\mathbf{q}}_e}{\mathrm{d}t}\,\mathrm{d}\Omega_e = \int_{\Omega_e} \frac{\partial \mathbf{\Psi}_e^\intercal}{\partial x_i} \mathbf{\Psi}_e \bar{\mathbf{f}}_{i,e}\,\mathrm{d}\Omega_e - \sum_b \int_{\Gamma_e^b} \mathbf{\Psi}_e^\intercal \mathbf{\Psi}_e \hat{\mathbf{f}}^b_e\,\mathrm{d}\Gamma^b_e + \int_{\Omega_e} \mathbf{\Psi}_e^\intercal \mathbf{\Psi}_e \bar{\mathbf{s}}_e\,\mathrm{d}\Omega_e\ , \tag{2.59}$$

for the weak form, and,

$$\begin{aligned}
\int_{\Omega_e} \mathbf{\Psi}_e^\intercal \mathbf{\Psi}_e \frac{\mathrm{d}\bar{\mathbf{q}}_e}{\mathrm{d}t}\,\mathrm{d}\Omega_e = &- \int_{\Omega_e} \mathbf{\Psi}_e^\intercal \frac{\partial \mathbf{\Psi}_e}{\partial x_i} \bar{\mathbf{f}}_{i,e}\,\mathrm{d}\Omega_e \\
&+ \sum_b \int_{\Gamma_e^b} \mathbf{\Psi}_e^\intercal \mathbf{\Psi}_e \left[\bar{\mathbf{f}}^b_{i,e} n_i - \hat{\mathbf{f}}^b_e\right] \mathrm{d}\Gamma^b_e + \int_{\Omega_e} \mathbf{\Psi}_e^\intercal \mathbf{\Psi}_e \bar{\mathbf{s}}_e\,\mathrm{d}\Omega_e\ ,
\end{aligned} \tag{2.60}$$

for the strong form, where the superscripts in the boundary flux integral indicate evaluation of the integral over element side, b. The nodal values of variable, v, of the solution, flux, numerical flux, and source term, are selected by, $\bar{\mathbf{q}}_{e,v}$, $\bar{\mathbf{f}}_{i,e,v}$, $\hat{\mathbf{f}}^b_{e,v}$, and $\bar{\mathbf{s}}_{e,v}$, respectively. The vectors of nodal values can be factored out of the above equations

resulting in the equations for variable, v,

$$\mathbf{M}\frac{\mathrm{d}\bar{\mathbf{q}}_{e,v}}{\mathrm{d}t} = \mathbf{S}_i\,\bar{\mathbf{f}}_{i,e,v} - \sum_b \mathbf{B}^b\,\hat{\mathbf{f}}^b_{e,v} + \mathbf{M}\bar{\mathbf{s}}_{e,v}, \tag{2.61}$$

for the weak form, and,

$$\mathbf{M}\frac{\mathrm{d}\bar{\mathbf{q}}_{e,v}}{\mathrm{d}t} = -\mathbf{S}_i^{\intercal}\,\bar{\mathbf{f}}_{i,e,v} + \sum_b \mathbf{B}^b\,\left(\bar{\mathbf{f}}^b_{i,e}n_i - \hat{\mathbf{f}}^b_e\right) + \mathbf{M}\bar{\mathbf{s}}_{e,v}, \tag{2.62}$$

for the strong form, where the element integrals have been defined as,

$$\{\mathbf{M}\}_{m,n} = \int_{\Omega_e} \psi_m\psi_n\,\mathrm{d}\Omega_e, \tag{2.63}$$

$$\{\mathbf{S}_i\}_{m,n} = \int_{\Omega_e} \frac{\partial\psi_m}{\partial x_i}\psi_n\,\mathrm{d}\Omega_e, \tag{2.64}$$

$$\left\{\mathbf{B}^b\right\}_{m,n} = \int_{\Gamma^b_e} \psi_m\psi_n\,\mathrm{d}\Gamma^b_e. \tag{2.65}$$

Multiplying Equations 2.61 and 2.62 by $\mathbf{M}^{-1}$, the local divergence and boundary flux lifting operators for the weak and strong formulations are defined as,

$$\mathbf{D}^{\mathrm{w}}_i = \mathbf{M}^{-1}\mathbf{S}_i, \tag{2.66}$$

$$\mathbf{D}^{\mathrm{s}}_i = \mathbf{M}^{-1}\mathbf{S}_i^{\intercal}, \tag{2.67}$$

$$\mathbf{L}^b = \mathbf{M}^{-1}\mathbf{B}^b. \tag{2.68}$$

The semi-discrete equations are in the form ready for temporal discretization,

$$\frac{\mathrm{d}\bar{\mathbf{q}}_{e,v}}{\mathrm{d}t} = \mathbf{D}^{\mathrm{w}}_i\,\bar{\mathbf{f}}_{i,e,v} - \sum_b \mathbf{L}^b\,\hat{\mathbf{f}}^b_{e,v} + \bar{\mathbf{s}}_{e,v}, \tag{2.69}$$

for the weak form, and,

$$\frac{\mathrm{d}\bar{\mathbf{q}}_{e,v}}{\mathrm{d}t} = -\mathbf{D}^{\mathrm{s}}_i\,\bar{\mathbf{f}}_{i,e,v} + \sum_b \mathbf{L}^b\,\left(\bar{\mathbf{f}}^b_{i,e}n_i - \hat{\mathbf{f}}^b_e\right) + \bar{\mathbf{s}}_{e,v}, \tag{2.70}$$

for the strong form. Notice that in the above formulations, the element matrices must be created and stored for each element in the computational domain. For large problems, the storage and computation of each matrix can be highly costly. The quadrature-free formulation described later in this chapter provides an efficient way to circumvent this problem for simplex elements.

2.5.3 Temporal discretization and the fully-discrete formulation

The semi-discrete forms, Equation 2.69 and 2.70, considered only the discretization of the governing equations in space and left the time derivative of the solution, $\frac{\mathrm{d}\bar{\mathbf{q}}_e}{\mathrm{d}t}$, continuous. To complete the scheme, the temporal discretization is now discussed. A common way of integrating the semi-discrete system of ordinary differential equations (ODEs) in time is to adopt a method of lines approach. Specifically, explicit Runge-Kutta approaches are a popular choice. In these approaches, past evaluations of the solution (in time) are used to update the solution to the next instance in time. In classic Runge-Kutta schemes, such as the fourth-order accurate, four-stage scheme (RK4), four evaluations (stages) of the right-hand side of Equations 2.69 and 2.70, are required at each time-step, and the global solution vector for each of the stages must be stored.

A popular set of schemes for aeroacoustics are low storage Runge-Kutta schemes, such as the fourth-order accurate, RK46-L scheme of Berland *et al.* [92], which requires storage of only two time-levels of the solution, in exchange for requiring a total of six evaluations of the residual. For the RK46-L scheme, the solution at time level $n+1$ can be obtained from the solution at time level n by,

$$\bar{\mathbf{q}}_e^{n+1} = \bar{\mathbf{q}}_e^{n} + \sum_{i=1}^{N_{\mathrm{st}}} \gamma_i \Delta t \mathbf{R}(\bar{\mathbf{q}}_e^{n}), \tag{2.71}$$

where i is the stage, N_{st} is the number of stages, Δt is the time-step, γ_i are optimized coefficients, and $\mathbf{R}$ is the right hand side of Equations 2.69 and 2.70. The particular choice of time integration scheme will depend on the relative importance of temporal accuracy to the computational cost for a given problem. Temporal accuracy and computational cost considerations are studied in detail in Chapter 3.

Stability considerations

In addition to accuracy and cost considerations, the stability of the time-domain numerical solutions is important to consider. The choice of time-step size largely dictates the stability of the problem. The global semi-discrete form can be expressed as,

$$\frac{\mathrm{d}\bar{\mathbf{q}}_{\mathrm{g}}}{\mathrm{d}t} = \mathbf{A}\bar{\mathbf{q}}_{\mathrm{g}} \ , \tag{2.72}$$

where matrix $\mathbf{A}$ contains all of the spatial operations for the global problem, and $\bar{\mathbf{q}}_{\mathrm{g}}$ is the vector of the DOF for the global problem. A *necessary* condition for stability is that the eigenvalues, λ, of the semi-discrete operator, $\mathbf{A}$, must be contained within the

stability region of the particular time integration scheme [55]. That is, for a stability region, S, the time step, Δt, must satisfy,

$$S \geq \Delta t \lambda \, , \tag{2.73}$$

for stability.

A typical way of estimating a stable time-step is by applying a Courant-Friedrichs-Lewy (CFL)-type condition [55], such as

$$\Delta t \leq C \frac{h f(p)}{v_c} \, , \tag{2.74}$$

where C is a constant, h is some measure of the element size, $f(p)$ is some function of the polynomial order, taken here as the smallest distance between nodes on the reference element, and the characteristic velocity, v_c is defined as the maximum wave speed, $|\vec{v}_\circ| + c_\circ$. This condition is therefore trying to restrict the distance traveled by a disturbance over a single time-step. Choosing too large of a time step can lead to instability and lower accuracy, while choosing too small of a time-step leads to increased computational cost. The time-step is therefore a critical parameter and must be chosen carefully. At fixed polynomial order, the smallest element with the highest wave speed, dictates the stability restriction. For meshing complex geometries, care must be taken so as to not introduce element sizes that are much smaller than required to achieve a fixed accuracy level, as it will lead to increased computational cost.

2.5.4 Quadrature-free formulation

While the above sections describe a complete DG scheme, the computational cost of such an approach has not yet been discussed. Previously, element matrices were defined for each element and were computed with a suitable quadrature rule and then stored. For problems requiring large numbers of elements to resolve the relevant aeroacoustic features, a large amount of memory is needed for storage of the element matrices. Furthermore, calculating each element matrix, even though it happens only once during every simulation, can take a considerable amount of time.

Atkins and Shu [56] addressed this problem by realizing that for element geometries with constant Jacobians, *i.e.* straight sided triangles and tetrahedra, the element matrices can be computed for a single *reference* element and then only the transformation Jacobians, mapping from $\vec{x} = (x, y, z)$ to $\vec{r} = (\xi, \eta, \zeta)$, must be stored for each element. This approach greatly reduces the overall storage requirements and has additional cost reduction benefits when vectorization is considered. Examples of reference elements for the straight-sided triangle and tetrahedron are shown in Figure 2.5. Defining the

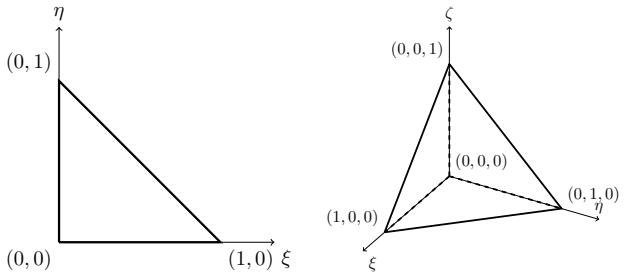

Figure 2.5: Reference triangle and tetrahedron elements.

element matrices for element, e, as transformed reference element matrices gives,

$$\{\mathbf{M}\}_{m,n} = |J_e| \int_{\Omega_{\text{ref}}} \psi_m \psi_n \, \mathrm{d}\Omega_{\text{ref}}, = |J_e| \, \{\mathbf{M}_{\text{ref}}\}_{m,n} \tag{2.75}$$

$$\{\mathbf{S}_i\}_{m,n} = |J_e| \left. \frac{\partial r_j}{\partial x_i} \right|_e \int_{\Omega_{\text{ref}}} \frac{\partial \psi_m}{\partial r_j} \psi_n \, \mathrm{d}\Omega_{\text{ref}} = |J_e| \left. \frac{\partial r_j}{\partial x_i} \right|_e \{\mathbf{S}_{j,\text{ref}}\}_{m,n}, \tag{2.76}$$

$$\left\{\mathbf{B}^b\right\}_{m,n} = |\Gamma_e^b| \int_{\Gamma_{\text{ref}}^b} \psi_m \psi_n \, \mathrm{d}\Gamma_{\text{ref}}^b = |\Gamma_e^b| \left\{\mathbf{B}_{\text{ref}}^b\right\}_{m,n}, \tag{2.77}$$

where J_e is the transformation Jacobian for element, e, $|\Gamma_e^b|$ is the length of side b, and r_j is the reference coordinate system.

Additional benefits of the quadrature-free approach include more efficient cache and memory usage by lumping together every element's residual calculation on a particular processor into a single, efficient matrix product. While the quadrature-free approach leads to significant computational cost reductions, it can only consider straight-sided elements. Near walls or other geometrical features, it is desirable to use curved elements, since they can accurately represent the geometry without having to substantially increase the local element density.

2.5.5 Implementation

To solve large aeroacoustic problems with millions of DOF, care must be taken to ensure that the implementation of the scheme is optimized for maximizing computational efficiency. The quadrature-free formulation significantly reduces the storage necessary for the DGM operator, and due to only requiring a few global template matrices, it can more efficiently utilize the cache. Coupling the quadrature-free approach with an efficient datastructure, such that all DOF and flux evaluations are stored contiguously in the order of operations, the implementation can take advantage of vectorized matrix products implemented through the Basic Linear Algebra Subprograms (BLAS) library [93].

Quadrature-free vectorized implementation

For each straight-sided simplex element, the equations for the residual update can be written in the reference element space using template element matrices, common to all of the elements, and transformed fluxes. This allows the residual update to be vectorized, updating all elements globally with a single matrix product. To bring the equations into a vectorized form, the nodal values of the solution, residual, and the transformed fluxes over all elements are stored in an array, ordered by the nodal index and element number, and occupying a contiguous region of memory,

$$\mathbf{Q}_v = \left[\bar{\mathbf{q}}_{1,v},\ \bar{\mathbf{q}}_{2,v},\ \ldots,\ \bar{\mathbf{q}}_{N_\mathrm{e},v}\right], \text{ and,} \tag{2.78}$$

$$\frac{\mathrm{d}\mathbf{Q}_v}{\mathrm{d}t} = \left[\frac{\mathrm{d}\bar{\mathbf{q}}_{1,v}}{\mathrm{d}t},\ \frac{\mathrm{d}\bar{\mathbf{q}}_{2,v}}{\mathrm{d}t},\ \ldots,\ \frac{\mathrm{d}\bar{\mathbf{q}}_{N_\mathrm{e},v}}{\mathrm{d}t}\right], \tag{2.79}$$

$$\bar{\mathbf{F}}_v = \left[\begin{array}{cccc}
\bar{\mathbf{f}}_{i,e,v}\left.\frac{\partial \xi}{\partial x_i}\right|_e & \bar{\mathbf{f}}_{i,e,v}\left.\frac{\partial \xi}{\partial x_i}\right|_e & & \bar{\mathbf{f}}_{i,e,v}\left.\frac{\partial \xi}{\partial x_i}\right|_e \\
\bar{\mathbf{f}}_{i,e,v}\left.\frac{\partial \eta}{\partial x_i}\right|_e & \bar{\mathbf{f}}_{i,e,v}\left.\frac{\partial \eta}{\partial x_i}\right|_e & & \bar{\mathbf{f}}_{i,e,v}\left.\frac{\partial \eta}{\partial x_i}\right|_e \\
\bar{\mathbf{f}}_{i,e,v}\left.\frac{\partial \zeta}{\partial x_i}\right|_e & \bar{\mathbf{f}}_{i,e,v}\left.\frac{\partial \zeta}{\partial x_i}\right|_e & & \bar{\mathbf{f}}_{i,e,v}\left.\frac{\partial \zeta}{\partial x_i}\right|_e \\
\frac{|\Gamma_e^{\{1\}}|}{|J_e|}\hat{\mathbf{f}}_{e,v}^{\{1\}} & \frac{|\Gamma_e^{\{1\}}|}{|J_e|}\hat{\mathbf{f}}_{e,v}^{\{1\}} & \cdots & \frac{|\Gamma_e^{\{1\}}|}{|J_e|}\hat{\mathbf{f}}_{e,v}^{\{1\}} \\
\frac{|\Gamma_e^{\{2\}}|}{|J_e|}\hat{\mathbf{f}}_{e,v}^{\{2\}} & \frac{|\Gamma_e^{\{2\}}|}{|J_e|}\hat{\mathbf{f}}_{e,v}^{\{2\}} & & \frac{|\Gamma_e^{\{2\}}|}{|J_e|}\hat{\mathbf{f}}_{e,v}^{\{2\}} \\
\vdots & \vdots & & \vdots \\
\underbrace{\frac{|\Gamma_e^{\{N_\mathrm{s}\}}|}{|J_e|}\hat{\mathbf{f}}_{e,v}^{\{N_\mathrm{s}\}}}_{e=1} & \underbrace{\frac{|\Gamma_e^{\{N_\mathrm{s}\}}|}{|J_e|}\hat{\mathbf{f}}_{e,v}^{\{N_\mathrm{s}\}}}_{e=2} & & \underbrace{\frac{|\Gamma_e^{\{N_\mathrm{s}\}}|}{|J_e|}\hat{\mathbf{f}}_{e,v}^{\{N_\mathrm{s}\}}}_{e=N_\mathrm{e}}
\end{array}\right], \tag{2.80}$$

where N_e is the total number of quadrature-free elements and N_s is the number of sides of the element. Additionally, the reference element matrices are stored contiguously such that,

$$\bar{\mathbf{D}} = \left[\mathbf{D}_\mathrm{ref}^{\{1\}},\ \mathbf{D}_\mathrm{ref}^{\{2\}},\ \mathbf{D}_\mathrm{ref}^{\{3\}},\ \mathbf{L}_\mathrm{ref}^{\{1\}},\ \mathbf{L}_\mathrm{ref}^{\{2\}},\ \ldots\ \mathbf{L}_\mathrm{ref}^{\{N_\mathrm{s}\}}\right], \tag{2.81}$$

where $\mathbf{D}_\mathrm{ref}^{i}$ and $\mathbf{L}_\mathrm{ref}^{b}$ are the divergence and flux lifting matrices evaluated on the reference element for reference coordinate direction, r_i, and side, b. Updating the residual for all elements at once is done through the matrix product,

$$\frac{\mathrm{d}\mathbf{Q}_v}{\mathrm{d}t} = \bar{\mathbf{D}}\bar{\mathbf{F}}_v, \tag{2.82}$$

for each variable, v. The source term, if required, can be computed and added to the residual.

2.5.5.1 Non-quadrature-free implementation

For elements with a non-constant Jacobian, it is no longer possible to factor out template matrices. Instead, each element matrix must be pre-computed and stored in memory and the residual updated for a single element at a time. The process is further complicated by the boundary flux integrals over the curved sides. In Section 2.5.2, the numerical flux was discretized through the same nodal expansion as the solution. Since the numerical flux depends on products of the solution variables with the surface normal field, it will nonlinearly depend on the element geometry for elements with curved sides. Also, the surface normal field will generally not be polynomial, and the collocation projection of the flux, Equation 2.58, will be under-resolved, causing aliasing errors. If these boundary integrals are treated improperly, they can cause inaccuracy of the solution and numerical instability [55].

To accurately evaluate the curved boundary integrals, the collocation-projection of the numerical flux is dropped, and instead, the boundary flux integrals are evaluated using a quadrature rule. Approximating the boundary flux integral for the weak formulation with a N_q point quadrature rule results in,

$$\int_{\Gamma_e} \boldsymbol{\psi}_e^\intercal \tilde{f}^b_{e,v} \, \mathrm{d}\Gamma_e \approx \sum_{n=1}^{N_q} \boldsymbol{\psi}_e^\intercal(\vec{\chi}_n) \tilde{f}^b_{e,v}(\vec{\chi}_n) w_n = \mathbf{B}_{\mathrm{q}}^{\{b\}} \hat{\mathbf{f}}^b_{e,v}(\vec{\chi}), \tag{2.83}$$

where $\boldsymbol{\psi}_e$ is the vector of nodal basis functions, and $\vec{\chi}_n$ and w_n are the n-th quadrature point location and weight, respectively. The numerical flux evaluated at the quadrature points, is denoted by $\hat{\mathbf{f}}^b_{e,v}(\vec{\chi})$ for variable, v. This implementation uses a symmetric quadrature rule over each triangular side defined by Cools [94]. Since the numerical flux is generally non-polynomial, the integration accuracy of the quadrature rule is chosen to be at least twice that required to integrate a polynomial of the solution order. For highly nonlinear sides, the integration accuracy may need to be increased. The matrix, $\mathbf{B}_{\mathrm{q}}^{\{b\}}$ is pre-computed, multiplied by the inverse mass matrix, and then stored for each curved side, replacing the boundary flux lifting matrix in Equation 2.69. The flux is evaluated using values of the solution found through the interpolation,

$$\bar{\mathbf{q}}^b_{e,v} = \mathbf{P}^{\{b\}} \boldsymbol{\mathcal{V}}^{-1} \bar{\mathbf{q}}_{e,v}, \tag{2.84}$$

with $\left\{\mathbf{P}^{\{b\}}\right\}_{n,m} = P_m(\vec{\chi}_n^{\{b\}})$, that interpolates the solution to the quadrature points on side, b. The same procedure can be used to compute the boundary flux integral for the strong form.

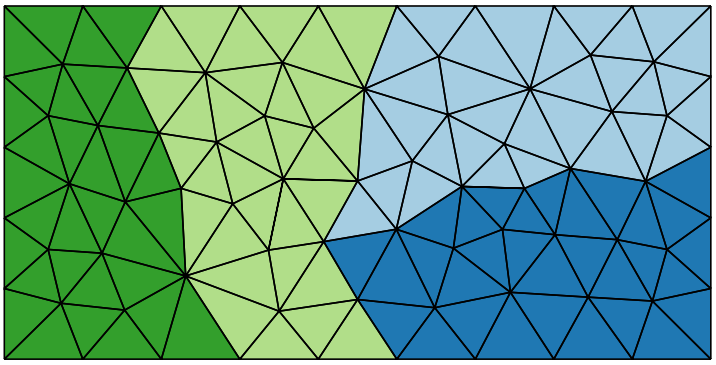

Figure 2.6: Example two-dimensional mesh partitioned into four sub-meshes.

Distributed memory implementation

The element-local nature of the solution for time-domain DGM, allows for efficient decomposition of the computational domain. Partitioning of the mesh is accomplished through the library, METIS, optimizing the size and connectivity to balance the computational cost [95]. The element connectivity information is represented by a graph, with elements as vertices and edges representing connections between elements. Using a k-way graph-partitioning algorithm, N partitions are created, minimizing the number of edges, or connections, between partitions. This minimizes the amount of information that must be shared between partitions at each time-step. After partitioning, the elements in each partition are reordered by the inverse Cuthill-McKee algorithm to improve the adjacency of elements. Since the cost to evaluate the residual for quadrature-free elements is lower than for non-quadrature-free elements, it is important to balance the more costly elements across the partitions. This is done to avoid a single partition limiting the speed of the others. To achieve this, the vertex weights in the METIS partitioning tool for the non-quadrature-free elements can be increased to better balance the cost. An example partitioned mesh is shown in Figure 2.6 with each partition highlighted in a different color. Once partitions are created and the element geometry and connectivity information for each partition are assigned to specific processes, the time-integration of the initial conditions can be performed. Before each update of the local processor's solution to the next time-level, solution information must be exchanged with partitions sharing an interface, to allow the evaluation of the numerical fluxes. Solution transfer is enabled through the use of the Message Passing Interface (MPI), implemented in the OpenMPI library [86]. For each evaluation of the residual, the

- fluxes are evaluated in the element volume and the along the sides,
- fluxes are transformed from the physical element to the reference element (if a quadrature-free element),

- source term is evaluated, if required,
- residual is updated individually for each non-quadrature-free element and with the vectorized implementation for the quadrature-free elements,
- solution is advanced in time,
- solution is interpolated at the quadrature points on the curved sides, and,
- the updated solution at the interfaces of the partitions is transferred via a message passing procedure if distributed, or stored if it exists in shared memory.

2.6 Verification of the implementation

Now that the numerical scheme and its implementation have been defined, benchmark problems with analytical solutions are solved to verify that the implementation is consistent with the governing physical equations and that the computational performance is as expected. Simple free-field propagation problems are solved first, to ensure that the numerical scheme can accurately simulate the behavior of each LEE solution mode, discussed in Section 2.3.1. Following the solution of the free-field problems, two time-harmonic problems with hard-wall boundary conditions are solved, verifying the curved element treatment and the boundary conditions. Finally, the parallel efficiency of the scheme is investigated.

While only basic verification problems are solved in this chapter, additional application-specific problems are compared to analytical solutions in later chapters. For instance, propagation through a non-uniform medium in Chapter 5, and the radiation of duct modes with flow in Chapters 6 and 7.

2.6.1 Acoustic pulse propagation initial value problem

To test the implementation of the DGM, a problem of propagation of a simple disturbance is solved. The problem consists of a one-dimensional acoustic pulse, varying only in the x-direction and centered at $x = x_\circ$ at time $t = 0$. The solution is allowed to develop into two disturbances propagating in opposite directions, with or against a uniform mean flow. The problem is solved in a two-dimensional computational domain and a convergence study with mesh size and polynomial order is performed.

Analytical Solution

Given an initial, Gaussian perturbation of pressure of the form,

$$F(x) = a \exp\left(-\frac{(x - x_\circ)^2}{2w^2}\right), \tag{2.85}$$

the solution will consist of the propagation of left and right moving disturbances. The width and center of the initial perturbation are given by w and $x_\circ$, and the initial amplitude by a. The time-evolution of the solution can be found to be

$$\begin{aligned} \rho'(x,t) &= \frac{1}{2c_\circ^2}\left[F(x-(u_\circ - c_\circ)t) + F(x-(u_\circ + c_\circ)t)\right], \\ u'(x,t) &= \frac{1}{\rho_\circ c_\circ}\left[F(x-(u_\circ - c_\circ)t) - F(x-(u_\circ + c_\circ)t)\right], \text{ and,} \\ p'(x,t) &= \frac{1}{2}\left[F(x-(u_\circ - c_\circ)t) + F(x-(u_\circ + c_\circ)t)\right], \end{aligned} \tag{2.86}$$

for the density, x-velocity, and pressure fluctuations, respectively. The velocity fluctuations in the y- and z-directions are zero. The uniform mean flow velocity in the x-direction and the mean sound speed are given by $u_\circ$ and $c_\circ$.

Accuracy

To evaluate both the convergence of the error with the element size and polynomial order, as well as the effect of the time integration scheme on the accuracy, a mesh convergence study is performed. Two integration times are chosen, $t_f = 1$, and $t_f = 7$. For $t_f = 1$, and for polynomial orders $p = 1$ through $p = 10$, the problem is solved on successively finer meshes. To attempt to highlight the effects of the time integration, a CFL of 1, as calculated by Equation 2.74, is chosen. After the final integration time is reached, the solution is interpolated onto quadrature points within each element and the relative-L^2 error,

$$\|E\|^2 = \frac{\sqrt{\int_\Omega |\mathbf{q}_{\text{num}} - \mathbf{q}_{\text{ex}}|^2 \, \mathrm{d}\Omega}}{\sqrt{\int_\Omega |\mathbf{q}_{\text{ex}}|^2 \, \mathrm{d}\Omega}}, \tag{2.87}$$

where $\mathbf{q}_{\text{num}}$ is the numerical solution and $\mathbf{q}_{\text{ex}}$ is the exact solution, is evaluated.

Figure 2.7a shows the results of the short time convergence study. The average element width, h, is non-dimensionalized by the width of the initial disturbance. For small h/w, each order achieves a $\mathcal{O}(h/w)^{p+1}$ convergence rate, indicating that the solution is resolved enough for the polynomial interpolation error to dominate and the error of the time integration scheme is sufficiently small enough to not impact the convergence.

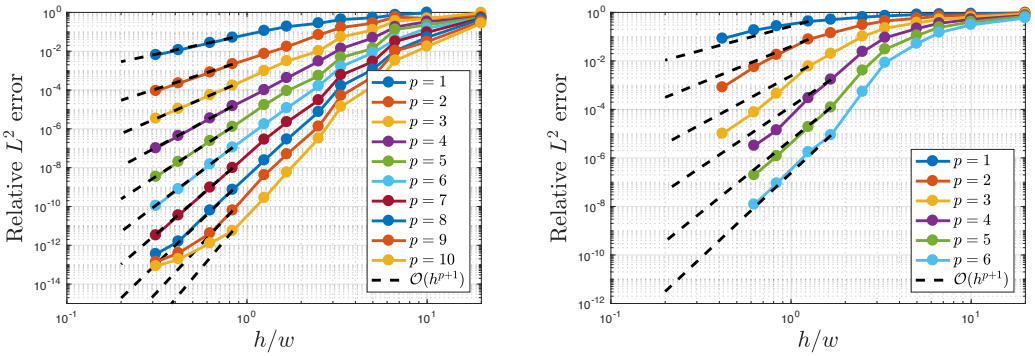

(a) $t = 1.0$ (b) $t = 7.0$

Figure 2.7: Mesh and order convergence study of a propagating Gaussian pulse in a channel at two times.

For large h/w, the convergence rate is far less than the theoretical interpolation error predicts, indicating that other sources of error are present. Errors in wave phase and amplitude (dispersion and dissipation), which were negligible for the highly resolved solutions, likely are the dominant sources of error for the large h/w solutions and are important for practical computations with lower DOF. These errors will be analyzed in greater detail using a dispersion analysis technique in Chapter 3.

The same procedure is performed again for a time of $t = 7$ and orders 1 through 6 and the results are shown in Figure 2.7b. At each polynomial order, the theoretical interpolation convergence rate of $\mathcal{O}(h/w)^{p+1}$ is again reached.

Computational Cost

To assess the impact of the high-order discretization on the computational cost, the CPU time for the above convergence study is recorded. Each computation is performed in serial to highlight the relationship between the mesh size, polynomial order, integration time, and the CPU time, only. All results are computed with a 2.3 GHz Intel Core i7 processor. Figures 2.8a and 2.8b illustrate the relationship between the L^2 error and the CPU time for times $t = 1.0$ and $t = 7.0$. For the high accuracy region, the benefit of using a high-order discretization is clear, as large reductions in CPU time are seen by increasing the order. For the lower accuracy region, large cost savings are seen up to approximately order $p = 5$, after which, the savings are minimal.

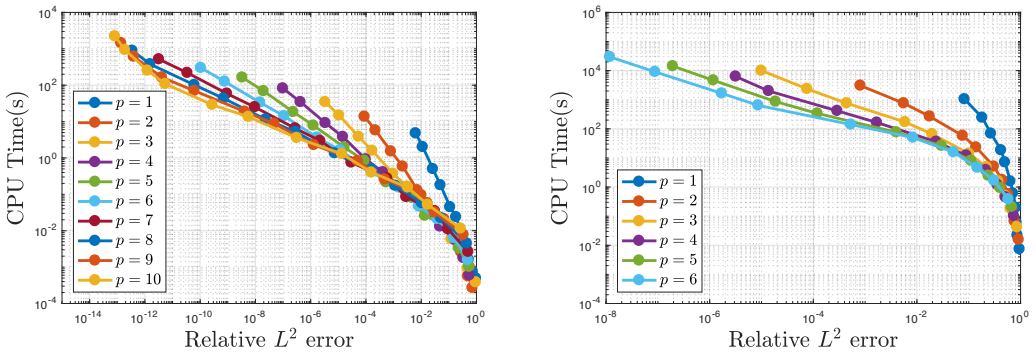

(a) $t = 1.0$ (b) $t = 7.0$

Figure 2.8: Computational cost study of a propagating Gaussian pulse in a channel at two times.

2.6.2 Entropy spot advection initial value problem

To test the capability of the three-dimensional DGM implementation to accurately predict the behavior of the entropy mode of the LEE, an advected, localized entropy perturbation initial value problem is solved. An entropy spot can represent a localized, thermal perturbation of the gas temperature, resulting only in changes to density, which are advected by the mean flow.

In this problem, a Gaussian entropy spot is considered,

$$\begin{aligned} \rho' &= Ae^{\left(\frac{\|\vec{\mathbf{d}}\|}{\sigma^2}\right)} \\ (\rho u)' &= \rho' u_\circ \\ (\rho v)' &= \rho' v_\circ \\ (\rho w)' &= \rho' w_\circ \\ p' &= 0, \end{aligned} \tag{2.88}$$

where A is the amplitude of the disturbance, $\|\vec{\mathbf{d}}\|$, is the magnitude of the distance to the initial center of the Gaussian, and σ is the width of the Gaussian. After initializing the density to Equation 2.88, the solution at any instance in time is given simply by,

$$\begin{aligned} \rho' &= Ae^{\left(\frac{\|\vec{\mathbf{d}}-\vec{v}_\circ t\|}{\sigma^2}\right)} \\ (\rho u)' &= \rho' u_\circ \\ (\rho v)' &= \rho' v_\circ \\ (\rho w)' &= \rho' w_\circ \\ p' &= 0, \end{aligned} \tag{2.89}$$

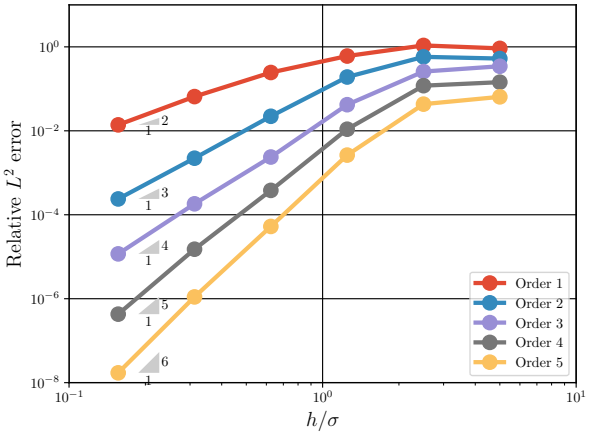

Figure 2.9: Mesh and order convergence of the relative L^2 error for advection of an entropy spot.

where $\vec{v}_\circ$ is the mean flow velocity vector and t is the time.

A convergence study of the relative L^2 error with increasing mesh size and polynomial order is used to assess the accuracy of the numerical implementation. Solutions are obtained with six increasing size meshes and at polynomial orders one through five, with fixed physical parameters for each case. At a non-dimensional time, $t = 0$, the entropy spot is initialized in a Mach number 0.5 mean flow in the $x-$direction, and allowed to advect with the mean flow until time $t = 20$ is reached. The width of the disturbance is fixed at $\sigma = 1$ and the initial amplitude fixed to $A = 1$. The distance traveled by the disturbance over the time period corresponds to ten widths of the initial disturbance. At the final instance in time, the relative L^2 errors are calculated in reference to the analytical solution, Equation 2.89 for all variables. Figure 2.9 shows the results of the convergence study for each mesh and order considered.

As indicated by the gray triangles, increasing the polynomial order has the expected effect of substantially increasing the convergence rate with mesh size, achieving the expected $\mathcal{O}(h/\sigma)^{p+1}$ rate for each order. For example, to achieve an error of approximately 2×10^{-2}, the order five solution requires a mesh of only $1,031$ tetrahedra, compared to a mesh of $54,000$ tetrahedra for the order two solution.

2.6.3 Vortex advection initial value problem

To test the capability of the three-dimensional DGM implementation to accurately predict the behavior of the vorticity mode of the LEE, an advected, vortex perturbation initial value problem is solved. With a uniform mean flow, the vortex propagates with

the velocity of the mean flow and its shape and magnitude remain unchanged. While the vortex is two-dimensional, the problem still offers an evaluation of the accuracy of the full 3D implementation since a 3D unstructured mesh is used.

The problem considers an initial vortex perturbation of the form,

$$\begin{aligned} \rho' &= 0 \\ (\rho u)' &= A e^{\left(\frac{-\|\vec{\mathbf{d}}\|^2}{\sigma^2}\right)} (y_\circ - y)\, \rho_\circ \\ (\rho v)' &= A e^{\left(\frac{-\|\vec{\mathbf{d}}\|^2}{\sigma^2}\right)} (x - x_\circ)\, \rho_\circ \\ (\rho w)' &= 0 \\ p' &= 0, \end{aligned} \tag{2.90}$$

where A is the amplitude of the velocity disturbance, $\|\vec{\mathbf{d}}\|$, is the magnitude of the distance to the center, and σ is the width. The coordinate $(x_\circ, y_\circ)$ is the center of the vortex at $t = 0$. After initializing the variables to Equation 2.90, the solution at any instance in time is given by,

$$\begin{aligned} \rho' &= 0 \\ (\rho u)' &= A e^{\left(\frac{-\|\vec{\mathbf{d}} - \vec{v}_\circ t\|^2}{\sigma^2}\right)} (y_\circ - y + v_\circ t)\, \rho_\circ \\ (\rho v)' &= A e^{\left(\frac{-\|\vec{\mathbf{d}} - \vec{v}_\circ t\|^2}{\sigma^2}\right)} (x - x_\circ - u_\circ t)\, \rho_\circ \\ (\rho w)' &= 0 \\ p' &= 0, \end{aligned} \tag{2.91}$$

where $\vec{v}_\circ$ is the mean flow velocity vector, $u_\circ$ is the $x-$component of the mean velocity, $v_\circ$ is the $y-$component of the mean velocity, and t is the time from the initialization of the disturbance.

A convergence study of the relative L^2 error with increasing mesh size and polynomial order is used to assess the accuracy of the numerical implementation. Solutions are obtained with six increasing size meshes and at polynomial orders one through five, with fixed physical parameters for each case. At a non-dimensional time, $t = 0$, the vortex is initialized in a Mach number 0.5 mean flow in the $x-$direction, and allowed to advect with the mean flow until the time $t = 20$ is reached. The width of the disturbance is fixed at $\sigma = 1$ and the initial amplitude fixed to $A = 1$. The distance traveled by the disturbance over the time period corresponds to ten widths of the initial disturbance. At the final instance in time, the relative L^2 errors are calculated in reference to the analytical solution, Equation 2.91. Figure 2.10 shows the results of

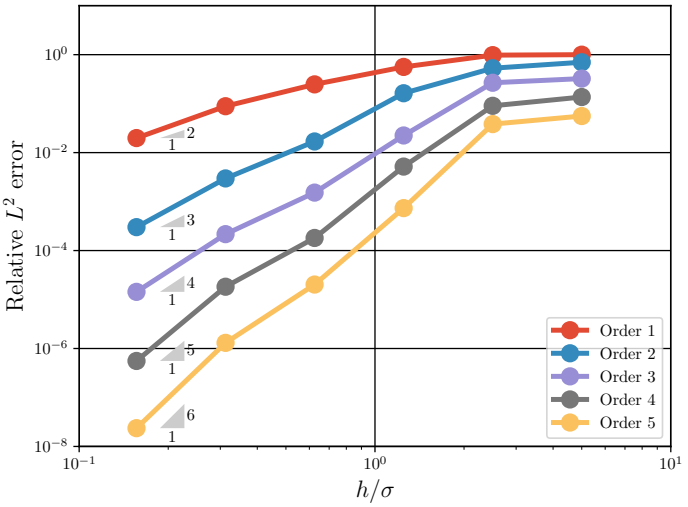

Figure 2.10: Mesh and order convergence of the relative L^2 error for advection of a 2D vortex perturbation.

the convergence study for each mesh and order considered. Similar to the results for the advection of the entropy spot in the previous section, the expected convergence rate of $\mathcal{O}(h/\sigma)^{p+1}$ is achieved.

2.6.4 Cylinder scattering problem

To evaluate how well the DGM implementation predicts acoustic scattering from curved, hard-wall geometries, a two-dimensional cylinder scattering problem is developed. An analytical solution is derived and then used to compare to long time integration numerical results. The problem, illustrated in Figure 2.11, consists of a cylinder of radius R, located a distance L from a time-harmonic, distributed source located at point S, of the form,

$$f(r_s) = e^{-\ln(2)\frac{r_s}{w}^2}, \tag{2.92}$$

where w is the source width and r_s is the radial distance from the center of the source. The point, O, is the observer point at which the solution is calculated. The analytical solution to this problem is given in Appendix A.3.

Results

The cylindrical computational domain of radius 20, shown in Figure 2.12a, is created with the distributed source of $w = \frac{1}{5}$ and frequency $\omega = 4\pi$ centered at the origin.

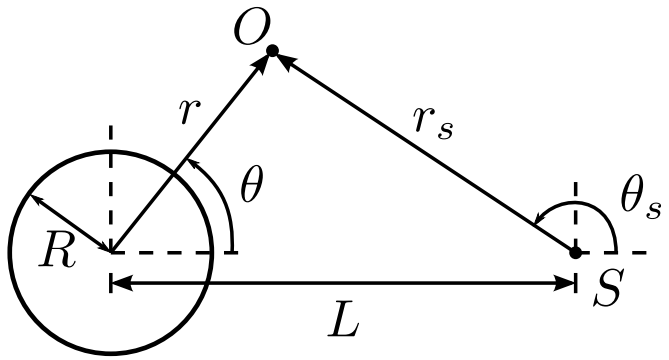

Figure 2.11: Cylinder scattering problem definition.

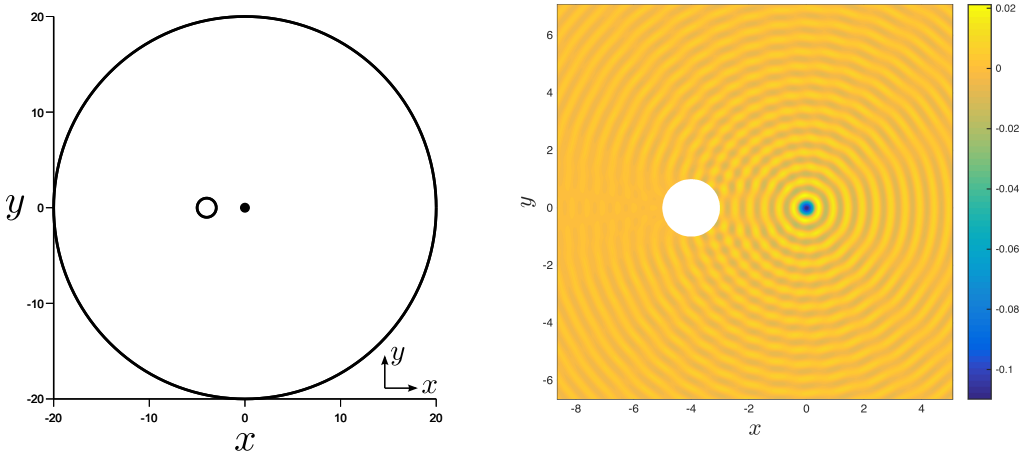

(a) (b)

Figure 2.12: (a): Computational domain of the cylinder scattering problem. Boundaries are shown with black lines and the distributed source is shown as a black patch. (b): Near-field pressure contours at an instance in time.

Characteristic boundary conditions are imposed on all far-field boundaries and a hard-wall boundary condition is imposed on the surface of the cylinder.

The solution is computed up to the time $t = 125$, corresponding to 250 periods of the source. The pressure field of the solution at an instance in time is illustrated in Figure 2.12b. Both the incident field and the scattered field are clearly visible including the expected shadow region behind the cylinder, opposite to the source.

The analytical solution is computed along the line $y = 0$ and compared to the numerical solution. Figure 2.13a shows the pressure perturbations along the line, computed numerically and compared to the analytical solution. The numerical and analytical solutions are in clear agreement. Figure 2.13b shows the root-mean-squared pressure over a single period. Again, the analytical and numerical solutions are in close agreement.

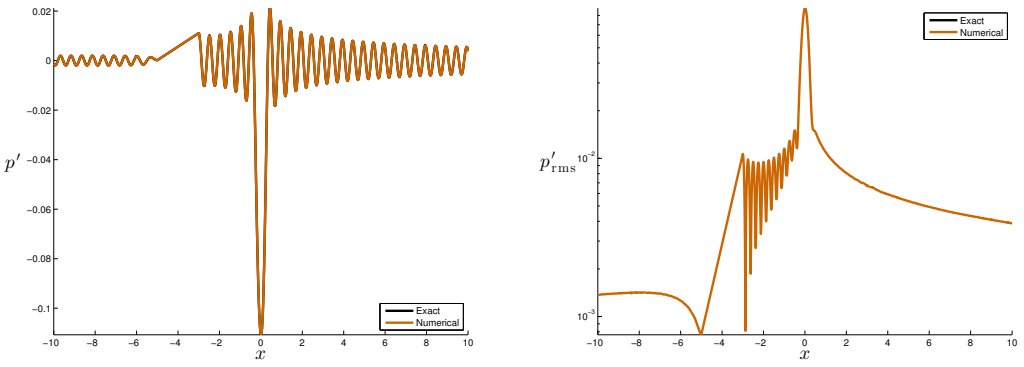

(a) (b)

Figure 2.13: (a): Pressure perturbation at and instance in time and (b): RMS pressure over one period. Comparison between the analytical and numerical solutions along the centerline.

2.6.5 Vibrating sphere boundary value problem

A problem of a vibrating sphere is solved in this section to assess the accuracy of the three-dimensional implementation when curved elements are used. The radius of the sphere vibrates with small amplitude like,

$$d(t) = d_\circ + d' e^{i\omega t}, \tag{2.93}$$

where d is the radius, $d_\circ$ is the stationary radius, d' is the amplitude, and ω is the angular frequency of vibration. The analytical solution to this problem is given in Appendix A.4.

Numerical solution

This problem is designed to evaluate the prediction of the acoustic mode of the LEE, and due to the non-trivial boundary geometry, also evaluate the treatment of curved-sided elements. Due to the symmetry of the problem, instead of considering a spherical domain, an eighth of a sphere, with symmetry boundary conditions is used instead. Two meshes are created, one with linear representation of the sphere, and one with quadratic representation, to identify the impact of curved elements on the solution accuracy. The propagation medium is defined as quiescent with $u_\circ = 0$, and with uniform quantities of mean density, $\rho_\circ = 1$, pressure, $p_\circ = 1$, and sound speed, $c_\circ = 1$. To consider only small vibrations of the sphere, the maximum radial perturbation is fixed to $d' = 0.01$, giving the resulting velocity of the sphere's surface as $v'(r = d_\circ) = 0.01 i\omega e^{i\omega t}$. For an angular frequency of $\omega = 3\pi$, the governing equations are integrated until the

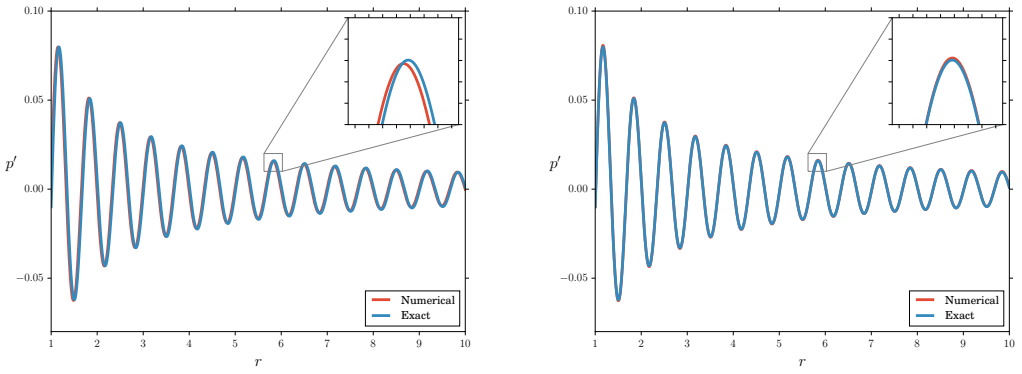

(a) (b)

Figure 2.14: Pressure extracted radially outward from the sphere surface. (a): linear geometry representation. (b): quadratic geometry representation.

time, $t = 10$, when the acoustic disturbances have reached the domain boundary. To achieve high accuracy with large elements, the order 6 polynomial basis is used.

Figure 2.14 shows the fluctuating pressure extracted along the radial direction, from the sphere surface to the end of the domain at the final time, for the linear and quadratic boundary cases. For the linear boundary case, it is clear that the numerical solution is shifted in space relative to the exact solution. This behavior can be explained by the linear representation of the surface. Even though a high polynomial order is used, the interpolation points are not placed exactly on the surface of the sphere, leading to an error in the wave's position. The quadratic boundary avoids the wave position error by nearly conforming the interpolation points to the sphere's surface, leading to a closer agreement to the analytical solution.

2.6.6 Parallel scaling

An important measure of performance for a parallel code is its scalability. The scalability measures to what extent adding additional compute units improves the overall execution time. The serial execution time, *i.e.* using a single compute unit, depends on the processor architecture, such as the clock speed and cache size, and the memory bandwidth. Additionally, the relative number of quadrature-free and non-quadrature-free elements will have an impact on the computational efficiency. The parallel execution time will depend on whether the problem is solved in shared memory on a single compute node, or distributed over a cluster of nodes with higher latency communication between compute units, as well as the load balancing of the problem over the compute units. Because of the additional overhead associated with parallelization of the scheme, one can not expect that simply distributing the problem over a factor N

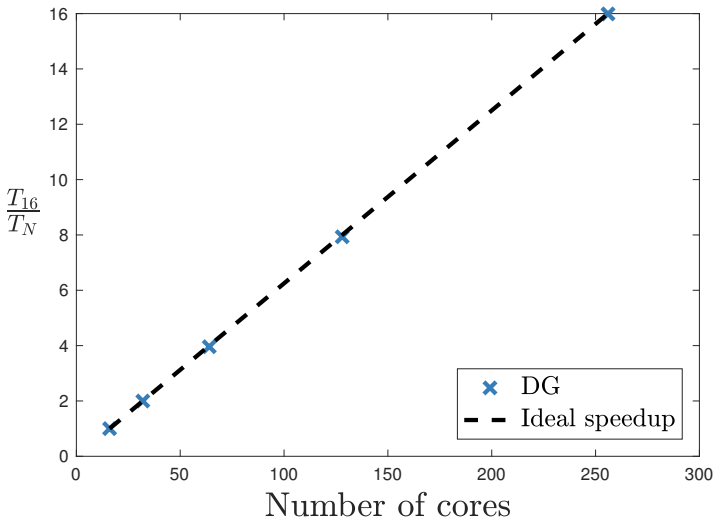

Figure 2.15: Strong scalability of the parallel DG implementation. The speedup is defined as $\frac{T_{16}}{T_N}$, where T_{16} is the wall time for a one node, 16 core, calculation.

compute units will always result in a factor N speedup relative to the serial execution time.

A common metric for parallel efficiency is strong scalability. Strong scalability measures how much of a speedup is attained when increasing the number of compute units for a fixed problem size. A perfect strong scaling would imply that doubling the number of compute units, halves the execution time of the code. To assess the strong scalability, a problem of an acoustic pulse in a cube domain is solved for a fixed mesh of approximately 1.3 million tetrahedra of polynomial order of six. Since the execution time is directly proportional to the number of time-steps taken, a short integration time can be taken to reduce the execution time for the single node calculation. The mesh is divided into one partition for each core used. The solution is computed on the University of Southampton Iridis 4 cluster which uses Intel 2.6GHz Sandybridge CPUs with 16 cores and 64 GB of memory per node. The inter-processor communication is facilitated by an Infiniband network.

Starting with a solution to the problem on a single node with 16 cores, additional solutions are computed using two, four, eight, and sixteen nodes, with 256 cores used for the sixteen node calculation. Figure 2.15 shows the speedup defined as the ratio between the execution time on a single node, T_{16}, to the execution time for N cores, T_N. For this range of nodes, the speedup matches closely to the ideal strong scaling speedup.

Chapter 3

Dispersion analysis of the discrete linearized Euler equations

Aeroacoustics problems, such as turbofan noise predictions, require both high accuracy, for far-field sound radiation, and high computational efficiency, for considering complex, three-dimensional problems. Nodal Discontinuous Galerkin Methods (DGM) have proven to be popular schemes for the solution of hyperbolic problems where both high-order accuracy and efficient scalability to large problem size are required.

When solving complex aeroacoustic problems in the time domain, one is required to choose the mesh size, polynomial order, and time-step to maximize spatial and temporal accuracy, to ensure the stability of the numerical solution, and while simultaneously minimizing the computational cost of the simulation. This chapter seeks to shed light on the relationships between the physical problem, the accuracy and stability of the numerical solution, and the computational cost, and also attempts to give guidelines for the choice of simulation parameters.

The accuracy of the DGM is well known to exhibit an optimal $\mathcal{O}\left(h^{p+1}\right)$ convergence rate of the interpolation, or truncation, error for smooth problems, where h is a measure of the mesh size, and p is the order of the polynomial basis [55]. For aeroacoustic problems, it is critical to consider errors associated with the propagation of the waves in space. These propagation errors are known as dissipation and dispersion error. Dissipation error causes a reduction in amplitude of the initial wave or disturbance as it propagates, while dispersion error causes a phase shift. Unlike the interpolation error, dissipation and dispersion errors are additive; as the waves propagate, the errors increase proportional to the distance and time traveled. These additive errors are

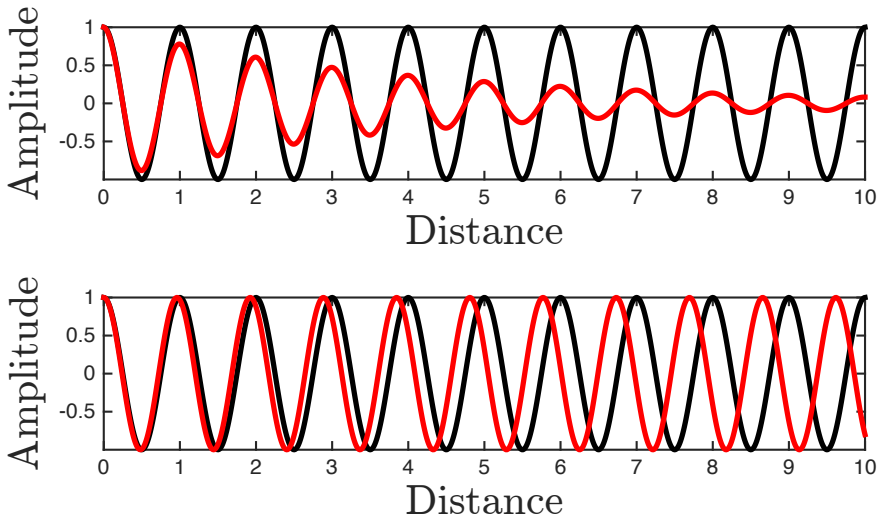

Figure 3.1: Top: **Dissipative** and **original** waves. Bottom: **Dispersive** and **original** waves.

also known as pollution error in the finite-element community [96]. Examples of both dissipation and dispersion are illustrated in Figure 3.1. The dissipative wave rapidly decays in amplitude and the dispersive wave's phase is nearly shifted by half a period after the wave propagates a short distance. The convergence of the absolute dissipation and dispersion errors of the semi-discrete DGM are found to follow $\mathcal{O}(h)^{2p+2}$ and $\mathcal{O}(h)^{2p+3}$, respectively, where h is a measure of the element size [68].

Relation to solving turbofan exhaust noise problems

Since the accuracy level of the numerical scheme depends not only on the wavenumber, but also the propagation distance, it can be complicated to estimate the accuracy levels attained in the far-field for all but the most trivial problems. Fan noise, propagating through the bypass duct of turbofan engines, reflects off of the duct walls, taking a complicated path through the engine. At the exit of the bypass duct, the sound waves are scattered, passing up-stream towards the fan as well as out of the duct, and through the shear layer. Often the fan tonal noise is modeled as eigenmodes of the duct, such as the single mode shown in Figure 3.2, which rotate around the duct axis as they propagate axially. Due to the complicated structure of these modes, the distance traveled by the sound waves is often much longer than the straight-line distance through the duct. For modes near cut-off, the acoustic waves are trapped and reflect back and forth between the walls of the duct with very little axial group velocity or energy flux. This example highlights how care must be taken to define the required accuracy levels for a given problem before using the results of an accuracy

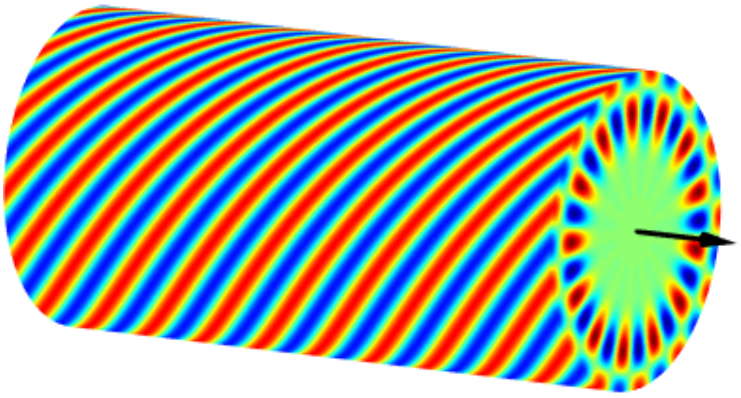

Figure 3.2: Example of an acoustic mode propagating along a circular duct.

study, such as the one in this chapter, to choose practical discretization parameters for a computational model.

Dispersion analysis tools

Dispersion analysis techniques, developed for the analysis of wave propagation accuracy of numerical solution schemes, have been extensively used to study the accuracy of the DGM. A dispersion analysis analyzes how accurately a numerical scheme predicts the propagation of simple waves over an infinite, periodic mesh, for varying wavenumber, frequency, or mesh size. Physically, a dispersion relation of a wave is an equation relating the wave's angular frequency to its wavenumber. For the acoustic mode of the LEE, the relationship between a wave's angular frequency and its wavenumber is,

$$k = \frac{\omega}{|\vec{v}_\circ| \cos(\theta) \pm c_\circ}, \tag{3.1}$$

where k is the wavenumber, ω is the angular frequency, and $|\vec{v}_\circ| \cos(\theta) \pm c_\circ$ is the propagation speed of the wave at angle θ to the mean flow velocity vector. There exist two waves, propagating with, $(+)$, and against, $(-)$, the mean flow. Entropy waves, associated with changes in density only, and hydrodynamic waves, associated with changes in velocity only, follow the dispersion relation,

$$k = \frac{\omega}{|\vec{v}_\circ|}. \tag{3.2}$$

These disturbances are transported with the mean flow. A dispersion analysis obtains a numerical dispersion relation for time-harmonic wave solutions of the discretized governing equations, and compares it to the physical dispersion relation to identify the approximation error in terms of numerical dispersion and dissipation. Hu *et al.*

[67] used one- and two-dimensional dispersion analysis techniques to study dissipation and dispersion accuracy of the DGM applied to the scalar advection equation and the mesh-induced anisotropy of the error for fixed wavenumber. Hu and Atkins [68] then created a new, one-dimensional dispersion analysis technique for fixed frequency to study the impact of grid non-uniformities on the solution accuracy for a linear system of equations. Ainsworth [69] derived error estimates of the dissipation and dispersion for multiple spatial resolutions. Alvarez *et al.* [97] studied the accuracy and cost estimates of solutions to Maxwell's equations in the time domain, using a fully-discrete, three-dimensional dispersion analysis technique. Chevaugeon [70] developed a technique to select a spatial discretization that attempted to balance dissipation error and computational cost. Sármány *et al.* [98] performed a dispersion analysis of Maxwell's equations in one and two dimensions for strong-stability-preserving Runge-Kutta (SSP-RK) time integration.

The aeroacoustics problems considered in this work are governed by the linearized Euler equations (LEE), derived in Section 2.3. Therefore, while past dispersion analyses gave estimates of the performance of the DGM for model problems or Maxwell's equations, considering the full linearized Euler equations may provide additional insight into the performance of the scheme for aeroacoustics applications. The following sections develop a semi- and fully-discrete dispersion analysis for the LEE in the presence of a uniform mean flow, then attempt to show the accuracy of the scheme for each LEE solution mode, estimate the computational cost, and develop guidelines for the choice of simulation parameters to minimize the computational cost. Finally, the time-step estimates as provided by the CFL condition, Equation 2.74, are compared to the maximum-stable time-step in the presence of a mean flow, to assess their performance.

3.1 Dispersion analysis over an infinite, periodic mesh

Consider the two-dimensional patch of triangular elements in an infinite, periodic, triangular mesh shown in Figure 3.3. Wave-like solutions to the LEE over the periodic mesh, $\mathbf{q} \sim e^{i(\omega t - \vec{k}\cdot\vec{x})}$, are sought, where ω is the angular frequency, and $\vec{k} = k_x\,\hat{\imath} + k_y\,\hat{\jmath}$ is the wavenumber vector, and $\hat{\imath}$ and $\hat{\jmath}$ are unit vectors in the x and y directions. The magnitude of the wavenumber vector is defined as k. The numerical solution in each element is discretized by nodal polynomial basis functions,

$$\mathbf{q}(x, y, t) \approx \mathbf{\Psi}_e(x, y)\bar{\mathbf{q}}_e\, e^{i\omega t}, \tag{3.3}$$

where $\bar{\mathbf{q}}_e$ is the vector of complex nodal solution amplitudes in element, e, and $\mathbf{\Psi}_e(x, y)$ are the nodal basis functions. In this work, the wavenumber vector is specified as a

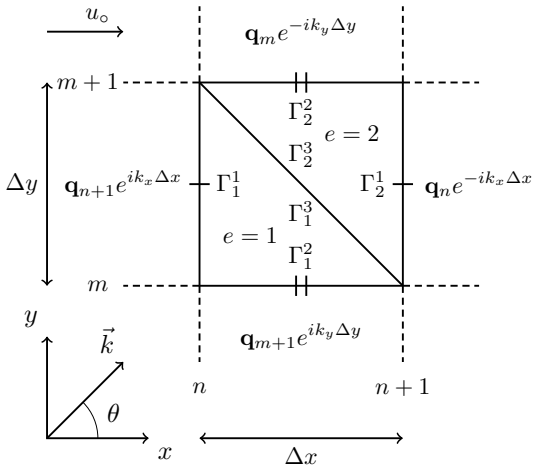

Figure 3.3: Formation of a dispersion analysis over an infinite, periodic, triangular mesh. Each edge is defined by Γ_e^b, indicating the local side, b, and the element number, e.

real number, and the complex angular frequency, predicted by the numerical scheme, is desired.

Since the mesh is periodic in both the x and y directions and the solution is assumed to be wave-like, the nodal solution values along the boundaries of the two element patch can be expressed in terms of a phase relation between the solution amplitudes on the opposite sides of the patch. For example, the solution along the n-th grid line can be written in terms of the solution on the $n+1$-th grid line, giving,

$$\mathbf{q}\Big|_{\Gamma_1^1} = \mathbf{q}\Big|_{\Gamma_2^1} e^{ik_x\Delta x}. \tag{3.4}$$

Similarly, along the m-th grid line the solution is,

$$\mathbf{q}\Big|_{\Gamma_1^2} = \mathbf{q}\Big|_{\Gamma_2^2} e^{ik_y\Delta y}. \tag{3.5}$$

The nodal DG scheme derived in Section 2.5.2 is applied to the elements in the infinite-periodic mesh in Figure 3.3. For each element, the degrees of freedom (DOF), which in this case are the solution amplitudes at the interpolation points, are stored as a vector,

$$\bar{\mathbf{q}}_e = \left[\rho'_1, (\rho u)'_1, (\rho v)'_1, \pi'_1, \ldots, \rho'_{N_p}, (\rho u)'_{N_p}, (\rho v)'_{N_p}, \pi'_{N_p}\right]^\mathsf{T}, \tag{3.6}$$

containing degrees of freedom at nodes $1, 2, \ldots, N_p$ for each element, e. The degrees of freedom of both elements are concatenated into a single vector,

$$\mathbf{Q} = \begin{bmatrix} \bar{\mathbf{q}}_1 \\ \bar{\mathbf{q}}_2 \end{bmatrix}. \tag{3.7}$$

Now that the discrete solution and computational domain are defined, the semi-discrete formulation from Section 2.5.2 can be built for the two-element patch. For clarity, the semi-discrete formulation is developed for each element individually and then combined to obtain the global expression. Starting with element, $e = 1$ of Figure 3.3, the semi-discrete weak form, Equation 2.69, can be written as,

$$\begin{aligned} i\omega\bar{\mathbf{q}}_1 = (\mathbf{D}^{\mathrm{w}}_{i,1} \otimes \mathbf{I})\, \mathbf{f}_{i,1}(\bar{\mathbf{q}}_1) &- (\mathbf{L}^1_1 \otimes \mathbf{I})\, \tilde{\mathbf{f}}^1_1(\bar{\mathbf{q}}_1\Big|_{\Gamma^1_1}, \bar{\mathbf{q}}_2\Big|_{\Gamma^1_2} e^{ik_x\Delta x}), \\ &- (\mathbf{L}^2_1 \otimes \mathbf{I})\, \tilde{\mathbf{f}}^2_1(\bar{\mathbf{q}}_1\Big|_{\Gamma^2_1}, \bar{\mathbf{q}}_2\Big|_{\Gamma^2_2} e^{ik_y\Delta y}), \\ &- (\mathbf{L}^3_1 \otimes \mathbf{I})\, \tilde{\mathbf{f}}^3_1(\bar{\mathbf{q}}_1\Big|_{\Gamma^3_1}, \bar{\mathbf{q}}_2\Big|_{\Gamma^3_2}). \end{aligned} \tag{3.8}$$

The internal flux and upwind numerical fluxes are represented by $\mathbf{f}_{i,e}$ and $\tilde{\mathbf{f}}^b_e$, respectively, where the superscript, b, indicates which face of the element the flux is evaluated at. The matrices implementing the divergence of the flux, $\mathbf{D}^{\mathrm{w}}_{i,e}$, and the boundary flux lifting matrices for face b, $\mathbf{L}^b_e$, are defined through Equations 2.66 and 2.68. The matrix, $\mathbf{I}$, is the 4×4 identity matrix and $\otimes$ is the Kronecker product. The phase relationship between elements $e = 1$ and $e = 2$ on opposite sides of the patch, is applied to the arguments of the numerical flux. The source term appearing in Equation 2.69 is dropped since sources are not considered in the present dispersion analysis. Following a similar line of reasoning, the semi-discrete equations for element, $e = 2$, are,

$$\begin{aligned} i\omega\bar{\mathbf{q}}_2 = (\mathbf{D}^{\mathrm{w}}_{i,2} \otimes \mathbf{I})\, \mathbf{f}_{i,2}(\bar{\mathbf{q}}_2) &- (\mathbf{L}^1_2 \otimes \mathbf{I})\, \tilde{\mathbf{f}}^1_2(\bar{\mathbf{q}}_2\Big|_{\Gamma^1_2}, \bar{\mathbf{q}}_1\Big|_{\Gamma^1_1} e^{-ik_x\Delta x}), \\ &- (\mathbf{L}^2_2 \otimes \mathbf{I})\, \tilde{\mathbf{f}}^2_2(\bar{\mathbf{q}}_2\Big|_{\Gamma^2_2}, \bar{\mathbf{q}}_1\Big|_{\Gamma^2_1} e^{-ik_y\Delta y}), \\ &- (\mathbf{L}^3_2 \otimes \mathbf{I})\, \tilde{\mathbf{f}}^3_2(\bar{\mathbf{q}}_2\Big|_{\Gamma^3_2}, \bar{\mathbf{q}}_1\Big|_{\Gamma^3_1}). \end{aligned} \tag{3.9}$$

To complete the global scheme, the semi-discrete formulations for each of the two elements should be combined into a single expression in terms of the global solution vector, $\mathbf{Q}$, and in the form,

$$i\omega\mathbf{Q} = \mathbf{A}\mathbf{Q}, \tag{3.10}$$

where the matrix, $\mathbf{A}$, implements all of the spatial operations of the global semi-discrete problem. To arrive at the above expression, the fluxes must first be written in a matrix form, factoring out the solution degrees of freedom. For the internal flux, the expressions, $\mathbf{f}_{i,e}(\bar{\mathbf{q}}_e)$, can be equivalently written as,

$$\mathbf{f}_{i,e}(\bar{\mathbf{q}}_e) = \mathbf{F}_{i,e}\, \bar{\mathbf{q}}_e, \tag{3.11}$$

where $\mathbf{F}_{i,e}$ are the block-diagonal flux matrices in the x and y directions of the form,

$$\mathbf{F}_{1,e} = \begin{pmatrix} \mathbf{F}_\circ(\vec{x}_{e,1}) & & & \mathbf{0} \\ & \mathbf{F}_\circ(\vec{x}_{e,2}) & & \\ & & \ddots & \\ \mathbf{0} & & & \mathbf{F}_\circ(\vec{x}_{e,N_p}) \end{pmatrix}, \mathbf{F}_{2,e} = \begin{pmatrix} \mathbf{G}_\circ(\vec{x}_{e,1}) & & & \mathbf{0} \\ & \mathbf{G}_\circ(\vec{x}_{e,2}) & & \\ & & \ddots & \\ \mathbf{0} & & & \mathbf{G}_\circ(\vec{x}_{e,N_p}) \end{pmatrix}, \tag{3.12}$$

where $\mathbf{F}_\circ$ and $\mathbf{G}_\circ$ are defined in Appendix A.1. The coordinate, $\vec{x}_{e,n}$, is the n-th interpolation node in the element. The expression for the upwind numerical flux is more complex due to its dependence on the element's face DOF and its neighbor's. In matrix form, the numerical flux can be written as,

$$\tilde{\mathbf{f}}_e^b = \frac{1}{2}\left[\left(\mathbf{F}_{\mathrm{n},e}^b + \mathbf{F}_{\mathrm{n},e}^{b+}\right)\mathbf{T}_{e,b}\bar{\mathbf{q}}_e + \left(\mathbf{F}_{\mathrm{n},e}^b - \mathbf{F}_{\mathrm{n},e}^{b+}\right)\mathbf{T}_{\mathrm{e}+,b}\bar{\mathbf{q}}_{\mathrm{e}+}\right], \tag{3.13}$$

for element face, b. The subscript, $e+$, indicates the neighbor along face b to element, e. The expressions, $\mathbf{T}_{e,b}$ and $\mathbf{T}_{\mathrm{e}+,b}$, are diagonal matrices of ones and zeros which select the $p+1$ DOF on face b from the element's solution, $\bar{\mathbf{q}}_e$, and its neighbor to face b, $\bar{\mathbf{q}}_{\mathrm{e}+}$, respectively. The normal numerical flux matrix for element, e, is then defined as,

$$\mathbf{F}_{\mathrm{n},e}^b = \begin{pmatrix} \mathbf{F}_{\circ,\mathrm{n}}(\vec{x}_{e,b,1}) & & & \mathbf{0} \\ & \mathbf{F}_{\circ,\mathrm{n}}(\vec{x}_{e,b,2}) & & \\ & & \ddots & \\ \mathbf{0} & & & \mathbf{F}_{\circ,\mathrm{n}}(\vec{x}_{e,b,p+1}) \end{pmatrix}, \tag{3.14}$$

where $\vec{x}_{e,b,n}$ is the n-th interpolation node on face b of element e, and the matrix, $\mathbf{F}_{\circ,\mathrm{n}}$ is defined in Appendix A.1. Similarly, the matrix $\mathbf{F}_{\mathrm{n},e}^{b+}$ is defined as,

$$\mathbf{F}_{\mathrm{n},e}^{b+} = \begin{pmatrix} \mathbf{W}\left|\mathbf{\Lambda}\right|\mathbf{W}^{-1}\Big|_{\vec{x}_{e,b,1}} & & & \mathbf{0} \\ & \mathbf{W}\left|\mathbf{\Lambda}\right|\mathbf{W}^{-1}\Big|_{\vec{x}_{e,b,2}} & & \\ & & \ddots & \\ \mathbf{0} & & & \mathbf{W}\left|\mathbf{\Lambda}\right|\mathbf{W}^{-1}\Big|_{\vec{x}_{e,b,p+1}} \end{pmatrix}. \tag{3.15}$$

The matrices, $\mathbf{W}$ and $\mathbf{\Lambda}$, are the eigenvectors and eigenvalues of the normal flux matrix, defined in Appendix A.1. With the fluxes defined, the matrix implementing the spatial

operations of the DGM on the two-element patch can be written concisely as,

$$\mathbf{A} = \begin{pmatrix} \sum_i (\mathbf{D}^{\mathrm{w}}_{i,1} \otimes \mathbf{I})\mathbf{F}_{i,1} & \mathbf{0} \\ \mathbf{0} & \sum_i (\mathbf{D}^{\mathrm{w}}_{i,2} \otimes \mathbf{I})\mathbf{F}_{i,2} \end{pmatrix} - \frac{1}{2}\sum_b \begin{pmatrix} \left(\mathbf{L}^b_1 \otimes \mathbf{I}\right)\left(\mathbf{F}^b_{\mathrm{n},1} + \mathbf{F}^{b+}_{\mathrm{n},1}\right)\mathbf{T}_{1,b} & \left(\mathbf{L}^b_1 \otimes \mathbf{I}\right)\left(\mathbf{F}^b_{\mathrm{n},1} - \mathbf{F}^{b+}_{\mathrm{n},1}\right)\mathbf{T}_{2,b}\, p_{1,b} \\ \left(\mathbf{L}^b_2 \otimes \mathbf{I}\right)\left(\mathbf{F}^b_{\mathrm{n},2} - \mathbf{F}^{b+}_{\mathrm{n},2}\right)\mathbf{T}_{1,b}\, p_{2,b} & \left(\mathbf{L}^b_2 \otimes \mathbf{I}\right)\left(\mathbf{F}^b_{\mathrm{n},2} + \mathbf{F}^{b+}_{\mathrm{n},2}\right)\mathbf{T}_{2,b} \end{pmatrix}, \tag{3.16}$$

where the constant, $p_{e,b}$, is the phase relation on element, e, face, b. The phase relation for face Γ^3_e in Figure 3.3, is equal to one, since it is an internal face of the patch. With the matrix $\mathbf{A}$ defined, the semi-discrete numerical dispersion relation, $D(\tilde{\omega}, k)$, can be obtained by solving for eigenvalues of $-i\mathbf{A}$, which are the $2 \times N_v \times N_p$ numerical frequencies, $\tilde{\omega}$, of the approximation, where N_v is the number of conserved variables. Eigenvectors of $-i\mathbf{A}$ give the nodal amplitudes of each numerical solution mode.

The above formulation assumed an analytical $e^{i\omega t}$ time-dependence of the solution. To analyze both the spatial and temporal accuracy of the scheme, time-dependency of the nodal solution values is introduced, such that,

$$\mathbf{q}(x, y, t) \approx \mathbf{\Psi}_e(x, y)\bar{\mathbf{q}}_e(t), \tag{3.17}$$

and the time-derivative is discretized, rather than specifying the analytical expression. Discretizing the time-derivative with the low-storage, Runge-Kutta scheme of Berland *et al.* [92], the solution at time level, $t = t + \Delta t$, can be related to the solution at time t, through,

$$\mathbf{Q}^{t+\Delta t} = \left[\mathbf{I} + \sum_{s=1}^{N_{\mathrm{st}}} \gamma_s \left(\mathbf{A}\Delta t\right)^s\right] \mathbf{Q}^t = \mathbf{A}_{\mathrm{RK}}\mathbf{Q}^t, \tag{3.18}$$

where $\mathbf{Q}^{t+\Delta t}$ is the global solution vector at time $t = t + \Delta t$ and $\mathbf{Q}^t$ is the solution at time t. The coefficient of the time integration scheme at stage, s, is given by γ_s. The matrix, $\mathbf{I}$, is the identity matrix of size $2N_pN_v \times 2N_pN_v$, and $(\cdot)^s$ implements the matrix power. The growth factor of the solution over the time-step is defined as,

$$\mathbf{Q}^{t+\Delta t} = g\,\mathbf{Q}^t. \tag{3.19}$$

Substituting the above definition into Equation 3.18, gives,

$$g\,\mathbf{Q}^t = \mathbf{A}_{\mathrm{RK}}\mathbf{Q}^t, \tag{3.20}$$

which is an eigenvalue problem with growth factors as eigenvalues and solution modes as eigenvectors. Growth factors can then be related to the numerical frequencies through,

$$g = e^{i(\omega \Delta t + n2\pi)}, \tag{3.21}$$

for integer values of n.

Solutions to the LEE are in the form of acoustic, entropy, and vorticity modes. Most of the modes found by solving the eigenvalue problem are non-physical, spurious modes that are the result of the discrete form of the governing equations. To identify which numerical frequencies represent the physical modes, each numerical frequency is compared to the exact frequencies determined by the analytical dispersion relations. Once the numerical frequencies are found, the errors defined in the following section are computed.

3.2 Accuracy assessment

This section compares the analytical and numerical values of the angular frequency to identify the relationship between the choice of the discretization, *i.e.* the mesh size, h, the order, p, and the time-step, Δt, and the accuracy levels of the numerical solution. First, a convergence study of the dispersion, dissipation, and L^2 error are performed for the semi-discrete form, and then time discretization is introduced. Mesh effects are investigated using an error anisotropy study with and without a mean flow field.

3.2.1 Error definitions

Using the two-element dispersion analysis method defined in the previous section for $\Delta x = \Delta y = h$, the spatial accuracy of the DGM with changing kh is demonstrated in this section. By changing kh, the impact of the grid size and wavenumber on the accuracy can be modeled. The spectral accuracy of the DGM is defined by how well the numerical frequencies, $\tilde{\omega}$, predict the exact frequencies governed by the exact dispersion relation of the LEE. Error in phase, called dispersion error, is caused by differences between the real part of the numerical frequency and the exact value. In this section, the dispersion error is reported as a relative dispersion error,

$$E_{\mathrm{dp}} = \left| \frac{\omega - \mathrm{Re}(\tilde{\omega})}{\omega} \right|. \tag{3.22}$$

High dispersion error will result in a phase shift over long propagation distances. Error in the wave amplitude is caused by dissipation error, and is the result of the numerical

frequency having a non-zero imaginary part, such that modes either grow, and are unstable, or decay, and are damped, in time. The dissipation error is reported as a non-dimensional dissipation rate,

$$E_{\mathrm{ds}} = \left| \frac{\mathrm{Im}(\tilde{\omega})}{\omega} \right|, \tag{3.23}$$

that is, the ratio between the imaginary part of the numerical frequency and the exact, real-valued, frequency.

The solution of the eigenvalue problem, Equation (3.10), for the eigenvectors gives the nodal solution amplitudes on the two-element patch. Eigenvectors corresponding to the acoustic, entropy, and vorticity modes can be found and compared to the exact solutions for each mode. To identify the solution amplitudes, the eigenvector associated with the closest numerical frequency to the exact dispersion relation, is scaled such that, $\mathbf{q}_{\mathrm{num}} = c\mathbf{Q}$, where c is a complex constant that matches the numerical solution to the exact solution amplitudes in the least-squares sense. Once the numerical solution mode is found, it is interpolated onto a set of quadrature points in each element and the L^2 error is computed by,

$$\|E\|_2 = \left(\int_{\Omega} |\mathbf{q}_{\mathrm{ex}} - \mathbf{q}_{\mathrm{num}}|^2 \, \mathrm{d}\Omega \right)^{\frac{1}{2}}, \tag{3.24}$$

where Ω is the two-element patch, $\mathbf{q}_{\mathrm{ex}}$ is the exact solution.

3.2.2 Semi-discrete acoustic mode convergence

The spatial accuracy of the DGM is evaluated by performing a convergence study of the errors defined above for changing kh. As mentioned in Section 2.3, solutions of the LEE are made up of combinations of acoustic, entropy, and vorticity modes. These solution modes are also present in the numerical dispersion analysis, but with the addition of many spurious, non-physical modes caused by the numerical approximation of the governing equations. The accuracy associated with correctly predicting the dispersion-relation of the acoustic mode with a zero mean flow is determined in this section. The following section considers a non-zero mean flow velocity, and compares the acoustic mode error convergence to that of the entropy and hydrodynamic mode.

The acoustic wave direction is fixed to $\theta = 0$, and kh is varied. For each polynomial order, $p = 1$ to $p = 10$, the semi-discrete eigenvalue problem, Equation 3.10 is solved, and the dissipation, relative dispersion, and L^2 errors are recorded. Figures 3.4a-3.4c show the semi-discrete convergence behavior of the acoustic mode with a zero mean flow velocity. For each polynomial order, the theoretical relative error convergence

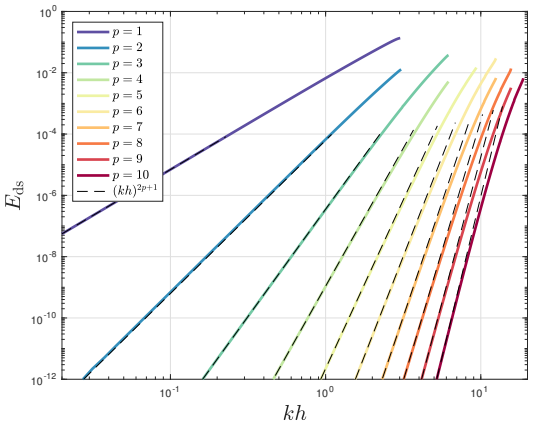

(a) Dissipation error vs. kh for orders 1-10.

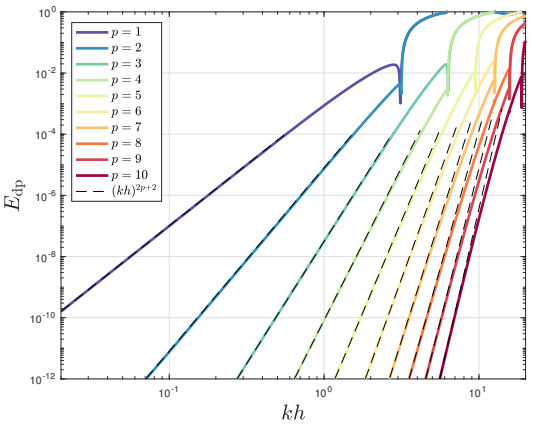

(b) Dispersion error vs. kh for orders 1-10.

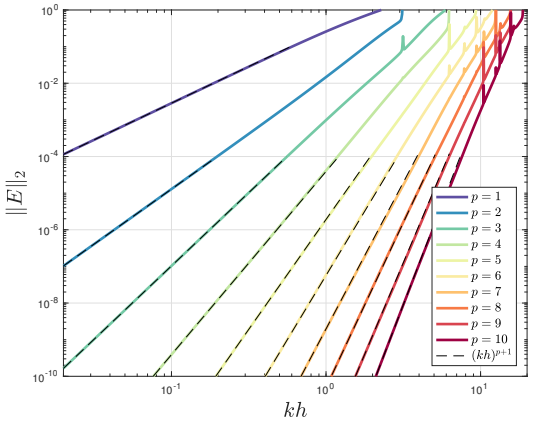

(c) Solution L^2 error vs. kh for orders 1-10.

Figure 3.4: Semi-discrete convergence of the dissipation (a), relative dispersion (b), and integrated L^2 (c) errors with kh for the acoustic mode. Each colored line represents convergence at a fixed polynomial order.

rates found by Hu and Atkins [68] and Ainsworth [69],

$$E_{\mathrm{ds}} \sim \mathcal{O}\left(kh\right)^{2p+1}, \quad E_{\mathrm{dp}} \sim \mathcal{O}\left(kh\right)^{2p+2}, \quad \|E\|_2 \sim \mathcal{O}\left(kh\right)^{p+1}, \tag{3.25}$$

are plotted as dashed lines. Note that the dissipation and dispersion errors are one order lower than the absolute errors in [68, 69], due to the definition of relative errors in this work. In each plot, two regions can be identified for each order, a highly-resolved region where kh is small and the convergence rate matches closely to the theoretical values, and a poorly-resolved region where kh is large and the convergence is suboptimal. Notice that for large kh, spikes are clearly visible in the convergence for higher polynomial orders. This behavior may be attributed to aliasing, in that the high-wavenumber oscillations of the exact wave, appear as lower wavenumber oscillations when interpolated onto the nodal basis points [96].

3.2.3 Effect of the mean flow

In the presence of a non-zero mean flow field, LEE solutions can support entropy, vorticity, and acoustic modes, with dispersion relations, Equation 3.1 for the acoustic mode, and Equation 3.2 for the entropy and hydrodynamic modes. To compare the convergence of the acoustic modes to the entropy and vorticity modes, the same semi-discrete eigenvalue problem, Equation 3.10 is solved in this section, but with mean flow Mach numbers of $M = 0.25$ and $M = 0.5$ in the x-direction, and the wave direction is fixed to $\theta = 0$. The numerical frequencies are recorded which best approximate the exact dispersion relations. Figures 3.5a and 3.5b show the dissipation and relative dispersion error for the acoustic mode (solid lines) and entropy and vorticity modes (dashed lines) for $M = 0.25$. It is apparent that in the highly-resolved wave region, the same convergence rates as the acoustic mode in a zero-mean flow are achieved. The L^2 error is given in Figure 3.5c for the acoustic mode, shown in solid lines, the entropy mode, in dashed lines, and the hydrodynamic mode in dotted lines. The convergence behavior of the entropy and vorticity modes are nearly identical, and achieve the expected $\mathcal{O}(kh)^{p+1}$ convergence rate for small kh. For all errors, at each kh, the entropy and hydrodynamic modes appear to be slightly more accurate than the acoustic mode. Figures 3.6a through 3.6c repeat the same analysis, but with a Mach number of $M = 0.5$. The increase in Mach number does not substantially impact the convergence behavior. Since the convergence behavior of the entropy and vorticity modes is similar to that of the acoustic mode, the following sections consider only the acoustic mode.

A limitation of the present study is that the wavenumber is a real, fixed value, and the complex numerical frequencies are found. At fixed frequency, the upstream and downstream propagating acoustic waves will be of a different wavenumber than the entropy and vorticity waves, as predicted by the dispersion relations. Therefore, each of the waves will have different mesh refinement requirements. Another approach would be to fix the frequency and write the eigenvalue problem in terms of complex wavenumbers. Hu and Atkins [68] formulated a similar method and used it to study nonuniform grid effects in one spatial dimension.

3.2.4 Fully-discrete convergence

Inclusion of time-discretization into the dispersion analysis shows how the temporal accuracy of the scheme impacts the optimal error convergence behavior demonstrated in the previous section. The time step, Δt, is bound by the stability requirements of the fully-discrete DGM and choices of this parameter impact both the stability and accuracy. Further details on the temporal discretization are given in Section 2.5.3. A

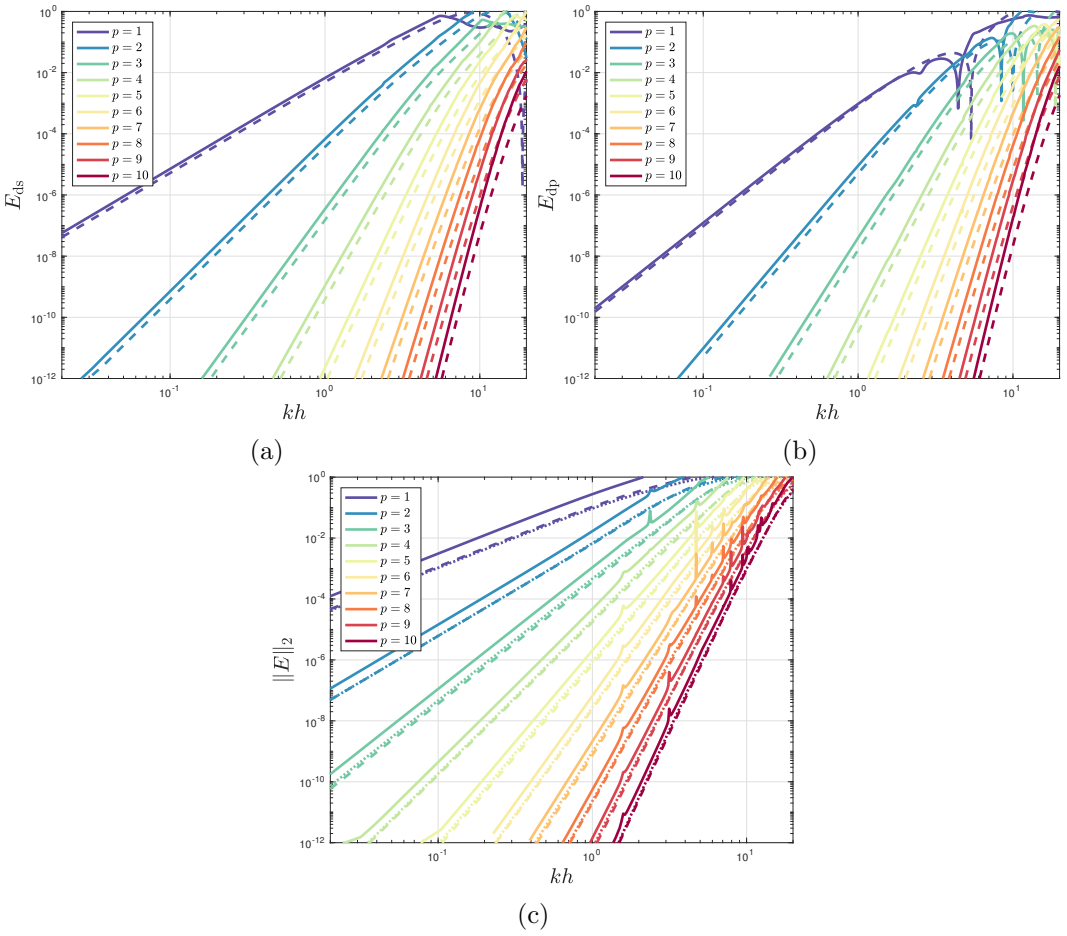

Figure 3.5: Semi-discrete convergence of the dissipation (a), relative dispersion (b), and integrated L^2 (c) errors with kh for all modes and $M = 0.25$. Solid lines indicate the acoustic mode, while dashed lines indicate the entropy and vorticity modes. The color of each line indicates which polynomial order is used.

grid-convergence study is performed by solving the fully-discrete eigenvalue problem defined by Equation 3.20. The propagation direction is fixed at $\theta = 0$ and kh is varied while the Mach number is zero. The time-step, Δt is calculated by the CFL criterion in Equation (2.74) at a CFL = 1. Again, the dissipation, dispersion, and integrated solution errors are found.

Figures 3.7a-3.7c show convergence of the dissipation, dispersion, and integrated solution errors with kh. Each colored line represents a particular choice of polynomial order. It is apparent that for large kh, the convergence behaves similarly to that of the semi-discrete problem. For small kh, or highly spatially resolved waves, the dispersion error strongly deviates from the semi-discrete convergence rates, attaining a suboptimal convergence rate in the relative error of $\mathcal{O}(kh)^4$. This is the result of the error of the fourth-order, low-storage Runge-Kutta scheme dominating the dispersion error for large kh and high polynomial order.

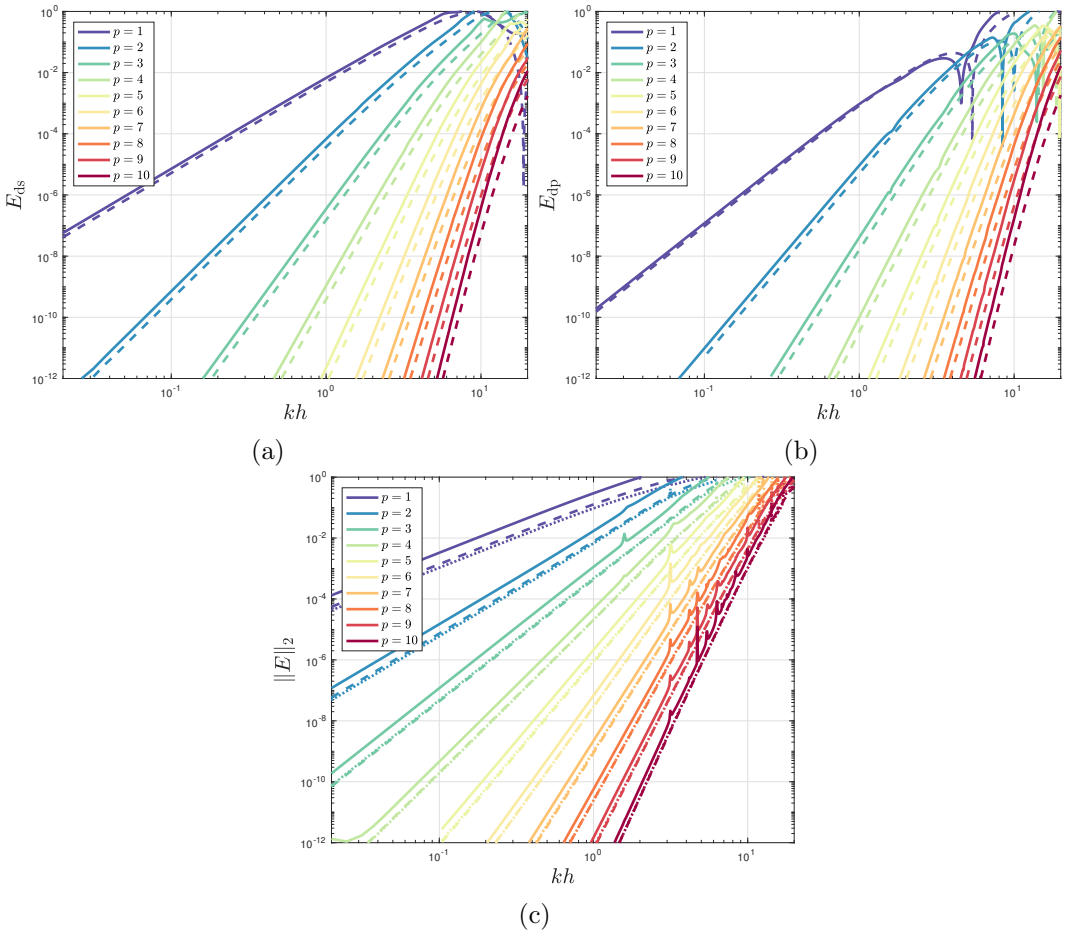

Figure 3.6: Semi-discrete convergence of the dissipation (a), relative dispersion (b), and integrated L^2 (c) errors with kh for all modes and $M = 0.5$. Solid lines indicate the acoustic mode, while dashed lines indicate the entropy and vorticity modes. The color of each line indicates which polynomial order is used.

While the time-integration error only impacts the highly spatially-resolved waves, since the dissipation and dispersion error are additive, these errors could be important for long distance/time propagation. By reducing the time-step or by using a more accurate integration scheme, this error could be controlled, but with an impact on the computational cost. Computational cost estimates for the fully-discrete scheme are discussed in Section 3.3.

3.2.5 Error anisotropy

An important measure of accuracy for wave-propagation problems is the anisotropy, or how well the scheme can propagate waves in different directions relative to mesh or mean flow directions. While estimating the impact of an arbitrary mesh or mean flow on the accuracy of the scheme would be impractical, this section serves to illustrate

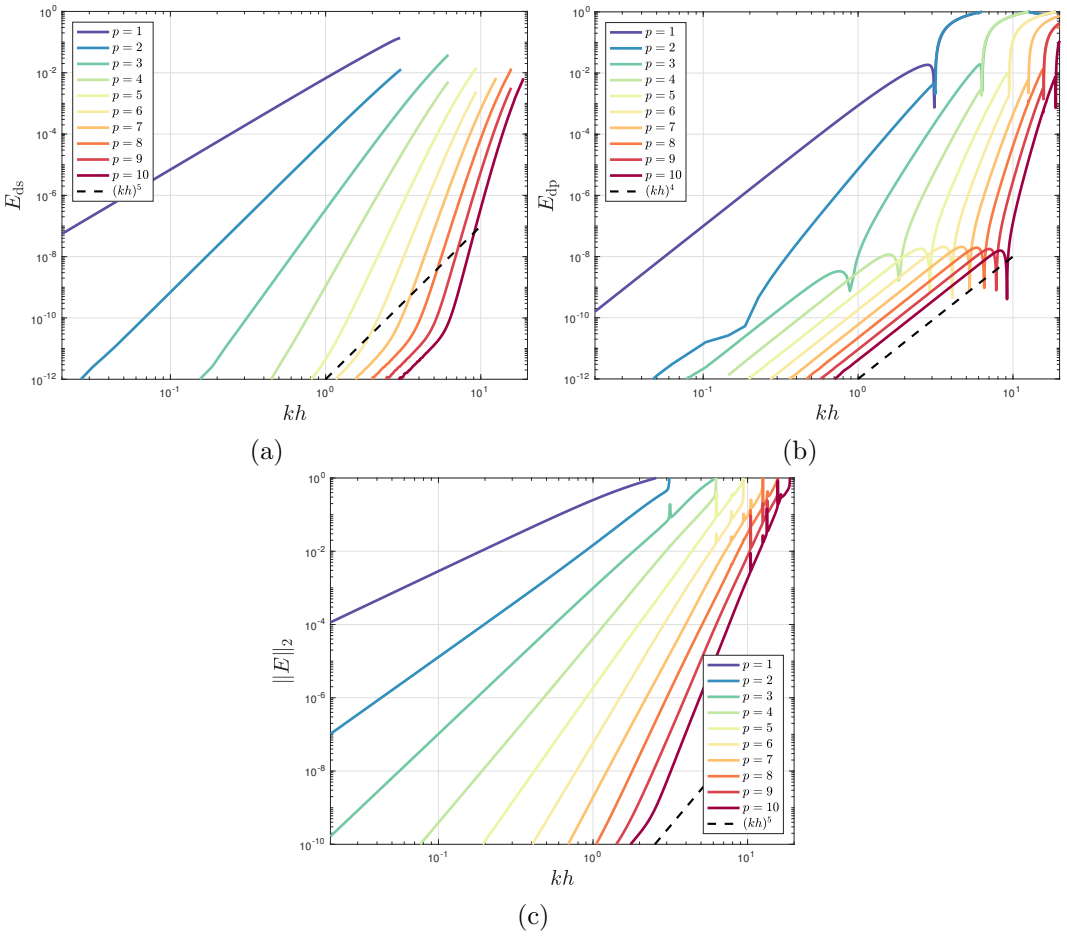

Figure 3.7: Fully-discrete convergence of the dissipation (a), relative dispersion (b), and integrated L^2 (c) errors with kh for the acoustic mode, computed with a CFL $= 1$ and a Mach number of $M = 0$. The color of each line indicates which polynomial order is used.

the general behavior of the accuracy with a small range of wave directions and mean flows.

To isolate the purely mesh-induced anisotropy from the mean flow-induced anisotropy, a zero mean flow case is considered first. Referring to Figure 3.3, the wave direction is defined by the angle, θ, between the x-axis and the wavenumber vector, $\vec{k}$. In this section, the wavenumber is defined through Equation 3.1, based on a range of $\omega h/c_\circ$. For $0 \leq \theta \leq 2\pi$, Figures 3.8a and 3.8b show the relative dispersion error and the non-dimensional dissipation error for $p = 4$. The error reaches minima and maxima as the wave direction over the two-element patch is varied. Specifically, the direction normal to the interface between elements is associated with the lowest error, while the direction tangential to the interface is associated with the highest error. Fixing the wavenumber based on a non-dimensional angular frequency of $\omega h/c_\circ = 1$, Figures 3.8c and 3.8d show the impact of varying the order of the polynomial basis. Increasing the

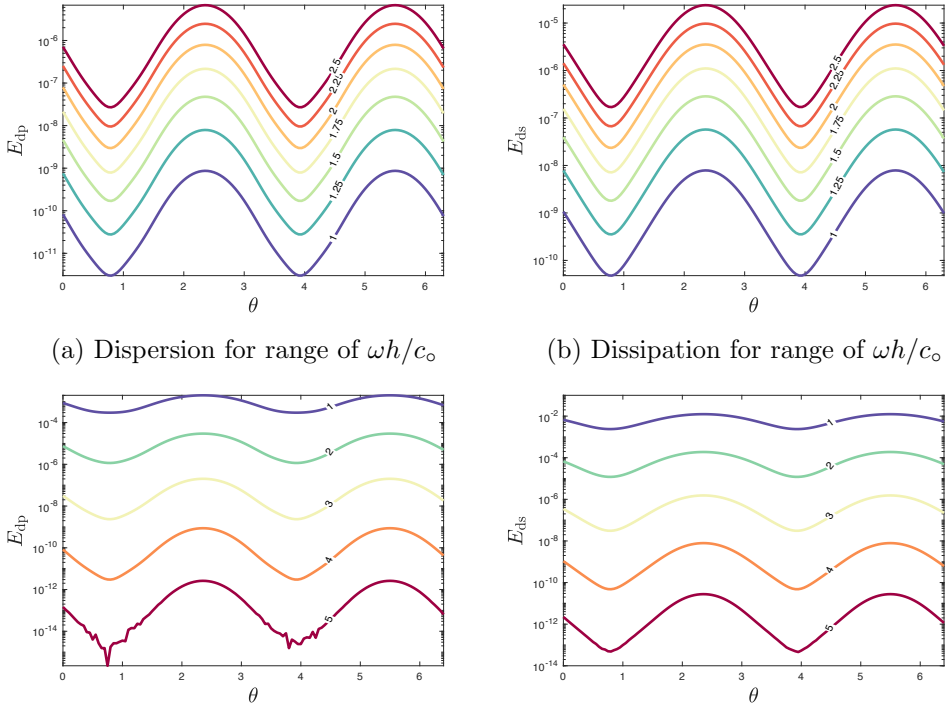

(a) Dispersion for range of $\omega h/c_\circ$

(b) Dissipation for range of $\omega h/c_\circ$

(c) Dispersion for range of orders

(d) Dissipation for range of orders

Figure 3.8: Anisotropic behavior of the relative dispersion error and the non-dimensional dissipation rate for $0 \leq \theta \leq 2\pi$ and zero mean flow. The top two figures show the effect of increasing frequency, $\omega h/c_\circ$, at $p = 4$ and the bottom two figures show the effect of increasing the polynomial order, p, of the scheme at fixed frequency.

polynomial order increases the anisotropy of the error, relative to the average value at each order. The oscillations in relative dispersion error, seen near the minima for order five in Figure 3.8c, can likely be attributed to reaching the machine precision limits.

To identify the anisotropy of the error induced by the mean flow, the error is calculated for $0 \leq \theta \leq 2\pi$ in the presence of a mean flow with Mach number of $M = 0.5$ in the positive x-direction. As the wave direction changes relative to the flow, the wavenumber changes according to the dispersion-relation, Equation 3.1. Propagating with the flow has the effect of increasing the acoustic wavelength, while propagating against the flow decreases the wavelength. The frequency is varied and the order is fixed to $p = 4$ in Figures 3.9a and 3.9b. In Figures 3.9c and 3.9d, the frequency is fixed to $\omega h/c_\circ = 1$, and the polynomial order is varied. The presence of a mean flow greatly impacts the anisotropy of the error. The error is largest near the direction where the wave is propagating against the flow ($\theta = \pi$). Propagation against the mean flow will have the effect of increasing the wavenumber, and therefore requiring more elements per wavelength to resolve the wave. Figures 3.9a-3.9d show the maximum error occurring at a slightly shallower angle than the upstream direction, $\theta = \pi$. This can be attributed

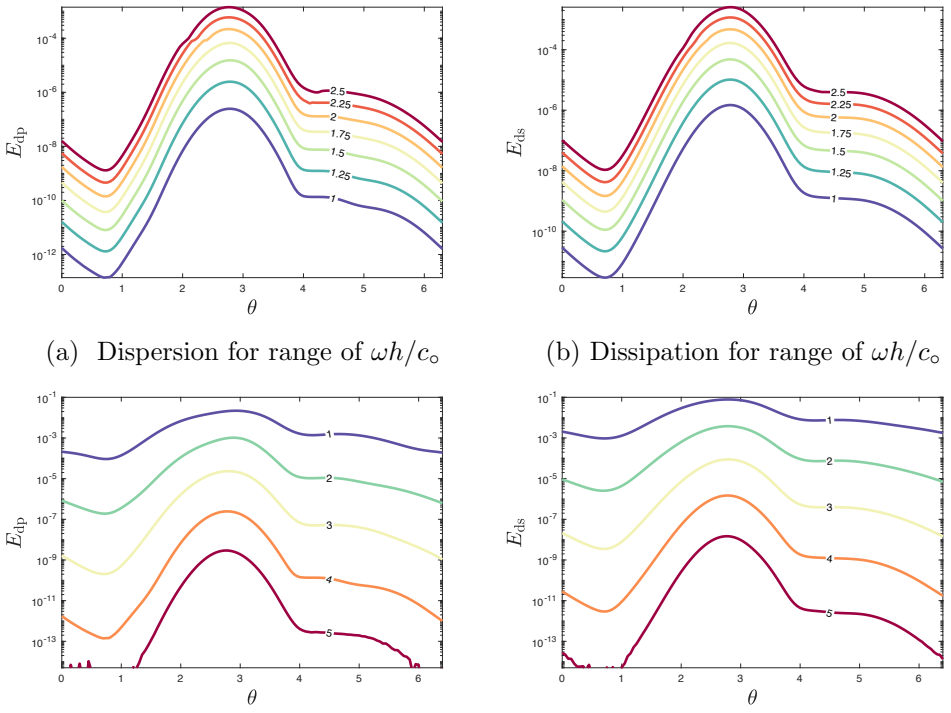

(a) Dispersion for range of $\omega h/c_\circ$

(b) Dissipation for range of $\omega h/c_\circ$

(c) Dispersion for range of orders

(d) Dissipation for range of orders

Figure 3.9: Anisotropic behavior of the relative dispersion error and the non-dimensional dissipation rate for a $0 \leq \theta \leq 2\pi$ and $M = 0.5$. The top two figures show the effect of increasing frequency and the bottom two figures show the effect of increasing the polynomial order of the scheme at fixed frequency.

to competing errors, namely the error induced by the propagation direction compared to the mean flow direction and the error induced by preferred propagation directions over the mesh.

3.3 Parameter choices to balance error and computational cost

Choosing element sizes, polynomial orders, and time-steps, such that the solution is accurate, stable, and requires minimal computational cost, is not a straightforward task. This section seeks to provide insight into the choice of parameters for a wave propagation problem and their impact on both the accuracy and computational cost. The errors are re-defined in this section as the relative amplitude error over N_T periods,

$$E_{\mathrm{a}} = \left|1 - e^{i\tilde{\omega}_i N_T t_p}\right|, \tag{3.26}$$

and the relative phase error over N_T periods,

$$E_{\mathrm{p}} = |1 - \tilde{\omega}_r/\omega| \, N_T, \tag{3.27}$$

where $\tilde{\omega}_i$ and $\tilde{\omega}_r$ are the imaginary and real parts of the numerical frequency, ω is the exact real angular frequency, t_p is the period of oscillation, and N_T is the number of periods considered. Since dispersion and dissipation errors build up in the solution as the waves propagate, it is important to also understand what impact the choice of parameters has on the errors for both short and long propagation distances. First, optimal discretizations in terms of mesh size and order are found for short and long propagation distances. Second, the computational cost of the optimal discretizations are estimated and then used to develop guidelines for the choice of parameters for minimizing the computational cost. While the definition of "short" and "long" distance propagation are highly problem dependent, the values chosen in this work are chosen to demonstrate how the error and computational cost can change with increasing propagation distance.

Accuracy for short and long propagation distances

Accuracy is computed for short and long distance propagation by performing a mesh convergence study for orders $1-10$ and then calculating the error from Equations (3.26) and (3.27). For these convergence studies, the CFL is fixed to 1. First, accuracy is analyzed for a short distance propagation, corresponding to the distance traveled over one period of oscillation. Figures 3.10a and 3.10c show the convergence of the relative amplitude and phase errors with the number of elements per squared wavelength, N_e/λ^2. From the convergence plots, optimal discretizations of order and mesh size are selected for each order at the fixed accuracy levels dictated by the dashed lines. These optimal discretizations are then compared in Figures 3.10b and 3.10d at fixed amplitude and phase error, respectively. For the amplitude error, it is clear that at all accuracy levels, increasing the order permits a sharp reduction in the number of elements per wavelength required to achieve a fixed accuracy level. This is also true for the phase error, except at the highest accuracy level, $E_{\mathrm{p}} = 10^{-8}$, where the temporal error begins to dominate. The same analysis is applied to a long distance propagation corresponding to 100 periods of oscillation. Figures 3.11a and 3.11b show the amplitude error. Again, for the amplitude error, increasing the order results in a sharp decrease in the required number of elements per squared wavelength to achieve a particular accuracy level. Figures 3.11c and 3.11d show the same analysis applied to the phase error. Increasing the propagation distance at fixed accuracy level effectively increases the impact of the temporal error. Note that for low accuracy levels, the number of elements required per wavelength to achieve a particular phase accuracy is less than

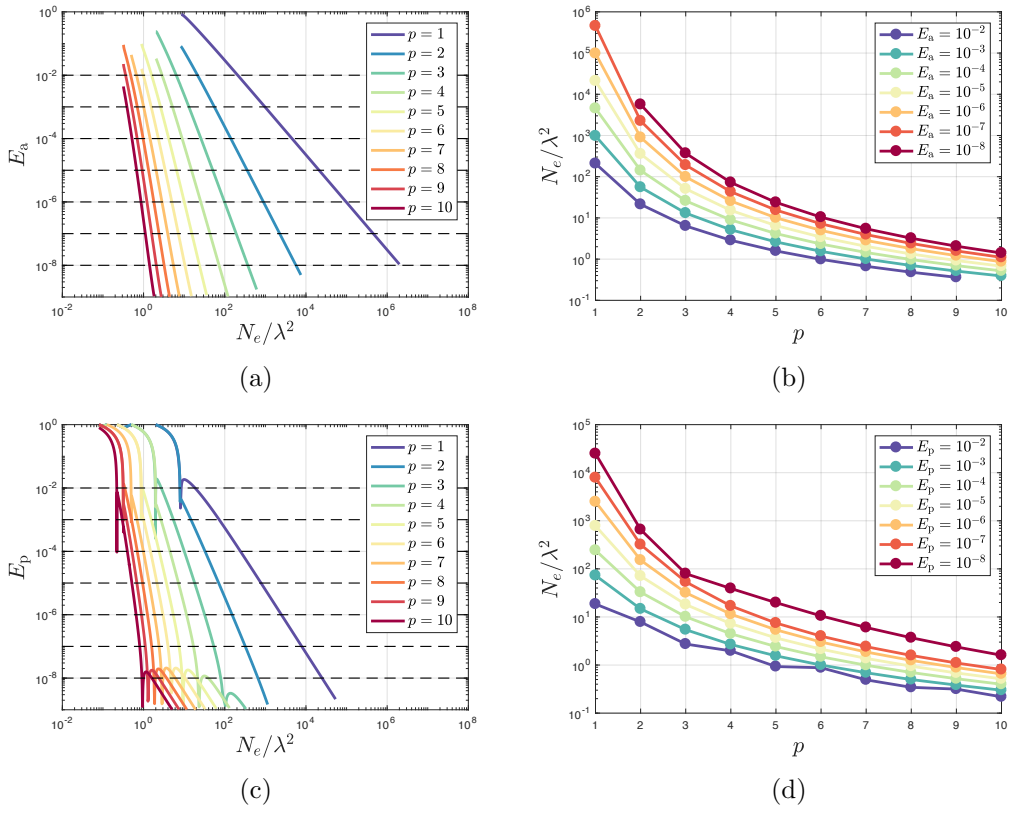

Figure 3.10: Convergence of E_a (a) and E_p (c) and optimal discretizations to achieve fixed E_a (b) and E_p (d) for one period of oscillation, $N_T = 1$.

the number required for the amplitude error. However, at high accuracy levels and/or long propagation distances, the phase error places stricter requirements on element size. For lower accuracy levels, *e.g.* $E_\mathrm{a} = E_\mathrm{p} = 10^{-3}$ for this problem, the spatial error dominates the temporal error.

3.3.1 Computational cost considerations

Using a similar approach to the cost analysis performed by Alvarez *et al.* [97] for Maxwell's equations, the accuracy-cost relationship of fully-discrete LEE solutions is estimated in this section. To roughly estimate the computational cost, every floating point operation required to compute the spatial operator and integrate the equations in time, is identified. This estimated cost can be computed by,

$$C = n_\mathrm{t} n_\mathrm{s} n_e \left(2M_\mathrm{div} + n_\mathrm{f} M_{Fn} + T + S_\mathrm{f} + F + F_\Gamma\right), \tag{3.28}$$

where M_div and M_{Fn} are the operations associated with matrix multiplications for the divergence of the flux and the lifting of the boundary flux, T is the time integration,

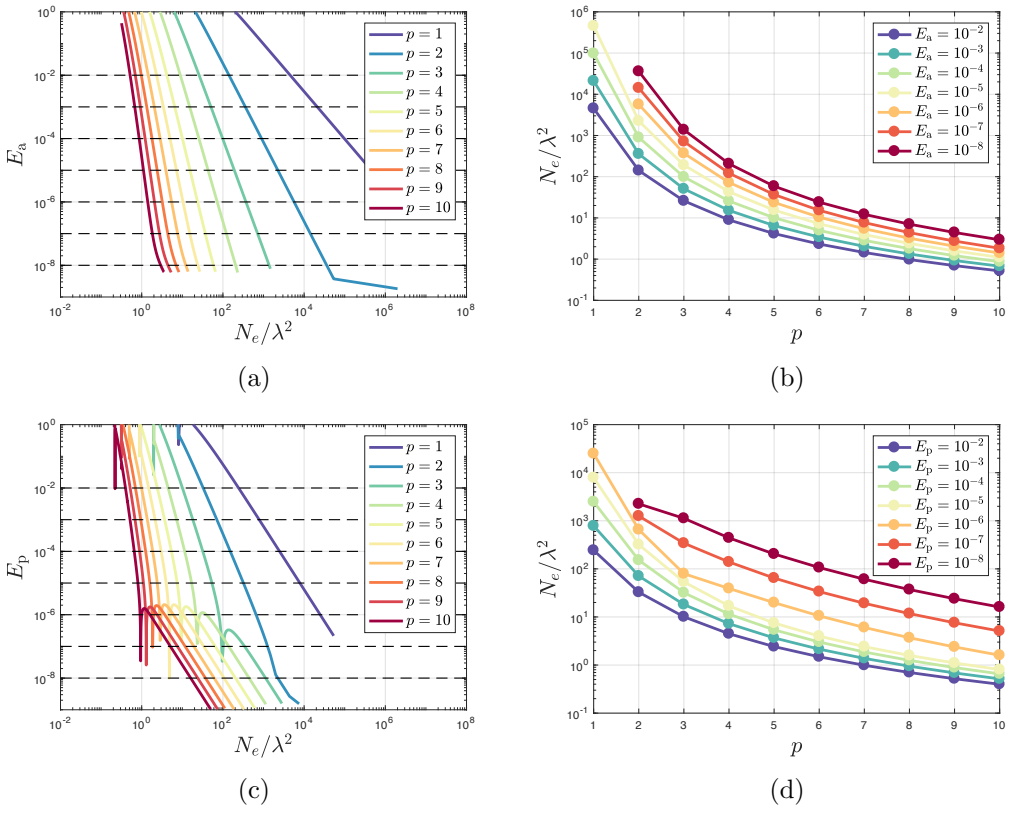

Figure 3.11: Convergence of E_a (a) and E_p (c) and optimal discretizations to achieve fixed E_a (b) and E_p (d) for 100 periods of oscillation, $N_T = 100$.

S_f is the scaling of the flux in the quadrature-free formulation, F is the computation of the interior fluxes, and F_Γ is the computation of the element numerical fluxes. The variables, n_f, n_t, and n_s are the number of element faces, number of time-steps, and the number of time integration stages, respectively. In addition to this estimation, there will be important overheads associated with the communication costs between processors, the memory usage, the cache, and other architecture- and implementation-specific costs, but these effects are not directly accounted for in this analysis.

Similar to the error analysis presented above, the estimated computational cost is computed for fixed amplitude and phase accuracy levels at both short and long propagation distances. Figures 3.12a and 3.12c show the computational cost required to achieve fixed levels of amplitude and phase accuracy using a CFL = 1.0. Each point along the curves corresponds to a particular optimal discretization of N_e/λ^2 and order, p. For a short propagation distance, Figure 3.12a indicates that the cost required to achieve a particular amplitude error level is higher than the cost required to achieve a particular phase error. This can be seen by noticing that at each error level, the amplitude error curve (dashed line) is above or directly on top of the phase error curve (solid line). At low accuracy levels, marginal cost reduction is achieved for high orders. The same

analysis is repeated using a CFL = 0.5 in Figure 3.12b. It is apparent that reducing the CFL reduces the temporal error, but increases the cost. Therefore at short propagation distances and all but the highest accuracy levels, it is beneficial in terms of cost to maximize the CFL.

Fixing the CFL to 1 and increasing the propagation distance, the cost analysis is repeated in Figure 3.12c. For accuracy levels, $E_a = E_p = 10^{-2}$ to $E_a = E_p = 10^{-6}$, amplitude error dictates the computational cost. In this case, at low accuracy levels, using high orders results in a larger relative cost reduction than in the short propagation case. However, at $E_a = E_p = 10^{-8}$, the phase error clearly dominates. This error level can be identified in Figure 3.11c as the region dominated by temporal error. Note that increasing the order has very little impact on cost reduction in this region. The same analysis is repeated using a CFL = 0.5 in Figure 3.12d. For low accuracy levels, decreasing the CFL increases the cost. However, for the highest accuracy level, decreasing the CFL results in a reduction in cost. Decreasing the CFL reduces the temporal error, allowing the use of larger, higher order elements. These results are summarized in Figure 3.13. It may be logical to choose the element size and polynomial order to minimize the amplitude error, and then determine which regime of Figure 3.13 is applicable to the problem. If, for instance, low accuracy and long propagation distance are required, the CFL should be maximized. If high accuracy and a long propagation distance is required, the CFL should be reduced to limit the temporal component of the phase error. These results are in contrast to those of Chevaugeon *et al.* [70], who showed that for a fixed-order Runge-Kutta scheme, the temporal error is much lower than the spatial error, indicating that only the spatial accuracy is important. However, unlike the present analysis, they did not consider the effect of pollution error which is a function of the distance traveled by the waves.

It is important to note that these results depend on the accuracy and the computational cost of the time integration scheme. For a different choice of time integration scheme than the one used in this work, the results may be different. For example, Sármány *et al.* [98] analyzed the accuracy of the DGM for Maxwell's equations and a SSP-RK scheme. They found that when the order of the SSP-RK scheme is fixed to $p + 1$, the optimal convergence rates for high order were recovered and that cost was not substantially higher than the fixed-order scheme due to the larger allowable time-step. However, the $p + 1$-th order SSP-RK scheme requires the storage of $p + 1$ evaluations of the solution in each element. For high polynomial order and high DOF problems, the memory requirements are substantial.

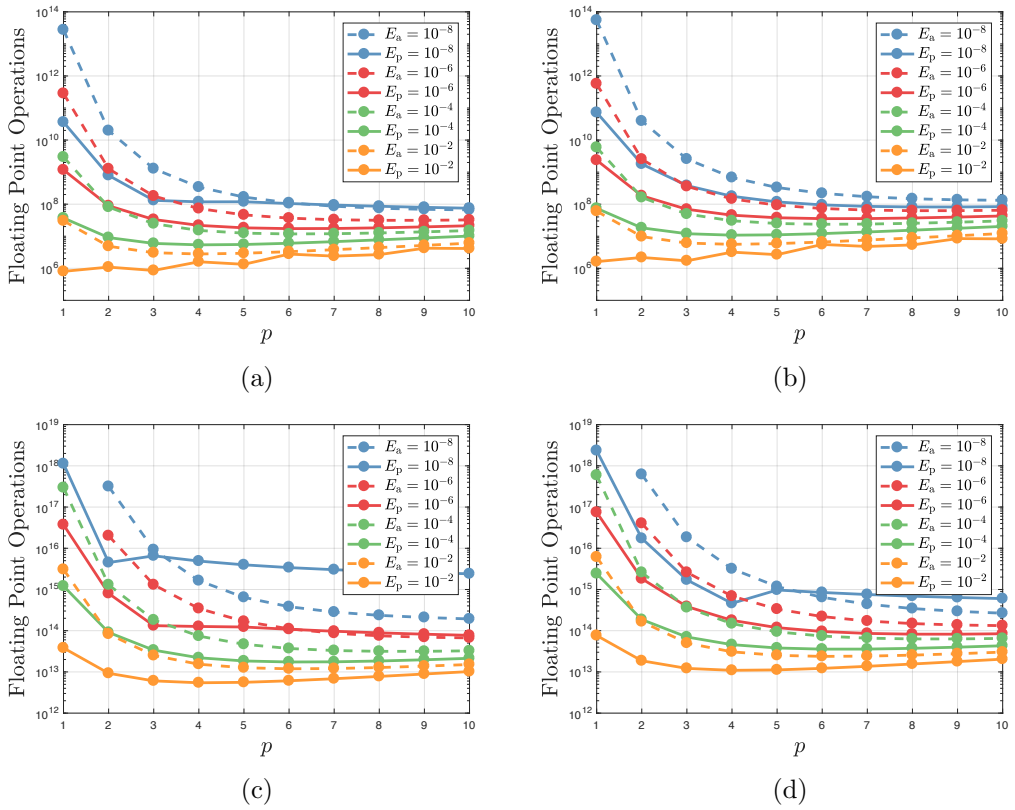

Figure 3.12: Estimated computational cost for fixed accuracies using a CFL = 1.0 (a) and a CFL = 0.5 (b) for one period of oscillation. Estimated computational cost for fixed accuracies using a CFL = 1.0 (c) and a CFL = 0.5 (d) for 100 periods of oscillation.

3.4 Stability

The time-step is a critical parameter that affects not only the accuracy and numerical stability, but also the computational cost. The above sections analyzed the impact of the time-step choice, as calculated by the CFL criterion, on the accuracy and computational cost of solutions. While the CFL criterion provides an estimate for choosing a stable time-step, it does not typically result in the largest time-step for stability, which is desired for minimizing computational cost at lower accuracy levels. This section investigates the discrepancy between the maximum time-step for stability and the time-step predicted by the CFL-criterion.

The stability of the DGM for various Runge-Kutta time integration schemes has been evaluated in one and two-dimensions, both theoretically and through numerical experiments [71, 72, 73]. Kubatko *et al.* [72] obtained numerical solutions to a linear advection equation over triangular meshes to connect the one-dimensional CFL condition to the two-dimensional results. They found that the two-dimensional criterion can

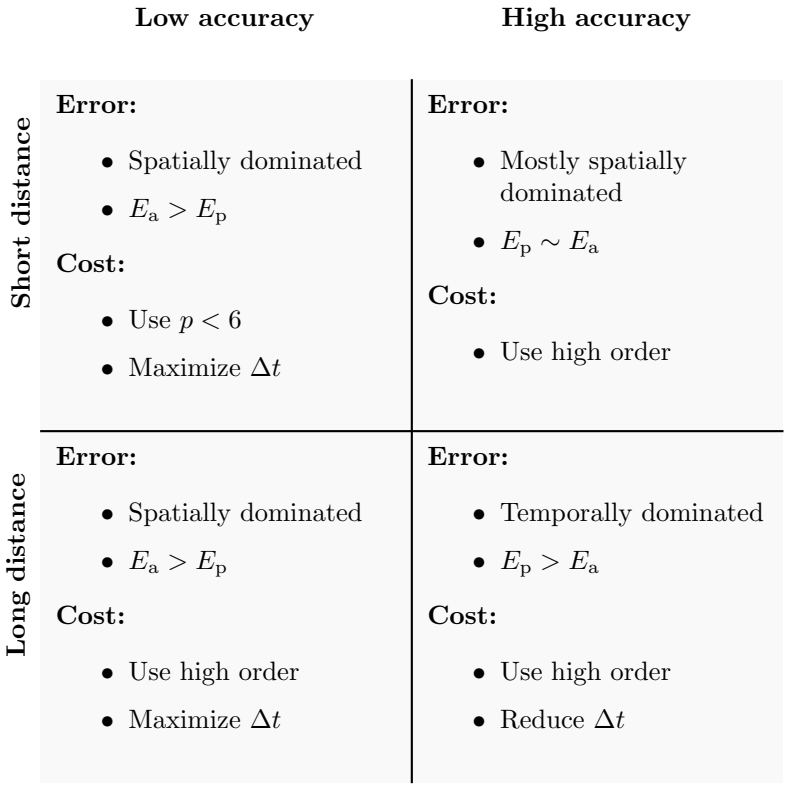

Figure 3.13: Guidelines for parameter choices based on low/high accuracy requirements and short/long distance propagation.

be found through the factor, $1/2^{1/(p+1)}$, multiplied by the one-dimensional criterion, for polynomial orders up to three and a SSP-RK scheme. Toulorge and Desmet [73] evaluated the stability of the DGM for two-dimensional solutions to a scalar advection equation, considering different time-integration schemes, flux functions, the element shape, and the element size estimates. They found that the element size estimates of inner radius or shortest height are the most accurate for the range of shapes considered. Through numerical experiments, they found that the local stability estimates were generally too restrictive compared to the global conditions. The above work considered linear advection equations only. In this section, the stability of the discrete LEE are analyzed, comparing the time-step estimate of Equation 2.74 to the maximum stable time-step, with the presence of a mean flow.

To estimate how closely the CFL condition predicts the maximum stable time-step, the maximum stable time-step is found for a range of element sizes, wave directions, and flow conditions. The maximum time-step for stability is found by iteratively solving the eigenvalue problem, 3.20, using a bisection algorithm with varying Δt until the stability limit, $|e^{i\tilde{\omega}\Delta t}| = 1$, is reached. Once the maximum stable growth rate is found, the time-step is recorded. The wave directions are varied from $\theta = 0$ to $\theta = 2\pi$, inclusive of the best and worst-case anisotropy directions, found in Section 3.2.5. The

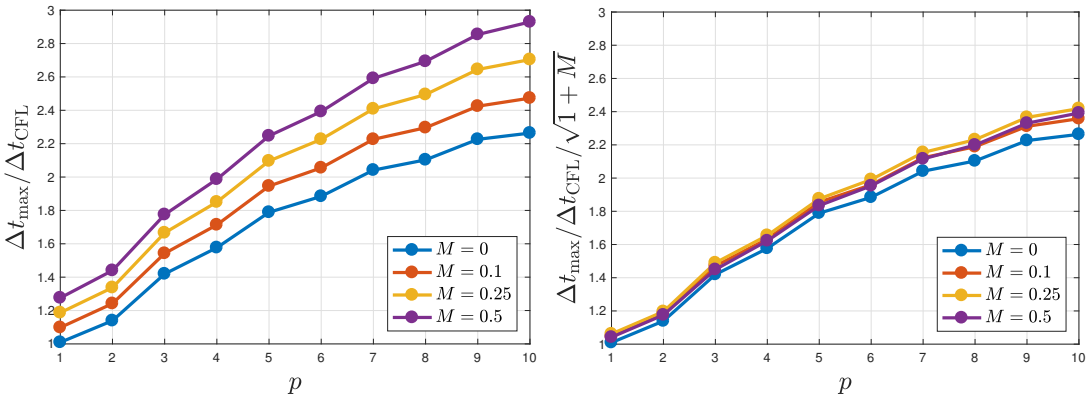

(a) (b)

Figure 3.14: Ratio between the maximum time-step for stability and the time-step from the CFL condition vs. order, with no scaling (a), and scaled by $1/\sqrt{1+M}$ (b).

ratio between the maximum stable time-step and the time-step for a CFL of one is computed, and the minimum ratio stored over all kh and wave directions. The mean flow direction is fixed to $+x$. Figure 3.14a shows the time-step ratio for a range of polynomial orders and Mach numbers.

For low polynomial orders, the CFL condition predicts a time-step that is close to the maximum stable time-step. However, for high order, the CFL condition substantially under predicts the maximum stable time-step. The dependence of the time-step ratio with order is worse than those found by Toulorge and Desmet [73]. This may be attributed to the relatively heuristic choice of the order-dependence in the CFL condition used in this work, as the minimum distance between nodes on the reference element. While the time-step estimate used in this work does not accurately predict the maximum stable time-step, it does not exceed the stability limit for any of the orders considered here.

Also apparent in Figure 3.14a is the over-prediction of the time-step with increasing Mach number. Interestingly, by inspecting the values of the time-step ratio at each Mach number, the over-prediction appears to follow a $\sqrt{1+M}$ dependence. Scaling the time-step ratio by $1/\sqrt{1+M}$, Figure 3.14b shows that the curves collapse, removing most of the dependence on Mach number.

3.5 Summary

This chapter attempted to understand the relationships between the choice of simulation parameters, *e.g.* mesh size, polynomial order, time-step, and flow parameters, *e.g.*

propagation direction, mean flow velocity, and wavenumber, on the accuracy, computational cost and stability of the numerical solutions. While the numerical performance of the DGM has been investigated before, for other governing equations, the LEE have not been considered. The dispersion analysis techniques presented in this chapter have focused solely on solutions to the linearized Euler equations to more closely represent applications to aeroacoustics problems.

Section 3.2 used the dispersion analysis, developed at the beginning of the chapter, to investigate the convergence of the dispersion, dissipation, and L^2 errors with mesh size and polynomial order for each of the solution modes of the LEE. First, the semi-discrete convergence was studied of the acoustic, entropy and hydrodynamic modes of the LEE, followed by the fully-discrete convergence. The convergence behavior of the entropy and hydrodynamic solution modes was found to be similar to that of the acoustic mode. However, the fixed-wavenumber analysis of this work is not able to predict the impact of the mean flow on the wavelength of each of the modes. Reformulating the dispersion analysis problem for fixed frequency, similar to the one-dimensional analysis of Hu and Atkins [68], could offer additional insight into the mean flow effects.

The fully-discrete convergence highlighted the impact of the time integration truncation error on the accuracy of solutions computed with high polynomial orders. Section 3.3 chose simulation parameters to balance accuracy and computational cost. First, the fully-discrete accuracy was studied for a model wave propagation problem involving short and long distance propagation. The results of the wave propagation study were used to estimate the computational cost associated with achieving fixed levels of dispersion and dissipation error. The build-up of dispersion error associated with the time-integration scheme was found to be important for long-distance/time wave propagation. Guidelines for the choice of parameters to balance error and computational cost were also discussed.

Section 3.4 calculated the maximum time-step for stability and compared this to the time-step calculated by the CFL condition. It was found that the CFL condition used in this work significantly over predicts the dependence of the polynomial order and the mean flow velocity on the stability. By applying a Mach number scaling factor to the time-step, a closer time-step to the maximum stable time-step could be found. Further analysis of the time-step dependence on Mach number, including numerical examples, will be required to understand the cause of this scaling factor.

Chapter 4

Aliasing-driven instabilities in DG solutions to the LEE

4.1 Introduction

In Chapter 2, the semi-discrete form of the governing equations was derived, leading to the weak form,

$$\int_{\Omega_e} \boldsymbol{\Phi}_e^\intercal \frac{\partial \mathbf{q}_e}{\partial t} - \frac{\partial \boldsymbol{\Phi}_e^\intercal}{\partial x_i} \mathbf{f}_i(\mathbf{q}_e) - \boldsymbol{\Phi}_e^\intercal \mathbf{s} \, \mathrm{d}\Omega_e + \int_{\Gamma_e} \boldsymbol{\Phi}_e^\intercal \tilde{\mathbf{f}}(\mathbf{q}_e, \mathbf{q}_{e+}) \, \mathrm{d}\Gamma_e = 0 \,, \tag{4.1}$$

where $\mathbf{f}_i\left(\mathbf{q}_e\right)$ is the i–th component of the flux tensor, $\vec{\mathbf{f}} = \mathbf{F}_\circ \mathbf{q}_e \, \hat{\imath} + \mathbf{G}_\circ \mathbf{q}_e \, \hat{\jmath} + \mathbf{H}_\circ \mathbf{q}_e \, \hat{k}$, evaluated over the element volume, and $\tilde{\mathbf{f}}(\mathbf{q}_e, \mathbf{q}_{e+})$ is the numerical flux normal to the element surface, evaluated with the solutions at the interface of element e and its neighbors, $e+$. Upon introducing the spatial discretization of the solution in Section 2.5.1 using a nodal polynomial expansion, the approximate solution becomes,

$$\mathbf{q}_e(\vec{x}, t) \approx \boldsymbol{\Psi}_e(\vec{x}) \bar{\mathbf{q}}_e(t) \,. \tag{4.2}$$

The solution expansion can be substituted into the time-derivative term of the weak form above, taking the test functions as the same nodal polynomial basis functions, resulting in,

$$\int_{\Omega_e} \boldsymbol{\Phi}_e^\intercal \frac{\partial \mathbf{q}_e}{\partial t} \, \mathrm{d}\Omega_e \approx \int_{\Omega_e} \boldsymbol{\Psi}_e^\intercal \boldsymbol{\Psi}_e \, \mathrm{d}\Omega_e \frac{\partial \bar{\mathbf{q}}_e}{\partial t} = \mathbf{M} \frac{\partial \bar{\mathbf{q}}_e}{\partial t}, \tag{4.3}$$

where the mass matrix, $\mathbf{M}$, is numerically integrated with a cubature rule accurate enough to integrate a polynomial of order $2p$. For the divergence term, it is convenient to approximate the flux using the same polynomial expansion as the solution vector, so that the flux function can be computed using the nodal solution values. The

approximated flux then becomes,

$$\mathbf{f}_i(\vec{x},t) \approx \mathbf{\Psi}_e(\vec{x})\bar{\mathbf{f}}_{i,e}(t)\ , \tag{4.4}$$

which upon insertion into the divergence term results in,

$$\int_{\Omega_e} \frac{\partial \mathbf{\Phi}_e^\intercal}{\partial x_i}\mathbf{f}_i(\mathbf{q}_e)\,\mathrm{d}\Omega_e \approx \int_{\Omega_e} \frac{\partial \mathbf{\Psi}_e^\intercal}{\partial x_i}\mathbf{\Psi}_e\bar{\mathbf{f}}_{i,e}\,\mathrm{d}\Omega_e = \mathbf{S}\bar{\mathbf{f}}_{i,e}. \tag{4.5}$$

The numerical flux is similarly discretized using the nodal values of the solution and mean flow. It appears that, provided that $\mathbf{S}$ and the boundary integral, $\mathbf{B}^b$, are computed exactly, the scheme for a uniform flow, and linear flux, will have similar stability properties to the nonuniform, nonlinear flux. However, this is generally not the case, and will often result in numerical instabilities [55]. The problem arises in the discretization of the flux polynomial using the same nodal basis as the solution. Since the flux is composed of products of mean flow variables, $\mathbf{q}_\circ$, which are discretized with polynomials of order p, and solution variables, $\mathbf{q}$, also polynomials of order p, the flux will be a polynomial of order $l > p$. When the flux is evaluated at the interpolation points, this results in a collocation projection of the flux of order $l > p$ onto the order p basis, resulting in the energy of the unresolved, higher wavenumber modes, being added as spurious, lower wavenumber modes. This error is known as aliasing, and if allowed to build up, it will result in numerical instability. Aliasing is also well known in signal processing with Fourier components. Here it is the same, but with polynomials. A visual depiction of aliasing is illustrated in Figure 4.1. The solid line depicts the exact flux polynomial over the 1D domain, Ω, and the dashed line is an interpolation of the exact flux at the nodes shown in black. Clearly, the interpolated function substantially disagrees with the exact function.

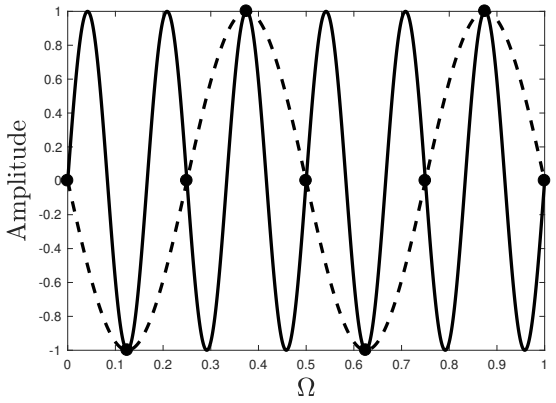

Figure 4.1: Example of an interpolation (dashed line) of a continuous signal (solid line) leading to aliasing. The interpolated signal has an entirely different wavenumber than the continuous signal.

Since aliasing results from a lack of spatial resolution of the flux, increasing the mesh resolution would result in lower aliasing error, but at increased computational cost. For the LEE, the higher order polynomial terms in the flux can be reduced by using a lower order representation of the mean flow quantities, $\mathbf{q}_\circ$. For example, the mean flow quantities could be taken as the mean value in each element, which would eliminate aliasing entirely. However, such a coarse representation of the mean flow could lead to solutions that poorly represent the physical problem, and even necessitate refinement of the mesh to reduce the variation in $\mathbf{q}_\circ$ from one element to the next, negating the efficiency benefits of a high-order scheme. The effect of the mean flow representation accuracy on the acoustic solution accuracy is explored in Chapter 5.

An alternative way to stabilize the scheme can be found by revisiting the definition of the fluxes. In Equation 4.4, the flux is discretized using nodal polynomial basis functions of order p, and these nodal values are obtained through computing products of the solution variables and the mean variables at the interpolation points. Since the exact flux is a polynomial of order $l > p$, aliasing will occur. Instead, the flux could be evaluated at the interpolation points of the order l basis, and then projected onto the order p basis, consistently treating the higher order terms in the flux and resulting in no aliasing. The discretization of the volume fluxes becomes,

$$\mathbf{f}_i(\vec{x},t) \approx \mathbf{\Psi}_e^p(\vec{x})\mathcal{P}^{lp}\,\mathbf{f}_i(\mathcal{I}^l\,\bar{\mathbf{q}}_e(t), \mathcal{I}^l\,\bar{\mathbf{q}}_{\circ,e}(t))\;, \tag{4.6}$$

where $\mathbf{\Psi}_e^p$ are the nodal basis functions of order p, and $\mathbf{f}_i(\mathcal{I}^l\,\bar{\mathbf{q}}_e, \mathcal{I}^l\,\bar{\mathbf{q}}_{\circ,e})$ is the flux evaluated at the interpolation points on the order l basis. The matrix, $\mathcal{I}^l$, interpolates the order p solution and mean variables to the order l interpolation nodes. The matrix which projects the order l flux onto the order p basis is $\mathcal{P}^{lp}$ which is defined by,

$$\mathcal{P}^{lp} = \left(\int_{\Omega_e} (\mathbf{\Psi}_e^p)^\intercal(\mathbf{\Psi}_e^p)\,\mathrm{d}\Omega_e\right)^{-1} \int_{\Omega_e} (\mathbf{\Psi})_e^p)^\intercal \mathbf{\Psi}_e^l\,\mathrm{d}\Omega_e, \tag{4.7}$$

where $\mathbf{\Psi}_e^l$ are the order l basis functions. While computing the flux via projection does offer a solution to the aliasing problem, it substantially increases the computational cost of the method. For the LEE, the flux may be at most a polynomial of order $2p$, resulting in a large number of flux evaluation points, and a more costly projection. In three-dimensions, the number of points for the order $p = 6$ basis is $N_p = 84$, and for order, $l = 2p$, the number of points is $N_p = 455$, resulting in a very costly flux computation. Interpolation of the solution at the order l interpolation nodes must be performed at every time-step and stored, and the mean variables must be precomputed and stored. The divergence matrices can be pre-multiplied by the projection matrix and stored, but they still result in more floating point evaluations at each time-step. This is not practical for aeroacoustic problems for which high-order is a necessity.

Aliasing-driven instabilities in high order, time-accurate discretizations have been studied in detail. Early research into aliasing for finite-difference schemes provided a solution to the aliasing by applying spatial filtering [99]. Orszag determined that to eliminate the build up of aliasing error, only the upper third of the resolved wavenumbers must be eliminated [99]. In the context of polynomial discretizations, this "2/3"–rds rule would require that after computing each time-step, the polynomial coefficients for the 1/3 highest degree terms would be set to zero. Aliasing has received a large amount of attention in the spectral methods [46, 100, 101, 102, 103, 104] and the DG and flux reconstruction [105, 106, 107, 108, 55, 13] community for nonlinear problems.

The control of aliasing-driven instabilities can be separated into methods for preventing aliasing errors, such as performing over integration of the nonlinear terms, and methods to control the buildup of aliasing errors, such as filtering. Kirby and Karniadakis [101] explored over integration in solutions to the Navier–Stokes equations with polynomial spectral methods. They used computational examples to show the stabilizing effects of over-integration and indicate that for quadratic terms in the flux, $3M/2$ points are required, and for cubic terms, $2M$ points are necessary, where M is the number of polynomial coefficients. Kirby and Sherwin [102] explored the error due to inexact collocation projection on triangular elements for collocation points located at quadrature points in collapsed coordinates and for rotationally symmetric points. Further links between the interpolation point choices and the aliasing behavior were found by Jameson *et al.* [105] in the context of flux reconstruction schemes, and by Williams and Jameson [106], who found quadrature points on the tetrahedron with good interpolation and stability qualities. Witherden and Vincent [109] evaluated interpolation and quadrature strength of different sets of interpolation points. Mengaldo *et al.* [103] treated aliasing error by using an over–integration approach for the nonlinearities in the PDE and the geometry. Hesthaven and Warburton discussed modal filters for nodal DG schemes [55] and Hesthaven and Kirby [110] derived conditions on filters for ensuring accuracy and stability. Filtering is generally simple to implement and computationally efficient. However, the filter must be tuned for each application to have enough dissipation to damp aliasing instabilities, but not so much that the solution quality degrades. While the above methods can reduce aliasing-driven instabilities, they do not completely eliminate the problem.

A number of works investigated alternative schemes that are provably stable. Gassner *et al.* [111] developed an energy stable DG scheme for variable-coefficient advection problems using a split form of the advection equations. Gassner *et al.* [112] again developed a stable scheme based on a split form of the shallow water equations, and for the compressible Euler equations [113]. Provably stable discretizations for problems with curved elements were found by Kopriva and Gassner [114]. These stable methods involve additional terms to discretize as well as restrictions on the interpolation

nodes and element types, making them potentially much more costly and difficult to implement than the standard scheme.

For the LEE and a fixed mesh size and polynomial order, aliasing errors are more prevalent in regions of the flow with strong non-uniformity, where a high order polynomial is required to resolve the flux. For turbofan exhaust noise applications, the shear layers between the core and bypass stream and the bypass and free stream have strong velocity gradients. In this region, aliasing errors are expected to be the most prevalent. To compound the problem, the LEE permit unstable vortical solutions in the shear layer that are energized by the mean flow as they advect downstream [115]. It is expected that these instabilities contribute to a higher growth rate of the aliasing-driven instabilities. Other regions of the flow-field that may lead to increased aliasing are the thin boundary layers near the walls or strong gradients of sound speed associated with temperature non-uniformities. A goal of this work is to study the formation of aliasing instabilities in problems with shear instabilities.

While there has been substantial research into aliasing mitigation strategies, there has not been a way to quantitatively compare the effect of different discretizations and dealiasing strategies on the stability of solutions. Additionally, much of the research on aliasing instabilities has focused on the solution of nonlinear problems, or model non-constant coefficient linear problems. To the author's knowledge, aliasing in solutions to the LEE with a realistic mean flow field have not yet been investigated. Dispersion analysis techniques have been useful for understanding the stability and accuracy of DG schemes for constant-coefficient linear problems [67, 68, 116, 69, 97, 70]. However, these techniques are not able to predict aliasing instabilities, due to having linear flux functions. This chapter develops a dispersion analysis that permits a non-uniform flow-field and uses it to study the formation of aliasing instabilities associated with the velocity gradients in the shear layer. Different discretizations are evaluated and compared to understand their effect on the solutions.

The chapter is outlined as follows, first an example of aliasing in a growing shear layer is discussed, followed by the development of the dispersion analysis and its verification for shear instabilities in a compressible shear layer. Lastly, several discretizations are evaluated, including varying the polynomial order, time-step, and filtering.

4.2 Aliasing instability in a 2D growing shear-layer

To illustrate the formation of aliasing-driven instabilities, a problem of practical significance to turbofan exhaust noise applications is solved in this section. A 2D planar

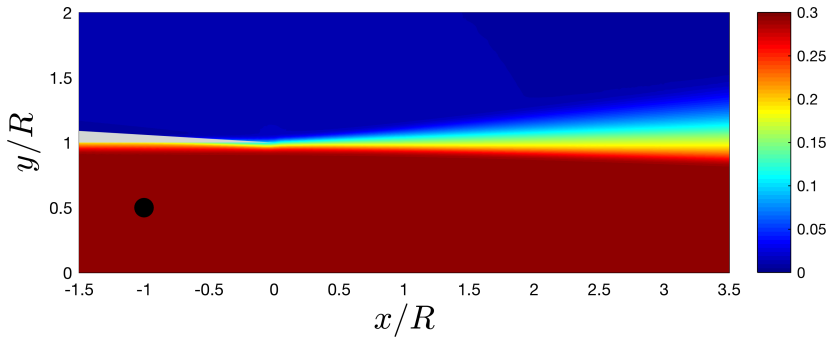

Figure 4.2: Computational domain and interpolated mean axial velocity, $u_\circ/c_\infty$. The nozzle wall is colored in gray and the source location is indicated by a black circle.

turbulent jet of Mach number $M = 0.3$ is modeled, exiting from a nozzle and discharging into a quiescent volume of air. The steady-state mean flow-field is obtained through a CFD solution using the κ–ϵ turbulence model at standard atmospheric conditions. As the jet exits the nozzle of height, R, the difference in velocity compared to the quiescent conditions, leads to the formation of a shear layer with strong gradients that grows in thickness rapidly with down-stream position. This flow-field is used as an analogue for the growing shear layers found emanating from turbofan bypass and core nozzles.

The two-dimensional acoustic domain is centered at the nozzle exit plane and non-dimensionalized by the nozzle height. The characteristic mesh spacing is fixed to approximately $\Delta x/R = 0.2$ and polynomials of order $p = 10$ are used to discretize the solution. Figure 4.2 illustrates the computational domain, the interpolated mean axial velocity, and the source location. Buffer zones surround the domain to damp any out-going waves and to reduce reflections.

A distributed sound source of the form,

$$\begin{Bmatrix} \rho' \\ (\rho u)' \\ (\rho v)' \\ \pi' \end{Bmatrix} = \begin{Bmatrix} 0 \\ 0 \\ 0 \\ 1 \end{Bmatrix} \exp\left[\frac{-((x-x_c)^2 + (y-y_c)^2)}{w^2}\right] \sin(\omega t), \tag{4.8}$$

is introduced into the domain, where ω is the source frequency, and w is the source width. The source is positioned at $x_c/R = -1$ and $y_c/R = 0.5$, outside of the shear layer, with a width, $w/R = 0.125$. The source frequency is fixed to $\omega R/c_\infty = 2\pi$ and the governing equations are integrated in time until an instability is observed.

Figure 4.3 shows the acoustic pressure at three multiples of the source period, t_p. At time $t/t_p = 7.5$, acoustic waves are generated inside the nozzle flow of $M = 0.3$ and pass through the shear layer, then exit the domain. Downstream of the nozzle,

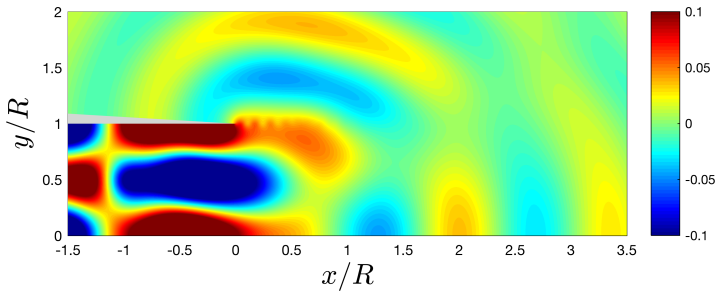

(a) $t/t_p = 7.5$

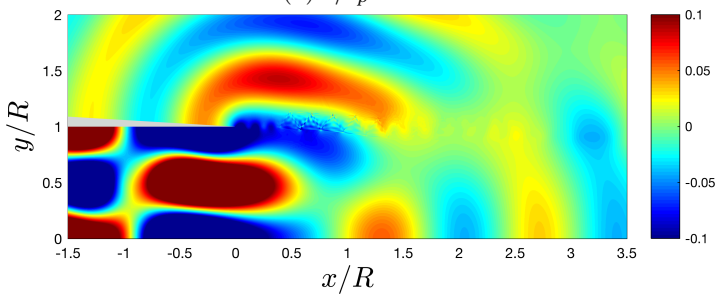

(b) $t/t_p = 19$

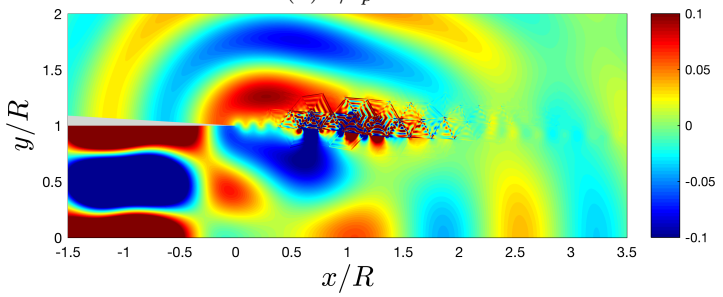

(c) $t/t_p = 30$

Figure 4.3: Contours of fluctuating pressure for acoustic disturbances radiating from a nozzle of radius, R, at three multiples of the source period, t_p.

pressure fluctuations associated with shedding of vortices are observed advecting with the mean flow. As time increases to $t/t_p = 19$, spurious oscillations begin forming in the center of the shear layer where mean velocity gradients are high. Initially, the spurious oscillations are smaller than the acoustic pressure of the source, but by time $t/t_p = 30$, the magnitudes of these fluctuations grow to approximately forty times the pressure at the center of the source. Eventually, the magnitude of the instability grows high enough to completely pollute the acoustic solution. This example illustrates how aliasing-driven instability can be detrimental to achieving accurate and computationally efficient solutions, especially when long integration times are required.

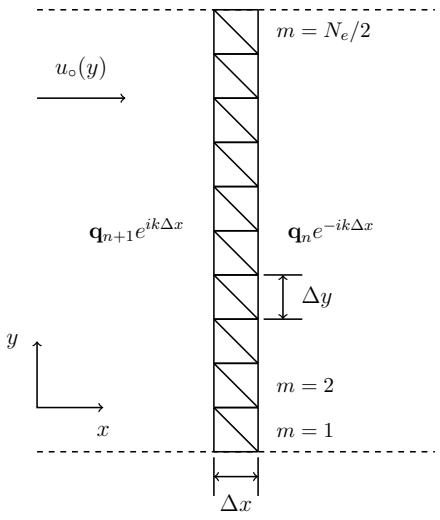

Figure 4.4: Definition of semi-infinite dispersion analysis, permitting a transversally nonuniform flow.

4.3 Dispersion analysis of the 2D LEE DGM model with a transversally non-uniform mean flow-field

Classical 2D dispersion analysis techniques for the DGM, such as the fully-discrete model developed in Chapter 3, consider only wave propagation over infinitely periodic meshes, which cannot be used to study propagation through spatially varying media. Additionally, dispersion analyses often consider model problems, which do not always reflect the complexities of the true application. To fully address the aliasing problem in shear layers, the dispersion analysis must be able to discretize the strong mean velocity gradients present in the LEE model. This section develops a fully-discrete dispersion analysis of the LEE, supporting a nonuniform mean flow, and uses it to study the formation and growth of aliasing instabilities.

To permit a nonuniform mean flow field, the computational domain shown in Figure 4.4 is used. Along the mesh transverse direction, y, the flow-field is allowed to vary and the domain is fully discretized using an even number, N_e, of triangular elements. Along the axial direction, x, the flow is constant, and the mesh is infinitely periodic. Although a uniformly-spaced mesh is shown, a variable mesh spacing in the y–direction is permitted, provided that the spacing in the axial direction is the same for all elements. At the boundaries of the mesh in the transverse direction, boundary conditions are applied, such as no-penetration conditions to model hard walls, or non-reflective conditions to model an open physical domain. Wave-like solutions to the LEE on the mesh of the form, $\mathbf{q} \sim e^{i(\omega t - kx)}$, are assumed, where k is the axial wavenumber and ω is the angular frequency. In this work, temporal instabilities are sought, so that k is a real, fixed value, and ω is generally complex. The solution in each element is

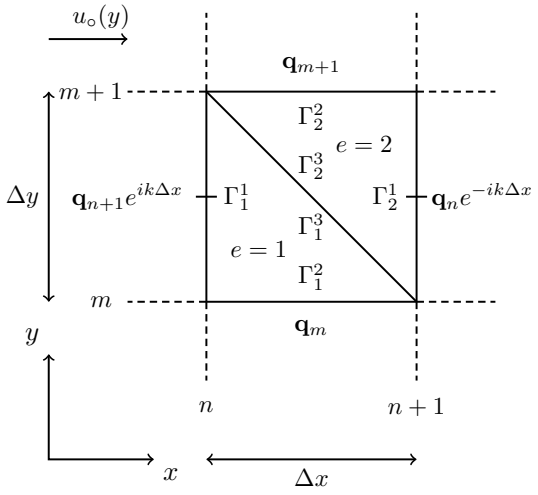

Figure 4.5: Two elements forming an interior patch of the mesh. Each edge is defined by Γ_e^b, indicating the local side, b, and the element number, e.

discretized in space by nodal polynomial basis functions,

$$\mathbf{q}(x,y,t) \approx \mathbf{\Psi}(x,y)\bar{\mathbf{q}}\, e^{i\omega t}, \tag{4.9}$$

where $\bar{\mathbf{q}}$ is the vector of nodal solution amplitudes. While chosen here for studying aliasing instabilities, this approach is also valid for the analysis of other features including the testing of boundary conditions, such as acoustic liner models or perfectly matched layers, anisotropic elements, or evaluating various mean flow interpolation strategies. Gabard and Brambley developed a similar dispersion analysis for a finite-difference scheme specifically to study the Myers impedance boundary condition [117].

The mesh is divided into multiple two-element patches, illustrated in Figure 4.5, to make the construction of the global problem similar to the two-element dispersion analysis developed in Section 3.1. Each two-element patch is indexed by m, where $m-1$ is the patch below m in the y–direction, and patch $m+1$ is the patch above m. Since the mesh is periodic in the x–direction, and the solution is assumed to be wave-like in space, a wavenumber phase relation is enforced on the solutions at the nth and $n+1$th boundaries of the patch such that,

$$\mathbf{q}\Big|_{\Gamma_1^1} = \mathbf{q}\Big|_{\Gamma_2^1} e^{ik\Delta x}, \text{ and, } \mathbf{q}\Big|_{\Gamma_2^1} = \mathbf{q}\Big|_{\Gamma_1^1} e^{-ik\Delta x}. \tag{4.10}$$

For each two-element patch, m, the solution amplitudes at the interpolation points for each variable are stored as the vector,

$$\bar{\mathbf{q}}_m = \begin{bmatrix} \bar{\mathbf{q}}_{m,1} \\ \bar{\mathbf{q}}_{m,2} \end{bmatrix}, \tag{4.11}$$

where,

$$\bar{\mathbf{q}}_{m,e} = \left[\rho'_1, (\rho u)'_1, (\rho v)'_1, \pi'_1, \ldots, \rho'_{N_p}, (\rho u)'_{N_p}, (\rho v)'_{N_p}, \pi'_{N_p}\right]^\intercal. \tag{4.12}$$

The subscript on the vector elements indexes the interpolation nodes, $1, 2, \ldots, N_p$. The degrees of freedom of all two-element patches are concatenated into a single vector,

$$\mathbf{Q} = \begin{bmatrix} \bar{\mathbf{q}}_1 \\ \bar{\mathbf{q}}_2 \\ \vdots \\ \bar{\mathbf{q}}_{N_e/2} \end{bmatrix}. \tag{4.13}$$

On all internal patches, *e.g.* $1 < m < N_e/2$, the semi-discrete form of the LEE for elements one and two in each patch are,

$$\begin{aligned} i\omega\bar{\mathbf{q}}_{m,1} = (\mathbf{D}^{\mathrm{w}}_{i,1} \otimes \mathbf{I})\, \mathbf{f}_{i,1}(\bar{\mathbf{q}}_{m,1}) &- (\mathbf{L}^1_1 \otimes \mathbf{I})\, \tilde{\mathbf{f}}^1_1 \left(\bar{\mathbf{q}}_{m,1}\Big|_{\Gamma^1_1}, \bar{\mathbf{q}}_{m,2}\Big|_{\Gamma^1_2} e^{ik\Delta x}\right), \\ &- (\mathbf{L}^2_1 \otimes \mathbf{I})\, \tilde{\mathbf{f}}^2_1 \left(\bar{\mathbf{q}}_{m,1}\Big|_{\Gamma^2_1}, \bar{\mathbf{q}}_{m-1,2}\Big|_{\Gamma^2_2}\right), \\ &- (\mathbf{L}^3_1 \otimes \mathbf{I})\, \tilde{\mathbf{f}}^3_1 \left(\bar{\mathbf{q}}_{m,1}\Big|_{\Gamma^3_1}, \bar{\mathbf{q}}_{m,2}\Big|_{\Gamma^3_2}\right), \text{ and,} \end{aligned} \tag{4.14}$$

$$\begin{aligned} i\omega\bar{\mathbf{q}}_{m,2} = (\mathbf{D}^{\mathrm{w}}_{i,2} \otimes \mathbf{I})\, \mathbf{f}_{i,2}(\bar{\mathbf{q}}_{m,2}) &- (\mathbf{L}^1_2 \otimes \mathbf{I})\, \tilde{\mathbf{f}}^1_2 \left(\bar{\mathbf{q}}_{m,2}\Big|_{\Gamma^1_2}, \bar{\mathbf{q}}_{m,1}\Big|_{\Gamma^1_1} e^{-ik\Delta x}\right), \\ &- (\mathbf{L}^2_2 \otimes \mathbf{I})\, \tilde{\mathbf{f}}^2_2 \left(\bar{\mathbf{q}}_{m,2}\Big|_{\Gamma^2_2}, \bar{\mathbf{q}}_{m+1,1}\Big|_{\Gamma^2_1}\right), \\ &- (\mathbf{L}^3_2 \otimes \mathbf{I})\, \tilde{\mathbf{f}}^3_2 \left(\bar{\mathbf{q}}_{m,2}\Big|_{\Gamma^3_2}, \bar{\mathbf{q}}_{m,1}\Big|_{\Gamma^3_1}\right), \end{aligned} \tag{4.15}$$

respectively.

Following the same definitions for the internal and numerical fluxes as Section 3.1 for the two-element dispersion analysis, the semi-discrete form for the solution over the entire two-element patch is combined to get,

$$i\omega\bar{\mathbf{q}}_m = \mathbf{B}_{m-1}\bar{\mathbf{q}}_{m-1} + \mathbf{A}_m\bar{\mathbf{q}}_m + \mathbf{B}_{m+1}\bar{\mathbf{q}}_{m+1}, \tag{4.16}$$

where $\mathbf{B}_{m-1}$ and $\mathbf{B}_{m+1}$ implement the contributions to the boundary flux integral from the solution on patches, $m-1$ and $m+1$.

At the boundaries of the mesh, patches $m = 1$ and $m = N_e/2$ must implement the boundary conditions. For element 1 of patch, $m = 1$, the numerical flux on face b in Equation 4.14 must be replaced by the desired boundary condition. Similarly, for element 2 of patch, $m = N_e/2$, the numerical flux on face b in Equation 4.15 is replaced. Including boundary conditions, the semi-discrete form for the elements at the top and bottom of the mesh can be written as,

$$\begin{aligned} i\omega\bar{\mathbf{q}}_{1,1} = (\mathbf{D}^{\mathrm{w}}_{i,1} \otimes \mathbf{I})\, \mathbf{f}_{i,1}(\bar{\mathbf{q}}_{1,1}) &- (\mathbf{L}^1_1 \otimes \mathbf{I})\, \tilde{\mathbf{f}}^1_1 \left(\bar{\mathbf{q}}_{1,1}\Big|_{\Gamma^1_1}, \bar{\mathbf{q}}_{1,2}\Big|_{\Gamma^1_2} e^{ik\Delta x} \right), \\ &- (\mathbf{L}^2_1 \otimes \mathbf{I})\, \tilde{\mathbf{f}}^2_1 \left(\bar{\mathbf{q}}_{1,1}\Big|_{\Gamma^2_1}, c_1\left(\bar{\mathbf{q}}_{1,1}\Big|_{\Gamma^2_1} \right) \right), \\ &- (\mathbf{L}^3_1 \otimes \mathbf{I})\, \tilde{\mathbf{f}}^3_1 \left(\bar{\mathbf{q}}_{1,1}\Big|_{\Gamma^3_1}, \bar{\mathbf{q}}_{1,2}\Big|_{\Gamma^3_2} \right), \text{ and,} \end{aligned} \tag{4.17}$$

$$\begin{aligned} i\omega\bar{\mathbf{q}}_{N_e/2,2} = (\mathbf{D}^{\mathrm{w}}_{i,2} \otimes \mathbf{I})\, \mathbf{f}_{i,2}(\bar{\mathbf{q}}_{N_e/2,2}) &- (\mathbf{L}^1_2 \otimes \mathbf{I})\, \tilde{\mathbf{f}}^1_2 \left(\bar{\mathbf{q}}_{N_e/2,2}\Big|_{\Gamma^1_2}, \bar{\mathbf{q}}_{N_e/2,1}\Big|_{\Gamma^1_1} e^{-ik\Delta x} \right), \\ &- (\mathbf{L}^2_2 \otimes \mathbf{I})\, \tilde{\mathbf{f}}^2_2 \left(\bar{\mathbf{q}}_{N_e/2,2}\Big|_{\Gamma^2_2}, c_2\left(\bar{\mathbf{q}}_{N_e/2,2}\Big|_{\Gamma^2_2} \right) \right), \\ &- (\mathbf{L}^3_2 \otimes \mathbf{I})\, \tilde{\mathbf{f}}^3_2 \left(\bar{\mathbf{q}}_{N_e/2,2}\Big|_{\Gamma^3_2}, \bar{\mathbf{q}}_{N_e/2,1}\Big|_{\Gamma^3_1} \right), \end{aligned} \tag{4.18}$$

where the functions, $c_1(\bar{\mathbf{q}}_{1,1}\big|_{\Gamma^2_1})$ and $c_2(\bar{\mathbf{q}}_{N_e/2,2}\big|_{\Gamma^2_2})$ implement the boundary conditions at the top and bottom of the mesh, respectively. In this work, an unbounded physical domain is modeled, so non-reflecting boundary conditions are implemented at the top and bottom of the computational domain. The boundary conditions then become, $c_1(\bar{\mathbf{q}}_{1,1}\big|_{\Gamma^2_1}) = \mathbf{0}$ and $c_2(\bar{\mathbf{q}}_{N_e/2,2}\big|_{\Gamma^2_2}) = \mathbf{0}$, respectively, for an approximate non-reflecting boundary. For a hard-wall boundary condition, the functions would instead reflect the momentum vector about the plane of the wall.

The semi-discrete form for the solution on patches $m = 1$ and $m = N_e/2$ can be written as,

$$i\omega\bar{\mathbf{q}}_{m=1} = \mathbf{A}_m\bar{\mathbf{q}}_m + \mathbf{B}_m\bar{\mathbf{q}}_m + \mathbf{B}_{m+1}\bar{\mathbf{q}}_{m+1}, \text{ and,} \tag{4.19}$$

$$i\omega\bar{\mathbf{q}}_{m=N_e/2} = \mathbf{B}_{m-1}\bar{\mathbf{q}}_{m-1} + \mathbf{A}_m\bar{\mathbf{q}}_m + \mathbf{B}_m\bar{\mathbf{q}}_m, \tag{4.20}$$

where $\mathbf{B}_m$ implements the contributions to the boundary flux integral from the boundary conditions.

Assembling the expressions for all internal and boundary patches in the mesh, the global semi-discrete form becomes,

$$i\omega\mathbf{Q} = \begin{bmatrix} \mathbf{A}_1 + \mathbf{B}_1 & \mathbf{B}_2 & \mathbf{0} & \dots & \mathbf{0} \\ \mathbf{B}_1 & \mathbf{A}_2 & \mathbf{B}_3 & \dots & \mathbf{0} \\ \vdots & & \ddots & & \vdots \\ \\ \mathbf{0} & \dots & \mathbf{0} & \mathbf{B}_{N_e/2-1} & \mathbf{A}_{N_e/2} + \mathbf{B}_{N_e/2} \end{bmatrix} \mathbf{Q}, \tag{4.21}$$

or,

$$i\omega\mathbf{Q} = \mathbf{A}\mathbf{Q}. \tag{4.22}$$

The above equation describes an eigenvalue problem, with eigenvalues ω, which are the numerical frequencies, and eigenvectors, $\mathbf{Q}$, which are the solution modes. For a given real wavenumber, k, the eigenvalue problem is solved for the numerical frequencies and solution modes. The imaginary part of the numerical frequencies represents the growth rate of a solution mode. A solution mode is unstable when the imaginary part is less than zero, *i.e.* $\mathrm{Im}(\omega) < 0$. Over a time interval, Δt, the solution mode grows, or decays, by a factor of $|e^{i\,\mathrm{Im}(\omega)\Delta t}|$.

4.3.1 Fully-discrete form

The above definition of the dispersion analysis discretizes the solution in space only. In Chapter 3, formulating a fully-discrete dispersion analysis allowed the study of the full effect of time-discretization on the solution accuracy and stability. In this chapter, a fully-discrete form of the dispersion analysis is used for assessing the impact of the time-step and allowing the use of a periodic solution filter.

To permit discretization of the solution in time, the definition of the discrete solution is changed to,

$$\mathbf{q}(x, y, t) \approx \mathbf{\Psi}(x, y)\bar{\mathbf{q}}(t), \tag{4.23}$$

where the nodal solution values now are time-dependent. Instead of analytically evaluating the time-derivative, the explicit scheme of Section 2.5.3 is applied. The solution at time level $t = t + \Delta t$ can be found from the solution at time, t, through the multi-stage, low-storage, time-integration scheme of Berland *et al.* [92],

$$\mathbf{Q}^{t+\Delta t} = \left[\mathbf{I} + \sum_{s=1}^{N_{\mathrm{st}}} \gamma_s \left(\mathbf{A}\Delta t\right)^s\right] \mathbf{Q}^t = \mathbf{A}_{\mathrm{RK}}\mathbf{Q}^t, \tag{4.24}$$

where $\mathbf{Q}^{t+\Delta t}$ is the global solution vector at time $t = t + \Delta t$ and $\mathbf{Q}^t$ is the solution at time t. The coefficient of the time integration scheme at stage, s, is given by γ_s. The matrix, $\mathbf{I}$, is the identity matrix of size $N_p N_e N_v \times N_p N_e N_v$, where N_v is the number of variables and N_p is the number of nodal solution values. The operator, $(\cdot)^s$, implements the matrix power. The growth factor of the solution over the time-step is defined as,

$$\mathbf{Q}^{t+\Delta t} = g\,\mathbf{Q}^t. \tag{4.25}$$

Substituting the above definition into Equation 4.24, gives,

$$g\,\mathbf{Q}^t = \mathbf{A}_{\mathrm{RK}}\mathbf{Q}^t, \tag{4.26}$$

which is an eigenvalue problem with growth factors as eigenvalues and solution modes as eigenvectors. Growth factors can then be related to numerical frequencies of the solution modes through,

$$g = e^{i(\omega\Delta t + n2\pi)}, \tag{4.27}$$

where n is an integer.

4.4 Verification of instability in a hyperbolic-tangent sheared mean velocity profile

The nonuniform flow dispersion analysis developed in the previous section is applied to the problem of instability in a compressible, parallel, shear layer to verify the implementation. Shear layers are an important feature of the flow-field in turbofan exhaust applications. Occurring at the boundary between adjacent flow streams of different velocity, shear layer velocity profiles can rapidly transition to instability when disturbed. The instability for linear, inviscid flow is associated with an increase in vorticity, advecting with phase velocity equal to the centerline velocity of the undisturbed velocity profile [118].

Parallel, hyperbolic-tangent velocity profiles have commonly been used as an analogue for real shear layers, due to them possessing an inflection point, which is a sufficient condition for instability [118]. Linear stability analysis of the disturbed hyperbolic-tangent velocity profiles have been used to understand the growth and shape of disturbances of a given wavenumber or frequency. Michalke developed an analytic solution to the instability in an incompressible shear layer and studied the growth rates, streamlines, and vorticity distribution for temporal and spatial growth of the instability [118, 119]. Later, Blumen [120] extended Michalke's analytical solution to a compressible shear layer.

In this section, the analytical solution of Blumen [120] is solved for growth rates of the instability for varying Mach number and compared to numerical solutions using the dispersion analysis. The solution process involves numerically integrating a set of ODEs across the shear layer and using a shooting method to solve for the instability growth rates for a disturbance of a given wavenumber. Full details of the solution process are given in [120]. To reduce aliasing errors in the dispersion analysis, the computational domain is discretized with a refined mesh of 160 elements of polynomial order, $p = 4$, and a truncating filter from Section 4.5.4, is applied to truncate the solution coefficients of the degree 3 and 4 basis functions.

A mean flow-field is prescribed with a hyperbolic-tangent velocity profile,

$$\frac{u_\circ}{c_\infty} = M \tanh(y/L), \tag{4.28}$$

with constants of length, L, and Mach number, M, introduced that characterize the transverse variation of the shear layer and its velocity scale, such that $M = U/c_\infty$, where U is the maximum absolute value of the shear layer velocity. The mean sound speed, density, and pressure are constant. The velocity profile is illustrated for a range of Mach numbers in Figure 4.6b.

For three Mach numbers, $M = 0.1$, $M = 0.3$, and $M = 0.5$, the dispersion analysis eigenvalue problem is solved to obtain the instability growth rates for a range of wavenumbers. Only the eigenvalue and eigenvector of the most unstable mode is stored, *e.g.* $\min(\mathrm{Im}(\omega))$. Figure 4.6a compares the analytical growth rates to the numerical growth rates for varying Mach number. For each Mach number, the growth rate of the unstable solution mode in the shear layer grows with increasing kL, reaches a maximum, and then decays with increasing kL. The prediction of the instability growth rates by the dispersion analysis is in close agreement with the analytical solution.

The eigenvector, $\mathbf{Q}$, corresponding to the maximum growth rate, gives the nodal values of the most unstable solution mode, which can be studied to determine the characteristics of the unstable shear layer. To effectively visualize the solution, the solution mode on the 160 element patch is tiled in the axial direction and shifted in phase by,

$$\mathbf{q}(x + \Delta x, y) = \bar{\mathbf{q}}(x, y) e^{-ik\Delta x}, \tag{4.29}$$

to make a square domain of 160×160 elements. Figures 4.7a and 4.7b show the real part of fluctuating pressure and vorticity of the unstable solution mode and the computational elements. The solutions are normalized by the magnitude of the eigenvector, $\|\mathbf{Q}\|$. Concentrations of vorticity are apparent near the center of shear layer, $y = 0$, where the mean velocity gradients are the highest. Parallel vortex sheets representing pairs of vortices rotating around each other as they advect with the flow, are observed.

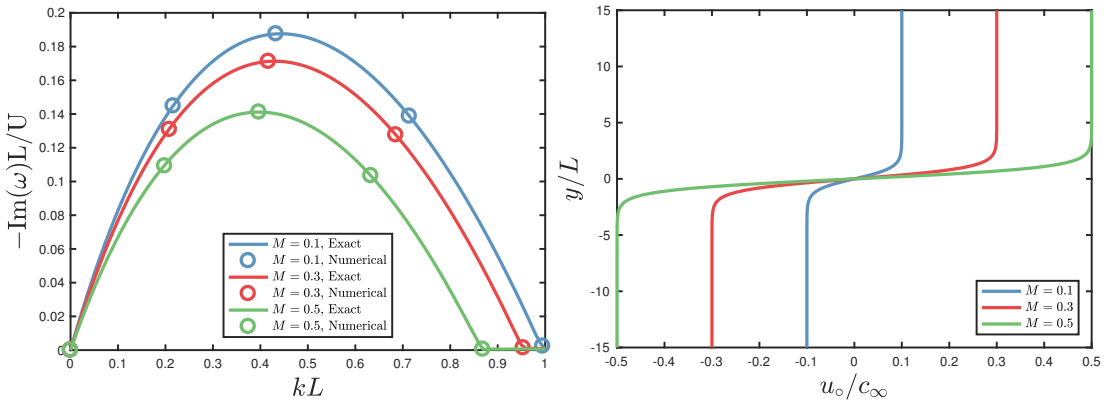

(a) (b)

Figure 4.6: (a): Comparison between the analytical instability growth rates with the dispersion analysis on a refined mesh for Mach numbers, $M = 0.1$, $M = 0.3$, and $M = 0.5$. (b) Shear layer velocity profile for Mach numbers, $M = 0.1$, $M = 0.3$, and $M = 0.5$.

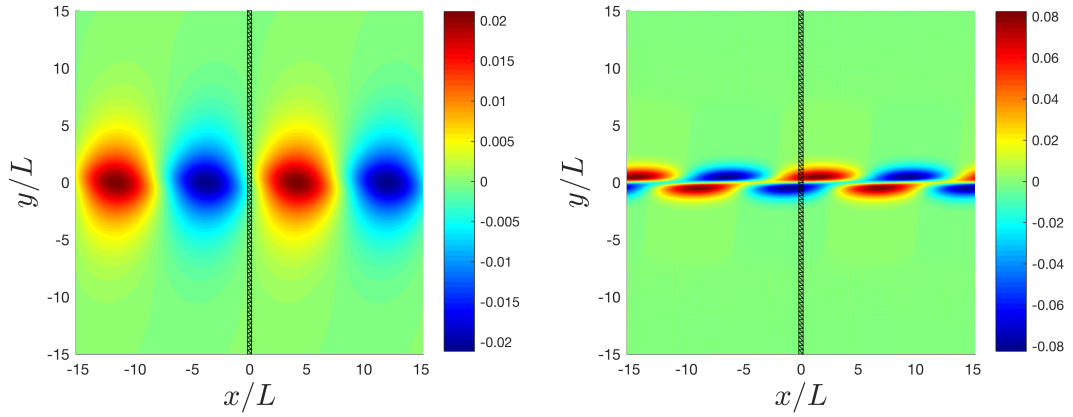

(a) (b)

Figure 4.7: Normalized solution mode corresponding to the largest growth rate in the $M = 0.5$ flow for (a): pressure and (b): vorticity. The outlines of individual elements are shown in black.

This general behavior is in agreement with the computations of vorticity by Michalke for an incompressible shear layer [118]. Figure 4.7a shows the fluctuations in pressure associated with the velocity fluctuations.

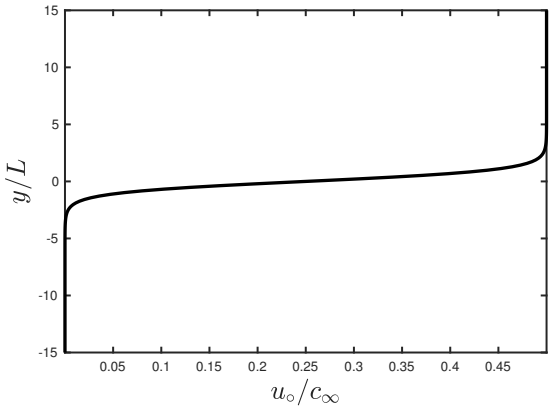

Figure 4.8: Hyperbolic-tangent mean velocity profile in the shear layer for $M = 0.5$.

4.5 Aliasing instability in a parallel, hyperbolic-tangent shear layer

Now that the ability of the dispersion analysis to accurately predict shear instabilities has been verified for a refined mesh, the tool is applied in this section to a coarser mesh, initially without filtering. With a coarser mesh, the flux will be less resolved by the discretization in the shear layer, leading to increased aliasing. It is expected that the increased aliasing will lead to instabilities similar to what was observed in Section 4.2 for the 2D growing shear layer. Using the dispersion analysis, the effect of different discretizations on the aliasing error can be identified by altering the polynomial order, flux function, or by adding filtering. The effect of varying polynomial order is first investigated, followed by the time integration scheme, and the numerical flux functions.

The shear layer velocity used in this study is the hyperbolic-tangent profile,

$$\frac{u_\circ}{c_\infty} = \frac{M}{2}(1 + \tanh(y/L)), \tag{4.30}$$

with Mach number, $M = 0.5$. Using the same 160 element mesh and truncating filter used in the verification section above, a reference solution for the numerical frequencies and solution modes is computed. The results in the following sections can be compared to the reference solution to identify the approximation error on the coarse mesh.

4.5.1 Properties of the instability with the standard nodal DG scheme

For minimal computational cost, it is important to use large elements with high order polynomial basis functions, to maximize the number of vectorized calculations and to minimize the total number of time steps. It is therefore important that the effect of increasing polynomial order on the aliasing error is investigated.

The theoretical convergence rate of the solution interpolation error, relative dissipation error, and relative dispersion error follow, $(kh)^{p+1}$, $(kh)^{2p+1}$ and $(kh)^{2p+2}$, respectively, where k is the solution wavenumber, h is the characteristic element size, and p is the order of the polynomial basis functions. For a constant mean flow-field and thermodynamic state, Chapter 3 verified that the 2D LEE DGM achieves the theoretical convergence rates. With a nonuniform mean flow, it is expected that aliasing error will be detrimental to the convergence rate. By keeping the mesh fixed and computing the numerical frequency of the instability at a range of disturbance wavenumbers, the polynomial convergence accuracy can be isolated.

The domain is discretized with 40 elements along the transverse direction of size $\Delta x = \Delta y = 1.5L$, and the polynomial order is varied from $p = 1$ to $p = 8$. Equation 4.30 describes the shear layer mean velocity profile, and the mean density, pressure, and sound speed are constant. The semi-discrete eigenvalue problem of Section 4.3 is solved for each order over a range of wavenumbers from $kL = 0$ to $kL = 1$. For each wavenumber, the numerical frequency and solution vector corresponding to the most unstable mode, $\max(-\operatorname{Im}(\omega))$, is stored and compared to the reference results.

The growth rates of the most unstable mode are shown in Figure 4.9a, with each point corresponding to a different kL and order, and the reference results shown as black circles. Increasing the polynomial order from one to four, the growth rates begin to approach the reference values for wavenumbers approximately in the range $0.15 \leq kL \leq 0.65$. Outside this range, and for higher polynomial orders, the predicted growth rates strongly deviate from the reference results. In fact, increasing the order has a negative effect on the accuracy, when one would expect convergence to the reference solution. It is important to note that no effort has been made to track the eigenvalues with kh, and therefore the most unstable mode may change with kh, explaining the sudden jumps for $kh > 0.5$ in Figure 4.9b. The most unstable mode is selected at each wavenumber since that limits the stability of the problem.

In the same manner as Section 4.4, the eigenvector associated with the most unstable mode can be tiled and plotted to identify the physical behavior of the solution. Referring to Figure 4.9a, two solutions are chosen at a fixed $kL = 0.4$: the $p = 4$ solution, which appears to agree well with the reference solution, and the $p = 8$ solution which deviates from the reference values by at least a factor of four. Figure 4.10a shows the normalized solution mode for pressure at order $p = 4$. This solution is consistent with the pressure solution observed in Figure 4.7a associated with the vortex sheets in the shear layer. Figure 4.10b shows the solution mode for pressure at order $p = 8$. In contrast to the $p = 4$ results, the solution mode is entirely spurious, composed of very high wavenumber oscillations and no physical mode can be identified. The unstable solution is concentrated near $y = 0$, which is the region where both the mean velocity

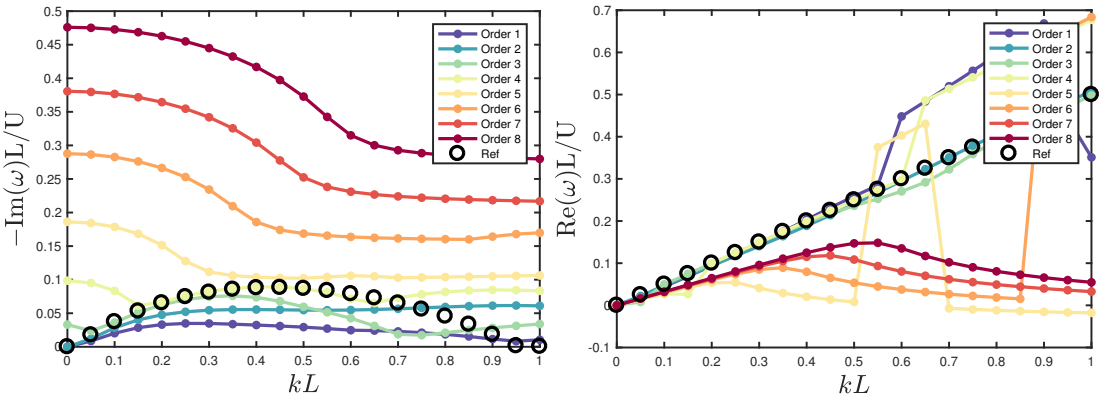

(a) (b)

Figure 4.9: Numerical frequencies at a range of wavenumbers and polynomial orders of the shear layer instability. (a): Imaginary part. (b): Real part. The reference result without aliasing is shown in black.

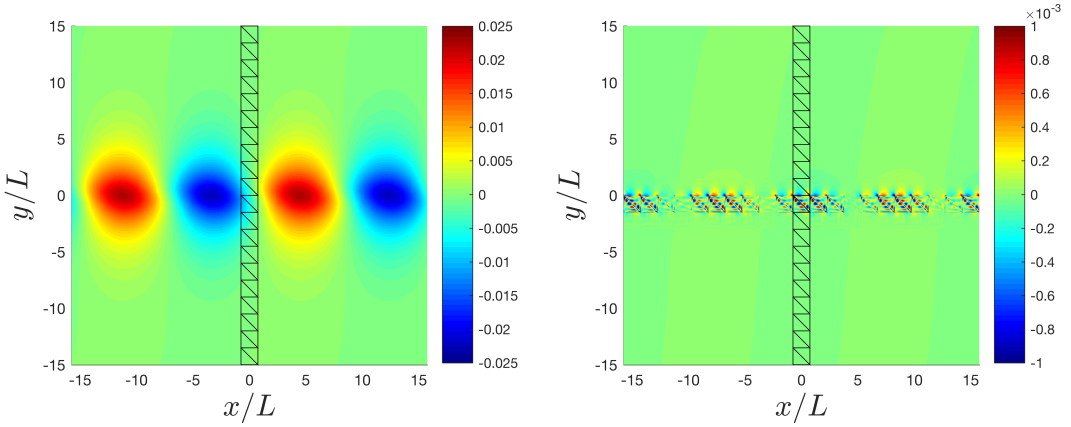

(a) $p = 4$ (b) $p = 8$

Figure 4.10: Normalized pressure, $p'/\|\mathbf{Q}\|$, for the most unstable mode at $kL = 0.4$ for the polynomial order $p = 4$ and $p = 8$ solutions. The mesh is shown at the center of the figure in black lines.

and the solution have the highest gradients. These high gradients are likely responsible for the aliasing, since the interpolation of the flux is the least well-resolved in this region.

The real part of the numerical frequency gives the dispersion relation, $\mathrm{Re}(\omega(k))$, of the most unstable mode. By computing the group velocity, $\frac{\mathrm{d}\,\mathrm{Re}(\omega)}{\mathrm{d}k}$, the propagation speed of the disturbances can be identified. When the group velocity associated with the most unstable mode is nonzero, it means that the unstable mode will advect away from the source as it grows. Conversely, a zero group velocity implies that the instability remains stationary as it grows [121]. Unstable modes with small or zero group velocity will rapidly pollute the solution as they will not exit the computational

domain before growing unbounded. The real part of the numerical frequency is shown for each wavenumber and order in Figure 4.9b. The group velocity for the reference mode is found by taking the slope of the line, resulting in $\frac{\mathrm{d}\,\mathrm{Re}(\omega)}{\mathrm{d}k} = 0.5U$, indicating that the physical unstable mode advects with the shear layer centerline velocity. The real numerical frequencies for orders one through four approximate the reference results well over the range $0 \leq kL \leq 0.55$. However, for polynomial orders $p > 4$, the dispersion error is high and for $kL > 0.55$, the group velocity approaches zero, indicating that the instability advects slowly or not at all.

4.5.2 Effect of the time integration

While the aliasing error described in this chapter is caused by a lack of spatial resolution of the flux, it is useful to eliminate the time integration as a source of the instability. Thus far, the semi-discrete dispersion analysis of Section 4.3 has been solved for numerical frequencies, and the ones associated with the most unstable solution mode are stored. To include the effect of the time integration, the fully-discrete dispersion analysis, developed in Section 4.3.1 is solved for growth factors of the solution modes over a single time step, Δt. From the growth factors, the numerical frequencies are obtained through the expression,

$$\omega = \frac{-i\ln(g) - n2\pi}{\Delta t}, \tag{4.31}$$

where g is the growth factor of the solution mode over a single time step, and n is an integer.

The calculation of the previous section for the hyperbolic-tangent shear layer is repeated using the fully-discrete dispersion analysis. Choosing a single polynomial order, $p = 4$, and a range of CFLs, the growth rates for the most unstable mode are calculated using Equation 4.31 and shown in Figure 4.11. There is no observable difference between the growth rates computed with different time-steps, indicating that the time-step has no impact on the aliasing instability and cannot be reduced to maintain stability.

4.5.3 Effect of the numerical flux function

Until now, the dispersion analysis considered only the exact upwind flux, derived in Section 2.4.1. This section will evaluate the behavior of the aliasing-driven unstable solution mode using the common, Lax-Friedrichs flux,

$$\tilde{\mathbf{f}}(\mathbf{q}_e, \mathbf{q}_{e+}) = \frac{1}{2}\left[\mathbf{F}_{\circ,n}\,\mathbf{q}_e + \mathbf{F}_{\circ,n}\,\mathbf{q}_{e+} + \max\left(|\mathbf{\Lambda}|\right)\,(\mathbf{q}_e - \mathbf{q}_{e+})\right]\,. \tag{4.32}$$

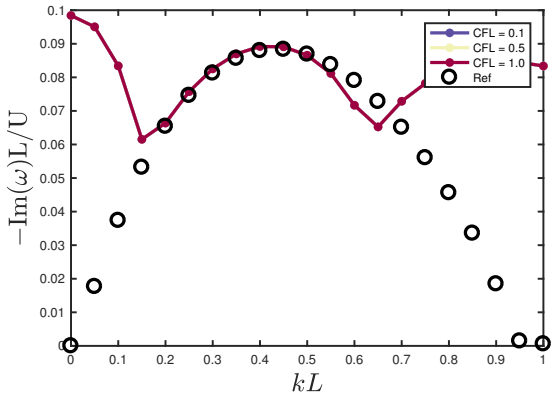

Figure 4.11: Growth rates of the most unstable mode computed using the fully-discrete dispersion analysis for the $p = 4$ discretization. Three time-steps are used based on CFL = 0.1, CFL = 0.5, and CFL = 1.0.

The Lax-Friedrichs flux can be thought of as a central flux plus a dissipation term that is proportional to the solution jump across the element interfaces. This additional dissipation may have a stabilizing effect on the aliasing-driven instabilities.

To add the new flux function to the dispersion analysis, the matrix $\mathbf{F}^{b+}_{\mathrm{n},e}$, defined in Section 3.1, must be changed to,

$$\mathbf{F}^{b+}_{\mathrm{n},e} = \begin{bmatrix} |\mathbf{\Lambda}|_{\max}\Big|_{\vec{x}_{e,b,1}} & \mathbf{0} & \mathbf{0} & \mathbf{0} \\ \mathbf{0} & |\mathbf{\Lambda}|_{\max}\Big|_{\vec{x}_{e,b,2}} & \mathbf{0} & \mathbf{0} \\ \mathbf{0} & \mathbf{0} & \ddots & \mathbf{0} \\ \mathbf{0} & \mathbf{0} & \mathbf{0} & |\mathbf{\Lambda}|_{\max}\Big|_{\vec{x}_{e,b,p+1}} \end{bmatrix}, \tag{4.33}$$

where $|\mathbf{\Lambda}|_{\max}$ is the absolute value of the maximum wave speed, $c_\circ + |u_\circ|$, at the flux evaluation point.

With the Lax-Friedrichs flux, a new solution to the semi-discrete dispersion analysis can be found and compared to the results in Section 4.5.1. Solutions are obtained on the same, 40 element mesh for a range of wavenumbers from $kL = 0$ to $kL = 1$, and polynomial orders $p = 1$ to $p = 8$. Figure 4.12a shows the growth rates of the most unstable mode for the Lax-Friedrichs flux. On first inspection, the growth rates appear lower than for the upwind flux, which are shown in Figure 4.9a, over the entire range of wavenumbers and for each order. For the upwind flux, the maximum growth rate over kL for each polynomial order, is proportional to the order. The behavior appears different for the Lax-Friedrichs flux. While there is certainly an order-dependent

increase in the maximum growth rate, it does not appear to be as strong as for the upwind flux. Figure 4.12b shows the dispersion relation of the most unstable mode for each polynomial order. In the range $0.3 \leq kL \leq 0.5$, the dispersion error appears lower than for the upwind flux, however, outside of this region, substantial inaccuracies are visible. The $p = 6$, $p = 7$, and $p = 8$ results exhibit much higher phase shift for wavenumbers which are not near the maximum of the shear-layer instability. However, the slope, or group velocity, for each order appears to be closer to the reference results. These results indicate that the Lax-Friedrichs flux offers better stability qualities than the fully upwind flux.

4.5.4 Effect of periodic modal filtering

A simple to implement and yet computationally efficient way to remove aliasing-driven instabilities is to periodically filter the solution to avoid the buildup of aliasing error. Aliasing error builds up in solutions as energy in the highest order modes and progressively corrupts the lower order modes, eventually leading to instability [46, 55, 102]. The filtering process selectively damps the higher order modes to avoid this cascade of energy into the lower order modes.

In this work, the filter of the type developed by Hesthaven and Kirby [55] is employed to filter the modal coefficients of the solution. The filtered solution takes the form of,

$$\mathbf{q}^*(\vec{x}) = \sum_{n=0}^{N_p-1} \sigma\,(n)\,\hat{\mathbf{q}}_n \phi_n(\vec{x}), \tag{4.34}$$

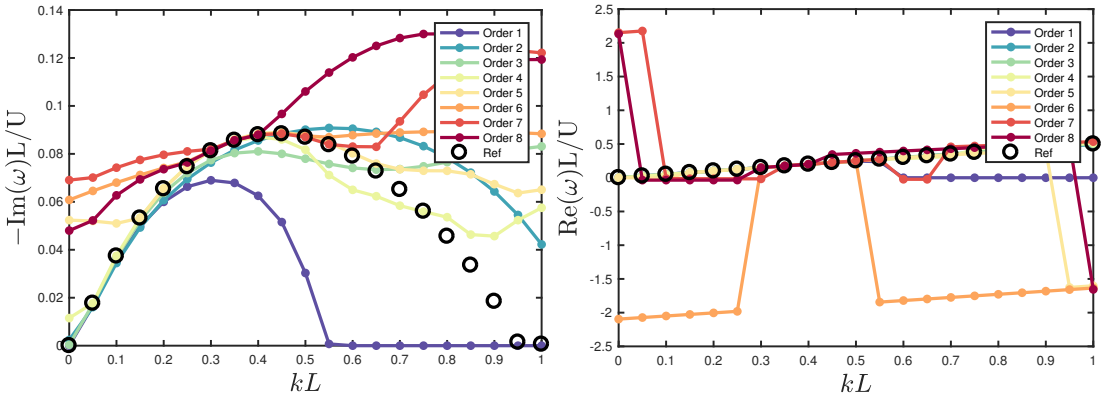

(a) (b)

Figure 4.12: Numerical frequencies at a range of wavenumbers and polynomial orders of the shear layer instability with the Lax-Friedrichs numerical flux. (a): Imaginary part. (b): Real part. The reference result without aliasing is shown in black.

where $\mathbf{q}^*$ is the filtered solution, σ is the filter function, ϕ_n is the nth modal basis function, and $\hat{\mathbf{q}}_n$ is the nth solution coefficient. The filter function is defined as,

$$\sigma(n) = \exp\left[-\alpha\left(\frac{o(n) - p_c}{p - p_c}\right)^s\right], \tag{4.35}$$

where $o(n)$ converts the modal coefficient number to the degree of the polynomial of that term, and p_c is the order below which, no modes are altered. The parameters α and s control the magnitude of filtering and the rate at which the filtering increases with the degree of each term. Alternatively, the truncating filter function,

$$\phi(n) = \begin{cases} 1 & \text{for } o(n) < p_c \\ 0 & \text{for } o(n) \geq p_c \end{cases}, \tag{4.36}$$

can be applied to cut-off all modes above p_c.

To filter the nodal values of the solution, a nodal filter matrix, $\mathcal{F}$, is defined as,

$$\mathcal{F} = \mathcal{V}\boldsymbol{\sigma}\mathcal{V}^{-1}, \tag{4.37}$$

where $\boldsymbol{\sigma}$ is a diagonal matrix with entries, $\{\boldsymbol{\sigma}\}_{n,n} = \sigma(n)$, and $\mathcal{V}$ is the Vandermonde matrix.

To implement this filter in the dispersion analysis, a global filter matrix, $\mathcal{F}_\mathrm{G}$, is defined that takes the entire solution vector, $\mathbf{Q}$, and applies the filter to the modal coefficients. The global filter matrix can be constructed from the local filter matrix through,

$$\mathcal{F}_\mathrm{G} = \mathbf{I}_{N_e} \otimes \mathcal{F} \otimes \mathbf{I}_{N_v}, \tag{4.38}$$

where $\mathbf{I}_{N_e}$ and $\mathbf{I}_{N_v}$ are the $N_e \times N_e$ and $N_v \times N_v$ identity matrices, respectively. To model filtering of the solution at the end of each time-step, the fully-discrete form is modified such that,

$$e^{i\omega\Delta t}\mathbf{Q} = \mathcal{F}_\mathrm{G}\left[\mathbf{I} + \sum_{s=1}^{N_\mathrm{st}} \gamma_s \left(\mathbf{A}\Delta t\right)^s\right]\mathbf{Q} = \mathbf{A}_\mathrm{RK}\mathbf{Q}. \tag{4.39}$$

To demonstrate the stabilizing effect of the filter, the fully-discrete dispersion analysis is applied to the shear instability problem and solved for a range of wavenumbers and polynomial orders. For each order, the parameters, α and s are fixed to 36 and 16, respectively. The order cut-off, p_c, varies with order as $p_c = 3/2\,p$, to impact only the upper third of the modes. Figure 4.13a shows the numerical growth rates predicted by the dispersion analysis of the filtered scheme. Unlike the unfiltered scheme, the growth rates converge to the reference solution with increasing order over the entire

wavenumber range. The real part of the numerical frequency, shown in Figure 4.13b, converges to the reference solution with increasing order, except for the regions near $kL = 0$ and $kL = 1$, which show significant phase error for high orders. This indicates that while the aliasing instability has been significantly damped, it has not been eliminated entirely, although the growth rates at $kL = 0$ and $kL = 1$ appear to be small. With a greater filter strength, the instability could be eliminated all together.

4.5.5 Discussion on interpolation points

It is well known that the choice of interpolation points on which to construct the nodal basis functions can impact the accuracy and stability of DG schemes [102, 105, 106, 109]. Williams and Jameson [106] determined that locating the interpolation points at quadrature points substantially reduces aliasing errors. Witherden and Vincent [109] analyzed different sets of interpolation points for their quadrature and interpolation qualities and determined that locating interpolation points at quadrature points may be necessary, but not sufficient for a stable and accurate scheme when solving marginally-resolved nonlinear problems.

Often, and in this work, the interpolation points are chosen to maximize the quality of the interpolation. The spacing of interpolation points on triangles and tetrahedra can be represented by a single constant, α, which can be varied to maximize some quality metric [55]. The resulting nodal sets are known as α–optimized nodes. One common

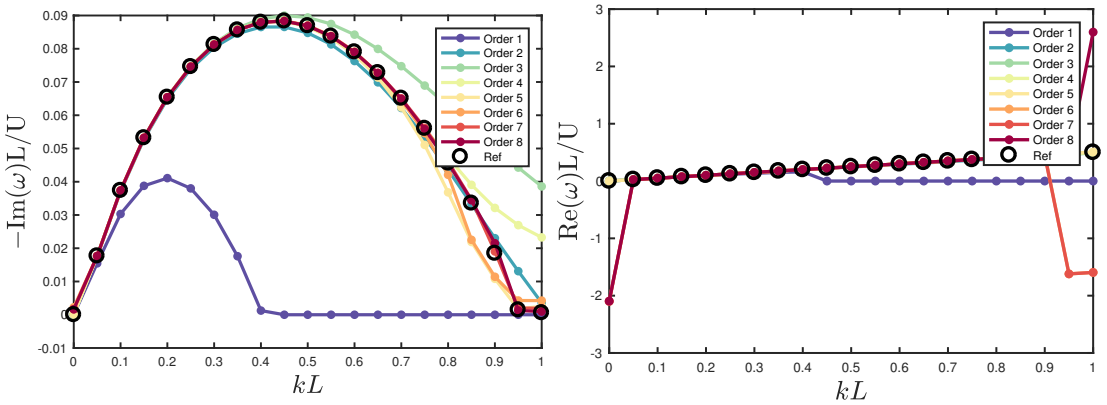

(a) (b)

Figure 4.13: Numerical frequencies at a range of wavenumbers and polynomial orders of the shear layer instability computed with polynomial filtering. (a): Imaginary part. (b): Real part. The reference result without aliasing is shown in black.

metric for the quality of an interpolation is known as the Lebesgue constant,

$$\Lambda = \max_{\mathbf{x}} \sum_{i=1}^{N_p} |\phi_i(\mathbf{x})|. \tag{4.40}$$

The Lebesgue constant measures how closely an interpolation is to the optimal polynomial with minimal interpolation error [55]. By adjusting α to minimize the Lebesgue constant, a point set with optimal interpolation qualities can be identified.

For problems with a nonlinear flux, the α–optimized nodes have been shown to have suboptimal stability qualities [106, 109]. Solution points must be not only good for interpolation, but for nonlinear problems, or non-constant coefficient linear problems, they must also minimize the error of the collocation-projection of flux to achieve low aliasing error. Locating the interpolation points to coincide with quadrature points has been shown to reduce aliasing [106, 109], but often, good quadrature points do not coincide with the edges of triangles or faces of tetrahedra. Therefore, to evaluate the boundary flux integrals, a separate set of quadrature points is required on the boundary of the element. This then requires application of an interpolation matrix that interpolates the solution from the volume of the element, to the face nodes, before evaluating the flux. For this reason, the α–optimized are still used in this work.

4.6 Aliasing instability in a mean temperature non-uniformity

The stability analysis of DG solutions to the LEE in a sheared flow, showed aliasing instabilities that grew rapidly in time. However, it is unclear whether the aliasing-driven instabilities are stronger when shear layer instabilities are present. To evaluate this idea, the dispersion analysis is applied to the problem of wave propagation through a mean temperature non-uniformity in a uniform mean flow. With a uniform mean flow velocity, solutions to the LEE are not expected contain an unstable mode, unless it is caused by aliasing.

A mean density profile of the form,

$$\rho_\circ/\rho_\infty = 1 + \frac{1}{4}\left[1 + \tanh(y/L)\right], \tag{4.41}$$

is chosen, where L is the characteristic length scale of the non-uniformity. This density profile has a nonlinearity similar to the shear layer velocity profile of Section 4.5. The uniform mean flow velocity and pressure are set to $u_\circ/c_\infty = 0.25$ and $p_\circ/p_\infty = 1$, respectively. To compare with the results of the previous sections, the same mesh and

range of polynomial orders are considered, and a reference solution is computed on the 160 element mesh with a truncating filter.

Figure 4.14a compares the growth rates of the most unstable mode over a range of wavenumbers from $kL = 0$ to $kL = 1$ for polynomial orders $p = 1$ to $p = 8$. On first inspection, the maximum growth rates achieved for orders $p = 7$ and $p = 8$ over the wavenumber range are an order of magnitude smaller than those predicted for the shear layer velocity profile. Figure 4.14b shows a zoomed-in region of the growth rates on a scale from $-\mathrm{Im}(\omega)L/U = 0$ to $-\mathrm{Im}(\omega)L/U = 1 \times 10^{-5}$. Notice that the maximum growth rates for orders $p = 1$ to $p = 5$ are three orders of magnitude smaller than for the shear layer aliasing instabilities. Similar to the shear layer problem, the maximum growth rates increase with increasing polynomial order.

This example shows that aliasing in solutions to the LEE is highly dependent on the specific form of the mean flow-field. When the solution to the governing equations is stable, the numerical errors satisfying the discrete system are damped, along with the solution. When the solution is unstable, the numerical errors along with the solution are amplified, leading to increased build-up of error and potentially numerical instability. Therefore, when the mean flow-field supports shear instabilities, aliasing mitigation becomes critical for long-time stability of solutions. For a nonuniform thermodynamic state and a uniform mean velocity field, such as the temperature nonuniformity, aliasing instabilities grow slower, and only a weak filter would be necessary to ensure stability.

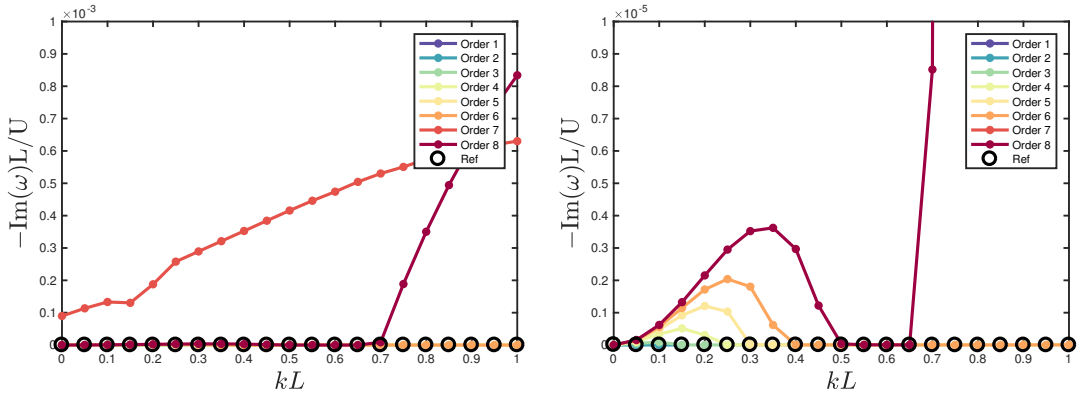

Figure 4.14: (a): Growth rate of the most unstable mode for a mean temperature nonuniformity and varying polynomial order. (b): Zoomed-in region of the most unstable mode growth rates.

4.7 Conclusion

This chapter investigated the problem of aliasing-driven instabilities in DG solutions to the LEE. For turbofan exhaust noise applications, the shear layers in the exhaust streams have large gradients of axial velocity, making them particularly prone to aliasing. The aliasing problem was demonstrated by computing 2D solutions to radiation of sound from a planar jet. A new dispersion analysis for the DGM with a non-uniform mean flow was developed and applied to the problem of predicting aliasing instabilities in a hyperbolic-tangent sheared mean flow. By changing the discretization parameters, the effect of polynomial order, time-step, flux-function, and filtering, on the aliasing instabilities was studied. The results indicate that,

- the maximum growth rate of the instabilities increases with increasing polynomial order when using the α–optimized interpolation points, an upwind flux, and a fixed mesh,
- solutions computed using the Lax-Friedrichs flux function offer greater stability than using the fully upwind flux function,
- periodic filtering of solution polynomial coefficients is an effective and computationally efficient way to stabilize solutions, and,
- mean flow-fields that permit unstable solution modes, such as shear layers, are particularly prone to strongly-growing aliasing instabilities, whereas flow-fields which do not permit unstable solution modes, have weaker growth of aliasing instabilities.

One aspect that has not been investigated in this chapter is geometrical aliasing. Discussed in Section 2.5.5, geometrical aliasing occurs in elements with a non-constant Jacobian. Since evaluating the boundary flux integrals with a sufficiently high quadrature rule eliminates the instabilities for the quadratic elements in this work, it was not deemed necessary to investigate in this section. However, the dispersion analysis could be applied to the study of geometrical aliasing in circular cross-section ducts with curved wall elements, computing growth rates of the instability for varying azimuthal wavenumber.

Chapter 5

Representation of the mean flow

The linearization process of the Euler equations, covered in Chapter 2, expresses the solution as a sum of a mean state plus a small, fluctuating state, so that,

$$\begin{aligned}
\rho &= \rho_\circ + \rho' \\
\rho u &= (\rho u)_\circ + (\rho u)' \\
\rho v &= (\rho v)_\circ + (\rho v)' \\
\rho w &= (\rho w)_\circ + (\rho w)' \\
\pi &= \pi_\circ + \pi'.
\end{aligned}$$

The fluctuating state, $\{\cdot\}'$, is obtained by solving the LEE, and the mean state, $\{\cdot\}_\circ$, must be specified *a priori*. Both the fluctuating and mean states are solutions to the Euler equations, however, in many applications, viscous effects are important for the accurate modeling of the mean flow-field. For example, the exhaust jet of a turbofan engine has turbulent shear layers with strong gradients of axial velocity, causing the refraction of acoustic waves and the transfer of acoustic energy into the formation of vortices that are convected downstream by the mean flow. To model these effects, the mean flow-field is often obtained from steady-state solutions to the Navier-Stokes equations.

Described in Chapter 2, the fluxes, Equation 2.3, are computed at the interpolation nodes of each element, requiring nodal values of the mean flow-field. Often, to save memory, the mean flow-field is stored as a linear or quadratic polynomial in each element which is used to interpolate the flow at each of the nodes. For high-order methods such as the DGM that permit the use of large elements for computational efficiency, a low order accurate representation of the mean flow in each element may not be sufficiently accurate to represent the spatial variation of the mean flow. An

alternative approach is to store a high-order representation of the mean flow in each element using the same polynomial basis functions as is used to discretize the solution. Using high-order polynomial basis functions to describe the mean flow state, can potentially lead to increased aliasing errors due to the increased polynomial degree of the fluxes [122, 123]. The aliasing problem is described in detail in Chapter 4. Therefore, before immediately adopting a higher-order representation of the mean state, a study of the impact of the representation accuracy on the acoustic solution accuracy should be performed. There exist many results on the impact of the solution interpolation on the solution accuracy, but little on how the interpolation error of the mean variables effects the solution in a hybrid aeroacoustics approach. The first half of this chapter is devoted to shedding light on this topic.

A low-order representation of the mean flow-field requires values of the CFD data at the nodes of the linear or quadratic shape functions in each element, while a high-order representation requires values at the DG interpolation nodes on each element. Unless an identical mesh and discretization are used for both the CFD and acoustic computation, an interpolation or approximation procedure is required that maps from the CFD mesh to the interpolation points on the acoustic mesh. A common approach is to triangulate the CFD data and use a linear interpolation [124]. However, using such an approach may lead to a non-smooth representation of the mean flow-field for strongly spatially-varying flow features such as shear layers [24]. Gracia *et al.* [125] developed a global least-squares approximation procedure for mapping mean flow data to the acoustic mesh. The global procedure finds an L^2 error-minimized fit of the CFD data to the DG polynomial basis, and filters the polynomial coefficients to reduce the potential for aliasing. However, to maintain a continuous mean flow across element boundaries, which is necessary to maintain conservation in the upwind numerical flux defined in Section 2.4.1, a global least-squares problem must be solved, which may be computationally costly for large 3D problems with millions of CFD grid points.

In this work, an alternative CFD-mesh to acoustic mesh mapping procedure is investigated based on moving least-squares approximations to scattered data [126, 127, 128]. Moving least-squares computes a continuous local polynomial fit at each interpolation point using only the surrounding CFD grid points inside a support radius, potentially making it computationally less restrictive than the global least-squares procedure and trivially parallelizable. Increasing the extent of the support radius leads to increased smoothing, allowing one to effectively transition from an interpolation to an approximation of the CFD data based on the resolution requirements of the particular problem.

Mean flow data in this work are obtained from solutions to the steady Reynolds averaged Navier-Stokes (RANS) equations, where the physical length scales are typically much smaller than that of the acoustic wavelength. The mean flow data are then

mapped from the RANS mesh to the acoustic mesh. Since the acoustic mesh is generally coarser than the CFD mesh, the fine-scale flow features in the RANS solution, such as thin boundary layers, are poorly resolved. However, the acoustic wavelength will generally be larger than the finest mean flow features, so refining the mesh enough to capture the mean flow features would waste computational resources. Alternatively, the mean flow-field could be approximated, neglecting the unresolved flow features which are much smaller than the acoustic wavelength, allowing the use of a coarser acoustic mesh. For turbofan exhaust noise applications, the thin boundary layers at the walls of the engine geometry are typically severely unresolved by the acoustic mesh, leading to spurious values of the interpolated mean flow at the walls. Rarata [65] used a quadratic representation of the mean flow-field in each element and removed the boundary layers by replacing the mean flow value at the mesh nodes on the wall, with the average of the interpolated wall value and the value at a node outside of the boundary layer. For a high-order accurate flow-field approximation, a more sophisticated approach is required and is developed in this chapter.

Part one of this chapter attempts to illustrate and quantify the impact of the mean flow representation on DGM solutions to the LEE, by comparing fully-discrete LEE solutions to an analytical solution of one-dimensional (1D) wave propagation through an inhomogeneous mean sound speed. The scattering of a two-dimensional (2D) plane wave by a mean, stationary, vortex at different accuracy levels, is compared to a reference solution. Part two investigates the use of a moving least-squares procedure to map a CFD-obtained mean flow to the DG interpolation nodes on the acoustic mesh to obtain a robust, high-order approximation of the mean flow-field. Finally, the removal of thin boundary layers in the mapping process for a turbofan geometry and flow-field is studied.

5.1 Accuracy assessment of the mean state representation

This section seeks to illustrate the effect of the mean flow representation accuracy on the acoustic solution. To accomplish this, 1D wave propagation through an inhomogeneous medium is studied with varying parameters, to identify any trends present in the acoustic solution error when the medium is represented inexactly. A more complex, 2D problem of a plane wave scattered by a stationary vortex is then studied, to see if the trends seen in the 1D problem extend to more realistic applications.

5.1.1 Acoustic wave propagation through a nonuniform sound speed

An analytical solution to the linearized Euler equations for a nonuniform propagation medium is necessary to understand the relationship between the mean quantity representation accuracy and the acoustic solution accuracy. Unfortunately, a sufficiently complex analytical solution to acoustic propagation through a nonuniform medium is not available to the author's knowledge. Therefore, this section develops an analytical solution to one-dimensional acoustic propagation through a sound speed nonuniformity in an unbounded domain. While the analysis is purely one-dimensional, it should be possible to follow a similar process to develop analytical solutions for two- and three-dimensional propagation, but this problem is not considered in this work.

Consider a problem governed by the one-dimensional LEE, for the fluctuating state of density, velocity, and pressure in a quiescent medium. The 1D LEE in primitive form for a quiescent medium can be written as,

$$\frac{\partial \rho}{\partial t} + \frac{\partial \rho_\circ u}{\partial x} = 0 \tag{5.1}$$

$$\rho_\circ \frac{\partial u}{\partial t} + \frac{\partial p}{\partial x} = 0 \tag{5.2}$$

$$\frac{\partial p}{\partial t} + \gamma p_\circ \frac{\partial u}{\partial x} = 0, \tag{5.3}$$

where the fluctuating density, pressure, and velocity are ρ, p, and u, dropping the primes for clarity. The mean state of density, pressure, and sound speed is given by $\rho_\circ$, $p_\circ$, and $c_\circ$, which are allowed to vary with the spatial coordinate, x. The constant ratio of specific heats of the gas is γ. From the above LEE, the wave equations for pressure and velocity can then be obtained,

$$\frac{\partial^2 u}{\partial t^2} - c_\circ^2 \frac{\partial^2 u}{\partial x^2} = 0 \tag{5.4}$$

$$\frac{\partial^2 p}{\partial t^2} - \frac{\partial}{\partial x}\left(c_\circ^2 \frac{\partial p}{\partial x}\right) = 0. \tag{5.5}$$

Solutions for the fluctuating velocity are assumed to be in the form of,

$$u = U e^{i(\omega t - k_\infty \phi(x))}, \tag{5.6}$$

where $\phi(x)$ is a complex-valued function with units of distance, and the free-field

wavenumber is defined as $k_\infty = \omega/c_\infty$, where $c_\infty = c_\circ(x)$ when $|x| \to \infty$. Differentiating the above solution with respect to x and t results in the following identities,

$$\frac{\partial^2 u}{\partial t^2} = -\omega^2 u \tag{5.7}$$

$$\frac{\partial u}{\partial x} = -ik_\infty \phi' u \tag{5.8}$$

$$\frac{\partial^2 u}{\partial x^2} = -ik_\infty \phi'' u - k_\infty^2 \phi'^2 u. \tag{5.9}$$

For clarity, quantities with primes, $\{\cdot\}'$, $\{\cdot\}''$, or $\{\cdot\}'''$, indicate first, second, and third derivatives of the variable with respect to x. Substituting the above expressions into the wave equation for u, Equation 5.4, and then defining the complex variable, ϕ, as $\phi = a + ib$, the wave equation for u becomes,

$$k^2 - k_\infty^2 \left(a'^2 - b'^2 + 2ia'b'\right) - ik_\infty a'' + k_\infty b'' = 0. \tag{5.10}$$

Splitting the above expression into an equation for the real and imaginary parts results in,

$$k^2 - k_\infty^2 \left(a'^2 - b'^2\right) + k_\infty b'' = 0 \tag{5.11}$$

$$2k_\infty^2 a'b' + k_\infty a'' = 0, \tag{5.12}$$

for which the real part can be used to obtain an expression for the spatially-varying sound speed in terms of spatial derivatives of a and b,

$$c_\circ = \frac{c_\infty}{\sqrt{a'^2 - b'^2 - \frac{b''}{k_\infty}}}. \tag{5.13}$$

To specify a sound speed non-uniformity, $a(x)$ must first be defined, and then the expressions for $b(x)$ and $c_\circ(x)$ can found. To relate a' and b, $b'(x)$ in Equation 5.12, can be integrated to result in the relation,

$$b(x) = -\frac{1}{2k_\infty} \ln(a'). \tag{5.14}$$

Assuming that $a' = 1 + f(x)$, where $f(x)$ specifies some spatial non-uniformity, then,

$$a''(x) = f'(x) \tag{5.15}$$

$$b''(x) = \frac{f'(x)^2 - f''(x)a'(x)}{2k_\infty a'(x)^2} \tag{5.16}$$

$$b'''(x) = \frac{2f'(x)^2 \left(\frac{f''(x)}{f'(x)} - \frac{a''(x)}{a'(x)}\right) - f''(x)a''(x) \left(\frac{a'(x)f'''(x)}{a''(x)f''(x)} - 1\right)}{2k_\infty a(x)'^2}. \tag{5.17}$$

A Gaussian spatial non-uniformity is defined, *e.g.*,

$$f(x) = \alpha \exp\left[-\frac{(x-x_\circ)^2}{\sigma^2}\right], \tag{5.18}$$

where α and σ are constants, and the center of the non-uniformity is denoted by $x_\circ$. The spatial derivatives of this function are,

$$f'(x) = -\frac{2\alpha}{\sigma^2}(x-x_\circ)\exp\left[-\frac{(x-x_\circ)^2}{\sigma^2}\right] \tag{5.19}$$

$$f''(x) = \frac{2\alpha}{\sigma^2}\left[\frac{2}{\sigma^2}(x-x_\circ)^2 - 1\right]\exp\left[-\frac{(x-x_\circ)^2}{\sigma^2}\right] \tag{5.20}$$

$$f'''(x) = \frac{4\alpha}{\sigma^4}(x-x_\circ)\left[3 - \frac{2}{\sigma^2}(x-x_\circ)^2\right]\exp\left[-\frac{(x-x_\circ)^2}{\sigma^2}\right]. \tag{5.21}$$

With the above definition of $f(x)$, the real part of $\phi(x)$ becomes,

$$a(x) = 1 + \sigma\alpha\frac{\sqrt{\pi}}{2}\mathrm{erf}\left[\frac{(x-x_\circ)}{\sigma}\right], \tag{5.22}$$

where $\mathrm{erf}(\{\cdot\})$ is the error function.

With the above expressions defining $\phi(x)$ and $c_\circ(x)$, the fluctuating velocity and pressure can then be obtained through Equation 5.6, and,

$$p = \frac{\rho_\circ c_\circ^2}{c_\infty}\phi'(x)u. \tag{5.23}$$

The fluctuating density can be found from Equation 5.6 and the conservation equation, resulting in,

$$\rho = \left[\left(a'(x)^2 - b'(x)^2 - \frac{b''(x)}{k_\infty}\right)\frac{\phi'(x)}{c_\infty} - \frac{2a'(x)a''(x) - 2b'(x)b''(x) - \frac{b'''(x)}{k_\infty}}{i\omega}\right]\frac{u}{c_\infty^2}. \tag{5.24}$$

5.1.2 Convergence study

The analytical solution developed above is used to study the impact of the mean state representation accuracy, element polynomial order, and mesh size, on solution accuracy. The mean sound speed profile and computational domain are shown in Figure 5.1. A wave with angular frequency, $\omega = 100\,\mathrm{rad/s}$, enters through the left boundary, passes through the inhomogeneity, and exits through a non-reflecting boundary condition. The 1D time-domain LEE are solved by the DGM with Runge-Kutta time

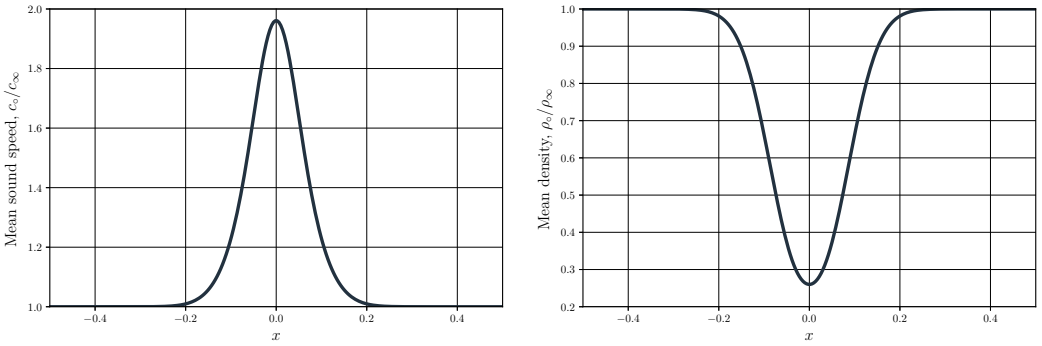

Figure 5.1: Profile of the mean sound speed and density in the computational domain.

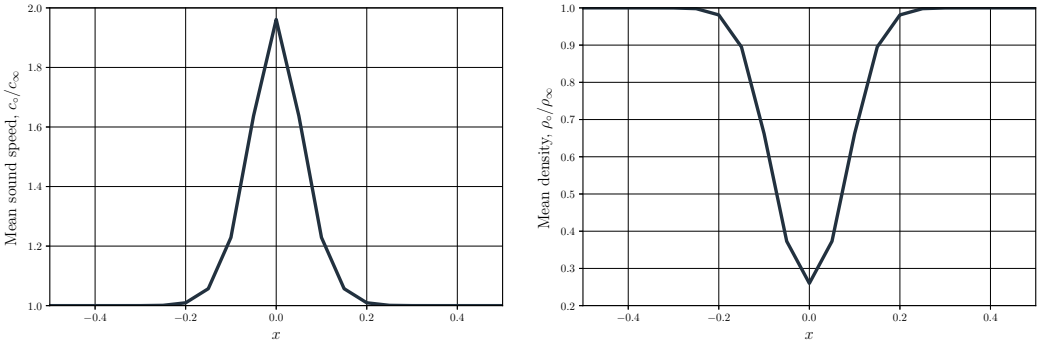

Figure 5.2: Profile of the mean sound speed and density in the computational domain for the $N_e = 20$ mesh with a linear representation.

integration and with the time-step chosen to be sufficiently small to ensure that the error is spatially dominated.

For mesh sizes with $N_e = 20$, $N_e = 40$, and $N_e = 80$ elements, a convergence study with increasing polynomial order, p, is performed for each mesh. The representation of the mean state is varied by using polynomial basis functions of orders 1–10, allowing the approximation accuracy of the solution and the mean flow to be varied independently. Figure 5.2 shows a linear representation of the mean sound speed and density profiles for the $N_e = 20$ element mesh. Relative, global integrated errors are then calculated by comparing the results with the above exact solution. Additionally, the interpolation error of the mean state is calculated.

Figures 5.3a, 5.3b, and 5.3c, show the convergence of relative solution error with increasing polynomial order, for a range of mean state representations, for mesh sizes $N_e = 20$, $N_e = 40$, and $N_e = 80$ elements, respectively. For a fixed mean state representation, *i.e.* orders 1–4, increasing the polynomial order of the solution only improves accuracy up until a certain limiting order is reached, after which the error levels stagnate. Therefore, for a mesh size of $N_e = 20$, the maximum order at which reductions

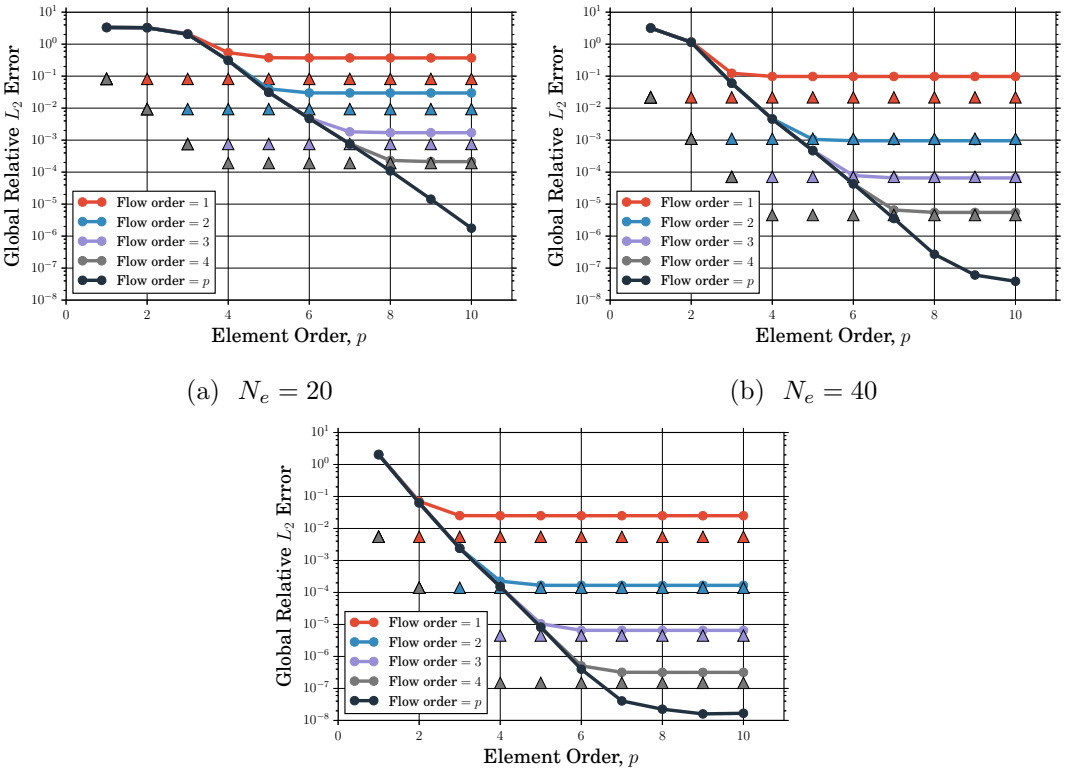

(a) $N_e = 20$ (b) $N_e = 40$

(c) $N_e = 80$

Figure 5.3: Convergence of relative solution error with polynomial order for three mesh sizes. The triangles show the relative interpolation error of the mean state variables, colored to indicate the polynomial order of representation.

in solution error are seen, is $p = c + p_F$, where p is the order of the solution basis, p_F is the order of the mean flow basis, and c is some integer related to the interpolation error of the acoustic solution. A similar behavior can be identified for the other two mesh sizes, but with a different value for c.

The mean variable interpolation errors are given by the colored triangles, showing that the global relative solution errors appear to always be higher than the mean state relative interpolation error. Comparing the convergence with a fixed mean state representation order to the convergence with the order equal to the solution order, it is clear that having a high-order representation of the mean flow is critical when high solution accuracy is required. Additionally, for computational efficiency, it is desired that high polynomial orders are used instead of refining the mesh. This suggests that a high-order accurate representation for the mean variables is desirable for both accuracy and efficiency. It is interesting to note the similarity of these results to errors in geometrical representation. Bassi and Rebay [129] found that for a high-order scheme, a high-order accurate solution is only obtained when the representation of the geometry is also of high-order.

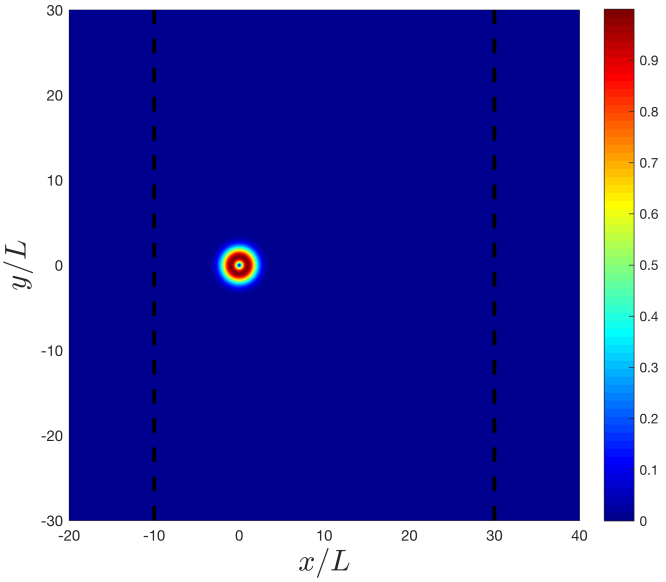

Figure 5.4: Computational domain and contours of the magnitude of mean vortex velocity, $v/v_{\max}$.

5.1.3 Scattering of a plane wave by a steady vortex

To assess the impact of mean flow representation accuracy on the acoustic solution for 2D applications, the more complex problem of plane wave scattering by a steady vortex, formulated by Colonius *et al.* [130], is solved. In this problem, a plane wave traveling in the x-direction, passes through a stationary mean flow vortex, scattering the wave, and creating a complex interference pattern. By using different representation accuracies of the vortex, the impact of mean flow accuracy on the scattered field can be shown at different radii and incident wave conditions. These results are compared to the semi-analytical frequency domain solution to the problem by Clair and Gabard [131].

The mean vortex velocity in cylindrical coordinates is defined by,

$$v_\theta(r) = v_{\max} \frac{r}{L} \exp\left[\frac{1-(r/L)^2}{2}\right] , \tag{5.25}$$

where r is the radial coordinate from the vortex center, and $v_{\max}$ is the maximum induced velocity at $r = L$. A characteristic vortex size of $L = 1$ is chosen and the mean sound speed and density are taken to be uniform throughout the domain so that $c_\circ/c_\infty = 1$ and $\rho_\circ/\rho_\infty = 1$. Contours of the mean vortex velocity magnitude are shown in Figure 5.4. To limit any spurious reflections, the plane wave is injected into the computational domain shown in Figure 5.4 through a buffer zone, and exits through a buffer zone. The solution is recorded at four radial positions, $r = 1L$, $r = 2L$, $r = 4L$, and $r = 10L$, and the simulation is stopped before the scattered field can reach the top and bottom boundaries.

To take advantage of the high spatial accuracy offered by the DGM, a coarse mesh with a characteristic length scale of approximately L, and a polynomial order of $p = 10$ is used. The vortex flow-field is interpolated onto the nodes of linear or quadratic shape functions in each element. The shape functions are used to interpolate the mean flow-field at the DGM interpolation nodes.

Results

For the incident plane wave, two wavelengths, $\lambda_\circ = 4L$ and $\lambda_\circ = 1L$, are chosen to highlight the impact of the mean flow on the scattered field complexity. For each wave, two problems are solved, propagation in a quiescent medium to get the incident field, and propagation through the mean vortex to get the total field. The scattered field is then found by taking the difference between the total field and the incident field at identical time levels.

Figures 5.5a and 5.5b show contours of the pressure field and the scattered field after the incident wave travels a distance of $30L$ for the mean flow data imposed analytically on the DGM interpolation nodes. Since the incident wave has a wavelength four times greater than the characteristic length scale of the vortex, the incident field can be seen to be only minimally scattered. Decreasing the wavelength of the incident wave to $\lambda_\circ = 1L$, Figures 5.6a and 5.6b show the total and scattered pressure fields, respectively. Since the wavelength is identical to the characteristic length scale of the vortex, substantial scattering of the incident wave occurs.

For assessing the impact of mean flow representation accuracy on the acoustic solution, two mean flow representations are used: linear and quadratic shape functions in each

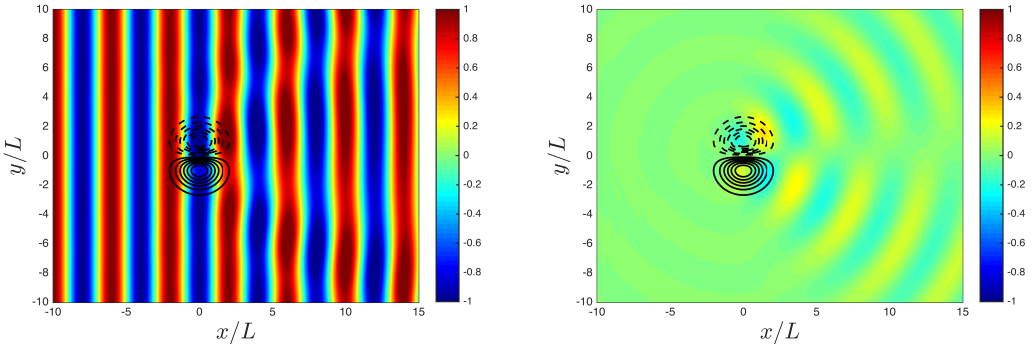

(a) Total field pressure (b) Scattered field pressure

Figure 5.5: Contours of pressure for the total field and scattered field for $\lambda_\circ = 4L$. Contours of mean axial velocity between -0.125 and 0.125 are shown in black, with dashed lines indicating negative values.

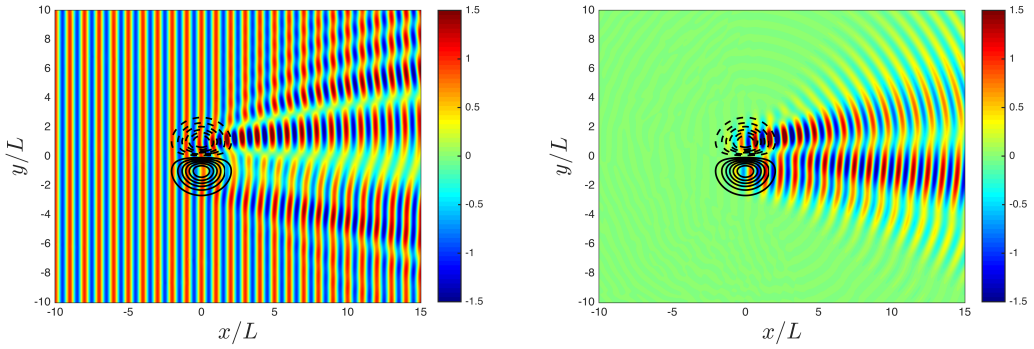

(a) Total field pressure

(b) Scattered field pressure

Figure 5.6: Contours of pressure for the total field and scattered field for $\lambda_\circ = 1L$. Contours of mean axial velocity between -0.125 and 0.125 are shown in black, with dashed lines indicating negative values.

element. The solution is recorded at four radial locations $r = 1L$, $r = 2L$, $r = 4L$, and $r = 10L$ and the RMS pressure is then compared to the semi-analytical solution. Figures 5.7a–5.7d compare the RMS pressure at each radius with that of the reference solution for an incident wavelength of $\lambda_\circ = 4L$. It is clear that even for the long incident wavelength relative to the vortex size, the mean flow representation accuracy is important. For $r = 1L$ and $r = 2L$, using a linear representation of the vortex, leads to a very poor prediction of the RMS pressure. However, increasing the mean vortex representation to quadratic, significantly improves the agreement with the reference solutions. Figures 5.8a–5.8d compare the RMS pressure at each radius with that of the reference solution for an incident wavelength of $\lambda_\circ = 1L$. Again, poor agreement can be seen near the vortex at $r = 1L$ and $r = 2L$ and farther away, a quadratic mean flow representation results in a closer agreement to the reference solution. It can be seen that the mean flow representation accuracy is significantly more important for accurate prediction of the near field region, and less important as the distance from the vortex increases. This may indicate that if only accurate far field results are desired, a coarser description of the mean flow could be sufficient for free-field propagation problems. However, for problems having wall boundaries near the flow non-uniformity, a coarse mean flow description may be inaccurate due to reflections of the waves at the walls in the near-field.

5.2 Moving least-squares local approximation

The previous sections showed the necessity for accurately representing the mean flow when the acoustic solution is discretized by high-order polynomials. It is natural to then try to achieve a better mean flow representation by interpolating the CFD data

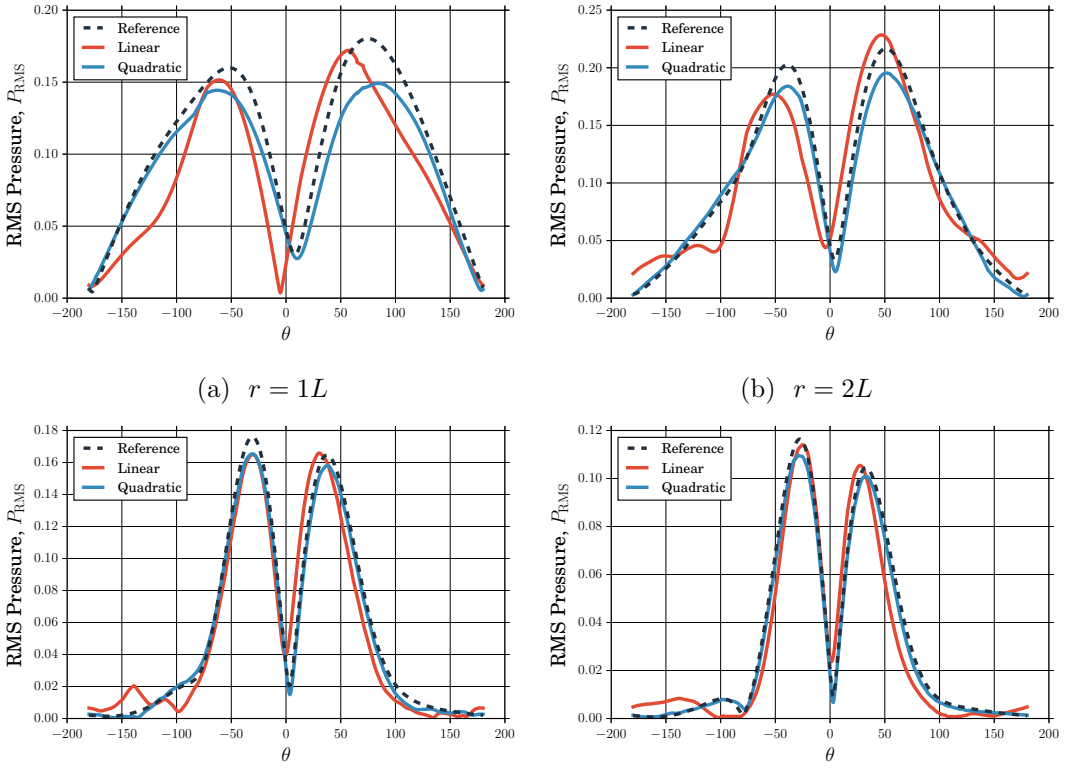

(a) $r = 1L$ (b) $r = 2L$

(c) $r = 4L$ (d) $r = 10L$

Figure 5.7: Comparison of RMS pressure for linear and quadratic mean flow representations with the reference solution at indicated radii for an incident wavelength of $\lambda = 4L$.

directly at each interpolation node on the element, to achieve a high-order representation of the mean flow-field. However, as mentioned in the introduction, the RANS flow-fields often support small scale flow features that are significantly smaller than the acoustic wavelength, such as thin boundary layers, that often cannot be resolved by the DG nodal polynomial basis on the acoustic mesh without excessive refinement of the acoustic mesh. Interpolation of these unresolved features onto the interpolation nodes can lead to spurious oscillations in the mean flow which can in turn lead to numerical errors or instabilities caused by aliasing in the fluxes [123].

An approach to find the closest fit of the nodal DGM basis to the CFD data and smooth out unresolved features was developed by Gracia *et al.* [125], using a least-squares procedure. The approach involved linearly interpolating the CFD data onto a fine "flow mesh", then finding a least-squares fit of the nodal DG basis to the data on the flow mesh. To maintain continuity of the mean flow across element boundaries, a global least-squares problem was solved over the entire computational domain, which for three-dimensional problems, may be prohibitively computationally expensive and

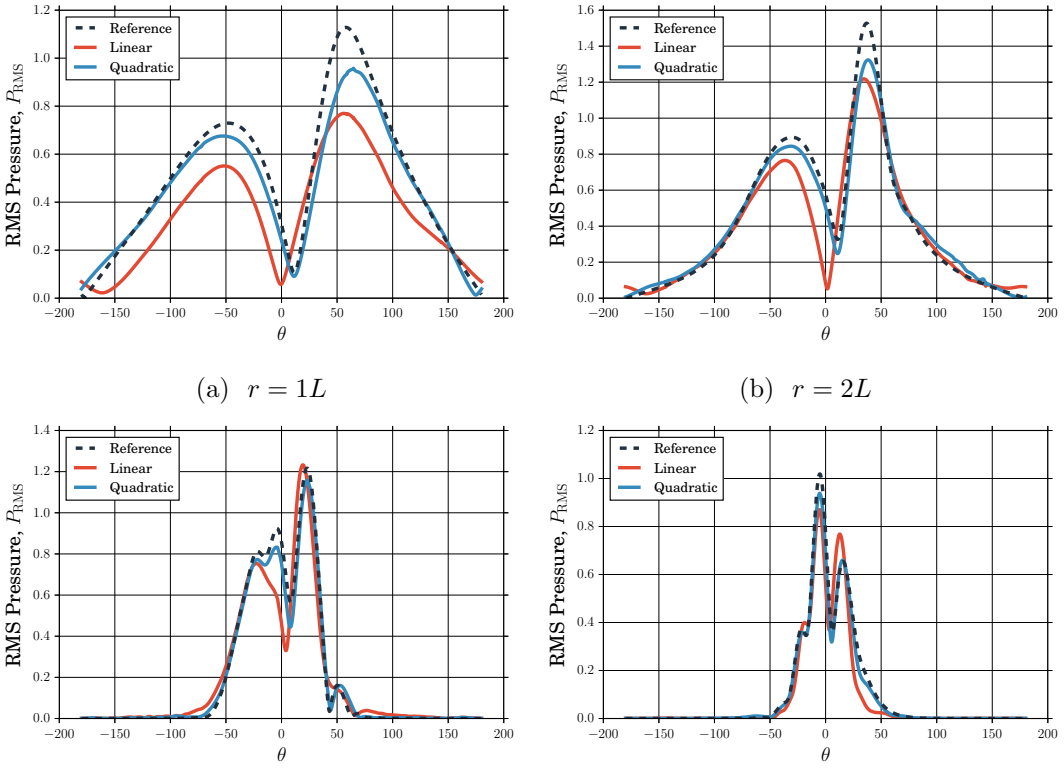

(a) $r = 1L$ (b) $r = 2L$

(c) $r = 4L$ (d) $r = 10L$

Figure 5.8: Comparison of RMS pressure for linear and quadratic mean flow representations with the reference solution at indicated radii for an incident wavelength of $\lambda = 1L$.

difficult to parallelize. The approach proposed in this work is to apply a moving least-squares approximation, centered on each DG interpolation node, to both approximate the surrounding CFD data and also to introduce smoothing of unresolved features. Since the approach is local to each interpolation node, no global problem must be solved to ensure continuity. Additionally, there is no need for a secondary flow mesh, since the approximated mean flow is computed directly from the CFD data, saving an additional step in the solution process.

Moving least-squares (MLS) approximation methods have had widespread use for computer graphics applications, such as scattered data interpolation and surface reconstruction [128], and also in mesh-free methods for solving partial differential equations [132]. MLS approaches have also been used to facilitate the transfer of solution information between computational meshes [127].

5.2.1 Formulation

The approach derived by Slattery *et al.* [127] for the transfer of solution information between computational meshes is adapted herein. Given an interpolation or target point, $\tilde{\mathbf{x}}$, where the values of the mean flow-field are desired, a set of N points, $\mathbf{x}$, defining the CFD mesh within a region around the target points, and the values of the CFD data, f_d, where $d = 1 \dots N$, a local weighted least-squares minimization problem at each interpolation node is formed,

$$\min \sum_d w(\|\tilde{\mathbf{x}} - \mathbf{x}_d\|) \|f(\tilde{\mathbf{x}}) - f_d\|^2, \tag{5.26}$$

where w is a radial weighting function, and $f(\tilde{\mathbf{x}})$ is an evaluation of the local polynomial fit to the data of the form,

$$f(\tilde{\mathbf{x}}) = \mathbf{p}(\tilde{\mathbf{x}})^\intercal \mathbf{c}, \tag{5.27}$$

where $\mathbf{p} = \begin{bmatrix} 1, & x, & y, & z, & xy, & xz, & yz, & x^2, & y^2, & z^2 \end{bmatrix}^\intercal$ is a quadratic polynomial basis and $\mathbf{c}$ is the unknown vector of its coefficients. In this work, the compactly supported weighting function of Wendland is used,

$$w(s) = \begin{cases} (1-s)^4(4s+1), & \text{if } 0 \leq s \leq 1 \\ 0, & \text{if } s > 1 \end{cases}, \tag{5.28}$$

where $s = \|\tilde{\mathbf{x}} - \mathbf{x}_d\|/R$, with R being the radius of the support. The support radius may be increased to provide more smoothing, or decreased, to be more interpolatory.

Solving the minimization problem in Equation 5.26 results in the expression for a single evaluation point,

$$f(\tilde{\mathbf{x}}) = \mathbf{p}(\tilde{\mathbf{x}})^\intercal \left[\mathbf{P}^\intercal \mathbf{W} \mathbf{P}\right]^{-1} \mathbf{P}^\intercal \mathbf{W} \mathbf{f} = \mathbf{p}(\tilde{\mathbf{x}})^\intercal \mathbf{c}, \tag{5.29}$$

where the Vandermonde matrix, $\mathbf{P}$, is defined as $\mathbf{P} = \begin{bmatrix} \mathbf{p}(\mathbf{x}_1), & \mathbf{p}(\mathbf{x}_2), & \dots, & \mathbf{p}(\mathbf{x}_N) \end{bmatrix}^\intercal$, the matrix, $\mathbf{W}$, is a diagonal weight matrix with values, $\{\mathbf{W}\}_{ii} = w(\|\tilde{\mathbf{x}} - \mathbf{x}_i\|/R)$, and $\mathbf{f}$, is the vector of mean flow-field values within the radius R on the CFD mesh. The pseudo-inverse is obtained by computing the singular value decomposition and inverting only the singular values which are greater than a small threshold. While this solution process must occur at every interpolation point, the approximation only depends on the values of the CFD data within the support radius, resulting in a small pseudo-inverse.

In contrast to the approach by Slattery *et al.*, before performing the MLS fit, the CFD data within the support radius are shifted to the local coordinate system of the target

location, $\tilde{\mathbf{x}}$, such that the matrix $\mathbf{P}$ is now evaluated at $\mathbf{x}_d - \tilde{\mathbf{x}}$ and $\mathbf{p}$ is evaluated at $\tilde{\mathbf{x}} = 0$. This is done to improve the stability of the approximation [126].

5.2.2 Regularity

The Vandermonde matrix can be ill-conditioned, making the pseudo-inverse difficult to compute accurately. Ill-conditioning generally happens when the CFD data points within the support radius, lie in a lower dimensional space than that of the polynomial basis. For example, if a quadratic polynomial fit to the CFD data is desired in three dimensions, and the CFD data within the support all lie on the same line, or plane, then the Vandermonde matrix may not be of full rank, and the MLS system may be ill-conditioned [127]. Slattery *et al.* [127], solve this problem by adding each column, *i.e.* each term of the polynomial basis, sequentially, and computing the vector of singular values, $\boldsymbol{\sigma}$. If any of the singular values violate the constraint,

$$\{\boldsymbol{\sigma}\}_i < \epsilon \max(\boldsymbol{\sigma}), \tag{5.30}$$

where ϵ is the machine precision, the column is rejected, and the process is repeated for the next column until the matrix is built. This process helps to ensure that the Vandermonde matrix is of full rank. Typically, this process is only required when the CFD mesh is highly nonuniform.

5.2.3 Finding data within the support radius

An efficient implementation of the proposed mapping procedure depends both on how efficiently the MLS system is solved and how efficiently the CFD data within the support radii are found. A typical RANS CFD mesh in three dimensions can contain millions of points, forcing the use of efficient radius neighbor searching algorithms. In this work, the CFD data are spatially partitioned using a quadtree data structure, for 2D problems, or an octree data structure, for 3D problems, making the search for radius neighbors highly efficient. The approach from Behley *et al.* [133] is used in this work. Because the MLS approximation at an interpolation point is computed independently of all other points, the mean flow approximation problem naturally fits within the framework of a parallel DG scheme; each partition reads only the CFD data required locally, and builds its own tree based on that data. This results in a continuous approximation of the mean flow-field without requiring any communication between processors.

5.2.4 Verification of MLS applied to scattering by a steady vortex

The moving least-squares procedure outlined above is now applied to the solution of the problem from Section 5.1.3, involving scattering of a plane wave by a mean vortex. The vortex mean flow is evaluated at a set of scattered points in the domain to represent CFD data. Moving least-squares is then used to find an approximation to the model CFD data at each interpolation point on the elements. For comparison, the results for a quadratic representation of the mean flow are repeated here. The MLS support radius is selected based on the characteristic size of the mean flow vortex. Choosing a large radius, relative to the vortex size, could result in excess smoothing, poorly approximating the vortex. Choosing a radius much smaller than the vortex size, essentially results in a nearest-neighbor interpolation of the mean flow data. Since the vortex is smooth, and there is sufficient mesh resolution to resolve it, the support radius is chosen to be on the order of the mean interpolation point spacing on the elements, *e.g.* $\frac{D}{p}$, where D is a measure of the element size, and p is the polynomial order. Figures 5.9a–5.9d show the comparison between quadratic, MLS, and the reference solutions at each radial location. The moving least-squares approximation is able to accurately represent the mean flow in each element, leading to a close agreement to the reference acoustic solution.

5.2.5 Impact of the support radius on the mapping accuracy

In the previous section, the support radius and the density of the model CFD data were fixed. In this section, the support radius and density are varied to better understand their impact on the accuracy of the approximation. The model CFD data are sampled from the Gaussian function,

$$g(\mathbf{x}) = \exp(-\|\mathbf{x} - \mathbf{x}_c\|^2/w^2), \tag{5.31}$$

where $\mathbf{x}_c$ is the center of the Gaussian and w controls the width, at an unorganized set of model grid points with characteristic spacing, h. The model CFD data are then given as an input to the MLS algorithm and an approximation of the CFD data is found at a regular 100×100 grid of interpolation points.

For a non-dimensional range of CFD point densities from $h/w = 0.07$ to $h/w = 0.47$, the non-dimensional inverse support radius is varied from $w/R = 0.1$ to $w/R = 3.0$. For each pair of h/w and w/R, the MLS problem is solved at each interpolation point

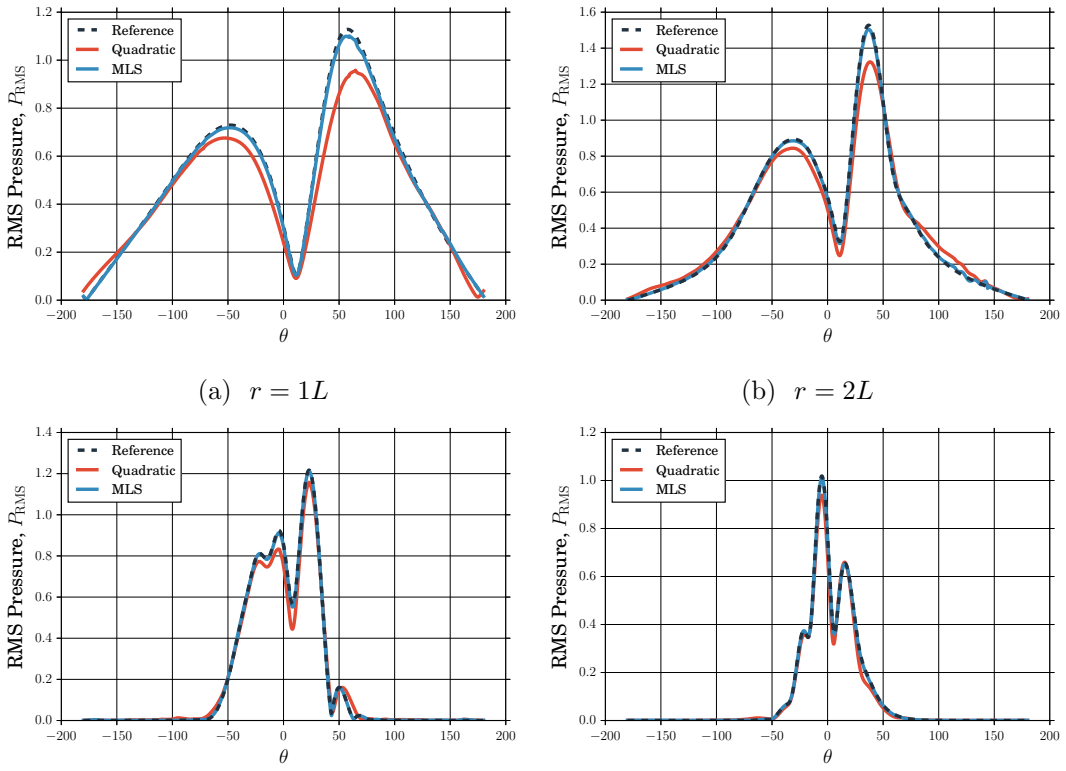

(a) $r = 1L$ (b) $r = 2L$

(c) $r = 4L$ (d) $r = 10L$

Figure 5.9: Comparison of RMS pressure for quadratic and moving least squares mean flow representations with the reference solution at indicated radii for an incident wavelength of $\lambda = 1L$.

and the total relative l_2-error is computed, defined as,

$$E_{l_2} = \frac{\sqrt{\sum_i \left(f(\tilde{\mathbf{x}}_i) - g(\tilde{\mathbf{x}}_i)\right)^2}}{\sqrt{\sum_i g(\tilde{\mathbf{x}}_i)^2}}, \tag{5.32}$$

where $f(\tilde{\mathbf{x}}_i)$ is the approximated value of $g(\tilde{\mathbf{x}}_i)$, at the interpolation point, $\tilde{\mathbf{x}}_i$. Figure 5.10a shows the contours of the exact solution, Equation 5.31, and Figure 5.10b shows the convergence of the relative l_2 error. For small w/R, *e.g.* large support radii, the convergence behavior of the error is nearly identical for each CFD point density considered. However, as w/R increases, a clear deviation in the convergence trend can be seen. For a high CFD point density of $h/w = 0.07$, the slope of the error convergence with increasing w/R remains nearly constant. For all other densities, as w/R increases, the error reverses its downward trend and begins increasing, with the worst case seen for a density of $h/w = 0.47$. This behavior can be attributed to having too few points within the support radius to achieve an accurate fit. As the support

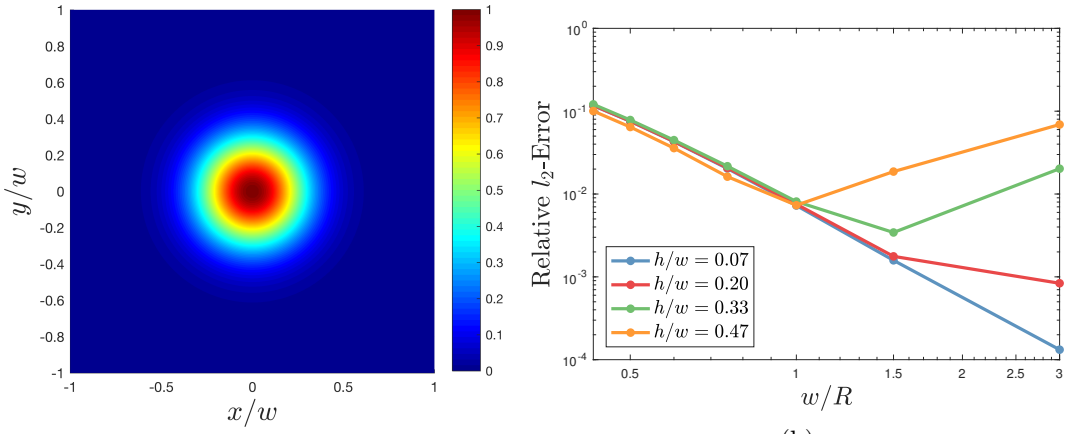

(a) (b)

Figure 5.10: (a) Contours of the function that is approximated by moving-least-squares. (b) Convergence of the relative l_2 error with changing CFD point density and support radius.

radius decreases, the error initially drops since MLS acts more like an interpolation, rather than an approximation to the CFD data. However, the number of points within the support decrease until there are too few to achieve an accurate polynomial fit. Therefore, it is important that the support radius is chosen based on both the desired amount of smoothing and the density of the input CFD data.

5.2.6 Boundary layer truncation

As alluded to in the introduction of this chapter, the thin boundary layers at the walls of the turbofan engine geometry present a challenge when mapping the mean flow-field from the CFD mesh to the acoustic mesh. If ignored, these small flow features may be unresolved by the acoustic mesh, leading to spurious oscillations in the mean flow nodal basis functions, causing increased aliasing error when computing the fluxes. A truncation of the thin boundary layers is proposed, where the near-wall region of the flow-field is neglected from the MLS approximation. To decide which CFD points to keep and which to disregard, a measure of the normal distance to the wall, robust enough for complex geometries, is required. Additionally, after removal of the near-wall CFD points, a change to the MLS approximation is required near the wall, to ensure that the fit is robust when there may be a low density of CFD points. Both of these considerations are discussed in the following sections.

5.2.7 Computation of a normal wall distance

A way to compute the normal distance to the walls is required that is computationally inexpensive and yet robust enough to handle complex geometries. In the turbulence modeling community, wall distance measures are a critical input for models that describe the near-wall region of the boundary layer. Simplistic approaches, such as computing the normal distance to the nearest wall element, break down when the geometry contains complicated internal and external surfaces and curved wall elements. While there exist many approaches to computing an exact or approximate wall distance field, the approach derived by Tucker [134] is used in this work, since it requires only the solution of a Poisson equation in the domain and is simple to implement. In the fluid volume, the Poisson equation,

$$\vec{\nabla}^2\phi = -1, \tag{5.33}$$

is solved for ϕ, with boundary conditions, $\phi = 0$ on the walls and $\frac{\partial\phi}{\partial n} = 0$, where n is the normal direction, on all other boundaries. Once ϕ and $\vec{\nabla}\phi$ are found, the normal distance to the wall can be estimated by the expression,

$$d_{\mathrm{n}} = \sqrt{\left(\frac{\partial\phi}{\partial x_i}\right)^2 + 2\phi} - \sqrt{\left(\frac{\partial\phi}{\partial x_i}\right)^2}, \tag{5.34}$$

where x_i indicates a sum over all spatial directions. Additionally, a local estimate of the wall normal direction can be obtained through,

$$\hat{n} = \frac{\vec{\nabla}\phi}{\|\vec{\nabla}\phi\|}. \tag{5.35}$$

In the present implementation, Equation 5.33 is solved on the acoustic mesh using a DG discretization for the Poisson equation as described by Hesthaven and Warburton [55], and solved using the conjugate-gradient method. Since only an estimate of the normal distance is desired, the Poisson solution is obtained using lower-order basis functions than that of the aeroacoustic solver to improve the solution time.

5.2.8 MLS approximation at the wall

Using the normal distance to the wall, CFD points within a user-defined distance from the wall, d, are rejected in the MLS process. Figure 5.11 shows an example of approximating a function defined by several points near a wall. The points which are rejected in the fitting process are colored in red. When the location where an approximation is desired falls within the truncated boundary-layer region, it is extrapolated from the CFD data outside of the boundary-layer region. To reduce the amount of

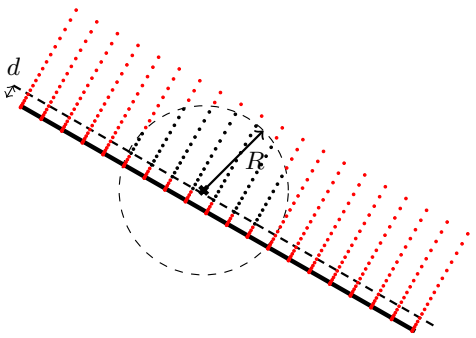

Figure 5.11: Truncation of the near-wall region CFD data. Points included in the MLS fit are shown as black dots and rejected points are shown as red dots.

extrapolation, a regularization of the fit is performed. Joldes *et al.* [135] developed a regularization process allowing the regularization of individual polynomial terms. In this work, a regularization is applied to the quadratic terms when the approximation location is in the boundary-layer region, adding a small diagonal term to Equation 5.29,

$$f(\tilde{\mathbf{x}}) = \mathbf{p}(\tilde{\mathbf{x}})^\intercal \left[\mathbf{P}^\intercal \mathbf{W}\, \mathbf{P} + \lambda \mathbf{H}\right]^{-1} \mathbf{P}^\intercal \mathbf{W}\, \mathbf{f}, \tag{5.36}$$

where $\mathbf{H}$ is diagonal matrix with non-zero terms on the diagonal in the location of the quadratic terms. For example, for the quadratic polynomial basis functions used in this work, the regularization matrix is, $\mathbf{H} = \text{diag}\left(\left[0,\ 0,\ 0,\ 0,\ 0,\ 0,\ 0,\ 1,\ 1,\ 1\right]^\intercal\right)$. The parameter, λ, is a small constant used to define the amount of regularization. The value $\lambda = 0.001$ is chosen in this work, however the exact choice of this parameter is not critical.

5.2.9 Application to a turbofan exhaust

The MLS algorithm is applied to the problem of a turbofan exhaust with a realistic mean flow-field. The axisymmetric geometry and RANS flow-field are obtained from the TURNEX project [136]. The flow-field is computed at the static approach experimental condition.

To compute the normal distance to the wall, required for the boundary-layer truncation, the method developed in Section 5.2.7 is used. Figure 5.12 shows contours of the wall-normal distance, d_n, for one-half of the turbofan geometry from $d_\text{n}/R_\text{e} = 0$ to $d_\text{n}/R_\text{e} = 0.1$, where R_e is the radius of the bypass duct at the exit plane of the engine. Even though the geometry is curved, the wall normal distance remains smooth throughout the domain.

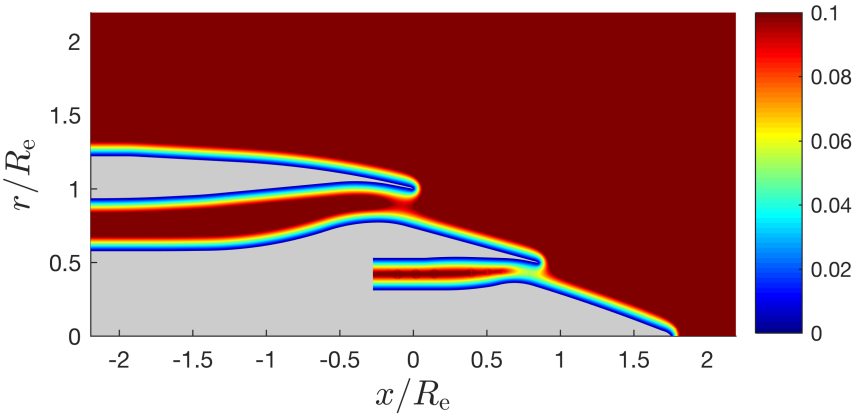

Figure 5.12: Contours of the normal distance to the wall from 0 to $d_n/R_e = 0.1$.

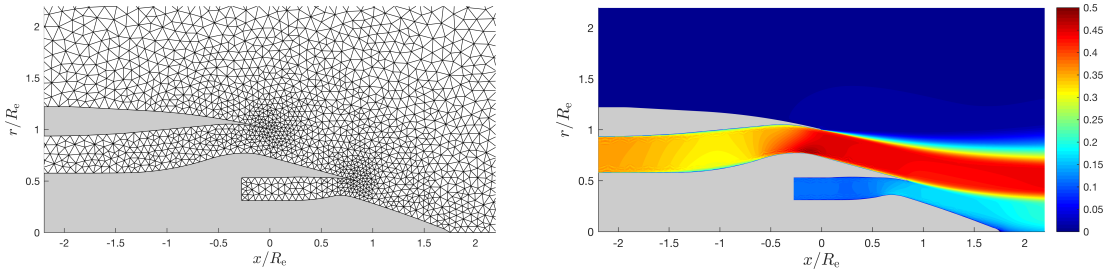

(a) Acoustic mesh for the TURNEX geometry.

(b) Linear interpolation of the CFD data.

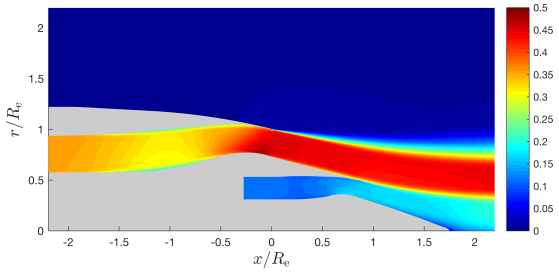

(c) MLS approximation of the CFD data with boundary-layer truncation.

Figure 5.13: Comparison between linear interpolation and MLS for the TURNEX geometry at the static approach experimental conditions.

For the acoustic domain, the unstructured mesh shown in Figure 5.13a is used with polynomial order $p = 6$ elements throughout the mesh. A linear interpolation directly from the CFD data to the DG interpolation points is performed and compared to the MLS fit with boundary-layer truncation. Figure 5.13b shows the contours of mean flow Mach number interpolated directly from the CFD mesh to the DG nodal basis functions and Figure 5.13c shows the MLS fit. Both methods qualitatively perform similarly in the smooth flow regions. However, by looking at the near-wall regions, shown in Figures 5.14a and 5.14b for MLS and linear interpolation, respectively, there

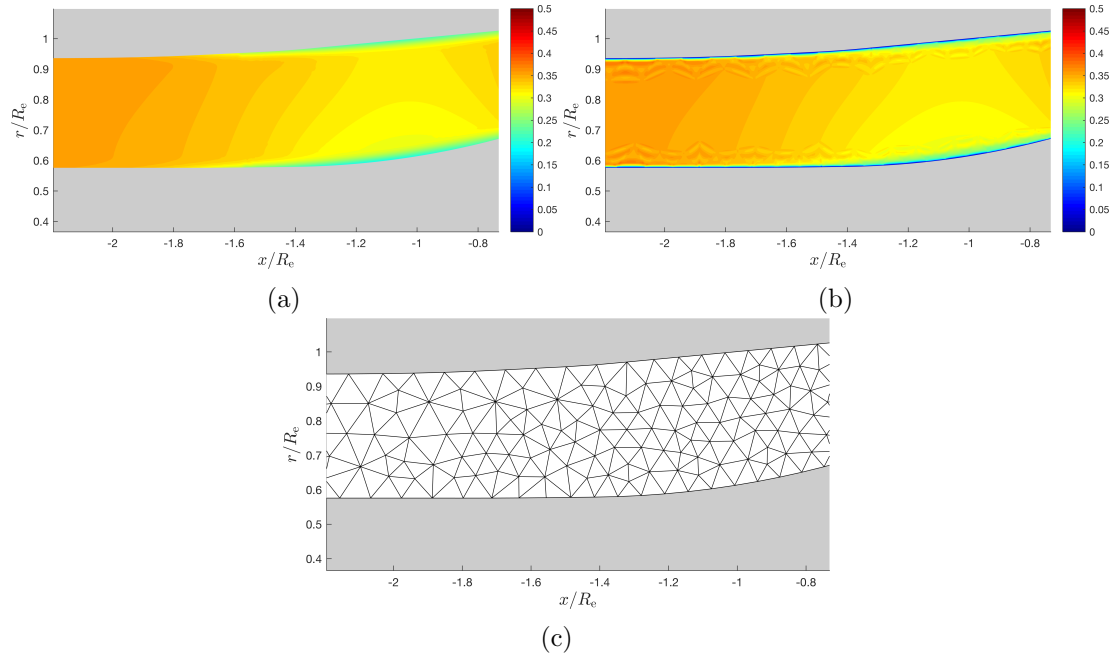

Figure 5.14: Near-wall region of the approximated flow-field using MLS with boundary-layer truncation (a), and using linear interpolation (b). The outlines of the elements are shown in figure (c).

are spurious oscillations of the mean flow Mach number when using linear interpolation near the wall. These oscillations of the mean flow-field could potentially pollute the solution and lead to additional aliasing error.

5.3 Conclusions

This chapter explored the representation of the mean state variables in the numerical model, from the impact of the flow-field representation on the solution error, to the practical implementation of a CFD mesh to acoustic mesh mapping procedure. First, an analytical solution to one-dimensional acoustic wave propagation through a sound-speed non-uniformity was compared to numerical solutions at different mean variable polynomial orders. When the mean variable order is less than the solution order, there exists a minimum solution error level that cannot be improved upon by increasing the order of the solution. The impact of the representation error in two-dimensional problems was shown qualitatively through solutions of acoustic wave-propagation through a steady mean-flow vortex. A procedure based on moving-least-squares approximations was outlined to map mean variable data from the CFD mesh to the interpolation points on the DG mesh. To treat thin boundary layers that are unresolved by the DG discretization, a boundary layer truncation process was developed that works effectively for complex geometries.

Chapter 6

Specification of source terms in the numerical model

6.1 Introduction

Source terms for the linearized Euler equations can describe injections of mass, application of external forces, or heat addition, causing fluctuations of density, momentum, or pressure in the fluid. Such source terms can generate acoustic fluctuations, such as modes in a duct, velocity fluctuations associated with turbulent eddies, or temperature perturbations, advecting downstream of a combustion process. This chapter discusses efficient ways to implement these sources in the numerical model.

Source terms can be imposed by adding to the right hand side of Equation 2.29 in the fluid volume, or through the boundary conditions at the extents of the computational domain. Canonical solutions to the LEE, such as duct modes or synthetic turbulent fields [137], can be used to model effects such as fan tonal noise or turbulent inflow fluctuations with specific statistics. A difficulty in implementing these sources is that the source region needs to match closely to the analytical problem, *i.e.* a uniform mean flow field, or an axially-infinite duct geometry. A source region is often defined by applying a spatial windowing function [137, 85]. The windowing function must be chosen to be large enough such that the source can be sufficiently resolved on the computational mesh, and yet compact enough compared to the constraints of the problem geometry and the non-uniformity of the mean flow field. Ensuring that the source remains acoustically compact, requires that the windowing is adjusted based on the problem being solved. Duct-mode source terms can be injected into the domain through a buffer region [37], which forces a duct-mode in the desired direction, while absorbing any disturbances traveling in the opposite direction. However, this requires

that the buffer zone is effective at both transmitting and absorbing waves. Source terms involving the generation of advecting vortices and/or entropy disturbances must also be treated carefully. Any distortion of these hydrodynamic or entropy waves may create spurious acoustic waves. A solution to these problems, proposed in this chapter, is to replace the source terms defined in the fluid volume, with equivalent sources defined as fluxes through a fictitious plane in the computational domain. By using the DG numerical flux on the element boundaries to impose the sources, source terms are defined only on a plane, so no spatial windowing functions are required.

Solving the LEE in the time-domain can be advantageous over a frequency domain approach. With a frequency domain approach, one must solve separately for the response of the system to each frequency of interest. For problems where the fundamental frequencies are not known in advance, this can require a large number of frequency domain solutions. For broad-band or stochastic sound sources, a time-domain approach is natural. When modeling sound sources in ducts, it is convenient to express the solution in terms of time-harmonic modes and to solve the problem for a range of modes and frequencies. For frequency domain solutions, different modes can be calculated efficiently by considering different right hand sides of the same discrete system of equations at fixed frequency. But for a time-domain approach, the LEE must be solved until a time-harmonic solution is found, and this process must be repeated for each mode and frequency. Such an approach can be computationally costly if there are a large number of cut-on modes in the problem. Furthermore, a single-frequency duct-mode source is not fully realized in the time-domain, due to temporal windowing or discretization error, creating transients in the solution, necessitating a longer integration time. Additionally, time-domain solutions in the presence of a sheared mean velocity profile can be unstable for some frequencies, growing in time and quickly polluting the acoustic solution before a time-harmonic state can be reached [115, 85].

An alternative approach is to take advantage of the time domain representation, and for each mode, build a source term containing all frequencies of interest and solve a single problem. Hu *et al.* [85], proposed the time domain wave-packet (TDWP) method, using a wave-packet to force the mode shape function for pressure at a continuous range of frequencies. The time-domain solution is then post-processed with the fast Fourier transform (FFT) to obtain the solution at any source frequency. Since the source term is compact in time, there is no need to integrate the equations until a time-harmonic solution is reached. However, in sheared mean flows, unstable solutions can still develop. Hu *et al.* used the fact that the wave-packet is compact in time, to filter unstable modes in the shear layer after the wave-packet passed through it, avoiding instability. They applied the TDWP method to the radiation of fan tones from the bypass duct of an axisymmetric turbofan geometry in cylindrical coordinates.

Arina [138] applied the TDWP method to discontinuous Galerkin solutions of the linearized Navier-Stokes equations (LNSE) in cylindrical coordinates.

A disadvantage of Hu *et al.*'s wave-packet source term is that all frequencies up to a user-defined frequency, $\omega_{\max}$, have a similar amplitude, including cut-off modes in the solution, which take an infinitely long time to exit the duct. Additionally, shear layer instabilities are known to be sensitive to low frequencies [118], making the TDWP solutions susceptible to these instabilities. In this work, a band-limited wave-packet source term is proposed, which allows one to specify a frequency range of the source and is derived for fully three-dimensional problems. A full discussion of the post-processing of these band-limited wave packet solutions is also presented. The wave-packet source term is also implemented as an interface source, making it compact in both space and time.

In the first part of this chapter, the interface source terms are derived for the time-domain nodal DGM and applied to problems involving free-field propagation of hydrodynamic and entropy disturbances, as well as acoustic mode radiation from a three-dimensional duct. The following sections derive the band-limited wave-packet source term as well as its implementation as an interface duct-mode source and then describe the post-processing procedure.

6.2 Interface Source Terms

A proposed solution to the difficulties of introducing volume source terms as outlined above, is to replace the volume source terms with an equivalent source defined as a flux through a plane in the computational domain. An example of a source plane in a duct is shown in Figure 6.3, although it need not be restricted to duct domains. The nodal DGM couples the solution in an element with its face neighbors using a numerical flux. This flux on the element boundaries can be modified to introduce source terms. Implementing the source term requires adding a source vector, $\mathbf{s}$, to the boundary flux integral defined in Section 2.4,

$$\int_{\Gamma_\mathrm{i}} \mathbf{\Phi}_e^\intercal \left[\tilde{\mathbf{f}} + \mathbf{s}\right] \mathrm{d}\Gamma_\mathrm{i}, \tag{6.1}$$

where Γ_i is the interface between elements on the source plane. With no source term, the standard DG numerical flux is recovered, making the interface transparent to any disturbances in the domain. The following sections describe the process of deriving interface source terms in the DGM and give examples for hydrodynamic and acoustic sources. Before deriving the interface source terms, the eigen-modes of the LEE, first introduced in Section 2.3.1, are repeated here.

6.2.1 Eigen-modes of the LEE

Solutions of the LEE can be described in terms of eigen-modes of the flux matrices, Equation 2.3. With a uniform mean flow, these eigen-modes correspond to entropy fluctuations (fluctuations of density only), vorticity fluctuations (fluctuations of velocity only), and acoustic fluctuations (fluctuations of all variables). Solution modes of the LEE are most easily described by projecting the flux vector onto an arbitrary direction in space, $\hat{n}$, and then diagonalizing this normal flux matrix,

$$\mathbf{F}_{\circ,n} = n_x \mathbf{F}_\circ + n_y \mathbf{G}_\circ + n_z \mathbf{H}_\circ, \tag{6.2}$$

where $\mathbf{F}_\circ$, $\mathbf{G}_\circ$, and $\mathbf{H}_\circ$ are the x, y, and z flux matrices, and $\hat{n} = n_x\hat{\imath} + n_y\hat{\jmath} + n_z\hat{k}$ is the arbitrary normal direction. Diagonalizing the normal flux matrix gives,

$$\mathbf{F}_{\circ,n} = \mathbf{W}\mathbf{\Lambda}\mathbf{W}^{-1}, \tag{6.3}$$

where the matrices, $\mathbf{\Lambda}$ and $\mathbf{W}$,

$$\mathbf{\Lambda} = \begin{bmatrix} v_{\circ,n} & 0 & 0 & 0 & 0 \\ 0 & v_{\circ,n} & 0 & 0 & 0 \\ 0 & 0 & v_{\circ,n} & 0 & 0 \\ 0 & 0 & 0 & v_{\circ,n} - c_\circ & 0 \\ 0 & 0 & 0 & 0 & v_{\circ,n} + c_\circ \end{bmatrix}, \tag{6.4}$$

$$\mathbf{W} = \begin{bmatrix} 1 & 0 & 0 & 1 & 1 \\ n_x v_{\circ,n} & 0 & -n_z & u_\circ - n_x c_\circ & u_\circ + n_x c_\circ \\ n_y v_{\circ,n} & -n_z & 0 & v_\circ - n_y c_\circ & v_\circ + n_y c_\circ \\ n_z v_{\circ,n} & n_y & n_x & w_\circ - n_z c_\circ & w_\circ + n_z c_\circ \\ 0 & 0 & 0 & \pi_\circ/\rho_\circ & \pi_\circ/\rho_\circ \end{bmatrix}, \tag{6.5}$$

are the wave speeds and solution modes of the LEE, and $v_{\circ,n} = u_\circ n_x + v_\circ n_y + w_\circ n_z$ is the normal mean flow velocity. The first column of $\mathbf{W}$ is the entropy mode with a wave speed of $v_{\circ,n}$; the second and third columns corresponding to the twice-repeated eigenvalue, $v_{\circ,n}$, are associated with the vorticity mode; and the fourth and fifth columns are the acoustic modes propagating with wave speeds, $v_{\circ,n} - c_\circ$ and $v_{\circ,n} + c_\circ$, against and with the mean flow, respectively.

6.2.2 Specifying the interface source vector

Taking the definition of the normal directions shown in Figure 6.3 as the direction to project the flux matrix onto, the interface source vector can be written as some

solution vector, $\mathbf{q}_s$, at the interface between Ω_{L} and Ω_{R}, multiplied by the normal flux matrix,

$$\mathbf{s} = \mathbf{F}_{\circ,n}\mathbf{q}_s. \tag{6.6}$$

To write this in a more useful form that is analogous to upwind flux functions, the flux matrix can be diagonalized and split based on the signs of the wave speeds,

$$\mathbf{s} = \mathbf{F}^{+}_{\circ,n}\mathbf{q}^{+}_s + \mathbf{F}^{-}_{\circ,n}\mathbf{q}^{-}_s, \tag{6.7}$$

where $\mathbf{F}^{+}_{\circ,n}$ is constructed by setting all wave speeds in $\mathbf{\Lambda}$ having a negative sign, *i.e.*, waves traveling in the opposite direction to the normal, to zero. Similarly, $\mathbf{F}^{-}_{\circ,n}$ is constructed by setting the wave speeds having a positive sign to zero. The vectors, $\mathbf{q}^{+}_s$ and $\mathbf{q}^{-}_s$ specify the source, with $\mathbf{q}^{+}_s$ specifying the waves traveling in the normal direction and $\mathbf{q}^{-}_s$ specifying the waves traveling in the opposite direction. The following sections give the explicit form of $\mathbf{q}^{+}_s$ and $\mathbf{q}^{-}_s$ for a localized entropy spot, a vortex and an acoustic source in a duct.

6.2.3 Advected entropy spot

A locally non-uniform temperature spot in terms of conserved variables is given by,

$$\mathbf{q}(\vec{x}, t_0) = \begin{Bmatrix} 1 \\ u_\circ \\ v_\circ \\ w_\circ \\ 0 \end{Bmatrix} A(\vec{x} - \vec{x}_0), \tag{6.8}$$

where $A(\vec{x} - \vec{x}_0)$ is the amplitude shape function, and $\vec{x}_0$ is the initial position at time, t_0. The entropy spot advects with the mean flow velocity, retaining its initial amplitude and shape as it propagates downstream,

$$\mathbf{q}(\vec{x}, t) = \begin{Bmatrix} 1 \\ u_\circ \\ v_\circ \\ w_\circ \\ 0 \end{Bmatrix} A(\vec{x} - \vec{x}_0 - \vec{v}_\circ t), \tag{6.9}$$

at time t. Since the entropy spot propagates in the direction of the mean flow, only one of $\mathbf{q}^{+}_s$ and $\mathbf{q}^{-}_s$ on the interface is retained. For an element with an edge on the interface having $v_{\circ,n} > 0$, the interface source is,

$$\mathbf{s} = \mathbf{F}^{+}_{\circ,n}\mathbf{q}(\vec{x}_{\mathrm{i}}, t), \tag{6.10}$$

where $\vec{x}_\mathrm{i}$ is the interface plane. Similarly, an element on the interface having $v_{\circ,n} < 0$, the interface source is,

$$\mathbf{s} = \mathbf{F}^{-}_{\circ,n}\mathbf{q}(\vec{x}_\mathrm{i}, t). \tag{6.11}$$

Advection of a hot spot in a Mach 0.3 flow

To verify the source term, consider a locally nonuniform, three-dimensional, density perturbation of the form,

$$A\left(\vec{x} - \vec{x}_0 - \vec{v}_\circ t\right) = \begin{cases} \frac{1}{2}\left(1 - \cos\left[\left(\pi \frac{\|\vec{x} - \vec{x}_0 - \vec{v}_\circ t\|}{w} + 1\right)\right]\right), & \text{if } \|\vec{x} - \vec{x}_0 - \vec{v}_\circ t\| \leq w \\ 0, & \text{otherwise} \end{cases}, \tag{6.12}$$

where $w = 1$ is the width, $\vec{x}_0 = -6w\hat{\imath}$ is the position at $t = 0$, and $\vec{v}_\circ = 0.3c_\circ\hat{\imath}$ is the mean flow velocity. At $t > 0$, the entropy spot advects through a channel centered at $x = 0$, with a square cross-section of $4w \times 4w$, at the mean flow velocity, $\vec{v}_\circ$. The domain is truncated with buffer zones added at opposite ends of the channel and the interface source plane is located at $x = -5w$. The boundary conditions in the transverse directions are non-reflecting.

The initial entropy spot is allowed to advect until it reaches the center of the domain, $x = 0$, and then is compared to the analytical solution, Equation 6.9. Figure 6.1 shows the comparison of the numerical solution contours with the exact solution at an x–y slice of the domain after propagating a distance of $7w$. Along the line $y = 0$, the numerical and analytical densities are compared in Figure 6.1c, showing close agreement. Integrating the error between the exact and numerical solutions over the domain, gives a relative L^2 error of $1.2e^{-3}$.

6.2.4 Advected vortex

A vortex tube varying only in the x–y plane can be described by the solution vector,

$$\mathbf{q}(\vec{x}, t_0) = \begin{Bmatrix} 0 \\ (y_\circ - y)\,\rho_\circ \\ (x - x_\circ)\,\rho_\circ \\ 0 \\ 0 \end{Bmatrix} A\left(\vec{x} - \vec{x}_0\right),$$

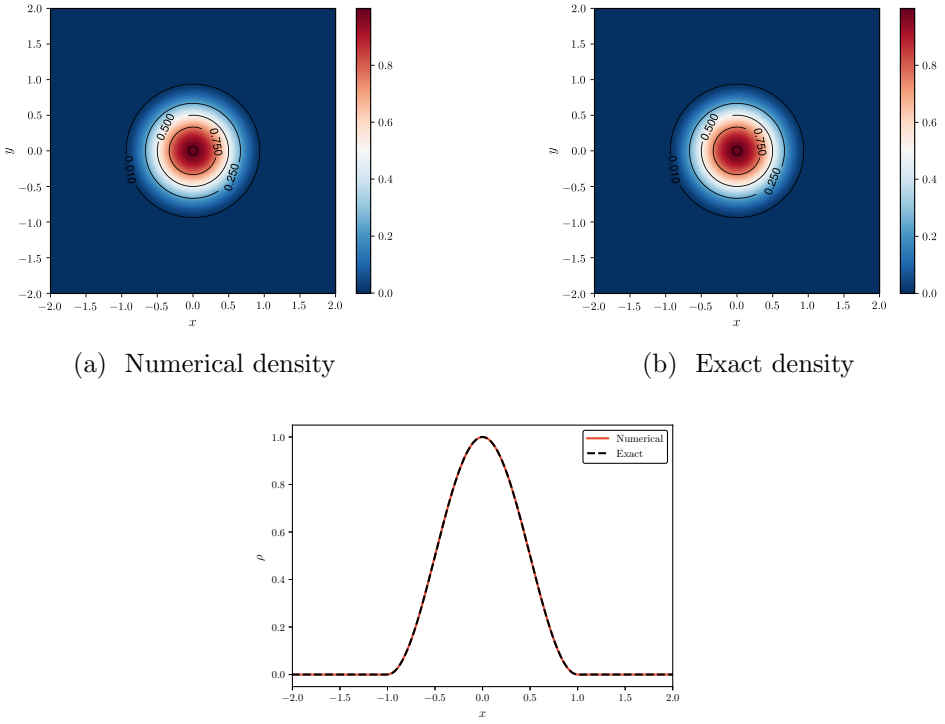

(a) Numerical density

(b) Exact density

(c) Centerline density, $y = 0$

Figure 6.1: Comparison between the numerical and the exact solutions for an advected entropy spot.

where the amplitude, $A\left(\vec{x} - \vec{x}_0\right)$ is defined by the expression,

$$A\left(\vec{x} - \vec{x}_0\right) = \exp\left(\frac{-\|\vec{x} - \vec{x}_0\|^2}{\sigma^2}\right), \tag{6.13}$$

where σ is a constant. The position of the vortex at time $t = 0$ is defined as $\vec{x}_0$. From $t = 0$, the vortex advects in the direction of the mean flow at the mean flow velocity. At any time, t, the vortex shape and position can be described by,

$$\mathbf{q}(\vec{x}, t) = \left\{ \begin{array}{c} 0 \\ \left(y_\circ - y + v_\circ t\right) \rho_\circ \\ \left(x - x_\circ - u_\circ t\right) \rho_\circ \\ 0 \\ 0 \end{array} \right\} A\left(\vec{x} - \vec{x}_0 - \vec{v}_\circ t\right),$$

where $\vec{v}_\circ = u_\circ\, \hat{\imath} + v_\circ\, \hat{\jmath} + w_\circ\, \hat{k}$ is the uniform mean flow velocity.

Analogous to the interface source term for the entropy spot defined in Section 6.2.3, the initial vortex propagates in the direction of the mean flow velocity. For an element

with an edge on the interface having $v_{\circ,n} > 0$, the interface source is,

$$\mathbf{s} = \mathbf{F}^{+}_{\circ,n}\mathbf{q}(\vec{x}_\mathrm{i}, t). \tag{6.14}$$

Similarly, an element on the interface having $v_{\circ,n} < 0$, the interface source is,

$$\mathbf{s} = \mathbf{F}^{-}_{\circ,n}\mathbf{q}(\vec{x}_\mathrm{i}, t). \tag{6.15}$$

Advected vortex in a $M = 0.3$ mean flow

Using the same three-dimensional computational domain as for the verification of the advected entropy spot, the ability of the interface source term to accurately describe the vorticity mode of the LEE is assessed with the form of the vortex defined above. At time $t = 0$, the initial position of the vortex of size, $\sigma = 0.25$, is defined as $\vec{x}_0 = -9\sigma$ and the mean flow velocity is $u_\circ = 0.3\, c_\circ$ in the x-direction only. The numerical solution is obtained when the vortex center point reaches the center of the computational domain. At this time, the numerical solutions for x-velocity, u', and y-velocity, v', are compared to the analytical solutions. Figures 6.2a and 6.2b show the numerical and exact solutions, respectively, for the u'-velocity as contours in the x–y plane. The solutions are compared in more detail by examining the v'-velocity along the line $y = 0$ in Figure 6.2c, showing good agreement. Integrating the error between the exact and numerical solutions over the domain, gives a relative L^2 error of $6.8e^{-4}$.

6.2.5 Acoustic modes in a cylindrical duct

Acoustic modes in a duct of radius, R, with uniform flow are found as solutions to the convected Helmholtz equation,

$$\frac{1}{c_\circ^2}\frac{\mathrm{d}_0^2 p'}{\mathrm{d}t^2} - \nabla^2 p' = 0, \tag{6.16}$$

where $\frac{\mathrm{d}_0}{\mathrm{d}t} = \frac{\partial}{\partial t} + u_\circ \frac{\partial}{\partial x}$ and p' is the acoustic pressure, subject to no-penetration boundary conditions at the hard walls. The mean flow velocity in the axial direction, $u_\circ$, is assumed to be uniform, and the mean flow in the y and z directions is zero. For a cylindrical duct, the primitive solution vector in cylindrical coordinates for a mode,

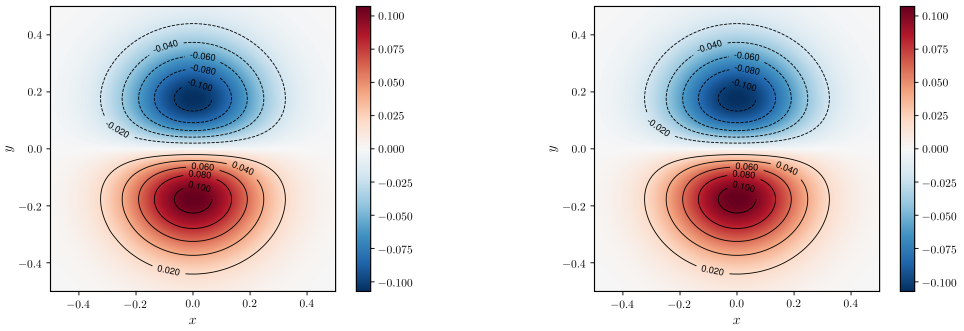

(a) Numerical u'-velocity

(b) Exact u'-velocity

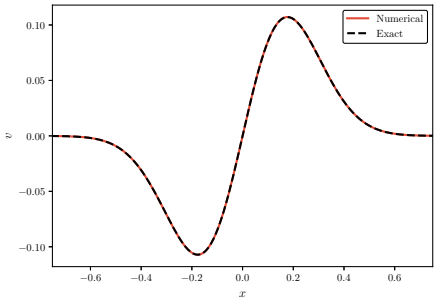

(c) Centerline v'-velocity, $y = 0$

Figure 6.2: Comparison between the numerical and the exact solutions for an advecting vortex.

(m, n), with a pressure amplitude, $A^{\pm}_{m,n}$, is,

$$\rho' = \frac{1}{c_\circ^2} A^{\pm}_{m,n} \Psi_m e^{i(\omega t - k_x^{\pm} x - m\theta)} \tag{6.17}$$

$$u'_x = \frac{A^{\pm}_{m,n}}{\rho_\circ c_\circ} \frac{k_x^{\pm}}{k_\circ - M k_x^{\pm}} \Psi_m e^{i(\omega t - k_x^{\pm} x - m\theta)} \tag{6.18}$$

$$u'_r = \frac{A^{\pm}_{m,n}}{\rho_\circ c_\circ} \frac{i}{k_\circ - M k_x^{\pm}} \frac{\partial \Psi_m}{\partial r} e^{i(\omega t - k_x^{\pm} x - m\theta)} \tag{6.19}$$

$$u'_\theta = \frac{A^{\pm}_{m,n}}{r\rho_\circ c_\circ} \frac{m}{k_\circ - M k_x^{\pm}} \Psi_m e^{i(\omega t - k_x^{\pm} x - m\theta)} \tag{6.20}$$

$$p' = A^{\pm}_{m,n} \Psi_m e^{i(\omega t - k_x^{\pm} x - m\theta)}, \tag{6.21}$$

where u'_x, u'_r, and u'_θ are the acoustic velocity components in the axial, radial, and azimuthal directions, respectively. The solution is time-harmonic with angular frequency, ω, free-field wavenumber, $k_\circ = \omega / c_\circ$, and fluctuates with a shape defined by $\Psi_m = J_m(k_r r)$ in the radial direction. The mode propagates with an axial wavenumber of $k_x^{\pm}$, where $\pm$ indicates propagation in opposite directions. The radial wavenumber, k_r, is found by applying the no-penetration condition, and solving $\frac{\mathrm{d}\Psi_m(k_r R)}{\mathrm{d}r} = 0$

for each successive zero, parameterized by n. Modes are defined based on the azimuthal and radial mode number pair, (m, n). The plane-wave mode is defined by $(m = 0, n = 0)$. The axial and radial wavenumbers are related to the frequency through the dispersion relation,

$$k_x^{\pm} = k_\circ \frac{\pm\sqrt{1-(1-M^2)k_r^2/k_\circ^2} - M}{1-M^2}. \tag{6.22}$$

When $k_\circ$ is small enough to make the argument of the square-root negative, the mode is considered cut-off, and does not propagate axially. A cut-on ratio can be defined as,

$$\eta_m = \sqrt{1-(1-M^2)k_r^2/k_\circ^2}, \tag{6.23}$$

where $\eta_m = 0$ indicates no axial propagation, and $\eta_m = 1$ indicates purely axial propagation. The full derivation of the duct modes is found in Appendix A.2.

Expressing the solution in conserved variables and in Cartesian coordinates, with x defined as the axial direction, the solution becomes,

$$\mathbf{q}_\mathrm{d}^{\pm} = \mathrm{Re}\left\{\begin{array}{c} \rho' \\ \rho_\circ u_x' + u_\circ \rho' \\ \rho_\circ(u_r'\cos(\theta) - u_\theta'\sin(\theta)) \\ \rho_\circ(u_r'\sin(\theta) + u_\theta'\cos(\theta)) \\ \frac{\pi_\circ}{\rho_\circ c_\circ^2} p' \end{array}\right\}. \tag{6.24}$$

Factoring out the amplitude and exponential term, the solution in the duct can be expressed more compactly as,

$$\mathbf{q}_\mathrm{d}^{\pm} = \mathrm{Re}\left[A_{m,n}^{\pm}\mathbf{\Theta}^{\pm}e^{i(\omega t - k_x^{\pm}x - m\theta)}\right]. \tag{6.25}$$

At the source plane, the solution consists of a right-traveling acoustic wave, with an amplitude, $A_{m,n}^{+}$, and an acoustic wave traveling in the opposite direction $(-x)$, with an amplitude, $A_{m,n}^{-}$. With a non-zero mean flow velocity, the amplitudes and axial wavenumbers of the upstream and downstream traveling waves are different, so rather than trying to specify $\mathbf{q}_s^{\pm}$ directly, a simple acoustic source term on the interface is introduced and then related to the amplitudes of the desired mode.

Consider the duct domain shown in Figure 6.3, with volumes, Ω_L and Ω_R on either side of the source plane, Γ_i, and with normal directions, $\vec{n}_L$ and $\vec{n}_R$. When an acoustic source is present at the source plane, acoustic waves are generated on both sides of the interface, traveling right into Ω_R and left into Ω_L. These waves are generated by an acoustic flux into each domain which is proportional to the eigenvector of the normal

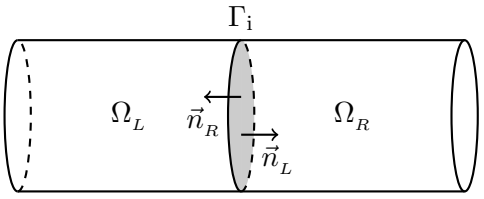

Figure 6.3: Example duct domain for an interface source, separating two volumes, Ω_L and Ω_R.

flux matrix on either side of the interface,

$$\mathbf{s} = A(\vec{x},t)\begin{Bmatrix} 1 \\ u_\circ - n_x c_\circ \\ v_\circ - n_y c_\circ \\ w_\circ - n_z c_\circ \\ \pi_\circ/\rho_\circ \end{Bmatrix}, \tag{6.26}$$

where n_x, n_y, and n_z are the normal components at the interface for Ω_L and Ω_R, and $A(\vec{x},t)$ is the amplitude at the source plane. For the duct in Figure 6.3, assuming that the axial coordinate is x, the source plane is perpendicular to the duct axis and there is no swirling flow, therefore, n_y, n_z, $v_\circ$, and $w_\circ$ are all zero. To generate duct modes at the interface, the coefficient, $A(\vec{x},t)$ is taken as a time-harmonic oscillation of the duct-mode shape function, *i.e.*,

$$A(\vec{x},t) = C_s \Psi_m(y,z)\,\mathrm{Re}\left(e^{i(\omega t - m\theta)}\right). \tag{6.27}$$

The real constant, C_s, defines the amplitudes, $A^{\pm}_{m,n}$, of the left- and right-traveling acoustic modes.

Relating C_s to the duct-mode amplitudes

To generate a mode with a specific $A^{-}_{m,n}$ or $A^{+}_{m,n}$, the correct coefficient, C_s, must be determined. Applying the DG discretization to the two semi-infinite volumes in Figure 6.3, a relationship between C_s and $A^{\pm}_{m,n}$ can be found. First, the solution in each half of the duct, separated by the interface, Γ_i, is defined as a superposition of the duct mode, $\mathbf{q}^{\pm}_\mathrm{d}$, and any other disturbance in the domain, $\hat{\mathbf{q}}$. In the left and right portions of the duct, Ω_L and Ω_R, the total solution can be written as,

$$\begin{aligned} \mathbf{q}_L &= \mathbf{q}^{-}_\mathrm{d} + \hat{\mathbf{q}}_L, \text{ and,} \\ \mathbf{q}_R &= \mathbf{q}^{+}_\mathrm{d} + \hat{\mathbf{q}}_R. \end{aligned} \tag{6.28}$$

Multiplying the LEE residual by test functions, $\mathbf{\Phi}_e^\intercal$, and then integrating over Ω_L and Ω_R, integration by parts is applied to get,

$$\int_{\Omega_L} \mathbf{\Phi}_e^\intercal \frac{\partial \mathbf{q}_L}{\partial t} - \frac{\partial \mathbf{\Phi}_e^\intercal}{\partial x_i}\mathbf{f}_i\left(\mathbf{q}_L\right) \mathrm{d}\Omega_L + \int_{\Gamma_\mathrm{i}} \mathbf{\Phi}_e^\intercal \left(\mathbf{s}_L + F_{n,L}^+ \mathbf{q}_L + F_{n,L}^- \mathbf{q}_R\right) \mathrm{d}\Gamma_\mathrm{i} + \int_{\Gamma_\mathrm{w}} \mathbf{\Phi}_e^\intercal F_\mathrm{w} \mathbf{q}_L \mathrm{d}\Gamma_\mathrm{w} = 0, \text{ and,} \tag{6.29}$$

$$\int_{\Omega_R} \mathbf{\Phi}_e^\intercal \frac{\partial \mathbf{q}_R}{\partial t} - \frac{\partial \mathbf{\Phi}_e^\intercal}{\partial x_i}\mathbf{f}_i\left(\mathbf{q}_R\right) \mathrm{d}\Omega_R + \int_{\Gamma_\mathrm{i}} \mathbf{\Phi}_e^\intercal \left(\mathbf{s}_R + F_{n,R}^+ \mathbf{q}_R + F_{n,R}^- \mathbf{q}_L\right) \mathrm{d}\Gamma_\mathrm{i} + \int_{\Gamma_\mathrm{w}} \mathbf{\Phi}_e^\intercal F_\mathrm{w} \mathbf{q}_R \mathrm{d}\Gamma_\mathrm{w} = 0, \tag{6.30}$$

where the upwind flux is used on the interface and $\mathbf{s}_L$ and $\mathbf{s}_R$ are the interface sources, Equation 6.26. The reflecting wall boundary conditions are implemented through the matrix, F_w, at the duct wall, Γ_w. The terms, $\hat{\mathbf{q}}_L$ and $\hat{\mathbf{q}}_R$ can be eliminated by recognizing that they satisfy the standard DG weak formulation, leaving the two equations,

$$\int_{\Omega_L} \mathbf{\Phi}_e^\intercal \frac{\partial \mathbf{q}_\mathrm{d}^-}{\partial t} - \frac{\partial \mathbf{\Phi}_e^\intercal}{\partial x_i}\mathbf{f}_i\left(\mathbf{q}_\mathrm{d}^-\right) \mathrm{d}\Omega_L + \int_{\Gamma_\mathrm{i}} \mathbf{\Phi}_e^\intercal \left(\mathbf{s}_L + F_{n,L}^+ \mathbf{q}_\mathrm{d}^- + F_{n,L}^- \mathbf{q}_\mathrm{d}^+\right) \mathrm{d}\Gamma_\mathrm{i} + \int_{\Gamma_\mathrm{w}} \mathbf{\Phi}_e^\intercal F_\mathrm{w} \mathbf{q}_\mathrm{d}^- \mathrm{d}\Gamma_\mathrm{w} = 0, \text{ and,} \tag{6.31}$$

$$\int_{\Omega_R} \mathbf{\Phi}_e^\intercal \frac{\partial \mathbf{q}_\mathrm{d}^+}{\partial t} - \frac{\partial \mathbf{\Phi}_e^\intercal}{\partial x_i}\mathbf{f}_i\left(\mathbf{q}_\mathrm{d}^+\right) \mathrm{d}\Omega_R + \int_{\Gamma_\mathrm{i}} \mathbf{\Phi}_e^\intercal \left(\mathbf{s}_R + F_{n,R}^+ \mathbf{q}_\mathrm{d}^+ + F_{n,R}^- \mathbf{q}_\mathrm{d}^-\right) \mathrm{d}\Gamma_\mathrm{i} + \int_{\Gamma_\mathrm{w}} \mathbf{\Phi}_e^\intercal F_\mathrm{w} \mathbf{q}_\mathrm{d}^+ \mathrm{d}\Gamma_\mathrm{w} = 0, \tag{6.32}$$

in terms of the interface sources and the duct modes only. Since the duct modes satisfy the wall boundary conditions by definition, the integral over Γ_w is zero. Finally, applying integration by parts to the second volume term in the above equations, eliminates all but the surface integral terms at the interface,

$$\int_{\Gamma_\mathrm{i}} \mathbf{\Phi}_e^\intercal \left(\mathbf{s}_L + F_{n,L}^+ \mathbf{q}_\mathrm{d}^- + F_{n,L}^- \mathbf{q}_\mathrm{d}^+ - F_{n,L} \mathbf{q}_\mathrm{d}^-\right) \mathrm{d}\Gamma_\mathrm{i} = 0, \text{ and,} \tag{6.33}$$

$$\int_{\Gamma_\mathrm{i}} \mathbf{\Phi}_e^\intercal \left(\mathbf{s}_R + F_{n,R}^+ \mathbf{q}_\mathrm{d}^+ + F_{n,R}^- \mathbf{q}_\mathrm{d}^- - F_{n,R} \mathbf{q}_\mathrm{d}^+\right) \mathrm{d}\Gamma_\mathrm{i} = 0. \tag{6.34}$$

Due to the general choice of test function and recognizing that $F_{n,L} = F_{n,L}^- + F_{n,L}^+$ and $F_{n,R} = F_{n,R}^- + F_{n,R}^+$, results in the two equations,

$$\mathbf{s}_L + F_{n,L}^- \mathbf{q}_\mathrm{d}^+ - F_{n,L}^- \mathbf{q}_\mathrm{d}^- = 0, \text{ and,} \tag{6.35}$$

$$\mathbf{s}_R + F_{n,R}^- \mathbf{q}_\mathrm{d}^- - F_{n,R}^- \mathbf{q}_\mathrm{d}^+ = 0, \tag{6.36}$$

that can be solved to determine the relationship between C_s and $A_{m,n}^\pm$. Substituting the expressions for $\mathbf{q}_\mathrm{d}^\pm$ and replacing the flux matrices by $F_{n,L}^- = \mathbf{W}_L \mathbf{\Lambda}_L^- \mathbf{W}_L^{-1}$ and

$F^{-}_{n,R} = \mathbf{W}_{R}\mathbf{\Lambda}^{-}_{R}\mathbf{W}^{-1}_{R}$, results in,

$$\tilde{\mathbf{s}}_L = \mathrm{Re}\left[\mathbf{\Lambda}^{-}_{L}\left(A^{-}_{m,n}\mathbf{W}^{-1}_{L}\mathbf{\Theta}^{-}_{m} - A^{+}_{m,n}\mathbf{W}^{-1}_{L}\mathbf{\Theta}^{+}_{m}\right)e^{i(\omega t - m\theta)}\right], \text{ and,} \tag{6.37}$$

$$\tilde{\mathbf{s}}_R = \mathrm{Re}\left[\mathbf{\Lambda}^{-}_{R}\left(A^{+}_{m,n}\mathbf{W}^{-1}_{R}\mathbf{\Theta}^{+}_{m} - A^{-}_{m,n}\mathbf{W}^{-1}_{R}\mathbf{\Theta}^{-}_{m}\right)e^{i(\omega t - m\theta)}\right], \tag{6.38}$$

where $\tilde{\mathbf{s}}_L = \mathbf{W}^{-1}_{L}\mathbf{s}_L$ and $\tilde{\mathbf{s}}_R = \mathbf{W}^{-1}_{R}\mathbf{s}_R$, for a source plane axial location of $x = 0$. Substituting the duct mode source, Equation 6.26, and again assuming n_y, n_z, $v_\circ$, and $w_\circ$ are all zero, $\tilde{\mathbf{s}}_L$ and $\tilde{\mathbf{s}}_R$ become,

$$\tilde{\mathbf{s}}_L = \begin{Bmatrix} 0 \\ 0 \\ 0 \\ C_s\Psi_m(y,z) \\ 0 \end{Bmatrix} \mathrm{Re}\left[e^{i(\omega t - m\theta)}\right], \quad \text{and,} \quad \tilde{\mathbf{s}}_R = \begin{Bmatrix} 0 \\ 0 \\ 0 \\ C_s\Psi_m(y,z) \\ 0 \end{Bmatrix} \mathrm{Re}\left[e^{i(\omega t - m\theta)}\right], \tag{6.39}$$

reducing the total number of equations relating C_s and $A^{\pm}_{m,n}$ to two. The duct mode amplitudes in terms of C_s are found to be,

$$A^{-}_{m,n} = -C_s\frac{c_\circ(1 + M\eta_m)}{(1 - M^2)\eta_m}, \quad \text{and,} \quad A^{+}_{m,n} = -C_s\frac{c_\circ(1 - M\eta_m)}{(1 - M^2)\eta_m}. \tag{6.40}$$

Application to the Munt problem

To verify the duct-mode source term, the classic radiation from a cylindrical duct problem of Munt [139] is solved. The source generates an acoustic mode with mode number, (5,0), and a Helmholtz number of He = 17, introduced at the shaded source plane illustrated in Figure 6.4. The flow conditions are uniform throughout the domain, with a mean sound speed and density of $c_\circ = 340.27\,\mathrm{m/s}$ and $\rho_\circ = 1.225\,\mathrm{kg/m^3}$, and a mean flow Mach number of $M = 0.3$. The mesh is three-dimensional with curved elements representing the duct wall and buffer zones inside the duct and surrounding the domain. A snapshot of the time-harmonic pressure field over an x–y slice of the domain is given in Figure 6.5a, showing the radiation away from the duct and the reflections traveling back into the duct. After a time-harmonic solution is reached, the RMS pressure along the measurement arc is compared to the analytical solution by Gabard [140], in Figure 6.5b. A strong agreement between the numerical and exact solutions can be seen inside and outside of the duct, even on the linear pressure scale. It is important to note that there is no specific enforcement of the Kutta-condition at the end of the duct. The DG LEE model naturally satisfies it without considering viscosity. In addition, the geometrical singularity appears to be well-behaved in the

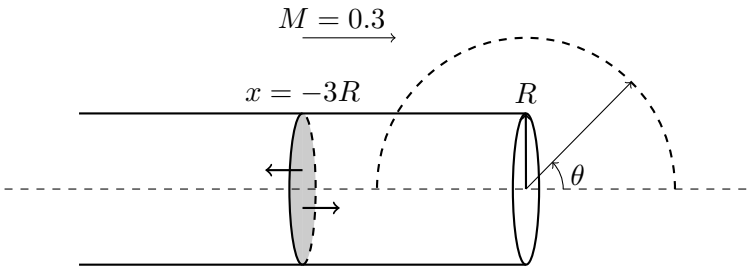

Figure 6.4: Munt problem definition showing the measurement arc over θ and the shaded source plane.

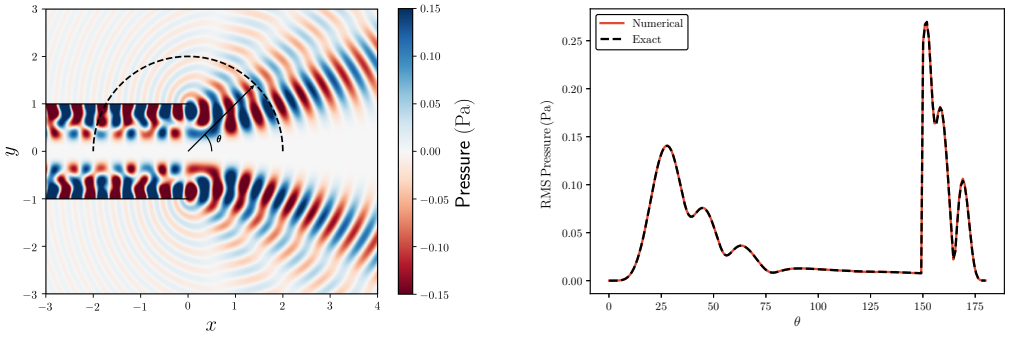

(a) Pressure contours on an x–y slice. (b) RMS pressure over θ.

Figure 6.5: Solution of the Munt problem for a source mode, $(5, 0)$, and a Helmholtz number of $\mathrm{He} = 17$.

DG solution. These are in contrast to finite-element methods that need to enforce the Kutta-condition manually and do not cope well with geometrical singularities.

To provide a second verification of the interface source, the Munt problem is solved again with identical geometry and flow conditions, but with a source mode $(0, 1)$ at a Helmholtz number of $\mathrm{He} = 8.5$. The governing equations are integrated until a time-harmonic solution is reached, and then the RMS pressure is recorded over the measurement arc defined in Figure 6.6a. Figure 6.6a shows the instantaneous pressure field at a given time over an x–y slice of the domain. The RMS pressure along the measurement arc is compared with the analytical RMS pressure in Figure 6.6b. Good agreement with the analytical pressure can be seen over the measurement angles.

6.3 Band-limited source terms

Simulating the acoustic response to a time-harmonic source in the time domain can be impractical when a large number of source frequencies are desired. For each frequency, a separate calculation must be completed and these frequencies must be known *a priori*.

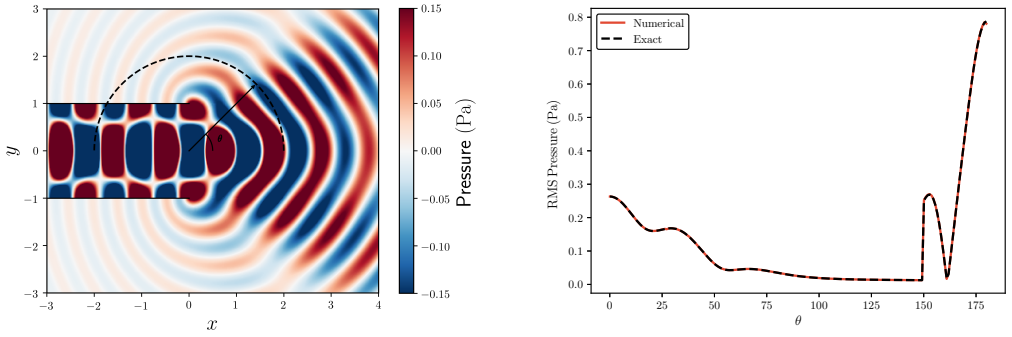

(a) Pressure contours on an x–y slice.

(b) RMS pressure over θ.

Figure 6.6: Solution of the Munt problem for a source mode, $(0, 1)$, and a Helmholtz number of $\mathrm{He} = 8.5$.

A more effective use of a time-domain solver is to build a source term containing the entire desired frequency range. This requires replacing the time-harmonic component of the signal with a band-limited forcing function. In a single time-domain calculation, the response of the system over a desired frequency range can be obtained.

6.3.1 Construction of a band-limited source

For source terms expressed at fixed frequency, such as duct modes, it is not immediately clear how to modify the source to excite a specific frequency range. One way is to derive a wave-packet forcing function, such as the one developed by Hu *et al.* [85], replacing the time-harmonic forcing function of the source. This section derives the general form of wave-packet forcing functions that are band-limited, and discusses the post-processing of solutions to obtain the desired result in the frequency domain.

Given a time-harmonic source term such as,

$$\mathbf{s} = \mathbf{A}(\vec{x}) \sin(\omega t), \tag{6.41}$$

where $\mathbf{A}(\vec{x})$ is a vector of the same size as the solution vector and ω is the angular frequency, to construct a source with a desired frequency range, the above source term can be integrated over the angular frequency range. Integrating the above expression from $\omega_{\min}$ to $\omega_{\max}$, results in,

$$\begin{aligned} \mathbf{s} &= \frac{\mathbf{A}(\vec{x})}{\omega_{\max} - \omega_{\min}} \int_{\omega_{\min}}^{\omega_{\max}} \sin(\omega t) \mathrm{d}\omega \\ &= \frac{\mathbf{A}(\vec{x})}{(\omega_{\max} - \omega_{\min})t} \left[\cos(\omega_{\min} t) - \cos(\omega_{\max} t)\right]. \end{aligned} \tag{6.42}$$

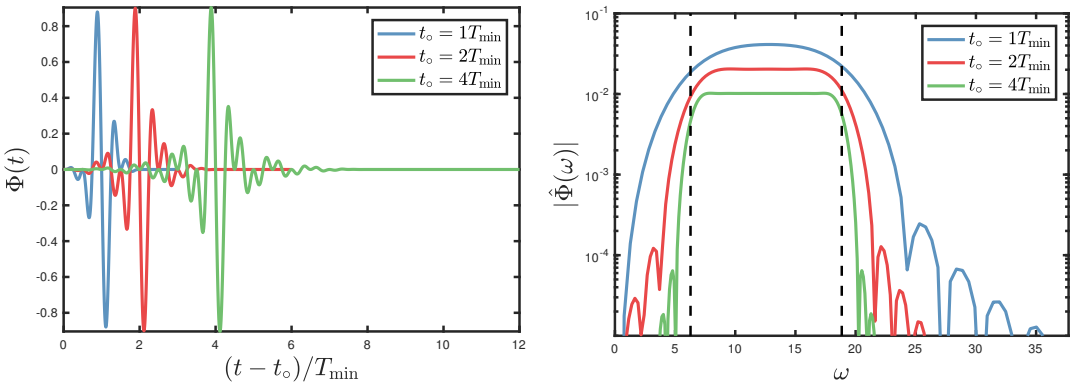

(a) Amplitude (b) Frequency spectrum

Figure 6.7: Time and frequency domain amplitude of the source for a range of $t_\circ$. Dashed lines show the minimum and maximum angular frequencies, $\omega_{\min}$ and $\omega_{\max}$.

When $t = 0$, this expression remains regular. The choice of using $\sin(\omega t)$ in Equation 6.41, rather than $\cos(\omega t)$, ensures that the signal has a zero mean. This can be important for sources inside ducts, since low-frequency acoustic disturbances near cut-off take a long time to leave the duct.

Notice that the above expression is not compact in time. The source term should ideally be active for as short as possible so that the total integration time is reduced. A temporal windowing function is applied to the source term to minimize the amount of time it is active. For example the window,

$$w_s(t) = \exp\left(\frac{-\alpha t^2}{t_\circ^2}\right), \tag{6.43}$$

decays exponentially in time. Alternatively, one could choose a compact window, such as,

$$w_s(t) = \begin{cases} \frac{1}{2}\left(1 + \cos\left(\frac{\pi t}{t_\circ}\right)\right), & \text{if } -t_\circ \leq t \leq t_\circ \\ 0, & \text{if } |t| > t_\circ \end{cases}, \tag{6.44}$$

to ensure that the source term is exactly zero outside of $-t_\circ \leq t \leq t_\circ$, which is an attractive property for the numerical implementation. Multiplying by the windowing function, the final form of the source term becomes,

$$\mathbf{s} = \mathbf{A}(\vec{x})\frac{w_s(t)}{(\omega_{\max} - \omega_{\min})t}\left[\cos(\omega_{\min} t) - \cos(\omega_{\max} t)\right]. \tag{6.45}$$

Figure 6.7 shows the amplitude of the source term in the time and frequency domain for a range of $t_\circ$, using the cosine window function. Increasing $t_\circ$ has the effect of narrowing the peak of the frequency spectrum, while increasing the length of time the source is active. Windowing of the source introduces energy at other frequencies

outside of ω_{min}–ω_{max}, with the amount depending on both the choice of the windowing function and $t_\circ$. Due to the cosine window, spectral lobes are visible in Figure 6.7b, which reduce when $t_\circ$ increases. The exponential window would avoid these lobes, but with the side-effect of a longer time that the source needs to be active. Many other choices of windows are available in the signal processing community, and the ones chosen in this work are not necessarily the optimal choice.

6.3.2 Post-processing of wave-packet responses

For a given wave-packet source term, the parameters, $t_\circ$, ω_{min}, and ω_{max} must be given to define the wave-packet duration and frequency content. In the numerical implementation, one must also define the sampling rate, f_{s}, at which the numerical solution is stored during the calculation. The parameter, $t_\circ$, is chosen based on the desired minimum angular frequency, ω_{min}. It must be long enough in duration such that there are multiple periods of the lowest frequency component within the envelope of the wave-packet. In contrast, the sampling rate is chosen based on the maximum angular frequency, ω_{max}, and must at least satisfy the Nyquist criterion, $f_{\text{s}} > \dfrac{\omega_{\text{max}}}{\pi}$, to avoid aliasing. An advantage of wave-packet sources is that the solution only needs to be recorded while the response at the measurement locations is non-zero, or above the desired accuracy threshold. That is, once the wave-packet passes the measurement locations, assuming that it radiates into the free-field, the integration process can end.

The Fast Fourier Transform (FFT) [141] is used to transform the time-domain solution to the frequency domain. If the solution is recorded at N_{fp} points in space, and sampled at N points in time for a total integration time of $\dfrac{N-1}{f_{\text{s}}}$, the FFT must be computed $N_{\text{fp}}N_v$ times, where N_v is the number of conserved variables, for a FFT size of N. Due to the storage, input-output (I/O) limitations, and the FFT cost, N_{fp} is generally chosen to be much less than the total number of DOF, requiring that the spatial locations where the solution is desired, are chosen *a priori*. The sampling rate of the solution is chosen to be uniform in this work, making the post-processing step simple. For problems of dispersive waves, such as duct modes, different frequency components of the initial disturbance will spread out in time and space. This could be exploited for potential savings in storage and I/O by considering a nonuniform sampling rate, adapting it in time to the signal measured at each measurement location. This could be an area of future work to reduce the computational cost of the method.

After computing the FFT, the solution in the frequency domain is obtained at integer multiples of $1/t_{\text{f}}$, where t_{f} is the duration of the signal. If the solution at a specific frequency is desired, for example to compare to experimental results, $1/t_{\text{f}}$ can be chosen in advance to be an integer multiple of the desired frequency, or the time-domain

solution can be re-sampled in the post-processing step. The re-sampling process takes the time-domain signal at each measurement location and interpolates it at a new sampling frequency, equal to a rational multiple of the desired frequency. The choice of interpolation scheme depends on the balance between accuracy of the interpolation and the computational cost. A simple interpolator is linear interpolation, interpolating between two adjacent time samples, while more complex methods such as cubic-spline interpolation exist [142]. It is important to note that the re-sampling process does not increase the frequency resolution of the results, which is still fixed at $1/t_{\mathrm{f}}$.

To examine the impact of the choice of interpolation scheme on the overall accuracy of the frequency-domain solution, a model wave-packet signal with an analytical frequency-domain solution is compared to the discrete solution using re-sampling and the FFT. Given a band-limited wave-packet solution of the form,

$$g(t) = \frac{\exp\left(\frac{-\alpha t^2}{t_\circ}\right)}{(\omega_{\max} - \omega_{\min})t}\left[\cos(\omega_{\min} t) - \cos(\omega_{\max} t)\right], \tag{6.46}$$

in the time-domain, its analytical solution in the frequency domain for positive frequencies is,

$$G(\omega) = \frac{i\pi}{\omega_{\max} - \omega_{\min}}\left[H(\omega - \omega_{\min}) + H(\omega + \omega_{\min}) - H(\omega - \omega_{\max}) - H(\omega + \omega_{\max})\right], \tag{6.47}$$

where $H(\omega) = \operatorname{erf}\left(\frac{\omega t_\circ}{2\sqrt{\alpha}}\right)$. The angular frequency range is fixed from $\omega_{\min} t_\circ = 16\pi$ to $\omega_{\max} t_\circ = 68\pi$, and the parameter α is equal to 10. Figure 6.8a shows the time-domain wave-packet, shifted from the origin to $t - t_{\mathrm{w}}$, where t_{w} is chosen to be long enough such that the wave-packet response decays to the desired error level *e.g.*,

$$t_{\mathrm{w}} = t_\circ \sqrt{\frac{-\ln(\epsilon)}{\alpha}}, \tag{6.48}$$

where ϵ is the desired error level. The corresponding power in the frequency domain is shown in Figure 6.8b. To assess the accuracy of the post-processing, for 100 evenly spaced angular frequencies from $\omega_{\min}$ to $\omega_{\max}$, the relative l_2 error between the exact frequency-domain solution and the discrete results from the FFT is computed as,

$$E_{l_2} = \frac{\sqrt{\sum_i \left|\tilde{G}(\omega_i) - G(\omega_i)\right|^2}}{\sqrt{\sum_i |G(\omega_i)|^2}}, \tag{6.49}$$

where G is the analytical solution and $\tilde{G}$ is the numerical solution, for linear and

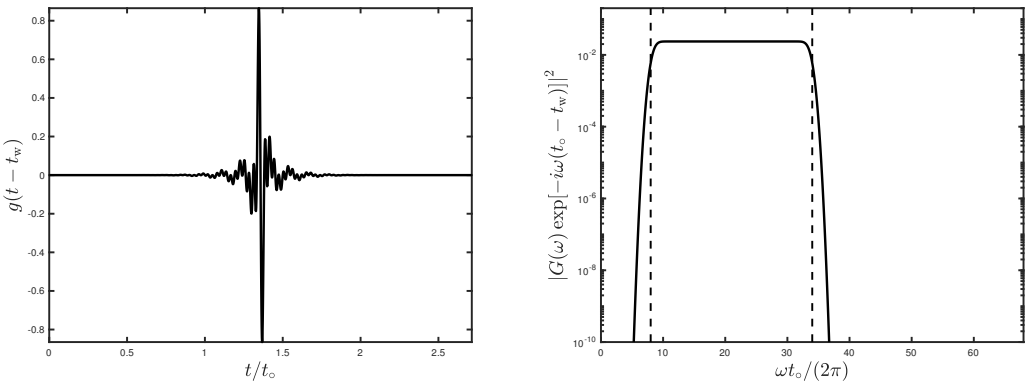

(a) (b)

Figure 6.8: (a): Time domain wave-packet signal. (b): Wave-packet frequency response.

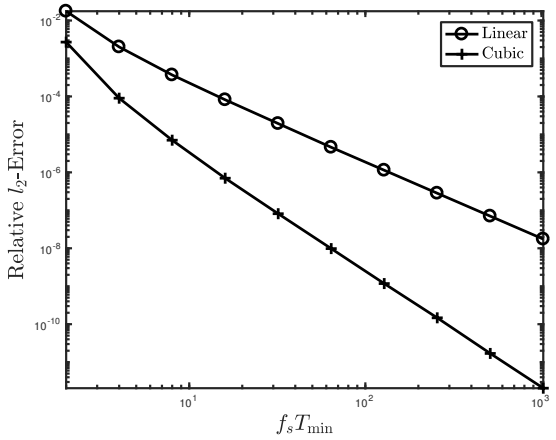

Figure 6.9: Convergence of the relative l_2 error of the frequency response over $\omega_{\min}$ to $\omega_{\max}$ for linear and cubic-spline time-domain re-sampling.

cubic-spline interpolation and a range of sampling rates, f_s. Figure 6.9 shows the convergence of E_{l_2} with increasing $f_s T_{\min}$, where $T_{\min}$ is the period associated with the highest frequency component of the wave-packet. Comparing the two interpolations, the error for the cubic-spline interpolation converges at $\mathcal{O}(1/(f_s T_{\min}))^3$, compared to $\mathcal{O}(1/(f_s T_{\min}))^2$ for linear interpolation. This means that for the same level of accuracy, linear interpolation requires a higher sampling rate. Due to the storage and computational time of writing solution data, a high sampling rate is undesirable. Therefore, in this work the cubic-spline interpolator is used when re-sampling is required. It is important to note that if no re-sampling is required, a lower sampling rate could be chosen.

6.3.3 Construction of a band-limited duct-mode interface source

In Section 6.2.5, the interface source for time-harmonic, acoustic modes of a duct was introduced, allowing one to specify a duct-mode source compactly at a fictitious interface between domains. A band-limited, duct-mode, interface source can be constructed by using the form of the wave-packet forcing function, Equation 6.45, and replacing $\mathbf{A}(\vec{x})$, so that,

$$\mathbf{s} = \Psi_m(y,z) \begin{Bmatrix} 1 \\ u_\circ - n_x c_\circ \\ 0 \\ 0 \\ \pi_\circ/\rho_\circ \end{Bmatrix} \frac{w_s(t)}{(\omega_{\max} - \omega_{\min})t} \left[\cos(\omega_{\min} t) - \cos(\omega_{\max} t)\right]. \tag{6.50}$$

Often, one would want to obtain a transfer function, relating a particular mode amplitude at the source plane to the amplitude of the solution at the monitor points, at specific frequencies, *i.e.*,

$$\mathbf{q}(\vec{x},\omega) = \mathbf{T}^{\pm}(\vec{x},\omega) A^{\pm}_{m,n}(\omega), \tag{6.51}$$

where $A^{\pm}_{m,n}(\omega)$ is the desired amplitude of the mode at the source plane, for either the positive or negative axial directions, $A^{+}_{m,n}$ and $A^{-}_{m,n}$, and $\mathbf{T}^{\pm}$ is the transfer function. By solving for the response to a wave-packet duct-mode source in the time-domain, and then transforming to the frequency domain, the numerical transfer function can be obtained.

Recall that the amplitude of the duct-mode, for a single frequency component, can be related to the amplitude of the interface source, C_s, through the relation,

$$A^{\pm}_{m,n} = -C_s(\omega) \frac{c_\circ(1 \mp M\eta_m)}{(1-M^2)\eta_m}, \tag{6.52}$$

for right (+) and left (-) running modes. For the time-harmonic source term, C_s is a constant. For the wave-packet source term, C_s varies with frequency and is obtained through application of the Fourier transform to the wave-packet forcing function,

$$C_s(\omega) = \int_{-\infty}^{\infty} \frac{w_s(t)}{(\omega_{\max} - \omega_{\min})t} \left[\cos(\omega_{\min} t - m\theta) - \cos(\omega_{\max} t - m\theta)\right] e^{-i\omega t} \mathrm{d}t. \tag{6.53}$$

Similarly, given the time-domain solution to the wave-packet source, recorded at the monitor points, $\mathbf{q}(\vec{x},t)$, the frequency domain domain solution is obtained as,

$$\mathbf{q}(\vec{x},\omega) = \int_{-\infty}^{\infty} \mathbf{q}(\vec{x},t) e^{-i\omega t} \mathrm{d}t. \tag{6.54}$$

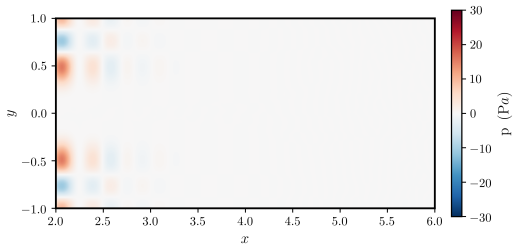

(a) $t = 5T_{\max}$

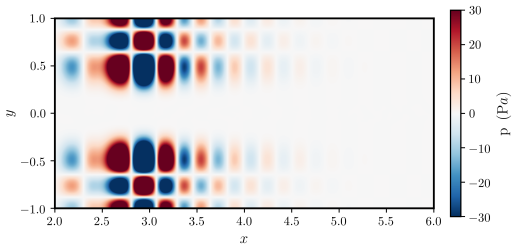

(b) $t = 10T_{\max}$

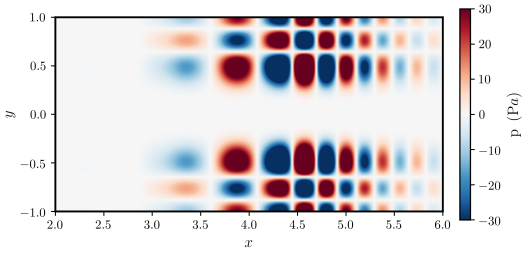

(c) $t = 15T_{\max}$

Figure 6.10: Evolution of the mode $(5, 2)$ wavepacket in time, at multiples of the longest period, $T_{\max}$.

The frequency domain solution is computed numerically using the procedure discussed in Section 6.3.2. Finally, to obtain the transfer function, $\mathbf{q}(\vec{x}, \omega)$ must be scaled by Equation 6.52, resulting in,

$$\mathbf{T}^{\pm}(\vec{x}, \omega) = -\frac{\mathbf{q}(\vec{x}, \omega)}{C_s(\omega)} \frac{(1 - M^2)\eta_m}{c_\circ(1 \mp M\eta_m)}. \tag{6.55}$$

6.3.4 Application to propagation within an infinite circular duct

To verify the band-limited wavepacket source term and post-processing, a problem of acoustic propagation in a 3D, infinite, cylindrical duct is solved. The source has an azimuthal mode number of 5 and a radial mode number of 2, and is injected into the cylindrical duct of radius $R = 1\,\text{m}$ at $x = 2\,\text{m}$ and allowed to propagate freely. Buffer zones at both ends of the duct smoothly absorb the out-going waves while generating minimal reflections. The mean flow conditions are uniform throughout the domain, with a sound speed and density of $c_\circ = 343\,\text{m/s}$ and $\rho_\circ = 1.225\,\text{kg/m}^3$, and a Mach number of $M = 0.3$. At $t = 0\,\text{s}$, a band-limited duct mode source with a Helmholtz number range of approximately 17.5–29, is injected at the source plane, $x = 0$. Figure 6.10 shows the evolution of the wavepacket pressure as time increases. The dispersive wavepacket starts with zero axial extent and then advects downstream with a growing axial envelope as the higher frequency components of the source propagate faster than the lower frequency components in the duct.

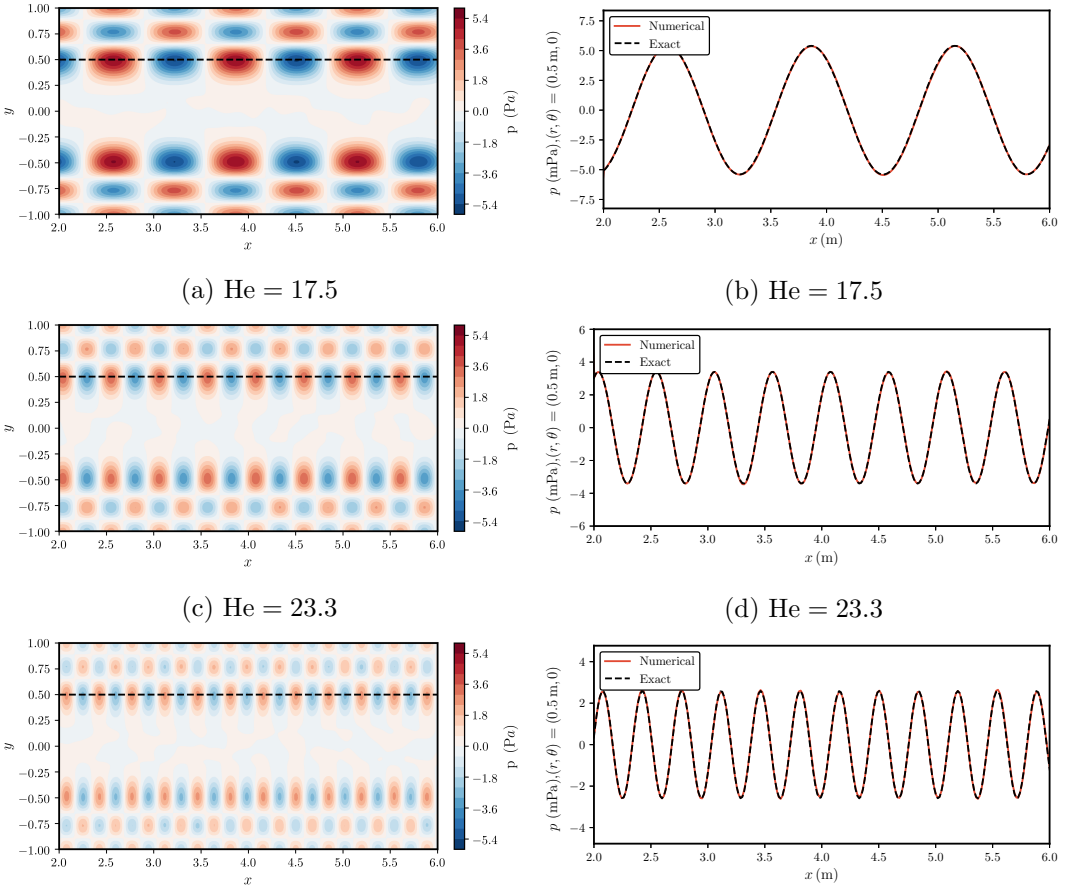

(a) He = 17.5 (b) He = 17.5

(c) He = 23.3 (d) He = 23.3

(e) He = 29.1 (f) He = 29.1

Figure 6.11: Left: Contours of acoustic pressure of the post-processed wavepacket solution at fixed frequencies. Right: Comparison of pressure to the analytical solution at the dashed line. The sources are normalized to have unit acoustic power through the duct cross-section.

After the wavepacket passes through the domain and is absorbed by the buffer zone, the time-domain solutions are post-processed at selected frequencies using the procedure outlined in Section 6.3.2. The results have all been normalized to correspond to a source acoustic power of one through the duct cross section. Figures 6.11a, 6.11c, and 6.11e show contours of the post-processed solution at Helmholtz numbers from 17.5 to 29, along a slice of the 3D duct. Figures 6.11b, 6.11d, and 6.11f show the acoustic pressure extracted along the dashed line and compared to the exact solution. The numerical solution agrees well with the exact solution over a wide frequency range.

To highlight the frequency resolution of the method, Figure 6.12 compares the post-processed numerical solution at a single point in the domain, $(x, r, \theta) = (3.5\,\text{m}, 0.5\,\text{m}, 0)$, over the full frequency range, $\omega_{\min}$ to $\omega_{\max}$, with the exact solution. It is clear that in

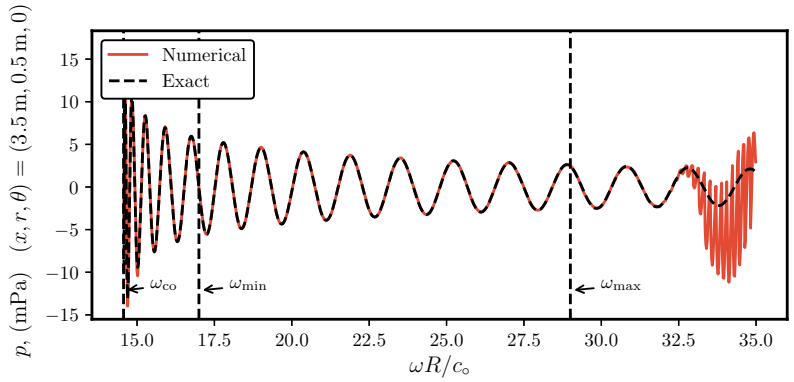

Figure 6.12: Pressure at a fixed location in the duct over a range of source frequencies, normalized for unit power at the source plane. The indicated angular frequencies, ω_{co}, ω_{min}, and ω_{max}, are the cut-off frequency, and minimum and maximum frequencies of the source, respectively.

a single simulation, the acoustic response of the duct over the entire source frequency range can be captured accurately.

6.3.5 Application to the Munt problem

To verify the wave-packet duct-mode interface source for a more realistic application, the Munt problem from Section 6.2.5 is solved for modes $(5, 0)$ and $(0, 1)$ again in this section. Both problems are solved using the identical flow, geometry, and mesh from the time-harmonic verification, and the solution is compared over the same measurement arc. At time $t = 0$, the wave-packet interface source is introduced and the pressure signal is recorded at each of the measurement locations. Once the amplitude of the pressure signals decay, the solution is stopped. Given the pressure signals at each of the measurement locations, the post-processing procedure defined in Section 6.3.2 is followed to obtain the frequency-domain solutions.

Figure 6.13a shows the numerically-predicted RMS pressure over the measurement arc compared with the analytical solution for mode $(5, 0)$. Similarly, the numerical and analytical RMS pressure for mode $(0, 1)$ is given in Figure 6.13b, showing a good agreement of the numerical and analytical solutions.

6.4 Conclusion

This chapter discussed the specification of source terms in the discrete LEE model. Interface source terms were developed to make volume source terms compact in space,

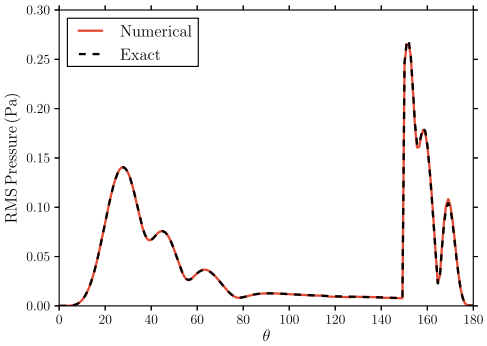

(a) Comparison of RMS pressure for mode $(5, 0)$.

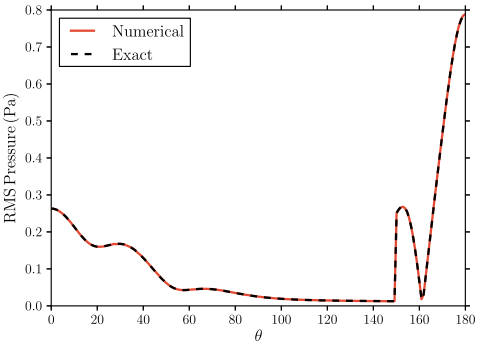

(b) Comparison of RMS pressure for mode $(0, 1)$.

Figure 6.13: Comparison of RMS pressure over the measurement arc for the Munt problem, (a): for mode $(5, 0)$ at $\mathrm{He} = 17$ and (b): for mode $(0, 1)$ at $\mathrm{He} = 8.5$.

without the need for spatial windowing. These source terms were verified by solving problems of hydrodynamic and entropy advection and the problem of acoustic radiation from a three-dimensional duct. Band-limited source terms were also derived, allowing the solution for a source of a range of frequencies in a single calculation. The efficient post-processing of these sources was outlined, and the choice of parameters such as sampling frequency and the re-sampling interpolator, were discussed. A band-limited version of the duct-mode interface source was derived and verified through the solution of acoustic mode propagation in a duct over a range of frequencies and the Munt problem.

Chapter 7

Diffraction of Tonal Noise by Chevrons in a Turbofan Exhaust

7.1 Chevrons for noise reduction

At takeoff, jet noise is a major contributer to the overall noise environment experienced on the ground. In the exhaust jet, the breakdown of small and large scale turbulent structures in the mixing layers are responsible for the production of noise. Early research by Lighthill [143] indicated that jet noise intensity scales with the eighth power of the jet Mach number, motivating the transition to turbofans with ever-larger bypass ducts to reduce the jet Mach number. Over the past several decades, jet noise has been reduced significantly through the use of modern, high-bypass, turbofan designs.

Further reductions in jet noise have been afforded by the addition of devices targeting the mixing layers and large scale turbulent structures [144]. Early designs were tabs or mixing lobes that protrude into the exhaust streams for enhanced mixing. However, these protuberances, while effective for jet noise reduction, generally had an unacceptable penalty on the thrust of the engine [145]. Modern designs are in the form of chevrons, or serrations, with minimal protuberance into the flow, striking a balance between noise reduction and thrust penalty. Chevrons are added to the trailing edges of the core nozzle or bypass duct and are in use on existing commercial aircraft. Traditionally, chevron patterns are periodic along the azimuthal direction, with the same chevron shape and level of protuberance. Recently, investigations into engine installation effects, mainly with pylons, have motivated the use of chevrons with a varying shape along the azimuthal direction, to further optimize the noise reduction [146], and variable geometry chevrons to limit the thrust penalty at all flight conditions [147].

Chevrons are designed to increase the mixing of adjacent exhaust streams, *e.g.*, the core and bypass streams, and the bypass and free streams. Increased mixing leads to an increase in stream-wise vorticity and reduces the size of the jet core [144]. The increase in stream-wise vorticity is balanced by a decrease in azimuthal vortical structures in the shear layer, which are generally highly unsteady [145]. Chevrons for jet noise reduction have been validated through extensive small and large scale experimental [146, 148, 149] and numerical studies [150, 151, 152].

7.2 Fan tonal noise and motivation

A byproduct of the success of jet noise reduction over the past several decades, has been the increase in the relative importance of other noise sources in the engine. One such noise source is created by the motion of the fan blades and the interaction of the rotating fan wake with the stationary guide vanes, producing interaction tones which propagate into the exhaust streams and are refracted by the shear layers. These interaction tones are caused by the constructive interference of the fluctuating pressure fields of the fan wake and the wake reflections. Constructive interference occurs at multiples, $m = nB + qV$, of the blade passing frequency and guide vanes, where B is the number of fan blades, V is the number of guide vanes, and m, n, and q are integers. Some of the interaction modes can be well cut-on and are poorly attenuated by the acoustic liners. Therefore, in design of fans and guide vanes, it is critical to ensure that combinations of B and V are chosen such that the cut-on interaction modes are minimized. To understand the overall acoustic signature of the engine noise, the propagation of these tones must be understood.

Much like the stationary guide-vanes, chevrons are periodic, geometrical features in the flow. It is possible that similar interaction tones may be produced at the exit of engine ducts when chevrons are added, which scatter and alter the propagation of fan tones. While the impact of chevrons on the reduction of jet noise has been considered in detail, to the author's knowledge, the impact of chevrons on the propagation and diffraction of fan tones has not yet been investigated. Therefore, the goal of this work is to understand what impact chevrons have on the structure and intensity of the radiated sound field. At the same time, this is an excellent test case for the 3D LEE DGM methodology developed in this work.

A numerical study is presented which attempts to characterize the impact of the addition of chevrons on the tonal noise radiation from the bypass duct. While chevrons can also be added to the exit of the core duct, their impact on the propagation of tonal noise in the engine core is not considered in this initial investigation. Additionally, due to the high variability of possible engine and chevron designs, the work is split into

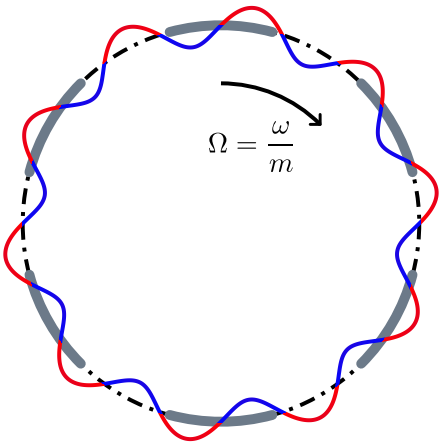

Figure 7.1: High and low pressure fluctuations, colored by red and blue lines, respectively, rotating along the circumference of the duct at an angular velocity, Ω. The chevrons are illustrated by gray line segments.

two parts: a study of simplified chevron geometries without a realistic flow-field, to identify trends, and a study of a more realistic engine and chevron design with a realistic flow-field derived from the TURNEX project [136]. The aim of using a realistic engine geometry and flow-field is to determine whether the trends found by analyzing the simplistic geometries can be generalized to real engine designs. Due to the non-azimuthally symmetric geometries, fully three-dimensional solutions to the time-domain LEE are computed using the nodal discontinuous Galerkin scheme developed in Section 2.4.

This work considers only the radiation of specific modes from the bypass duct, while in a real engine there will be broadband, multi-modal sources in the bypass duct and core, which due to their random nature, the sound field scattered by the chevrons may cancel on average. However, it is assumed that some specific strong tones will still dominate, and therefore it is still important to study deterministic tones.

7.3 The chevron scattering problem

In its most simple form, the scattering problem can be expressed as a rotating pressure field interacting with an azimuthally-periodic chevron geometrical pattern. Figure 7.1 illustrates the scattering problem for a duct with six chevrons and a rotating pressure field with azimuthal mode number, m, and angular frequency, ω. This problem is analogous to the derivation for compressor tonal noise by Tyler and Sofrin [153]. As the pressure field rotates with angular velocity, $\Omega = \frac{\omega}{m}$, each chevron produces a scattering response delayed in azimuthal angle by $\Delta\theta$ and in time by Δt. For a given geometry with D chevrons, where each chevron is numbered as, $d = 1, 2, \ldots, D$, the

q	-3	-2	-1	0	1	2	3
n	-12	-6	0	6	12	18	24

Table 7.1: Scattered field azimuthal modes, n, for a duct with $D = 6$ chevrons and an incident pressure field of azimuthal order, $m = 6$.

angular and time delays are,

$$\Delta\theta = \frac{2\pi d}{D}, \quad \text{and} \quad \Delta t = \frac{2\pi d}{\Omega D} = \frac{2\pi d m}{\omega D}. \tag{7.1}$$

The scattered pressure field due to a single chevron can be written as a summation of Fourier modes,

$$p(\theta, t) = \sum_{n=-\infty}^{\infty} a_n \exp\left[i(\omega t - n\theta)\right]. \tag{7.2}$$

Substituting the angle and time delays into the above expression and summing over all chevrons results in the total scattered field,

$$p(\theta, t) = \sum_{n=-\infty}^{\infty} \sum_{d=1}^{D} a_n \exp\left[i\omega\left(t - \frac{2\pi d m}{\omega D}\right) - in\left(\theta - \frac{2\pi d}{D}\right)\right], \tag{7.3}$$

which can be written as,

$$p(\theta, t) = \sum_{n=-\infty}^{\infty} a_n \exp\left[i(\omega t - n\theta)\right] \sum_{d=1}^{D} \exp\left[i\frac{2\pi d}{D}(n - m)\right]. \tag{7.4}$$

Notice that the second summation is non-zero for only specific values of the scattered mode number, n,

$$\sum_{d=1}^{D} \exp\left[i\frac{2\pi d}{D}(n - m)\right] = \begin{cases} D, & n = qD + m \\ 0, & n \neq qD + m \end{cases}, \tag{7.5}$$

for any integer, q. For scattered mode numbers, $n = qD + m$, there is constructive interference of the scattered field, resulting in a higher pressure amplitude for those mode numbers. Alternatively, for $n \neq qD + m$, there is destructive interference and no scattered field.

A series of scattered mode numbers is tabulated for a duct with six chevrons and an incident pressure field of azimuthal mode number, $m = 6$, in Table 7.1. It is expected that the sound field radiating from the duct will have significant energy in mode $m = 6$, due to the incident mode, of which some of the energy will be scattered into other azimuthal mode orders by the chevrons at the end of the exhaust duct.

7.4 Definition of the numerical methodology

The chevrons at the end of the bypass duct are expected to scatter the acoustic modes radiating from the duct, creating a sound field with azimuthal modal content as described in the previous section. The scattering may also impact the directivity of the sound field, depending on the mode number of the source and its frequency. To identify the impact that chevrons have on the overall radiated sound field, this study should answer the following questions:

- For an incident duct mode with a given azimuthal mode number, what is the azimuthal modal content of the radiated sound field and how is the acoustic power distributed over the modes?
- How is the directivity altered by the addition of chevrons?
- What is the effect of source frequency on the scattered field and the acoustic power?

This section defines a numerical study comparing the radiation of specific modes from unmodified engine geometries, to that of modified geometries with chevrons, to answer the above questions. To reduce the problem complexity, trends are identified by first considering simplified engine geometries, and then these results are compared to a small number of results for a more realistic engine geometry and flow-field. In this section, the geometries are defined and the methodology is developed to compare the results. In the following sections, the results for several incident modes at varying frequency, are presented for both the simplified geometries and the realistic geometry.

7.4.1 Geometry definitions

A difficulty in generalizing the results of this study is the high number of possible chevron and engine geometries. However, it may be possible to consider a simplified geometry that embodies many of the features which are present in the realistic geometry, and identify any trends in the results. With the simplified geometry it is then possible to efficiently obtain results for a number of incident modes and frequencies. A small set of detailed solutions can be computed for a realistic geometry to verify that the trends generalize to the more realistic case.

Two simplified geometries are required, a baseline exhaust to compare the results with, and an exhaust with a number of chevrons. A single, circular duct of radius, R, represents the baseline engine geometry. Triangular chevrons are added to the

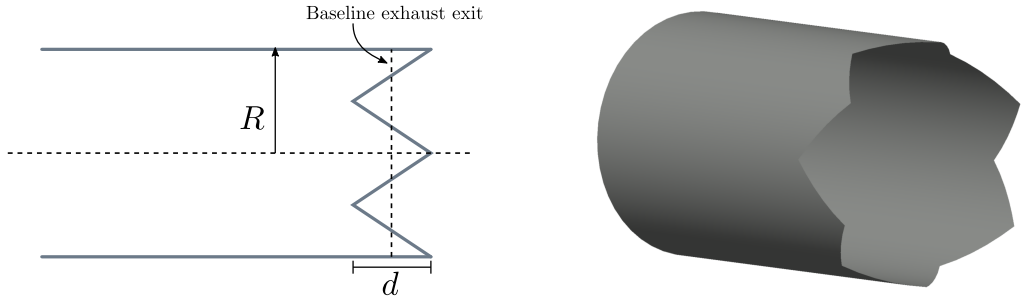

(a) Exhaust geometry definition. (b) 3D exhaust model.

Figure 7.2: The simplified exhaust duct geometry with 6 chevrons.

circumference of the baseline geometry, centered axially on the exit plane of the baseline duct, preserving the surface area of the two geometries. Alternatively, the chevrons could be extended from or cut into the baseline geometry, so this definition can be seen as a balance between the two. Figure 7.2a shows the definition of the chevrons which are parameterized by the exhaust duct radius, R, the number of chevrons, D, and the depth of the chevrons, d. The three-dimensional duct geometry with six chevrons is shown in Figure 7.2b.

For comparison to the simplified geometry results, a realistic engine geometry is created based on the short-cowl TURNEX project experimental geometry [136]. Figure 7.3a shows the three-dimensional baseline geometry, with visible bypass and core ducts. The engine is at experimental model scale, with a bypass duct inner and outer radius of $R_i = 0.0787\,\text{m}$ and $R_o = 0.128\,\text{m}$, respectively. Consistent with the definition of the simplified geometry above, the baseline geometry is modified by adding 18 chevrons shown in Figure 7.3b. The chevron pattern is chosen as blended triangles of axial depth, $d = 0.024\,\text{m}$, placed in a periodical pattern along the circumference of the bypass duct. The baseline exit plane is located halfway between the tip and root of each chevron, resulting in the chevrons extending 0.012 m further downstream than the baseline exit plane. This engine geometry offers a compromise between a simplified exhaust geometry and an overly realistic geometry, such as one containing a pylon, support structures, or non-azimuthally periodic chevrons.

Due to the azimuthal asymmetry of the exhaust duct geometry, the radiated RMS sound field is not necessarily azimuthally symmetric, so care must be taken in defining suitable measurement locations to compare with the baseline directivity. To capture the behavior of the entire sound field radiated from the exhaust duct, the solution is recorded on the spherical surface defined in Figure 7.4. The directivity sphere of radius, R_d, is centered on the exit plane of the baseline duct geometry, intersecting the geometry. The spherical surface is described by a regular mesh over azimuthal and axial angles, θ and ϕ, respectively. Fluctuating quantities are measured along

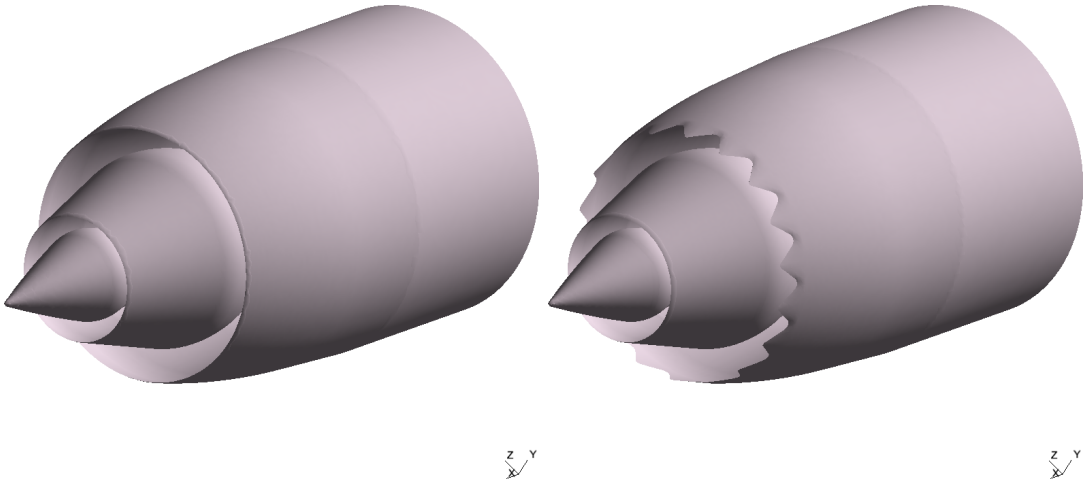

(a) Baseline (b) Modified

Figure 7.3: The baseline TURNEX geometry and the modified geometry with 18 chevrons.

azimuthal angles, $\theta = 0$ to 2π, for a range of axial angles, $\phi = 0$ to π, capturing the directivity through the entire spherical surface.

7.4.2 Azimuthal modal decomposition

In this section, to differentiate between quantities defined in the frequency domain, time domain, and for a specific azimuthal mode, variables defined with a caret, *e.g.* $\{\hat{\cdot}\}$, are defined in the frequency domain, and quantities with a mode label, *e.g.* $\{\cdot\}_m$, are specific azimuthal Fourier mode components. Quantities without the caret and without the mode subscript are defined in the time domain.

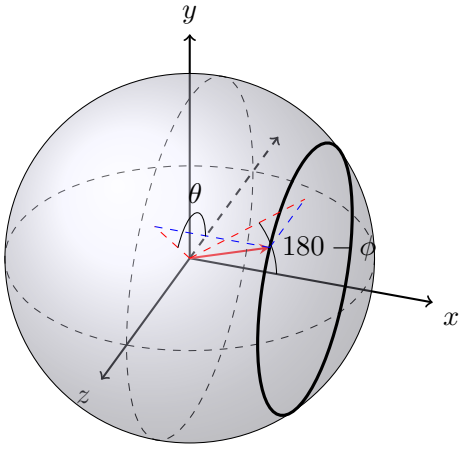

Figure 7.4: Definition of the directivity measurement surface centered on the exit plane of the exhaust duct. The x-direction is defined as the duct axis.

The baseline duct case, with an incident mode of a given azimuthal mode order, m, has a radiated sound field that can be described by a single Fourier mode, m. When chevrons are added, the incident mode is scattered by the chevrons and the radiated sound field is composed of a summation of many azimuthal Fourier modes. To understand clearly the distribution of energy over the scattered modes, the sound field must first be decomposed into azimuthal modes,

$$\hat{p}(r,\theta,\phi) = \sum_{m=-\infty}^{\infty} \hat{p}_m(r,\phi)e^{-im\theta}. \tag{7.6}$$

Based on the definitions of the directivity sphere, Figure 7.4, at each axial angle, $\phi = 0$ to π, a Fourier transform along the θ-direction is performed to obtain the modal amplitudes,

$$\hat{p}_m(r,\phi) = \frac{1}{2\pi}\int_0^{2\pi} \hat{p}(r,\theta,\phi)e^{im\theta}\mathrm{d}\theta. \tag{7.7}$$

7.4.3 Comparison metrics

Acoustic intensity and power

The time-averaged acoustic intensity over the directivity sphere for a single azimuthal mode in a quiescent medium, is defined as,

$$I_m = \frac{1}{2}\mathrm{Re}\left(\hat{p}_m\hat{v}_m^*\right), \tag{7.8}$$

where $\hat{p}_m$ is the pressure on the surface of the sphere, and $\hat{v}_m^*$ is the complex conjugate of the velocity normal to the surface. The acoustic power for a single azimuthal mode order can then be obtained by integrating the intensity over the entire surface of the sphere, S, resulting in,

$$W_m = 2\pi\int_S I_m(\phi)\, r^2 \sin(\phi)\,\mathrm{d}\phi. \tag{7.9}$$

The total power over all azimuthal modes is defined as,

$$W = \int_S I(\theta,\phi)\, r^2 \sin(\phi)\,\mathrm{d}\theta\,\mathrm{d}\phi, \tag{7.10}$$

where $I(\theta,\phi) = \frac{1}{2}\mathrm{Re}\left(\hat{p}\hat{v}^*\right)$ is the total, time-averaged intensity.

Another definition of power that can be used to measure the directivity along the axial angles, ϕ, is defined here as the *distributed power*, computed for each axial angle by

integrating the normal intensity over the azimuthal angles only,

$$W_d = \int_S I(\theta, \phi)\, r \sin(\phi)\, \mathrm{d}\theta. \tag{7.11}$$

The sound power levels reported in this work are all measured in decibels through the expression,

$$\mathrm{PWL} = 10 \log_{10} \left(\frac{W}{W_{\mathrm{ref}}} \right) \mathrm{dB}, \tag{7.12}$$

where W_{ref} is a reference power level. For a non-uniform mean flow, Equation 7.8, does not exactly define the acoustic intensity. For a general, rotational flow, the acoustic intensity is not well-defined. However, the free-stream Mach number for the realistic geometry study is fixed to zero in the static-approach condition, and the directivity sphere is of a larger radius than the exhaust jet, so the acoustic intensity is only inexact where the sphere intersects the jet. In this region, the acoustic intensity is defined based on the irrotational approximation by Goldstein [21] for the instantaneous normal intensity,

$$I = \left(\frac{p}{\rho_\circ} + \vec{v} \cdot \vec{v}_\circ \right) (\rho_\circ \vec{v} + \rho \vec{v}_\circ) \cdot \hat{n}, \tag{7.13}$$

where $\hat{n}$ is the outward-pointing unit normal vector to the sphere. In general nonuniform flows, the energy associated with purely acoustic fluctuations cannot be distinguished from the total perturbation energy, consisting of both acoustic and hydrodynamic fluctuations. Therefore, the above expression for acoustic intensity is only a rough approximation in regions where the base flow is rotational.

Sound pressure level

The sound pressure level is defined as,

$$\mathrm{SPL} = 20 \log_{10} \left(\frac{\hat{p}_{\mathrm{rms}}}{p_{\mathrm{ref}}} \right) \mathrm{dB}, \tag{7.14}$$

where $\hat{p}_{\mathrm{rms}}$ is the root-mean-square sound pressure, and p_{ref} is a reference pressure. The sound pressure level is used in this work to compare the structure of the radiated sound field for the modified geometry to the baseline case. To highlight relative increases or decreases in sound pressure level over the directivity sphere, the ΔSPL is measured, which is the difference between the SPL for the modified geometry and the baseline geometry. Positive values of ΔSPL indicate increases in sound pressure level over the baseline case, and negative values indicate decreases.

7.4.4 Duct mode source

The acoustic source consists of duct modes, defined in Section 6.2.5, which are injected into the exhaust duct inlet and then radiate from the engine into the far-field. The azimuthal mode orders of the source are chosen to ensure that both even and odd multiples of the number of chevrons are considered. To allow comparisons between results computed with different source azimuthal orders to be made, the duct modes are normalized to ensure that the acoustic power through a cross-section of the duct is equal to one. To efficiently compute solutions at a range of frequencies, the band-limited interface source term of Section 6.3.1 is used here.

7.4.5 Flow conditions and CFD results

For the simplified geometries, no mean-flow effects are included in the analysis by setting the free-stream and exhaust Mach numbers to zero. Mean-flow effects are ignored in an attempt to isolate the influence of the geometry alone.

A mean-flow field is included in the study of the realistic geometry to match with the static-approach configuration in the experimental setup of the TURNEX project [42]. The flow conditions consist of a flow through the bypass duct, and a heated core jet, exhausting into a static volume of air. At the inlet of the bypass duct, a Mach number of $M = 0.447$ is prescribed, and a sound speed of $c_\circ = 347.19\,\mathrm{m/s}$ and a density of $\rho_\circ = 1.177\,\mathrm{kg/m^3}$ are recorded. The core stream has a Mach number of $M = 0.223$ and a sound speed and density of $c_\circ = 527.62\,\mathrm{m/s}$ and $\rho_\circ = 0.509\,\mathrm{kg/m^3}$, respectively. For the baseline geometry, the mean flow is obtained through an axisymmetric incompressible steady RANS simulation with the k-ϵ turbulence model. For the modified geometry, a fully-3D incompressible steady RANS flow-field is computed. Figures 7.5a and 7.5b show contours of axial velocity along an x-y slice in the domain. In both flow-fields, the higher velocity bypass jet exits the duct and mixes with the stationary free-stream and the lower velocity core jet, forming shear layers at the duct and core exits which grow rapidly with downstream ($+x$) position. A transverse slice of the exhaust jet at an axial location of $x = 0.15\,\mathrm{m}$ is shown in Figures 7.6a and 7.6b for the baseline and modified geometries, respectively. The chevron pattern on the modified geometry induces a strong non-axisymmetric pattern in the shear layer between the bypass duct and the free-stream.

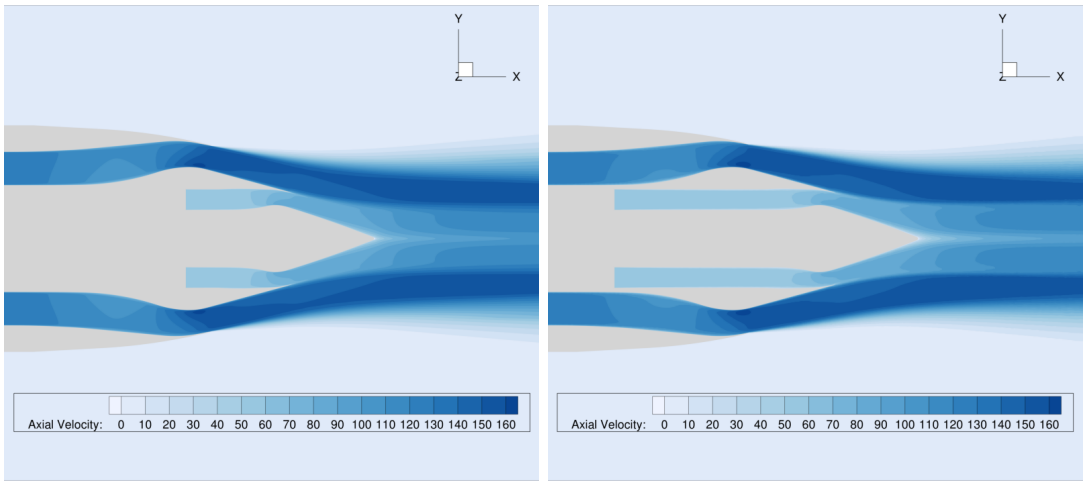

(a) (b)

Figure 7.5: Slices of the mean flow axial velocity field in m/s at $z = 0\,\mathrm{m}$. The baseline flow-field is shown in Figure (a), and the modified geometry flow-field is shown in Figure (b).

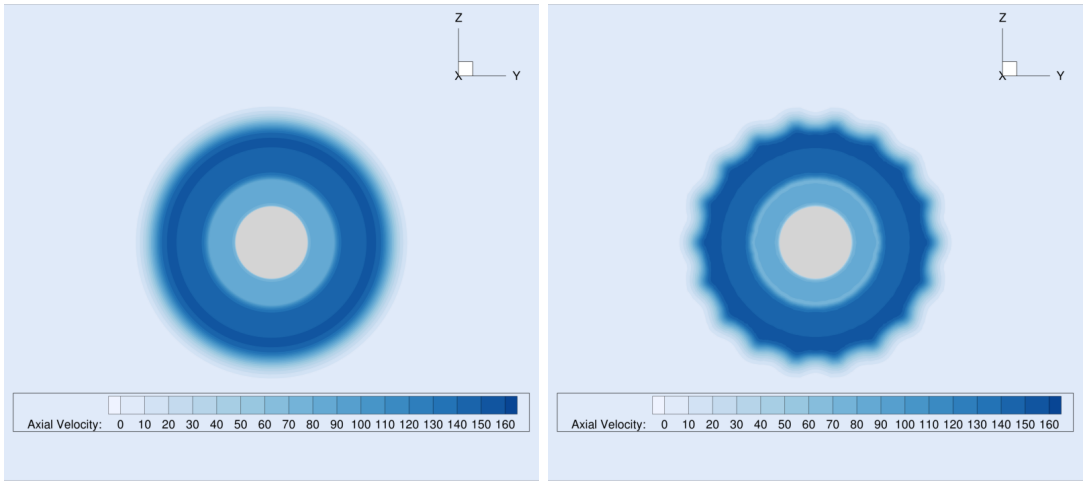

(a) (b)

Figure 7.6: Slices of the mean flow axial velocity field in m/s at $x = 0.15\,\mathrm{m}$. The baseline flow-field is shown in Figure (a), and the modified geometry flow-field is shown in Figure (b).

7.4.6 Selection of the source frequency

The frequency of the source will affect the directivity and the amount of azimuthal scattering by the chevrons. In order to compare results computed with different incident mode numbers and identify any trends, frequencies must be chosen that allow a fair comparison between modes, because for different incident modes, the same degree of scattering is not expected at fixed frequency. Two parameters are chosen to compare results at: an effective wavelength and the mode's cut-on ratio.

A single duct mode has specific radial, axial, and azimuthal wavenumbers, k_r, k_x, and m, respectively. The wavenumber at the circumference of the duct can also be defined as $k_\theta = m/R$. As the mode exits the duct, the effective wavenumber that the chevrons experience is,

$$k_e = \sqrt{k_x^2 + k_\theta^2}. \tag{7.15}$$

The non-dimensional quantity of the effective wavelength over the characteristic size of the chevrons, $\lambda_e/d = 2\pi/(k_e d)$ is used in this chapter when comparing the relative amount of scattering by the chevrons.

The mode's cut-on ratio, using the definition by Sinayoko *et al.* [154], is defined as,

$$\eta = \sqrt{1 - (1 - M^2)k_r^2/k_\circ^2}, \tag{7.16}$$

where $k_\circ = \omega/c_\circ$. The cut-on ratio is a non-dimensional quantity between zero and one, indicating to what extent the mode is propagating axially in the duct. For a plane-wave, the cut-on ratio is equal to one, indicating that the mode is propagating normal to the duct cross-section. Conversely, a mode with a cut-on ratio equal to zero, is not propagating axially, and is directed tangential to the cross-section. As the cut-on ratio gives a measure of the relative amount of axial and radial propagation of the mode, the parameter is important for understanding the directivity on planes tangent to the axis.

7.5 Results for simplified geometries

The chevron exhaust geometry with six chevrons, shown in Figure 7.2b, is compared with the results for the baseline geometry. Two incident modes are considered first, $(6, 0)$ and $(13, 0)$, to understand the impact of the azimuthal mode number. Following the comparison of the two azimuthal modes, the solutions to modes, $(6, 1)$ and $(7, 1)$, are compared, to understand what impact the radial mode has on the directivity.

7.5.1 Computational setup

The nodal discontinuous Galerkin scheme, defined in Section 2.4 is used to solve for the propagation of duct modes through the baseline and chevron exhaust geometries. Hard reflecting wall boundary conditions are imposed on the exhaust duct walls and the buffer zone, of Section 2.4.3, is employed at all outflow regions to reduce spurious reflections. All simulations use a fixed polynomial order of six in every element. The

solution is recorded on the surface of the directivity sphere of radius, $2.5R$, at a sufficient number of points to accurately compute the azimuthal decomposition and to integrate the acoustic intensity.

7.5.2 Results for varying incident mode order and frequency

Mode (6,0)

The first set of results are computed with an incident azimuthal mode number equal to the number of chevrons, and varying the cut-on ratio, η, from 0.5 to 0.85. This case is identical to the analytical problem considered in Section 7.3.

Computing the azimuthal decomposition of the sound field over the directivity sphere, the sound power level for each azimuthal mode of the solution for $\eta = 0.5$ is shown in Figure 7.7a. Red symbols indicate the power in each azimuthal order for the exhaust duct with six chevrons, and the black values indicate the power in each order for the baseline, no chevron exhaust duct. It can be seen that for the baseline case, nearly all the radiated power is concentrated at a single mode order. This is expected due to the azimuthal symmetry of the baseline duct geometry; the source will not be scattered into additional azimuthal modes. Ideally, one would expect a peak only at an azimuthal mode order of six and no energy in any of the other modes. In actuality, the discretized problem introduces errors which can be attributed to inaccuracies in the geometrical description, the approximately non-reflecting outflow boundaries, and the discretization. However, these noise or error levels are 30-40 dB lower than the power levels of the dominant mode. The red and black dashed lines indicate the total power integrated over the whole sphere for the geometry with six and zero chevrons, respectively. As expected, little difference can be seen in the total power levels, and any differences can likely be attributed to slightly increased or decreased back-scattering from the chevrons.

At a higher cut-on ratio of $\eta = 0.85$ in Figure 7.7b, increased azimuthal scattering of the dominant mode can be identified. Peaks at mode numbers, $m = -18, -12, -6, 0, 6, 12,$ and 18, can be clearly seen, agreeing with the predictions given in Table 7.1. The scattering seen when increasing η is due to the smaller λ_e/d seen locally by the chevrons.

In addition to altering the azimuthal structure of the sound field, chevrons are also expected to impact the directivity along the angles, ϕ, defined in Figure 7.4. The distributed power level is now compared between the chevron and baseline results to identify differences in the directivity over ϕ. Again, solutions are compared at cut-on ratios, $\eta = 0.5$ and $\eta = 0.85$. Considering first $\eta = 0.5$ in Figure 7.8a, the red line indicates the results for the duct with chevrons and the black line indicates the results

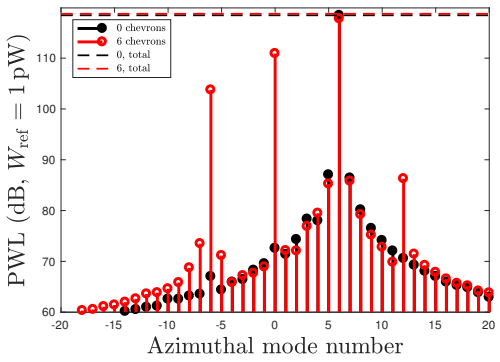

(a) Sound power level, $\eta = 0.5$, $\lambda_e/d = 1.70$

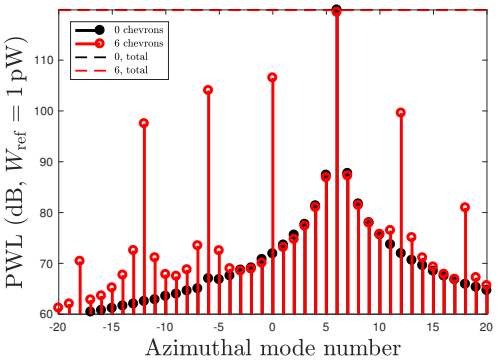

(b) Sound power level, $\eta = 0.85$, $\lambda_e/d = 0.93$

Figure 7.7: Sound power level for each azimuthal mode order for varying η for an incident mode $(6, 0)$.

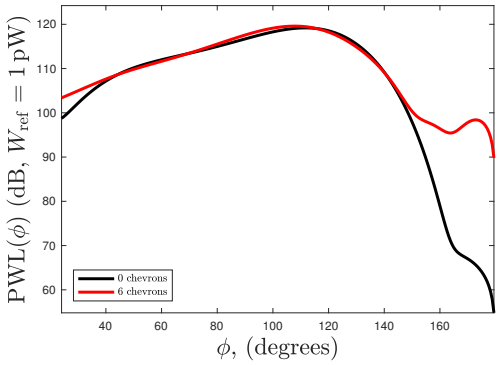

(a) Distributed power level, $\eta = 0.5$, $\lambda_e/d = 1.70$

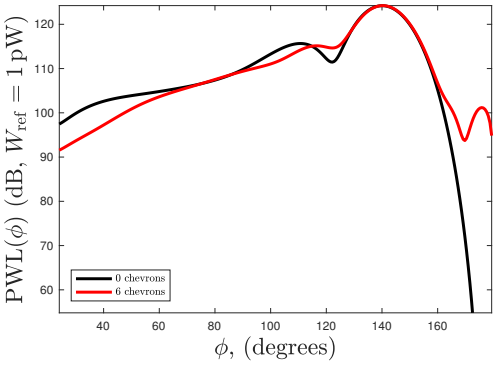

(b) Distributed power level, $\eta = 0.85$, $\lambda_e/d = 0.93$

Figure 7.8: Distributed sound power level for varying η for an incident mode $(6, 0)$.

for the duct without chevrons. For angles, $\phi > 150°$, or near the axis downstream of the duct exit plane, a strong increase in power can be seen relative to the baseline. This could be attributed to the scattering of the incident mode into the plane wave mode, $m = 0$, which is more directed along the axis. For $\phi < 50°$, which is directed in the opposite direction to the propagation of the mode in the duct, a relative increase in power level is identified for the chevron geometry.

Increasing the cut-on ratio to $\eta = 0.85$, again for $\phi > 150°$, substantial increases in power level are seen for the chevron results. For $\phi < 50°$, an opposite behavior to the $\eta = 0.5$ result is seen, showing a decrease in power level relative to the baseline, and for a larger range of angles. Also notable is the slight smoothing of the lobes of the directivity, essentially eliminating some of the local minima and maxima.

To better visualize the strong azimuthal asymmetry of the RMS sound pressure, relative to the baseline case, the ΔSPL is computed over the entire directivity sphere and plotted in Figures 7.9a and 7.9b for $\eta = 0.5$ and $\eta = 0.85$, respectively. The

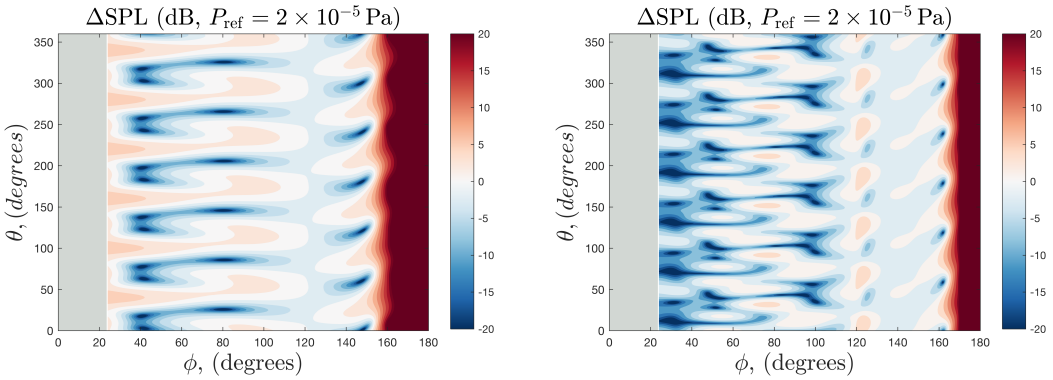

(a) ΔSPL, $\eta = 0.5$, $\lambda_e/d = 1.70$ (b) ΔSPL, $\eta = 0.85$, $\lambda_e/d = 0.93$

Figure 7.9: ΔSPL for varying η for an incident mode $(6, 0)$.

sound pressure level for the baseline case with a single tone as a source, is azimuthally-symmetrical. With the addition of chevrons, this azimuthally-symmetrical sound field is scattered into additional modes, creating a highly non-axisymmetric sound field. Increases in SPL relative to the baseline are shown in red, while decreases are shown in blue. As identified in the azimuthal decomposition, the lower-frequency result has visibly less azimuthal variation than the higher-frequency result. Also, the increases and decreases identified in the distributed power level in the $\phi < 50°$ and $\phi > 150°$ regions are apparent. An azimuthal pattern equal to the number of chevrons is visible for both cut-on ratios.

Mode (13,0)

For mode (6,0), the azimuthal mode number matched the number of chevrons. In contrast, for mode (13,0), the azimuthal mode number is not a multiple of the number of chevrons. The results of this section should show whether or not the azimuthal mode number matching with the number of chevrons impacts the radiated sound field differently. Two cut-on ratios are considered again, $\eta = 0.5$ and $\eta = 0.85$, and the azimuthal decomposition, distributed power level, and ΔSPL are computed over the directivity sphere.

The azimuthal decomposition shown in Figures 7.10a and 7.10b, show peaks in power level at azimuthal modes $n = qD + m$, corresponding to the definition of Section 7.3. With increasing cut-on ratio and effective wavenumber, scattering into azimuthal modes -17 and 19 becomes stronger. The total power levels over all modes remain unchanged.

Figures 7.11a and 7.11b illustrate the distributed power level over ϕ for mode (13,0), for cut-on ratios from $\eta = 0.5$ to $\eta = 0.85$. Similar to the results observed for mode

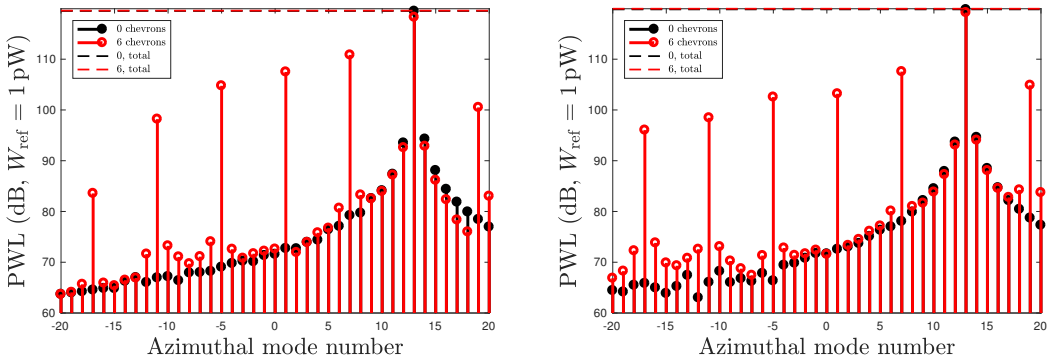

(a) Sound power level, $\eta = 0.5$, $\lambda_e/d = 0.81$ (b) Sound power level, $\eta = 0.85$, $\lambda_e/d = 0.46$

Figure 7.10: Sound power level for each azimuthal mode order for varying η for an incident mode $(13, 0)$.

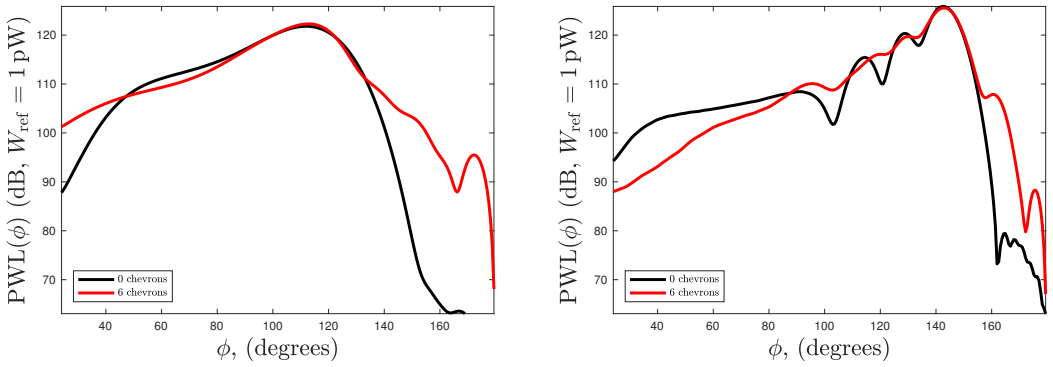

(a) Distributed power level, $\eta = 0.5$, $\lambda_e/d = 0.81$

(b) Distributed power level, $\eta = 0.85$, $\lambda_e/d = 0.46$

Figure 7.11: Distributed sound power level for varying η for an incident mode $(13, 0)$.

(6,0), for both cut-on ratios and $\phi > 140$–$150°$, the power level increases substantially with respect to the baseline power level. The increases downstream near the axis can be attributed to scattering into modes of low azimuthal order, *e.g.* mode 1 in Figures 7.10a and 7.10b. These modes exit the exhaust duct at higher angles (using the convention for ϕ) than the incident mode and thus increase the observed power level over the directivity sphere at large ϕ. For $\phi < 50 - 60°$, an increase in power level is observed for $\eta = 0.5$ and a decrease for $\eta = 0.85$, agreeing with the behavior seen for mode (6,0). Smoothing of the local maxima and minima of the directivity is observed for the $\eta = 0.85$ results.

The ΔSPL for $\eta = 0.5$ and $\eta = 0.85$ is shown in Figures 7.12a and 7.12b, respectively. Comparing the ΔSPL for mode (13,0) to the results for mode (6,0), a more complex azimuthal structure can be seen for mode (13,0) as well as the strong asymmetry in the azimuthal direction. An azimuthal pattern with a multiplicity equal to the number of chevrons can be clearly identified in the plots.

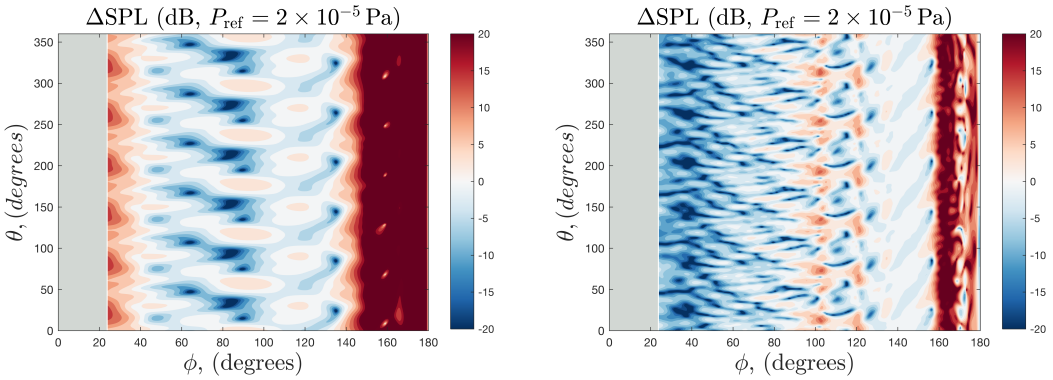

(a) ΔSPL, $\eta = 0.5$, $\lambda_e/d = 0.81$ (b) ΔSPL, $\eta = 0.85$, $\lambda_e/d = 0.46$

Figure 7.12: ΔSPL for varying η for an incident mode $(13, 0)$.

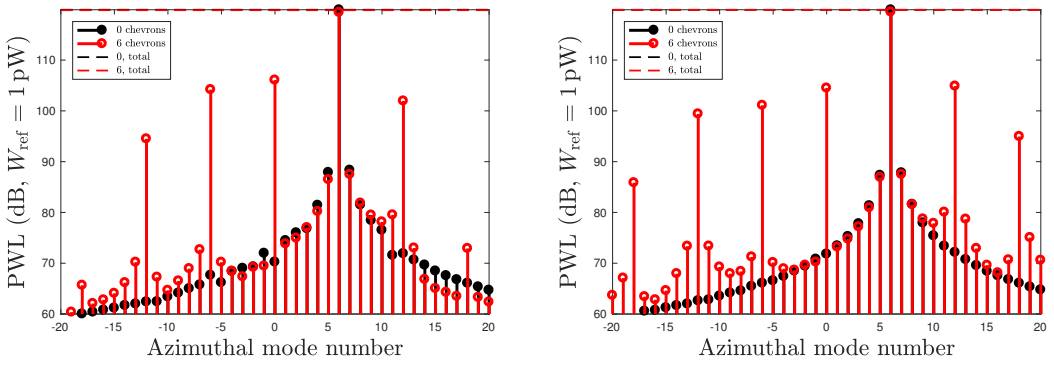

(a) Sound power level, $\eta = 0.5$, $\lambda_e/d = 1.39$ (b) Sound power level, $\eta = 0.72$, $\lambda_e/d = 0.92$

Figure 7.13: Sound power level for each azimuthal mode order for varying η for an incident mode $(6, 1)$.

7.5.3 Impact of the radial mode

The results for mode (6,0) and (13,0) highlighted the changes in directivity and azimuthal scattering produced by the chevrons. Thus far, the impact of the radial mode on the directivity has not yet been investigated. In this section, the radiation of two modes, mode (6,1) and mode (7,1) are solved for and compared with the results for a zeroth-order radial mode.

Mode (6,1)

Two cut-on ratios are selected for comparison, $\eta = 0.5$ and $\eta = 0.72$. Figures 7.13a and 7.13b show the azimuthal modal decomposition of the sound field for each cut-on ratio. The azimuthal modes agree well with the predicted values, $n = qD + m$.

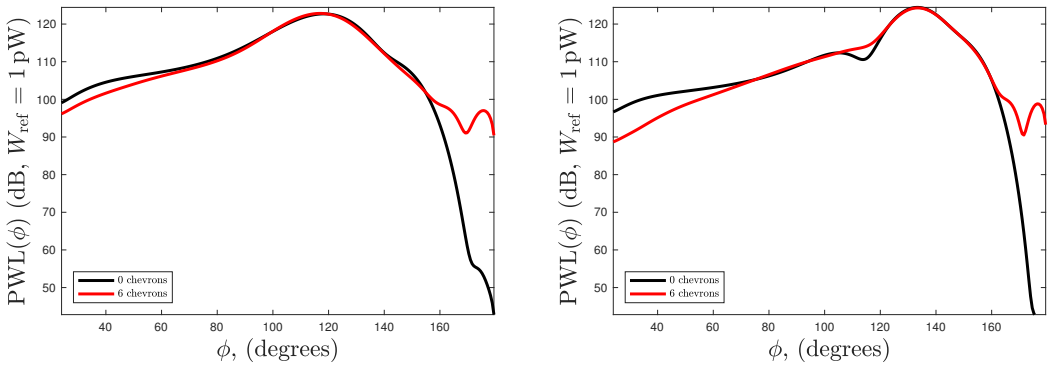

(a) Distributed power level, $\eta = 0.5$, $\lambda_e/d = 1.39$

(b) Distributed power level, $\eta = 0.72$, $\lambda_e/d = 0.92$

Figure 7.14: Distributed sound power level for varying η for an incident mode $(6, 1)$.

The distributed power level for $\eta = 0.5$ is shown in Figure 7.14a. For $\phi > 150°$, the increase in power level near the axis, associated with scattering into the zeroth azimuthal mode is present, agreeing with the results for modes (6,0) and (13,0). In contrast, the expected increase in power level for $\phi < 50$–$60°$ is not observed, and instead, there is a decrease with respect to the baseline. At higher cut-on ratio and lower effective wavelength, Figure 7.14b shows a decrease in power level at lower angles, consistent with the results for the other modes.

Figures 7.15a and 7.15b show the ΔSPL over the directivity sphere for mode (6,1). Decreases in SPL can be seen for $\phi < 50 - 60°$ and increases for $\phi > 150°$. Also present is the azimuthal structure of periodicity equal to the number of chevrons, found for mode (6,0) and mode (13,0).

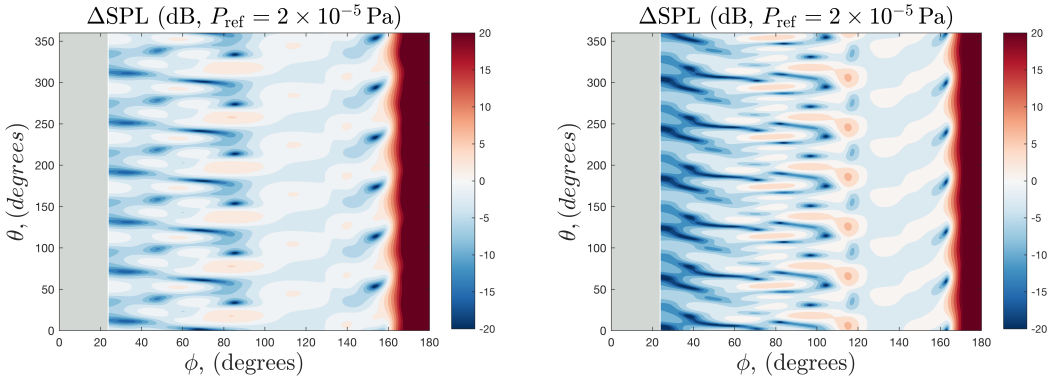

(a) ΔSPL, $\eta = 0.5$, $\lambda_e/d = 1.39$

(b) ΔSPL, $\eta = 0.72$, $\lambda_e/d = 0.92$

Figure 7.15: ΔSPL for varying η for an incident mode $(6, 1)$.

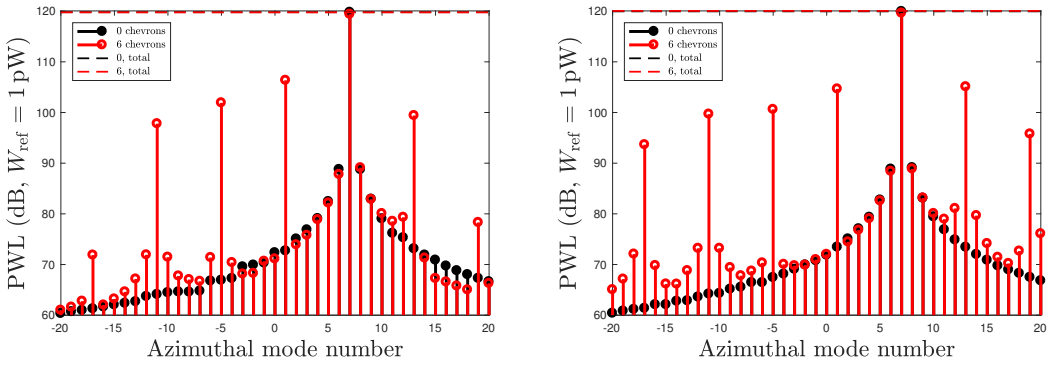

(a) Sound power level, $\eta = 0.5$, $\lambda_e/d = 1.23$ (b) Sound power level, $\eta = 0.72$, $\lambda_e/d = 0.82$

Figure 7.16: Sound power level for each azimuthal mode order for varying η for an incident mode $(7, 1)$.

Mode (7,1)

The above analysis is repeated again for mode (7,1) in which the azimuthal mode number is not a multiple of the number of chevrons. Again, two cut-on ratios of $\eta = 0.5$ and $\eta = 0.72$ are considered. Figures 7.16a and 7.16b show the azimuthal decomposition of the sound field, with the expected peaks at mode numbers corresponding to $n = qD + m$. The distributed power level for both cut-on ratios is given in Figures 7.17a and 7.17b. Agreeing with the results for other modes, for $\phi > 150°$ an increase in acoustic power level relative to the baseline, is seen for both cut-on ratios. For $\phi < 60°$, a decrease in power level is visible for both cut-on ratios, and no increase is visible for $\eta = 0.5$. Also agreeing with the results for other modes, Figures 7.18a and 7.18b show the ΔSPL with increases and decreases in SPL relative to the baseline and a periodicity equal to the number of chevrons.

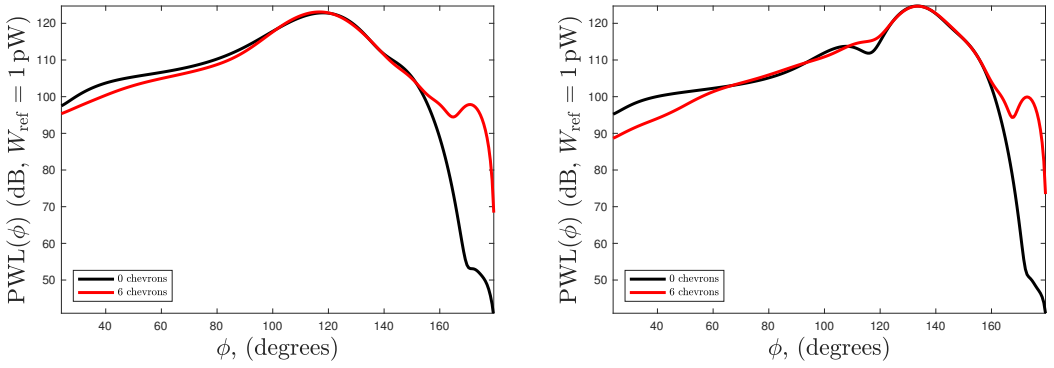

(a) Distributed power level, $\eta = 0.5$, $\lambda_e/d = 1.23$

(b) Distributed power level, $\eta = 0.72$, $\lambda_e/d = 0.82$

Figure 7.17: Distributed sound power level for varying η for an incident mode $(7, 1)$.

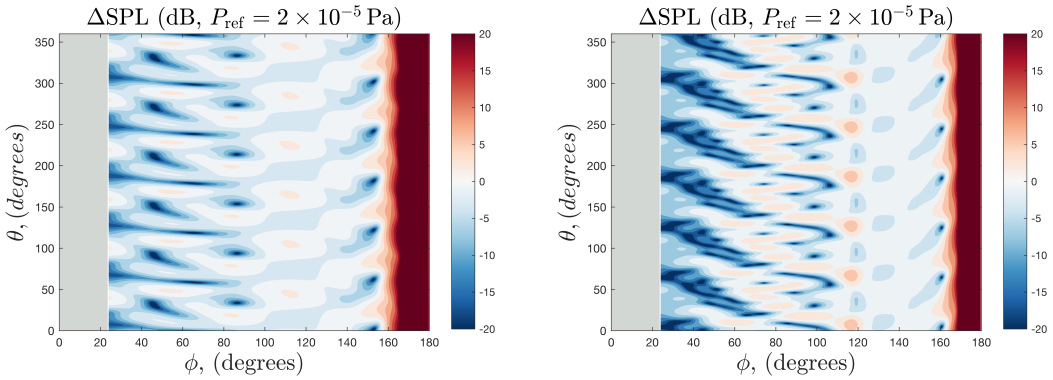

(a) ΔSPL, $\eta = 0.5$, $\lambda_e/d = 1.23$ (b) ΔSPL, $\eta = 0.72$, $\lambda_e/d = 0.82$

Figure 7.18: ΔSPL for varying η for an incident mode $(7, 1)$.

Additional solutions

Solutions for additional modes are computed for fixed λ_e/d, λ_x/d, and η, in Table 7.3. The total power level calculations are condensed into four values computed over the directivity surface, $W_m^{0\text{C}} - W_m^{6\text{C}}$, in dB, which is the difference in radiated power level at the azimuthal order corresponding to the incident azimuthal mode number, m, between the baseline and chevron geometries. The difference in radiated power level of the m-th azimuthal component with all scattered modes is denoted, $W_m^{6\text{C}} - W_{sct}^{6\text{C}}$, for the six chevron geometry. Finally, the total power over all azimuthal orders is denoted as $W_{all}^{0\text{C}}$, for the baseline, zero-chevron geometry, and $W_{all}^{6\text{C}}$, for the six chevron geometry. The small differences in total power can likely be attributed to some reflections at the exit plane of the exhaust duct, traveling back towards the source-plane.

7.5.4 Summary of simplified geometry results

This section computed solutions to acoustic mode radiation from simplified exhaust duct geometries, comparing results for a duct with and without chevrons. Four different incident modes were considered in detail, at varying frequency described by the cut-on ratio and the effective wavelength.

For all modes, the azimuthal modal content in the radiated sound field matched well with the analytical predictions in Section 7.3. For incident modes with zeroth-order radial modes and at low cut-on ratio, increases in distributed power level were found at low angles, ϕ, corresponding to the definition in Figure 7.4. In contrast, at higher cut-on ratio or effective wavelength, decreases were found for low ϕ. The differences between the low and high frequency results can likely be attributed to the difference in the direction of the acoustic energy, varying with cut-on ratio. For cut-on ratios closer

to one, the acoustic energy travels more axially, so it is expected that the acoustic pressure at small ϕ, will be decreased compared to lower cut-on ratios. Incident duct modes with a radial mode were observed to have no increases in distributed power level at small ϕ.

For all modes, increases in sound power level were observed near the axis, for large ϕ angles. These increases can be attributed to scattering of the incident mode into lower-azimuthal mode orders, which are more cut-on and radiate closer to the axis. Therefore the decreases in sound power level at low ϕ may be caused by redistribution of the incident mode power into lower azimuthal orders, which are more cut-on, causing increases near the axis.

7.6 Results for a realistic geometry

The purpose of this section is to determine whether the trends found in the simplified geometry study in the previous section generalize to a more realistic geometry and flow-field. The geometries are based on the experimental-scale TURNEX geometry shown in Figure 7.3a and the modified geometry with eighteen chevrons shown in Figure 7.3b. The flow-field is defined based on the static-approach experimental conditions, and the CFD results for both geometries are discussed in Section 7.4.5. While the geometry has a core and bypass duct, only the radiation of an acoustic mode from the bypass duct is considered in this work.

7.6.1 Computational setup

To prescribe the acoustic mode in the bypass duct, the band-limited interface source term of Section 6.3.1 is used so that only a single computation is required to obtain the frequency response. The mean flow-field in each element is mapped from the CFD mesh and the thin boundary layers are removed using the tools developed in Section 5.2. Due to the highly non-uniform mean velocity field, aliasing-driven instabilities, discussed in Chapter 4, are expected to occur. These instabilities are controlled by application of a periodic filter to the solution DOF, which is discussed in Section 4.5.4.

Aeroacoustic computational domain

The acoustic computational domain is a spherical shape of radius $r = 0.5\,\mathrm{m}$, centered at $(0.0, 0.0, 0.0)$, with buffer zones at the outflow region, and at the bypass duct and core inlets. The mesh, shown in Figure 7.19a is comprised of approximately 690,000

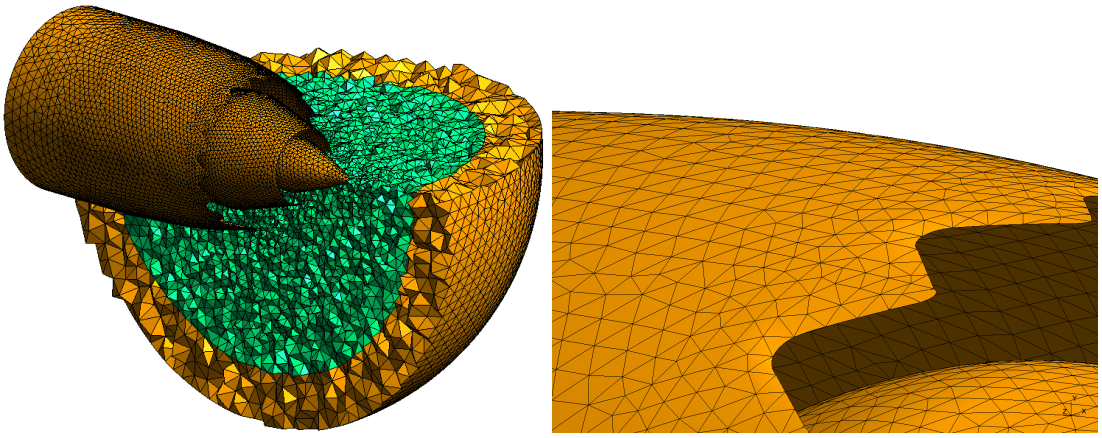

(a) (b)

Figure 7.19: Left: Section of the aeroacoustic mesh for the modified TURNEX geometry. The buffer zone is colored by yellow elements. Right: near-wall region for the chevron geometry mesh, showing curved surface elements.

tetrahedral elements, which are allowed to be curved to accurately represent the engine geometry. Each DG element has a fixed polynomial order of six, resulting in approximately 290 million degrees of freedom for the total problem. The mesh density and polynomial order are chosen based on the maximum wavenumber of the duct mode source.

7.6.2 Results for mode $(10, 0)$ and varying source frequency

A single tone, $(10, 0)$, is prescribed in the bypass duct inlet with no source prescribed in the core. Computations are carried out with an incident mode frequency corresponding to an effective wavelength of $\lambda_e/d = 2$, to $\lambda_e/d = 1$ and amplitudes are normalized by the acoustic power in the bypass duct inlet. This frequency range is chosen to highlight differences in the radiated sound field for low and high scattering. All of the results are recorded over the surface of a measurement sphere of radius 0.3 m, centered at $(0.0, 0.0, 0.0)$, which is the exit plane of the baseline bypass duct. Instantaneous contours of π' on an x–y slice of the domain are shown at two times, $t = 0.001\,\mathrm{s}$ and $t = 0.002\,\mathrm{s}$, in Figures 7.20a and 7.20b, respectively. The wave-packet acoustic disturbance is clearly visible, including the reflections at the end of the bypass and core ducts. It is important to note that instabilities did not pollute the acoustic solution. This can be attributed to the rapidly-growing shear-layer and a frequency range of the band-limited source that is high enough to not excite the shear layer at its most unstable frequency. In addition, periodic filtering of solution DOF is enough to eliminate aliasing-driven instabilities for the time-scales required to propagate the wave-packet past the monitor points.

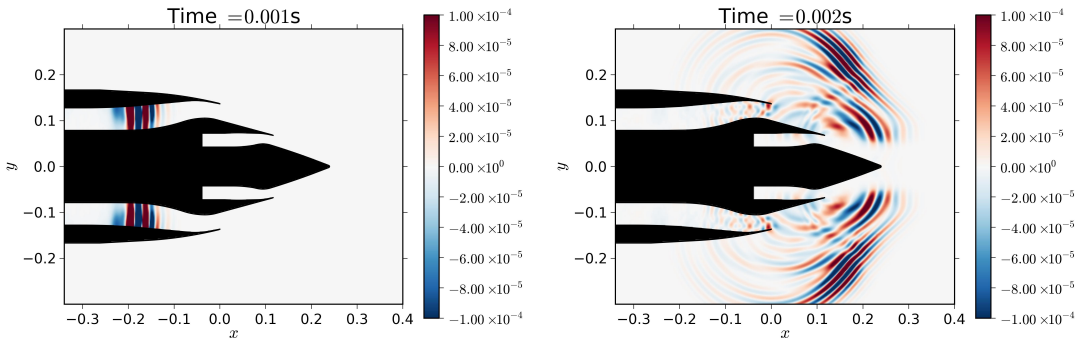

(a) $t = 0.001\,\mathrm{s}$ (b) $t = 0.002\,\mathrm{s}$

Figure 7.20: Instantaneous contours of π' on an x–y slice of the computational domain at times $t = 0.001\,\mathrm{s}$ and $t = 0.002\,\mathrm{s}$.

Figure 7.21 shows the sound power level over the measurement sphere for each azimuthal mode for the two source frequencies. For $\lambda_e/d = 2$, the primary $m = 10$ mode along with scattered modes, $m = -26, -8, 28$ are clearly identified. Increasing the frequency, the $\lambda_e/d = 1$ results show additional scattered modes at $m = -44$ and $m = 46$, which agree with the predictions given in Section 7.3.

The distributed power level over the range of angles, ϕ, is shown in Figure 7.22 for both source frequencies. It is clear that for the lower frequency case, $\lambda_e/d = 2$, the distributed power level for the modified geometry matches the baseline results over most of the angles. Around $\phi = 90°$, an increase relative to the baseline is observed. This behavior may be similar to the smoothing of the directivity observed in the results in Section 7.5. The lack of deviation from the baseline results over the rest of the angles and the fewer number of azimuthal scattered modes in Figure 7.21a, indicate that the acoustic wavelength is too large for the chevrons to cause a large scattering effect. In

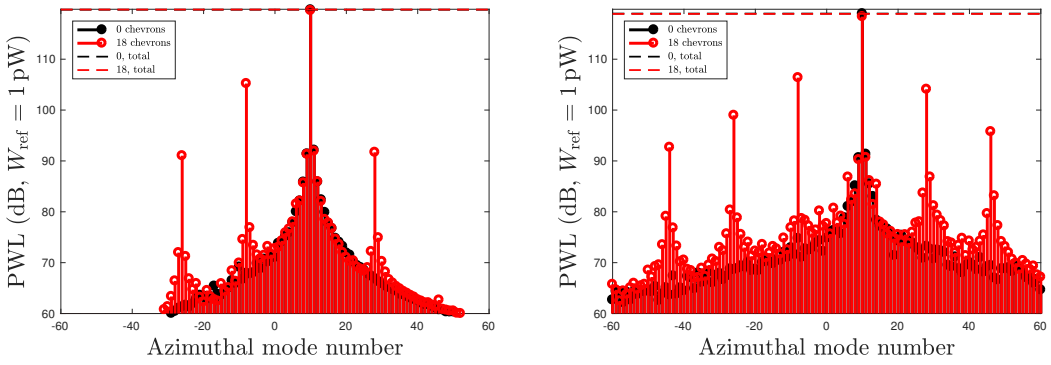

(a) $\lambda_e/d = 2$ (b) $\lambda_e/d = 1$

Figure 7.21: Sound power level over the measurement sphere for each azimuthal mode order for an incident mode $(10, 0)$.

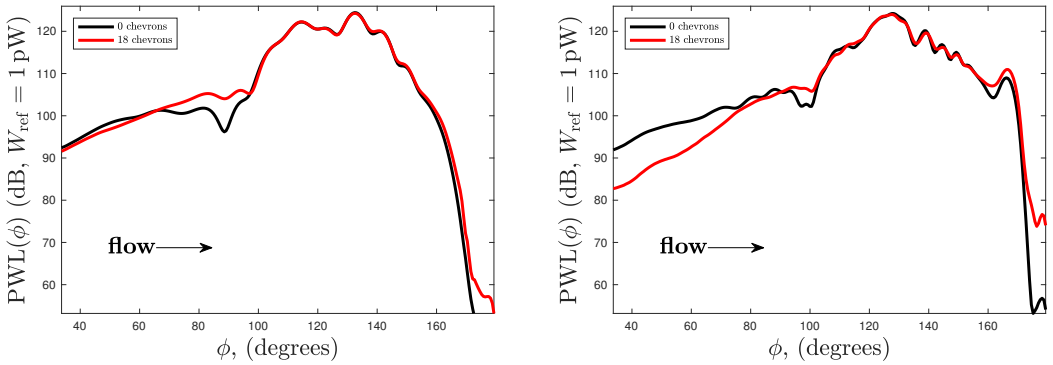

(a) $\lambda_e/d = 2$ (b) $\lambda_e/d = 1$

Figure 7.22: Distributed power level over the range of axial angles, ϕ, for an incident mode $(10, 0)$.

comparison, at higher frequency, $\lambda_e/d = 1$, strong decreases in the distributed power level are seen for angles $\phi < 80°$, matching the behavior observed for the simplified geometries at higher frequency or cut-on ratio. At $\phi > 160°$, while there are increases in sound power level, they are not as strong as what was observed for the simplified geometries. This could be attributed to the lack of scattering into low azimuthal mode orders, which would radiate more axially, and the presence of the engine hub.

The apparent differences in the directivity can be clearly seen in the ΔSPL plots in Figures 7.23a and 7.23b for $\lambda_e/d = 2$ and $\lambda_e/d = 1$, respectively. At $\phi < 80°$ and $\lambda_e/d = 1$, the strong decreases seen in the power level are observed in the ΔSPL plot. Along the azimuthal direction for both frequencies, a periodic structure can be observed, with a number of repetitions equal to the number of chevrons, which is also apparent in the results for the simplified geometries.

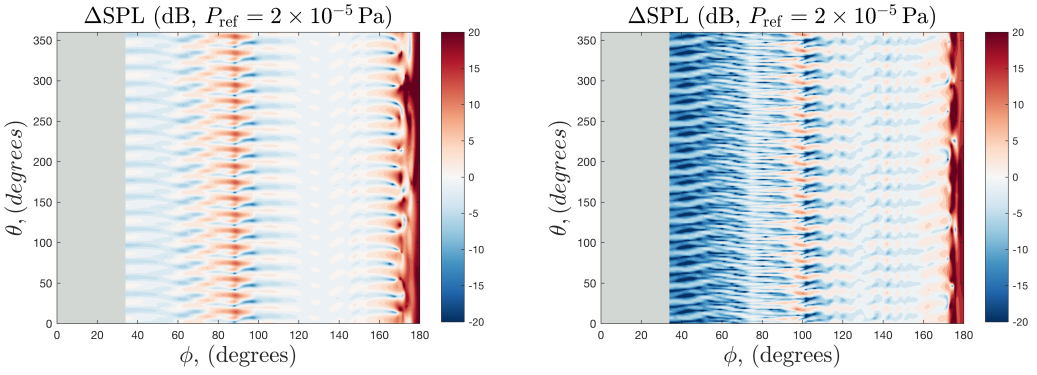

(a) $\lambda_e/d = 2$ (b) $\lambda_e/d = 1$

Figure 7.23: ΔSPL over the measurement sphere for an incident mode $(10, 0)$.

7.6.3 Computational cost

Numerical solutions to the detailed geometry study were computed using the University of Southampton Iridis 4 cluster. Each node of Iridis has two 2.6 GHz. Sandy Bridge processors with a total of 16 cores and 64 GB of RAM. The results for both geometries were obtained using four nodes with a total of 64 cores. Due to the distinct geometries, the meshes, and therefore the total computational cost to obtain the final solutions, were different. The total number of quadrature-free and standard tetrahedral elements are listed in Table 7.2. Notice that the number of standard elements for the mesh of the modified geometry is much larger than that of the baseline mesh. This can be attributed to the more complex geometry of the chevrons, shown in Figure 7.19b, requiring more elements to discretize it.

A lower-bound for the total memory usage for each case is estimated in Table 7.2, by counting the number of double precision variables stored during the calculation for the quadrature-free and standard elements. Even though there are far fewer standard elements, the memory for storing them is the same or greater than for the quadrature-free elements, since the element matrices must be stored. Comparing the total memory usage over four nodes to the available memory of 64 GB. per node, the total storage is not a limiting factor in these calculations.

Counting the total number of floating point operations per stage of a single time-step and then multiplying by the total number of time-steps and stages, an estimation of the floating point operations per second (FLOP/s) is given in Table 7.2 for each case in giga-flop (GFLOP). These estimates do not include the additional cost of damping the solution in the buffer zone, filtering the solution, interpolating the solution to curved faces, or interpolating the solution at each of the measurement locations. For the 2.6 GHz. Sandy Bridge processors, a theoretical per-core peak efficiency can be estimated as, 2.6 GHz. $\times 8$ double-precision ops/s $= 20.8$ GFLOP/s [155]. While these estimates show the DGM implementation achieving approximately 30% of the theoretical peak-efficiency of the cluster, it is important to note that the theoretical estimates assume an equal number of additions and multiplications per cycle, and of course do not include the latency associated with communication in solving the distributed problem.

One potential area of inefficiency is the frequency of computing the solution at the measurement locations and then writing the data to disk. At each sampling time, pre-computed interpolation coefficients in each element that contains a measurement location, are used to interpolate the solution. For sampling a large portion of the computational domain, the cost of writing to disk could become excessive. It may be more efficient to store this data in memory and then periodically write several samples to disk at once.

	Baseline	Modified
N_e Standard	56787	74026
N_e Quad-free	598839	614730
Polynomial order	6	6
Time steps	12000	13000
Cores	64	64
Wall time (Min.)	641.2	721.8
Est. Mem. Quad-free (GB.)	16.9	17.3
Est. Mem. Standard (GB.)	16.5	21.5
Est. Mem. Total (GB.)	33.4	38.8
Est. GFLOP/s	412	420

Table 7.2: Computational cost of the detailed geometry study.

7.7 Conclusions

This study attempted to understand to what extent the addition of chevrons to the exit of the bypass duct impacts the propagation of tones, in terms of changes to the radiated power level and directivity. A simplified analytical expression framed the problem in terms of interaction tones, analogous to fan-guide-vane or rotor-stator interaction noise. Fully three-dimensional computations were performed for simplified engine geometries in an attempt to determine any trends observed for varying incident mode numbers and frequency.

The results for the simplified geometry study indicated that the chevrons scatter the source acoustic mode into predictable azimuthal modes with the intensity of scattering increasing with increasing source frequency. The total sound power integrated over the directivity surface, associated with the azimuthal mode of the source, is not substantially changed by the addition of chevrons. However, when considering changes to the directivity, there can be strong increases or decreases in the intensity and sound pressure levels, dependent on the frequency of the source. For a low cut-on ratio and a zeroth-order radial mode, increases in sound power level, relative to the baseline geometry, are observed for low angles, ϕ. At higher cut-on ratio or effective wavenumber, the opposite effect is observed, with strong decreases in the sound power level. Downstream toward the axis, or high values of ϕ, strong increases in sound power level are observed, and are likely a result of the incident mode scattering into low azimuthal mode orders which are more cut-on and radiate closer to the axis. Overall, at higher cut-on ratio or effective wavenumber, the local minima or maxima in the distributed power level appear less pronounced with the addition of chevrons.

Following the simplified geometry study, the experimental geometry of the TURNEX project was used to determine if the results for the simplified geometries can generalize

to more realistic configurations. Eighteen, triangular shaped chevrons were added to the exit of the bypass duct. A realistic mean flow-field, based on the static approach experimental conditions, was included in the simulations. The radiation of a single tone over a range of source frequencies for the modified geometry was compared to the results for the baseline, no chevron geometry. Many of the features observed for the simplified geometries were present, except for the strong increases in sound power level along the axis, or high ϕ. It is assumed that the lack of strong increases along the axis are caused by the lack of scattering of the incident mode into low azimuthal mode orders, which are more cut-on.

While this study considered only single tones, a more complete picture of the scattering by the chevrons could be obtained by investigating broad-band, multi-modal sources. However, it is assumed that with broad-band sound sources in the duct, some strong tones will still exist, making the results of the present study still applicable to the more realistic case. Additionally, only radiation from the bypass duct was studied, however chevrons can also be added to the core. Therefore future work can investigate both broad-band, multi-modal sources, as well as radiation from the core with chevrons added. Additionally, for installed engines, the bypass duct is typically not exactly annular, and includes bifurcations in the duct associated with the placement of the pylon and the engine support structure. These bifurcations will likely alter the scattering and radiation of the incident mode and should be included in more detailed future studies.

m	n	ω	k_e	k_x	k_t	k_r	η	λ_x/d	λ_e/d	$W_m^{0C} - W_m^{6C}$	$W_m^{6C} - W_{sct}^{6C}$	W_{all}^{0C}	W_{all}^{6C}
6	0	9.79	8.69	6.28	6.00	7.50	0.64	2.00	1.45	0.34	8.40	119.63	119.85
6	0	14.63	13.93	12.57	6.00	7.50	0.86	1.00	0.90	0.49	9.52	119.92	119.87
6	1	13.31	8.69	6.28	6.00	11.73	0.47	2.00	1.45	0.42	9.14	119.89	119.95
6	1	17.19	13.93	12.57	6.00	11.73	0.73	1.00	0.90	0.36	9.97	119.93	119.97
7	0	10.63	9.41	6.28	7.00	8.58	0.59	2.00	1.34	0.55	6.81	119.50	119.75
7	0	15.21	14.38	12.57	7.00	8.58	0.83	1.00	0.87	0.48	9.56	119.86	119.81
12	0	15.23	13.55	6.28	12.00	13.88	0.41	2.00	0.93	0.64	4.66	118.84	119.43
12	0	18.72	17.38	12.57	12.00	13.88	0.67	1.00	0.72	0.63	7.66	119.86	119.87
13	0	16.20	14.44	6.28	13.00	14.93	0.39	2.00	0.87	0.68	3.66	118.66	119.47
13	0	19.51	18.08	12.57	13.00	14.93	0.64	1.00	0.70	0.86	6.64	119.92	119.86
6	0	17.35	16.76	15.64	6.00	7.50	0.90	0.80	0.75	0.45	8.74	119.89	119.96
6	0	25.53	25.13	24.41	6.00	7.50	0.96	0.51	0.50	0.35	9.43	119.88	119.98
6	1	19.56	16.76	15.64	6.00	11.73	0.80	0.80	0.75	0.25	11.14	119.90	119.95
6	1	27.08	25.13	24.41	6.00	11.73	0.90	0.51	0.50	0.23	12.22	119.95	119.95
7	0	17.47	16.76	15.22	7.00	8.58	0.87	0.83	0.75	0.38	8.81	119.78	119.91
7	0	25.62	25.13	24.14	7.00	8.58	0.94	0.52	0.50	0.46	9.22	119.93	119.94
12	0	18.15	16.76	11.69	12.00	13.88	0.64	1.07	0.75	0.81	6.69	119.92	119.91
12	0	26.08	25.13	22.08	12.00	13.88	0.85	0.57	0.50	0.67	7.43	119.94	119.94
13	0	18.29	16.76	10.57	13.00	14.93	0.58	1.19	0.75	1.07	5.75	119.77	119.67
13	0	26.18	25.13	21.51	13.00	14.93	0.82	0.58	0.50	0.69	7.10	119.89	119.92
6	0	8.66	7.40	4.33	6.00	7.50	0.50	2.90	1.70	0.65	5.99	118.43	118.74
6	0	14.24	13.51	12.10	6.00	7.50	0.85	1.04	0.93	0.45	9.88	119.89	119.84
6	1	13.55	9.05	6.78	6.00	11.73	0.50	1.85	1.39	0.50	9.81	119.91	119.82
6	1	17.04	13.73	12.35	6.00	11.73	0.72	1.02	0.92	0.41	9.96	119.90	119.89
7	1	14.93	10.23	7.47	7.00	12.93	0.50	1.68	1.23	0.39	10.39	119.80	119.77
7	1	18.78	15.31	13.61	7.00	12.93	0.72	0.92	0.82	0.31	9.86	119.96	120.05
13	0	17.24	15.60	8.62	13.00	14.93	0.50	1.46	0.81	1.18	4.58	119.50	119.56
13	0	28.34	27.37	24.09	13.00	14.93	0.85	0.52	0.46	0.58	7.19	119.82	119.94

Table 7.3: Results of the simplified geometry study for a range of modes and for fixed λ_x/d, λ_e/d, and η. The angular frequencies, ω, are given in rad/s. The wavenumbers, $k_{\{\cdot\}}$ are in rad/m. All power levels, W, are given in dB.

Chapter 8

Conclusions and Future Applications

This project further developed the time-domain nodal discontinuous Galerkin method (DGM) for application to turbofan exhaust noise propagation. Several key challenges were defined, namely, *i*) the choice of discretization parameters for optimal accuracy and computational cost, *ii*) the stability of solutions when the flow-field is highly nonuniform, *iii*) the interfacing of the RANS CFD data and the acoustic propagation solver, and, *iv*) the accurate and efficient specification of source terms in the numerical model. In addressing these challenges, several original contributions were made and are described in the following section.

The numerical results presented in this work were computed by a nodal discontinuous Galerkin scheme, solving the three-dimensional linearized Euler equations (LEE), implemented over the course of this work. This solver was developed with the intent of solving industrial scale aeroacoustic propagation applications, permitting curved elements, arbitrary-shaped acoustic-damping outflow regions, CFD to acoustic mesh mapping, interface and band-limited source terms, an efficient data structure to take advantage of BLAS [93] optimized matrix products, and parallelization to utilize the University of Southampton Iridis 4 cluster.

8.1 Summary of contributions

Accuracy and computational cost analysis

A two-dimensional dispersion analysis of the time-domain nodal DGM was presented, and used to study the impact of discretization parameters on the accuracy and computational cost of solutions. The linearized Euler equations with a uniform mean flow-field were discretized, rather than the more commonly considered model advection equations. To the author's knowledge, this was the first dispersion analysis of the complete LEE system. This allowed the study of the dispersion, dissipation, and L^2 solution error with varying mesh size and polynomial order, for the acoustic, entropy, and hydrodynamic solution modes. It was determined that the convergence of the entropy and hydrodynamic mode error followed a similar behavior to the convergence of the acoustic mode. To understand the impact of the wave propagation directions relative to the mesh and the mean flow, an error anisotropy study was performed, and the best and worst case propagation directions were identified over the structured, triangularized mesh. A fully-discrete dispersion analysis characterized the impact of the explicit time integration scheme and the choice of time-step. This was also used to estimate the computational effort required for varying wave propagation distances, showing the importance of high temporal accuracy for long distance wave propagation.

Aliasing in solutions to the LEE

The formation and growth of aliasing-driven instabilities in DG solutions to the LEE were investigated. A new, two-dimensional dispersion analysis of the DGM for the LEE was developed, supporting a nonuniform mean flow-field. Using an analytical solution to compressible parallel shear flow instability, the dispersion analysis correctly predicted the growth rates of the instability with varying Mach number, to verify the method. The fully-discrete dispersion analysis considered the effect of the polynomial order, filtering, flux function, flow-field, and time integration on the strength of the aliasing-driven instabilities. With an upwind flux, the predicted growth rates of the instabilities increase with increasing order and fixed mesh size. Using the Lax-Friedrichs flux markedly improved the stability over the exact upwind flux. Periodic filtering of the solution coefficients were shown to nearly eliminate the aliasing instabilities with the correct choice of filter parameters. The flow-field supporting unstable solution modes was found to be more susceptible to aliasing instability than one that does not support unstable solution modes with a similar non-uniformity. This work differed from past work that consisted of theoretical estimates and numerical experiments, in that both the growth and advection behavior of aliasing was identified including the

effect of the discretization. Furthermore, this work considered aliasing in unstable solutions to the LEE which arise in applications with sheared mean-velocity fields.

Representation and mapping of the mean flow-field

An analytical solution to one-dimensional acoustic wave propagation through a temperature non-uniformity, was derived and compared to numerical solutions with varying mean variable representation accuracy. It was found that, similar to errors in geometrical representation, the error in the representation of the mean variables leads to degraded solution accuracy. If the polynomial order of the mean variables in each element is less than the order of the solution, then convergence of the solution error with polynomial order will be severely degraded. Following the one-dimensional study, a two-dimensional study of acoustic wave propagation through a mean flow vortex was studied qualitatively, illustrating the degradation of solution accuracy with an inaccurate representation of the mean flow-field. To the author's knowledge this is the first study of the impact of the mean flow representation error on the acoustic solution in a hybrid aeroacoustics approach.

Using moving-least-squares approximations, a strategy for mapping CFD data to the solution interpolation nodes on the DG mesh was developed. Past methods involved linear interpolation, which does not enforce smoothness and requires a triangulation of the CFD data, or solution of a global least-squares problem, which is computationally costly and typically requires first linearly interpolating to a secondary flow-mesh. By using a local approach, the method scales well, with each processor needing to load only a small subset of the CFD data to perform the fit. Smoothness in the mapping can be enforced through altering the support radius, allowing control over fine-scale flow features that are unresolved on the DG mesh. To improve the mapping regularity of RANS solutions containing thin boundary layers, a boundary layer truncation process was developed, smoothly removing the high mean velocity gradient regions adjacent to the geometry. A Poisson-based normal wall distance estimate was used for locating the near wall regions for an arbitrary, three-dimensional geometry. While truncation of the boundary layer has been considered before, past methods considered only a low-order representation of the mean flow and were less general for complex geometries.

Specification of source terms

A new method of introducing source terms into the discrete LEE model was developed, using the flux function at the element interfaces. By defining a source-plane at

an arbitrary location in the computational domain, acoustic, entropy, and hydrodynamic source terms can be introduced using only the values of the flux at the plane. Traditionally, certain source terms, such as duct-modes, were injected into the domain through buffer-zones, requiring a buffer-zone that is accurate at both damping and generating waves, or by application of a spatial windowing function that must be compact enough relative to the changing geometry and mean flow-field. The interface source terms avoid this complexity. The method was verified for the advection of entropy and vorticity sources in a three-dimensional domain, and the propagation of acoustic modes in a cylindrical duct. For turbofan exhaust noise applications, a band-limited, acoustic source term was derived and applied to the LEE. In contrast to other broadband source terms, it allows a specific frequency range of the source to be defined, avoiding high energy in the lower frequencies, which can trigger shear layer instabilities and also increase the total integration time. The new band-limited source term was defined as an interface source term, making it compact in both time and space.

Application to scattering of fan tones by bypass chevrons

The culmination of this work was the application of the above developments to a three-dimensional acoustic propagation problem of industrial complexity. Chevrons on the exit circumference of the bypass duct were investigated to understand how fan tones exiting the bypass are scattered by their presence, and their effect on the radiated sound field. This work differs from past work in that the scattering of tonal noise was studied, rather than assessing the jet noise-reducing qualities of the chevrons. To the author's knowledge, this is the first study of the impact of chevrons on the radiation of fan tones from the bypass duct. Numerical studies of representative exhaust duct geometries were used to understand the relationship between the azimuthal mode number and the scattered field, by performing a modal decomposition of the radiated sound field and computing the acoustic power. Solutions to acoustic radiation from the bypass duct of a realistic engine geometry with a RANS mean flow field at varying frequency, were then compared to the representative geometry results. The results indicated that, while the overall radiated acoustic power associated with the incident mode was not substantially altered by the addition of chevrons, the directivity was significantly impacted. Decreases in sound pressure level were found at directivity angles, $\phi < 90°$, for higher frequencies, and increases found along the axis, $\phi \approx 180°$, associated with scattering into lower azimuthal mode orders.

8.2 Next steps

Applying the three-dimensional nodal DGM developed in this work to the study of acoustic scattering by bypass chevrons, showed that the present scheme can accurately and efficiently solve problems of engineering complexity. However, the present implementation could be extended with several developments that may improve the efficiency, accuracy, or robustness of the solver. Several potential improvements are discussed below.

8.2.1 Efficiency

Solution adaptivity

Addressing the efficiency of the numerical scheme, one of the limitations of the present implementation is the fixed polynomial order of the basis functions. Allowing the order to vary over the computational domain could be used to better balance the computational cost by locally increasing the order where the solution exhibits higher error and decreasing the order where the solution is more spatially uniform. To effectively choose the local polynomial order, the scheme must have an efficient estimator for the time-dependent local error in the solution.

Solution sampling

Mentioned in Section 7.6.3, wavepacket source terms require sampling of the solution at multiple times per period of the highest frequency component of the source. Writing data to the disk frequently can be detrimental to performance due to the slow rate at which the data can be written. To maintain efficiency, it could be beneficial to cache solution data in memory and then periodically write it to disk. In addition, the amount of unsteady solution data could be reduced by nonuniform sampling in time, effectively compressing the solution data.

Many-core architectures

An advantage of using the nodal DGM is the ability to vectorize many of the spatial operations of the scheme. Many core architectures, such as graphics processing units (GPUs), can further exploit this capability to reduce computational cost [74, 75, 76]. However, maintaining efficiency when p–adaptivity and mixed element types are used, is an open area of research. For unsteady problems, the time-step size greatly influences

the total cost of obtaining solutions, and is directly related to the smallest element size in the computational domain. By varying the time-step over the domain, the cost can be improved when there are disparate element sizes. Such nonuniform time-stepping methods have been shown to reduce computational cost and can be combined with GPUs [74].

8.2.2 Accuracy and robustness

Element types

The present implementation permits only triangular or tetrahedral elements with up to quadratic curvature. While meshes containing these elements are straightforward to create, different applications may benefit from mixed element types. For example, hexahedral elements could be used to cover the volume region between the geometry and far-field boundary to reduce the total number of elements. Additionally, in regions where the mean flow or fluctuating solution is anisotropic, hexahedral or prism elements could better discretize the domain without leading to over-refinement or poor element quality. Furthermore, implementing higher-order curvature of near-wall elements would allow a coarser mesh to be used, improving efficiency, or increasing accuracy at a fixed mesh refinement level.

Outflow regions

Care has been taken to implement the buffer regions to be as flexible as possible, allowing an arbitrary shape without requiring much user input. However, the effectiveness of the buffer region used in this work is limited by the ratio of the maximum wavelength to the buffer thickness. A buffer thickness that is thinner than the maximum wavelength causes more reflections at the outflow region, while a thick buffer requires more elements and therefore increases the computational cost. More advanced outflow regions should be implemented, such as perfectly matched layers (PMLs), which can potentially damp out-going waves while using less elements. However, the effectiveness of PMLs in the time-domain for entropy and vorticity waves remains to be proven.

Aliasing-driven instability mitigation

While aliasing-driven instabilities are covered in detail in Chapter 4, a solution to the aliasing problem that is robust, is efficient, and minimally impacts the solution accuracy, was not found. To achieve that, further developments are required, such as

finding interpolation points that have both good interpolation qualities and mitigate aliasing, altering the scheme to ensure stability even in the presence of aliasing error, or developing solution filters which minimally degrade the acoustic solution accuracy. These developments could be beneficial to not only the solution of the LEE, but also other linear and nonlinear systems of equations.

8.3 Future applications

The effectiveness of time-domain DGM for linear turbofan exhaust noise propagation has been demonstrated, but there exist several related applications which may prove challenging. Some of these application areas and potential difficulties are discussed below.

Nonlinearities

At high engine power settings, the assumption of linear propagation becomes less physical. In the exhaust jet, the interaction between shock waves and shear layer vortices leads to noise that radiates far from the source. In the inlet, the supersonic tip-speed of the fan blades leads to shock waves propagating forward through the inlet, causing so-called buzz-saw tones [156]. To model these important effects, solution of the fully nonlinear governing equations is necessary.

Shock waves are particularly challenging to capture in the numerical model, due to their high spatial gradients, requiring high local mesh resolution. In high-order schemes, these strong nonlinearities cause spurious oscillations in the solution, often necessitating some form of limiting of the local polynomial order or addition of artificial dissipation. However, it is unknown whether or not such limiting procedures cause excessive dissipation of the acoustic solution in the far-field. Since aeroacoustics applications are necessarily unsteady, some form of unsteady mesh or order adaptation may be required to accurately track these locally nonlinear waves, without excessive global refinement of the mesh.

Installation effects

Installation effects include the overall impact of the airframe on the radiation of sound from the engines. Such effects are important for characterizing the overall aircraft acoustic directivity, as well as the engine noise transmitted into the cabin via the fuselage. For analysis of isolated engines, it is possible to restrict the LEE computational

domain to the nonuniform flow region near the engine, and then use an efficient uniform flow acoustic propagation solver to predict the far-field noise. This is not possible for an aircraft in flight or at take-off where the computational domain must consider the entire aircraft, due to the nonuniform flow-field around the aircraft. For example, the deployment of high-lift devices on the wings and the increased aircraft weight during take-off leads to more distortion of the exhaust jet by down-wash, changing the refraction of acoustic waves. Near the fuselage, the boundary layer refracts the acoustic waves, leading to potentially different cabin noise than what would be predicted in quiescent conditions.

The increased computational domain size leads to longer propagation distances, necessitating higher order and highly accurate time-integration schemes. Realistic aircraft geometry presents additional challenges with mesh generation. Particularly, how high-order curved elements can be generated from the CAD geometry without leading to excessive mesh refinement or poor quality elements in complicated regions such as the narrow gaps between high-lift devices and the wing.

Time-domain impedance models with flow

To reduce the noise emitted by turbofan engines, acoustic liners are commonly added. These liners are typically composed of small holes and cavities which dissipate acoustic energy through the formation of small vortices. Since the geometry of the acoustic liners is small relative to the acoustic wavelength, and the dissipation process relies on viscosity and nonlinearity, the damping effect of the liners is generally modeled, rather than fully discretized. A challenge of developing liner models is the difficulty in considering the effect of the mean flow boundary layer. Some models which work in the frequency domain, exhibit unphysical instabilities in the time-domain [117]. While recently, more physical models have been shown to exist for the finite difference method [157], their implementation in a time-domain DG model remains unclear.

Appendix

A.1 The two-dimensional linearized Euler equations

The two-dimensional linearized Euler equations (LEE) govern the propagation of small disturbances, $\mathbf{q}$, in a mean flow-field, $\mathbf{q}_\circ$, where $\mathbf{q} \ll \mathbf{q}_\circ$. In conservative variables, the fluctuating quantities and the mean flow-field are defined by,

$$\mathbf{q} = \begin{bmatrix} \rho' \\ (\rho u)' \\ (\rho v)' \\ \pi' \end{bmatrix}, \quad \text{and} \quad \mathbf{q}_\circ = \begin{bmatrix} \rho_\circ \\ \rho_\circ u_\circ \\ \rho_\circ v_\circ \\ \pi_\circ \end{bmatrix}, \tag{8.1}$$

where the flow density is defined as $\rho = \rho_\circ + \rho'$, the x- and y-momentum by $\rho u = \rho_\circ u_\circ + (\rho u)'$ and $\rho v = \rho_\circ v_\circ + (\rho v)'$, and the pressure ratio variable by, $\pi = \pi_\circ + \pi'$. Substituting the change of variables into the Euler equations and setting to zero any products of the fluctuating variables, results in the system of equations,

$$\frac{\partial \mathbf{q}}{\partial t} + \frac{\partial \mathbf{F}_\circ \mathbf{q}}{\partial x} + \frac{\partial \mathbf{G}_\circ \mathbf{q}}{\partial y} = \mathbf{S}, \tag{8.2}$$

where $\mathbf{F}_\circ$, $\mathbf{G}_\circ$, and $\mathbf{H}_\circ$ are the flux matrices in the x and y directions, defined as,

$$\mathbf{F}_\circ = \begin{bmatrix} 0 & 1 & 0 & 0 \\ -u_\circ^2 & 2u_\circ & 0 & \frac{c_\circ^2 \rho_\circ}{\pi_\circ} \\ -u_\circ v_\circ & v_\circ & u_\circ & 0 \\ -\frac{\pi_\circ u_\circ}{\rho_\circ} & \frac{\pi_\circ}{\rho_\circ} & 0 & u_\circ \end{bmatrix}, \quad \mathbf{G}_\circ = \begin{bmatrix} 0 & 0 & 1 & 0 \\ -u_\circ v_\circ & v_\circ & u_\circ & 0 \\ -v_\circ^2 & 0 & 2v_\circ & \frac{c_\circ^2 \rho_\circ}{\pi_\circ} \\ -\frac{\pi_\circ v_\circ}{\rho_\circ} & 0 & \frac{\pi_\circ}{\rho_\circ} & v_\circ \end{bmatrix}. \tag{8.3}$$

The matrix, $\mathbf{S}$, represents any sources present in the problem.

Eigenstructure of the 2D LEE

Defining an arbitrary unit normal direction, $\hat{n} = n_x\hat{i} + n_y\hat{j}$, where $\hat{i}$, $\hat{j}$, are the unit vectors associated with the x and y directions, the flux Jacobian along the normal is,

$$\mathbf{F}_{\circ,n} = \mathbf{F}_\circ n_x + \mathbf{G}_\circ n_y. \tag{8.4}$$

Assuming a uniform $\mathbf{F}_{\circ,n}$, the homogeneous LEE along the normal direction becomes,

$$\frac{\partial \mathbf{q}}{\partial t} + \mathbf{F}_{\circ,n}\frac{\partial \mathbf{q}}{\partial x_n} = 0. \tag{8.5}$$

The flux Jacobian can be decomposed into eigenvalues and eigenvectors,

$$\mathbf{F}_{\circ,n} = \mathbf{W}\mathbf{\Lambda}\mathbf{W}^{-1}, \tag{8.6}$$

where the right eigenvectors are given as the columns of,

$$\mathbf{W} = \begin{bmatrix} 1 & 0 & 1 & 1 \\ n_x v_{\circ,n} & -n_y & u_\circ - n_x c_\circ & u_\circ + n_x c_\circ \\ n_y v_{\circ,n} & n_x & v_\circ - n_y c_\circ & v_\circ + n_y c_\circ \\ 0 & 0 & \pi_\circ/\rho_\circ & \pi_\circ/\rho_\circ \end{bmatrix}, \tag{8.7}$$

and the eigenvalues are the diagonal values of,

$$\mathbf{\Lambda} = \begin{bmatrix} v_{\circ,n} & 0 & 0 & 0 \\ 0 & v_{\circ,n} & 0 & 0 \\ 0 & 0 & v_{\circ,n} - c_\circ & 0 \\ 0 & 0 & 0 & v_{\circ,n} + c_\circ \end{bmatrix}, \tag{8.8}$$

for a normal mean flow velocity of $v_{\circ,n} = u_\circ n_x + v_\circ n_y$. The characteristic variables are defined as $\mathbf{w} = \mathbf{W}^{-1}\mathbf{q}$.

A.2 Cylindrical duct modes

Acoustic modes in a hard-walled, cylindrical duct with uniform flow in the axial direction, taken here as the x-direction, are governed by the convected Helmholtz equation,

$$\frac{1}{c_\circ^2}\frac{\mathrm{d}_0^2 p}{\mathrm{d}t^2} - \nabla^2 p = 0, \tag{8.9}$$

where $\frac{\mathrm{d}_0}{\mathrm{d}t} = \frac{\partial}{\partial t} + u_\circ \frac{\partial}{\partial x}$ and p is the acoustic pressure. These equations can be derived from the LEE assuming a uniform, axial mean flow. The boundary conditions at the hard walls are the no-penetration conditions,

$$\frac{\partial p}{\partial n} = \hat{n} \cdot \nabla p = 0, \tag{8.10}$$

where $\hat{n}$ is the direction normal to the wall.

Solutions of the above equations take the form of,

$$p'(r, \theta, t) = \sum_{m=-\infty}^{+\infty} A_m \Psi_m(r) e^{i(\omega t - k_x x - m\theta)}, \tag{8.11}$$

where $\Psi_m(r)$ is the m-th azimuthal Fourier mode of the shape function. Substituting the above expression for pressure into the governing equation and boundary contidition, we obtain,

$$\frac{1}{r}\frac{\partial}{\partial r}\left(r\frac{\partial \Psi_m}{\partial r}\right) + \left(k_r^2 - \frac{m^2}{r^2}\right)\Psi_m = 0, \tag{8.12}$$

with the boundary condition,

$$\frac{\partial \Psi_m}{\partial r} = 0, \text{for } r = R. \tag{8.13}$$

The general solution for the mode shape functions is,

$$\Psi_m(r) = AJ_m(k_r r) + BY_m(k_r r), \tag{8.14}$$

, where for a cylindrical duct, $B = 0$. The boundary condition gives the equation for the radial wavenumber, $J'_m(k_r R) = 0$, where for each azimuthal mode m, there exist an infinite number of solutions for k_r, defined as radial modes and labeled with the integer, n.

Using the expression for pressure in Equation 8.11 and the linearized Euler equations in cylindrical coordinates, one can derive the primitive solution vector describing the

duct modes,

$$\rho' = \mathrm{Re}\left\{\frac{1}{c_\circ^2} A_{m,n}^{\pm} \Psi_m e^{i(\omega t - k_x^{\pm} x - m\theta)}\right\} \tag{8.15}$$

$$u_x' = \mathrm{Re}\left\{\frac{A_{m,n}^{\pm}}{\rho_\circ c_\circ} \frac{k_x^{\pm}}{k_\circ - M k_x^{\pm}} \Psi_m e^{i(\omega t - k_x^{\pm} x - m\theta)}\right\} \tag{8.16}$$

$$u_r' = \mathrm{Re}\left\{\frac{i A_{m,n}^{\pm}}{\rho_\circ c_\circ} \frac{1}{k_\circ - M k_x^{\pm}} \frac{\partial \Psi_m}{\partial r} e^{i(\omega t - k_x^{\pm} x - m\theta)}\right\} \tag{8.17}$$

$$u_\theta' = \mathrm{Re}\left\{\frac{m A_{m,n}^{\pm}}{r \rho_\circ c_\circ} \frac{1}{k_\circ - M k_x^{\pm}} \Psi_m e^{i(\omega t - k_x^{\pm} x - m\theta)}\right\} \tag{8.18}$$

$$p' = \mathrm{Re}\left\{A_{m,n}^{\pm} \Psi_m e^{i(\omega t - k_x^{\pm} x - m\theta)}\right\}, \tag{8.19}$$

where $k_\circ = \omega / c_\circ$ is the free-field wavenumber, $M = u_\circ / c_\circ$ is the Mach number, and $\pm$ indicates propagation in the $-x$ or the $+x$ direction. Expressing the solution in terms of conserved variables and in Cartesian coordinates we get,

$$\rho' = \mathrm{Re}\left\{\frac{1}{c_\circ^2} A_{m,n}^{\pm} \Psi_m e^{i(\omega t - k_x^{\pm} x - m\theta)}\right\} \tag{8.20}$$

$$(\rho u)' = \rho_\circ u' + u_\circ \rho' \tag{8.21}$$

$$(\rho v)' = \rho_\circ (u_r' \cos(\theta) - u_\theta' \sin(\theta)) \tag{8.22}$$

$$(\rho w)' = \rho_\circ (u_r' \sin(\theta) + u_\theta' \cos(\theta)) \tag{8.23}$$

$$\pi' = \frac{\pi_\circ}{\rho_\circ c_\circ^2} p'. \tag{8.24}$$

A.3 Acoustic scattering by a cylinder analytical solution

The problem, illustrated in Figure 8.1, consists of a cylinder of radius R, located a distance L from a time-harmonic, distributed source located at point S of the form

$$f(r_s) = e^{-\ln(2)\frac{r_s}{w}^2}, \tag{8.25}$$

where w is the source width and r_s is the radial distance from the center of the source. The point, O, is the observer point at which the solution is calculated.

The total field is given by an incident field and a scattered field such that,

$$\phi = \phi_i + \phi_s, \tag{8.26}$$

where ϕ_i and ϕ_s are the incident and scattered fields, respectively. The field scattered by the cylinder can be written as,

$$\phi_s = \sum_{n=-\infty}^{\infty} A_n H_n^{(2)}(kr) e^{-in\theta}, \tag{8.27}$$

where A_n is the n^{th} scattered field coefficient, k is the wavenumber, and $H_n^{(2)}$ is the Hankel function of the second kind and of order n. Assuming no mass flux through the surface of the cylinder and only tangential velocity, the boundary condition at the cylinder surface is written as,

$$\left.\frac{\partial \phi}{\partial r}\right|_{r=R} = 0. \tag{8.28}$$

Projecting this onto the cylindrical harmonics yields,

$$\int_0^{2\pi} e^{im\theta} \frac{\partial \phi_i}{\partial r} R \mathrm{d}\theta + R \sum_{n=-\infty}^{\infty} A_n \int_0^{2\pi} \left(k H_n^{(2)'}(kr) - in \frac{\partial \phi}{\partial r} \right) e^{(m-n)i\theta} \mathrm{d}\theta = 0. \tag{8.29}$$

Removing terms for $m \neq n$, the resulting system becomes,

$$2\pi R k \sum_{n=-\infty}^{\infty} A_n H_n^{(2)'}(kR) = -\int_0^{2\pi} e^{im\theta} \frac{\partial \phi_i}{\partial r} R \mathrm{d}\theta, \text{ for } m = n. \tag{8.30}$$

Therefore,

$$A_n = \frac{S_n}{2\pi R k H_n^{(2)'}(kR)}, \tag{8.31}$$

where S_n is the right hand side of Equation 8.30 and the derivative of the Hankel function is defined as,

$$H_n^{(2)'}(kR) = \frac{1}{2}\left[H_{n-1}^{(2)}(kR) - H_{n+1}^{(2)}(kR) \right]. \tag{8.32}$$

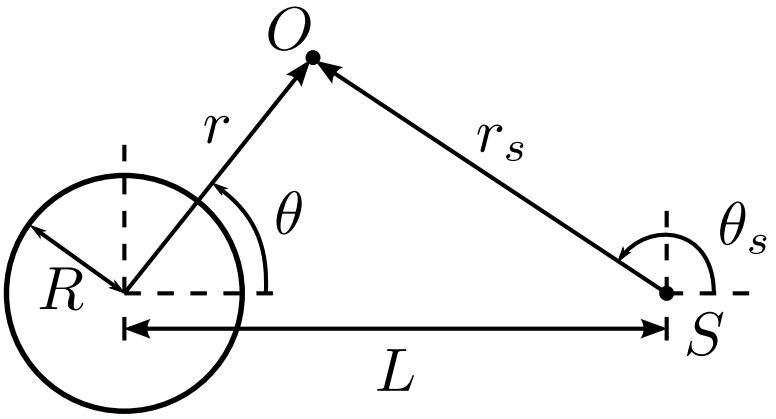

Figure 8.1: Cylinder scattering problem definition.

Morris [158] derived the incident field centered on the source as,

$$\phi_i(r_s) = -\int_0^\infty \frac{sJ_0(sr_s)\tilde{F}(s)}{(s^2-k^2)}\mathrm{d}s, \tag{8.33}$$

where $\tilde{F}(s)$ is given as,

$$\tilde{F}(s) = \frac{-ik}{2d}e^{\frac{-s^2}{4d}}, \tag{8.34}$$

for a source of the type Equation 8.25, and $d = \dfrac{\ln(2)}{w^2}$. The function, J_0, is the Bessel function of order 0. The derivative of the incident field is found to be,

$$\frac{\partial\phi_i}{\partial r}(r_s) = \frac{\partial\phi_i}{\partial r_s}\frac{\partial r_s}{\partial r} = \frac{\partial r_s}{\partial r}\int_0^\infty \frac{s^2J_1(sr_s)\tilde{F}(s)}{(s^2-k^2)\mathrm{d}s}. \tag{8.35}$$

To avoid the singularity in the integrand at $s = k$, a change of variables is given by Morris [158] as $s = \tau - i\alpha e^{-\Delta(\tau-k)^2}$ which bends the integration path into the complex plane around $s = k$. The constants α and Δ are defined as $\alpha = \dfrac{k}{10}$ and $\Delta = -\ln(1\times10^{-10}/\alpha)/k^2$. The scattered field coefficients are found by numerical integration of the right hand side of Equation 8.30 and then substituted into Equation 8.31.

A.4 Vibrating sphere analytical solution

Consider the small amplitude vibration of a hard-walled sphere, where the radius of the sphere, d, varies in time like [159],

$$d(t) = d_\circ + d'e^{i\omega t}, \tag{8.36}$$

where $d_\circ$ is the radius of the sphere when stationary, d' is the maximum perturbation of the radius, and ω is the angular frequency of the vibration. The motions of the sphere disturb the surrounding fluid, causing small fluctuations of density, pressure, and velocity in a quiescent fluid. The linearized Euler equations in spherical coordinates can be expressed as,

$$\frac{\partial(\rho' r^2)}{\partial t} + \rho_\circ\frac{\partial(u' r^2)}{\partial r} = 0 \tag{8.37}$$

$$\rho_\circ\frac{\partial u'}{\partial t} + \frac{\partial p'}{\partial r} = 0, \tag{8.38}$$

where r is the radial distance in the spherical coordinate system. If homentropy is assumed, $p' = c_\circ\rho'$, and the above equations can be combined into a wave equation for

rp',

$$\frac{1}{c_\circ^2}\frac{\partial^2(rp')}{\partial t^2} - \frac{\partial^2(rp')}{\partial r^2} = 0, \tag{8.39}$$

which supports solutions for out-going waves from the sphere surface of the type,

$$p' = \frac{1}{r}Ae^{i(\omega t - kr)}, \tag{8.40}$$

where k is the wavenumber.

The fluctuating velocity can be found by substituting the above expression for pressure into Equation 8.38, resulting in,

$$u' = \frac{A}{\omega\rho_\circ r}\left(k - \frac{i}{r}\right)e^{i(\omega t - kr)}. \tag{8.41}$$

To determine the complex coefficient, A, the boundary condition for the velocity at the surface of the sphere, $u' = \dfrac{\mathrm{d}d(t)}{\mathrm{d}t} = i\omega d' e^{i\omega t}$ is used, giving,

$$A = \frac{-d'\omega^2\rho_\circ d_\circ}{ik + \frac{1}{d_\circ}}e^{ikd_\circ}. \tag{8.42}$$

Works Cited

[1] A. L. Hansell, M. Blangiardo, L. Fortunato, S. Floud, K. de Hoogh, D. Fecht, R. E. Ghosh, H. E. Laszlo, C. Pearson, L. Beale, S. Beevers, J. Gulliver, N. Best, S. Richardson, and P. Elliott, "Aircraft noise and cardiovascular disease near Heathrow airport in London: small area study," *BMJ*, vol. 347, Oct. 2013.

[2] M. Basner, B. Griefahn, and M. v. d. Berg, "Aircraft noise effects on sleep: Mechanisms, mitigation and research needs," *Noise and Health*, vol. 12, no. 47, pp. 95–109, 2010.

[3] M. Basner, C. Clark, A. Hansell, J. Hileman, S. Janssen, K. Shepherd, and V. Sparrow, "Aviation Noise Impacts: State of the Science," *Noise and Health*, vol. 19, no. 87, pp. 41–50, 2017.

[4] S. Hygge, G. W. Evans, and M. Bullinger, "A Prospective Study of Some Effects of Aircraft Noise on Cognitive Performance in Schoolchildren," *Psychological Science*, vol. 13, no. 5, pp. 469–474, 2002.

[5] S. A. Stansfeld, B. Berglund, C. Clark, I. Lopez-Barrio, P. Fischer, E. Öhrström, M. M. Haines, J. Head, S. Hygge, I. v. Kamp, and B. F. Berry, "Aircraft and road traffic noise and children's cognition and health: a cross-national study," *The Lancet*, vol. 365, no. 9475, pp. 1942 – 1949, 2005.

[6] R. Girvin, "Aircraft noise-abatement and mitigation strategies," *Journal of Air Transport Management*, vol. 15, no. 1, pp. 14 – 22, 2009.

[7] A. Mahashabde, P. Wolfe, A. Ashok, C. Dorbian, Q. He, A. Fan, S. Lukachko, A. Mozdzanowska, C. Wollersheim, S. R. H. Barrett, M. Locke, and I. A. Waitz, "Assessing the environmental impacts of aircraft noise and emissions," *Progress in Aerospace Sciences*, vol. 47, no. 1, pp. 15 – 52, 2011.

[8] "ICAO Environmental Report 2010," tech. rep., International Civil Aviation Organization, 2010.

[9] R. J. Astley, "Numerical methods for noise propagation in moving flows, with application to turbofan engines," *Acoustical Science and Technology*, vol. 30, no. 4, pp. 227–239, 2009.

[10] C. K. W. Tam, "Computational aeroacoustics - Issues and methods," *AIAA Journal*, vol. 33, pp. 1788–1796, Oct. 1995.

[11] P. Moin and K. Mahesh, "Direct numerical simulation: a tool in turbulence research," *Annual review of fluid mechanics*, vol. 30, no. 1, pp. 539–578, 1998.

[12] F. Hindenlang, G. J. Gassner, C. Altmann, A. Beck, M. Staudenmaier, and C.-D. Munz, "Explicit discontinuous Galerkin methods for unsteady problems," *Computers & Fluids*, vol. 61, pp. 86–93, May 2012.

[13] A. D. Beck, T. Bolemann, D. Flad, H. Frank, G. J. Gassner, F. Hindenlang, and C.-D. Munz, "High-order discontinuous Galerkin spectral element methods for transitional and turbulent flow simulations," *International Journal for Numerical Methods in Fluids*, vol. 76, pp. 522–548, Nov. 2014.

[14] C. Bogey, C. Bailly, and D. Juvé, "Noise Investigation of a High Subsonic, Moderate Reynolds Number Jet Using a Compressible Large Eddy Simulation," *Theoretical and Computational Fluid Dynamics*, vol. 16, no. 4, pp. 273–297, 2003.

[15] C. Brun, D. Juve, M. Manhart, and C.-D. Munz, *Numerical Simulation of Turbulent Flows and Noise Generation*. Springer, 2008.

[16] S. Marié, D. Ricot, and P. Sagaut, "Comparison between lattice Boltzmann method and Navier–Stokes high order schemes for computational aeroacoustics," *Journal of Computational Physics*, vol. 228, no. 4, pp. 1056 – 1070, 2009.

[17] G. Brès, F. Pérot, and D. Freed, "A Ffowcs Williams - Hawkings Solver for Lattice-Boltzmann Based Computational Aeroacoustics," in *16th AIAA/CEAS Aeroacoustics Conference*, Aeroacoustics Conferences, American Institute of Aeronautics and Astronautics, June 2010. DOI: 10.2514/6.2010-3711.

[18] D. J. Bodony and S. K. Lele, "Current Status of Jet Noise Predictions Using Large-Eddy Simulation," *AIAA Journal*, vol. 46, pp. 364–380, Feb. 2008.

[19] M. J. Lighthill, "On Sound Generated Aerodynamically. I. General Theory," *Proceedings of the Royal Society A: Mathematical, Physical and Engineering Sciences*, vol. 211, pp. 564–587, Mar. 1952.

[20] J. F. Williams and D. L. Hawkings, "Sound generation by turbulence and surfaces in arbitrary motion," *Philosophical Transactions of the Royal Society of London A: Mathematical, Physical and Engineering Sciences*, vol. 264, no. 1151, pp. 321–342, 1969.

[21] M. E. Goldstein, *Aeroacoustics*. 1976.

[22] R. Ewert, "RPM-the fast Random Particle-Mesh method to realize unsteady turbulent sound sources and velocity fields for CAA applications," *parameters*, vol. 4, p. 1, 2007.

[23] Y. Özyörük, "Numerical prediction of aft radiation of turbofan tones through exhaust jets," *Journal of Sound and Vibration*, vol. 325, pp. 122–144, Aug. 2009.

[24] T. Toulorge, *Efficient Runge–Kutta Discontinuous Galerkin Methods Applied to Aeroacoustics*. PhD thesis, Ph. D. Thesis, Katholieke Universiteit Leuven, 2012.

[25] R. Ewert and W. Schröder, "Acoustic perturbation equations based on flow decomposition via source filtering," *Journal of Computational Physics*, vol. 188, pp. 365–398, July 2003.

[26] C. K. Tam and J. C. Webb, "Dispersion-Relation-Preserving Finite Difference Schemes for Computational Acoustics," *Journal of Computational Physics*, vol. 107, pp. 262–281, Aug. 1993.

[27] J. Manera, B. Schiltz, R. Leneveu, S. Caro, J. Jacqmot, and S. Rienstra, "Kelvin-Helmholtz Instabilities Occurring at a Nacelle Exhaust," in *14th AIAA/CEAS Aeroacoustics Conference (29th AIAA Aeroacoustics Conference)*, Aeroacoustics Conferences, American Institute of Aeronautics and Astronautics, May 2008. DOI: 10.2514/6.2008-2883.

[28] A. Iob, R. Della Ratta Rinaldi, and R. Arina, "A Frequency-Domain Linearized Euler Model for Noise Radiation," 2011.

[29] R. Della Ratta Rinaldi, A. Iob, and R. Arina, "An efficient discontinuous Galerkin method for aeroacoustic propagation," *International Journal for Numerical Methods in Fluids*, vol. 69, pp. 1473–1495, July 2012.

[30] R. J. Astley, G. Gabard, X. Zhang, and X. Chen, "IUTAM Symposium on Computational Aero-Acoustics for Aircraft Noise Prediction Time-domain computation of multimode propagation in an aeroengine duct," *Procedia Engineering*, vol. 6, pp. 173 – 182, 2010.

[31] X. Chen, X. Huang, and X. Zhang, "Sound Radiation from a Bypass Duct with Bifurcations," *AIAA Journal*, vol. 47, pp. 429–436, Jan. 2018.

[32] T. Colonius and S. K. Lele, "Computational aeroacoustics: progress on nonlinear problems of sound generation," *Progress in Aerospace Sciences*, vol. 40, pp. 345–416, Aug. 2004.

[33] S. Redonnet and Y. Druon, "Computational Aeroacoustics of Aft Fan Noises Characterizing a Realistic Coaxial Engine," *AIAA Journal*, vol. 50, pp. 1029–1046, May 2012.

[34] S. K. Richards, X. X. Chen, X. Huang, and X. Zhang, "Computation of Fan Noise Radiation through an Engine Exhaust Geometry with Flow," *International Journal of Aeroacoustics*, vol. 6, no. 3, pp. 223–241, 2007.

[35] C. Tam, S. Parrish, E. Envia, and E. Chien, "Physics of Acoustic Radiation from Jet Engine Inlets," in *18th AIAA/CEAS Aeroacoustics Conference (33rd AIAA Aeroacoustics Conference)*, American Institute of Aeronautics and Astronautics, Jan. 2018. DOI: 10.2514/6.2012-2242.

[36] R. J. LeVeque, *Finite volume methods for hyperbolic problems*. Cambridge; New York: Cambridge University Press, 2002.

[37] J. Kok, "Computation of Sound Radiation from Cylindrical Ducts with Jets Using a High-Order Finite-Volume Method," American Institute of Aeronautics and Astronautics, May 2007.

[38] D. V. Nance, K. Viswanathan, and L. N. Sankar, "Low-Dispersion Finite Volume Scheme for Aeroacoustic Applications," *AIAA Journal*, vol. 35, pp. 255–262, Feb. 1997.

[39] S. Kim, S. Lee, and K. H. Kim, "Wavenumber-extended high-order oscillation control finite volume schemes for multi-dimensional aeroacoustic computations," *Journal of Computational Physics*, vol. 227, no. 8, pp. 4089 – 4122, 2008.

[40] L. L. Thompson, "A review of finite-element methods for time-harmonic acoustics," *The Journal of the Acoustical Society of America*, vol. 119, no. 3, p. 1315, 2006.

[41] P. P. Rao and P. J. Morris, "Use of Finite Element Methods in Frequency Domain Aeroacoustics," *AIAA Journal*, vol. 44, pp. 1643–1652, Jan. 2018.

[42] A. Iob, R. Arina, and C. Schipani, "Frequency-Domain Linearized Euler Model for Turbomachinery Noise Radiation Through Engine Exhaust," *AIAA Journal*, vol. 48, pp. 848–858, Apr. 2010.

[43] K. Hamiche, G. Gabard, and H. Bériot, "A higher-order finite element method for the linearised Euler equations.," 2014.

[44] F. Ihlenburg and I. Babuska, "Finite Element Solution of the Helmholtz Equation with High Wave Number Part II: The h-p Version of the FEM," *SIAM Journal on Numerical Analysis*, vol. 34, no. 1, pp. 315–358, 1997.

[45] H. Bériot, A. Prinn, and G. Gabard, "Efficient implementation of high-order finite elements for Helmholtz problems," *International Journal for Numerical Methods in Engineering*, vol. 106, no. 3, pp. 213–240, 2016.

[46] J. Boyd, *Chebyshev and Fourier Spectral Methods: Second Revised Edition*. Dover Books on Mathematics, Dover Publications, 2001.

[47] A. T. Patera, "A spectral element method for fluid dynamics: Laminar flow in a channel expansion," *Journal of Computational Physics*, vol. 54, no. 3, pp. 468 – 488, 1984.

[48] D. Gottlieb and J. S. Hesthaven, "Spectral methods for hyperbolic problems," *Journal of Computational and Applied Mathematics*, vol. 128, no. 1, pp. 83 – 131, 2001.

[49] H. L. Atkins and D. P. Lockard, "A High-Order Method Using Unstructured Grids for the Aeroacoustic Analysis of Realistic Aircraft Configurations," *AIAA*, no. AIAA-99-1945, 1999.

[50] D. Stanescu, M. Y. Hussaini, and F. Farassat, "Aircraft engine noise scattering by fuselage and wings: a computational approach," *Journal of sound and vibration*, vol. 263, no. 2, pp. 319–333, 2003.

[51] C. P. A. Blom, *Discontinuous Galerkin method on tetrahedral elements for aeroacoustics*. PhD thesis, University of Twente, Enschede, 2003.

[52] M. Bernacki and S. Piperno, "A dissipation-free time-domain discontinuous Galerkin method applied to three-dimensional linearized Euler equations around a steady-state non-uniform inviscid flow," *Journal of Computational Acoustics*, vol. 14, no. 04, pp. 445–467, 2006.

[53] Y. Reymen, "3d High-Order Discontinuous Galerkin Methods for Time-Domain Simulation of Flow Noise Propagation (3d Discontinue Galerkin methoden voor simulatie in het tijdsdomein van devoortplanting van stromingsgeluid)," 2008.

[54] K. Hillewaert, *Development of the discontinuous Galerkin method for high-resolution, large scale CFD and acoustics in industrial geometries*. PhD Thesis, 2013.

[55] J. S. Hesthaven, *Nodal Discontinuous Galerkin Methods: Algorithms, Analysis, and Applications*. No. 54 in Texts in applied mathematics, New York: Springer, 2008.

[56] H. L. Atkins and C.-W. Shu, "Quadrature-Free Implementation Of The Discontinuous Galerkin Method For Hyperbolic Equations," Tech. Rep. 96-51, NASA Langley Research Center, Hampton, Virginia, Aug. 1996.

[57] J. S. Hesthaven and T. Warburton, "High-order/Spectral Methods on Unstructured Grids I. Time-domain Solution of Maxwell's Equations," Tech. Rep. 2001-6, NASA Langley Research Center, Hampton, Virginia, Mar. 2001.

[58] D. Flad, A. D. Beck, G. Gassner, and C.-d. Munz, "A Discontinuous Galerkin Spectral Element Method for the direct numerical simulation of aeroacoustics," in *20th AIAA/CEAS Aeroacoustics Conference*, American Institute of Aeronautics and Astronautics, Jan. 2018. DOI: 10.2514/6.2014-2740.

[59] N. Castel, G. Cohen, and M. Duruflé, "Application of Discontinuous Galerkin Spectral Method on Hexahedral Elements for Aeroacoutic," *Journal of Computational Acoustics*, vol. 17, no. 02, pp. 175–196, 2009.

[60] G. Gabard, "Discontinuous Galerkin methods with plane waves for time-harmonic problems," *Journal of Computational Physics*, vol. 225, no. 2, pp. 1961 – 1984, 2007.

[61] M. Dumbser and C.-D. Munz, "Building Blocks for Arbitrary High Order Discontinuous Galerkin Schemes," *Journal of Scientific Computing*, vol. 27, pp. 215–230, Dec. 2005.

[62] H. T. Huynh, "A Flux Reconstruction Approach to High-Order Schemes Including Discontinuous Galerkin Methods," in *18th AIAA Computational Fluid Dynamics Conference*, American Institute of Aeronautics and Astronautics, Jan. 2018. DOI: 10.2514/6.2007-4079.

[63] H. T. Huynh, Z. J. Wang, and P. E. Vincent, "High-order methods for computational fluid dynamics: A brief review of compact differential formulations on unstructured grids," *Computers & Fluids*, vol. 98, pp. 209 – 220, 2014.

[64] J. Manera and R. Leneveu, "Broadband turbomachinery noise: exhaust noise computations with ACTRAN/TM and ACTRAN/DGM," in *15th AIAA/CEAS Aeroacoustics Conference*, 2009.

[65] Z. Rarata, *Application and assessment of time-domain DGM for intake acoustics using 3D linearized Euler equations*. Doctoral Thesis, University of Southampton, 2014.

[66] G. R. Richter, "An Optimal-Order Error Estimate for the Discontinuous Galerkin Method," *Mathematics of Computation*, vol. 50, p. 75, Jan. 1988.

[67] F. Q. Hu, M. Hussaini, and P. Rasetarinera, "An Analysis of the Discontinuous Galerkin Method for Wave Propagation Problems," *Journal of Computational Physics*, vol. 151, pp. 921–946, May 1999.

[68] F. Q. Hu and H. L. Atkins, "Eigensolution Analysis of the Discontinuous Galerkin Method with Nonuniform Grids," *Journal of Computational Physics*, vol. 182, pp. 516–545, Nov. 2002.

[69] M. Ainsworth, "Dispersive and dissipative behaviour of high order discontinuous Galerkin finite element methods," *Journal of Computational Physics*, vol. 198, pp. 106–130, July 2004.

[70] N. Chevaugeon, K. Hillewaert, X. Gallez, P. Ploumhans, and J.-F. Remacle, "Optimal numerical parameterization of discontinuous Galerkin method applied to wave propagation problems," *Journal of Computational Physics*, vol. 223, pp. 188–207, Apr. 2007.

[71] B. Cockburn and C.-W. Shu, "Runge–Kutta discontinuous Galerkin methods for convection-dominated problems," *Journal of scientific computing*, vol. 16, no. 3, pp. 173–261, 2001.

[72] E. J. Kubatko, C. Dawson, and J. J. Westerink, "Time step restrictions for Runge–Kutta discontinuous Galerkin methods on triangular grids," *Journal of Computational Physics*, vol. 227, pp. 9697–9710, Dec. 2008.

[73] T. Toulorge and W. Desmet, "CFL Conditions for Runge–Kutta discontinuous Galerkin methods on triangular grids," *Journal of Computational Physics*, vol. 230, pp. 4657–4678, June 2011.

[74] N. Godel, S. Schomann, T. Warburton, and M. Clemens, "GPU Accelerated Adams-Bashforth Multirate Discontinuous Galerkin FEM Simulation of High-Frequency Electromagnetic Fields," *IEEE Transactions on Magnetics*, vol. 46, pp. 2735–2738, Aug. 2010.

[75] J. Chan, Z. Wang, A. Modave, J.-F. Remacle, and T. Warburton, "GPU-accelerated discontinuous Galerkin methods on hybrid meshes," *Journal of Computational Physics*, vol. 318, pp. 142–168, 2016.

[76] A. Modave, A. St-Cyr, and T. Warburton, "GPU performance analysis of a nodal discontinuous Galerkin method for acoustic and elastic models," *Computers & Geosciences*, vol. 91, pp. 64 – 76, 2016.

[77] L. Liu, X. Li, and F. Q. Hu, "Nonuniform time-step Runge–Kutta discontinuous Galerkin method for Computational Aeroacoustics," *Journal of Computational Physics*, vol. 229, pp. 6874–6897, Sept. 2010.

[78] B. Seny, J. Lambrechts, T. Toulorge, V. Legat, and J.-F. Remacle, "An efficient parallel implementation of explicit multirate Runge–Kutta schemes for discontinuous Galerkin computations," *Journal of Computational Physics*, vol. 256, pp. 135–160, Jan. 2014.

[79] C. Dawson, C. J. Trahan, E. J. Kubatko, and J. J. Westerink, "A parallel local timestepping Runge–Kutta discontinuous Galerkin method with applications to coastal ocean modeling," *Computer Methods in Applied Mechanics and Engineering*, vol. 259, pp. 154–165, June 2013.

[80] L. Wang and D. J. Mavriplis, "Implicit solution of the unsteady Euler equations for high-order accurate discontinuous Galerkin discretizations," *Journal of Computational Physics*, vol. 225, pp. 1994–2015, Aug. 2007.

[81] A. Kanevsky, M. H. Carpenter, D. Gottlieb, and J. S. Hesthaven, "Application of implicit–explicit high order Runge–Kutta methods to discontinuous-Galerkin schemes," *Journal of Computational Physics*, vol. 225, pp. 1753–1781, Aug. 2007.

[82] M. Hochbruck, T. Pazur, A. Schulz, E. Thawinan, and C. Wieners, "Efficient time integration for discontinuous Galerkin approximations of linear wave equations," *Zeitschrift für Angewandte Mathematik und Mechanik*, 2013.

[83] P. Houston and E. Süli, "*hp* -Adaptive Discontinuous Galerkin Finite Element Methods for First-Order Hyperbolic Problems," *SIAM Journal on Scientific Computing*, vol. 23, pp. 1226–1252, Jan. 2001.

[84] J.-F. Remacle, J. E. Flaherty, and M. S. Shephard, "An adaptive discontinuous Galerkin technique with an orthogonal basis applied to compressible flow problems," *SIAM review*, vol. 45, no. 1, pp. 53–72, 2003.

[85] F. Q. Hu, X. D. Li, X. Y. Li, and M. Jiang, "Time Domain Wave Packet method and suppression of instability waves in aeroacoustic computations," *Journal of Fluids Engineering*, vol. 136, no. 6, p. 060905, 2014.

[86] E. Gabriel, G. E. Fagg, G. Bosilca, T. Angskun, J. J. Dongarra, J. M. Squyres, V. Sahay, P. Kambadur, B. Barrett, A. Lumsdaine, and others, "Open MPI: Goals, concept, and design of a next generation MPI implementation," in *Recent Advances in Parallel Virtual Machine and Message Passing Interface*, pp. 97–104, Springer, 2004.

[87] J. D. Anderson, *Fundamentals of Aerodynamics*. Anderson series, New York: McGraw-Hill, 5th ed ed., 2011. OCLC: ocn463634144.

[88] A. D. Pierce and R. T. Beyer, "Acoustics: An Introduction to Its Physical Principles and Applications. 1989 Edition," *The Journal of the Acoustical Society of America*, vol. 87, no. 4, pp. 1826–1827, 1990.

[89] M. E. Goldstein, "An exact form of Lilley's equation with a velocity quadrupole/temperature dipole source term," *Journal of Fluid Mechanics*, vol. 443, pp. 231–236, 2001.

[90] S. Richards, X. Zhang, X. Chen, and P. Nelson, "The evaluation of non-reflecting boundary conditions for duct acoustic computation," *Journal of Sound and Vibration*, vol. 270, pp. 539–557, Feb. 2004.

[91] R. J. Fattah, J. R. Gill, and X. Zhang, "Towards a Generic Non-Reflective Characteristic Boundary Condition for Aeroacoustic Simulations," American Institute of Aeronautics and Astronautics, May 2016.

[92] J. Berland, C. Bogey, and C. Bailly, "Low-dissipation and low-dispersion fourth-order Runge-Kutta algorithm," *Computers & Fluids*, vol. 35, pp. 1459–1463, Dec. 2006.

[93] "An Updated Set of Basic Linear Algebra Subprograms (BLAS)," *ACM Trans. Math. Softw.*, vol. 28, pp. 135–151, June 2002.

[94] R. Cools, "Monomial cubature rules since "Stroud": a compilation — part 2," *Journal of Computational and Applied Mathematics*, vol. 112, no. 1–2, pp. 21 – 27, 1999.

[95] G. Karypis and V. Kumar, "A Fast and High Quality Multilevel Scheme for Partitioning Irregular Graphs," *SIAM Journal on Scientific Computing*, vol. 20, pp. 359–392, Jan. 1998.

[96] H. Bériot, G. Gabard, and E. Perrey-Debain, "Analysis of high-order finite elements for convected wave propagation," *International journal for numerical methods in engineering*, vol. 96, no. 11, pp. 665–688, 2013.

[97] J. Alvarez, L. D. Angulo, M. R. Cabello, A. R. Bretones, and S. G. Garcia, "An Analysis of the Leap-Frog Discontinuous Galerkin Method for Maxwell's Equations," *IEEE Transactions on Microwave Theory and Techniques*, vol. 62, pp. 197–207, Feb. 2014.

[98] D. Sármány, M. A. Botchev, and J. J. W. Vegt, "Dispersion and Dissipation Error in High-Order Runge-Kutta Discontinuous Galerkin Discretisations of the Maxwell Equations," *Journal of Scientific Computing*, vol. 33, pp. 47–74, Aug. 2007.

[99] S. A. Orszag, "On the elimination of aliasing in finite-difference schemes by filtering high-wavenumber components," *Journal of the Atmospheric sciences*, vol. 28, no. 6, pp. 1074–1074, 1971.

[100] J. S. Hesthaven, *Spectral methods for time-dependent problems*. No. 21 in Cambridge monographs on applied and computational mathematics, Cambridge ; New York: Cambridge University Press, 2007.

[101] R. M. Kirby and G. E. Karniadakis, "De-aliasing on non-uniform grids: algorithms and applications," *Journal of Computational Physics*, vol. 191, pp. 249–264, Oct. 2003.

[102] R. M. Kirby and S. J. Sherwin, "Aliasing errors due to quadratic nonlinearities on triangular spectral/hp element discretisations," *Journal of engineering mathematics*, vol. 56, no. 3, pp. 273–288, 2006.

[103] G. Mengaldo, D. D. Grazia, D. Moxey, P. E. Vincent, and S. J. Sherwin, "Dealiasing techniques for high-order spectral element methods on regular and irregular grids," *Journal of Computational Physics*, vol. 299, pp. 56 – 81, 2015.

[104] F. Bassi, N. Franchina, A. Ghidoni, and S. Rebay, "A numerical investigation of a spectral-type nodal collocation discontinuous Galerkin approximation of the Euler and Navier-Stokes equations: SPECTRAL-TYPE COLLOCATION DISCONTINUOUS GALERKIN APPROXIMATION," *International Journal for Numerical Methods in Fluids*, vol. 71, pp. 1322–1339, Apr. 2013.

[105] A. Jameson, P. E. Vincent, and P. Castonguay, "On the Non-linear Stability of Flux Reconstruction Schemes," *Journal of Scientific Computing*, vol. 50, pp. 434–445, Feb. 2012.

[106] D. M. Williams and A. Jameson, "Nodal Points and the Nonlinear Stability of High-Order Methods for Unsteady Flow Problems on Tetrahedral Meshes," American Institute of Aeronautics and Astronautics, June 2013.

[107] P. Castonguay, P. E. Vincent, and A. Jameson, "Application of high-order energy stable flux reconstruction schemes to the Euler equations," in *49th AIAA Aerospace Sciences Meeting*, vol. 686, 2011.

[108] F. D. Witherden, *On the Development and Implementation of High-Order Flux Reconstruction Schemes for Computational Fluid Dynamics*. PhD thesis, 2015.

[109] F. D. Witherden and P. E. Vincent, "An Analysis of Solution Point Coordinates for Flux Reconstruction Schemes on Triangular Elements," *Journal of Scientific Computing*, vol. 61, pp. 398–423, Nov. 2014.

[110] J. Hesthaven and R. Kirby, "Filtering in Legendre spectral methods," *Mathematics of Computation*, vol. 77, no. 263, pp. 1425–1452, 2008.

[111] D. A. Kopriva and G. J. Gassner, "An Energy Stable Discontinuous Galerkin Spectral Element Discretization for Variable Coefficient Advection Problems," *SIAM Journal on Scientific Computing*, vol. 36, no. 4, pp. A2076–A2099, 2014.

[112] G. J. Gassner, A. R. Winters, and D. A. Kopriva, "A well balanced and entropy conservative discontinuous Galerkin spectral element method for the shallow water equations," *Applied Mathematics and Computation*, vol. 272, Part 2, pp. 291 – 308, 2016. Recent Advances in Numerical Methods for Hyperbolic Partial Differential Equations.

[113] G. J. Gassner, A. R. Winters, and D. A. Kopriva, "Split Form Nodal Discontinuous Galerkin Schemes with Summation-By-Parts Property for the Compressible Euler Equations," *arXiv preprint arXiv:1604.06618*, 2016.

[114] D. A. Kopriva and G. J. Gassner, "Geometry effects in nodal discontinuous Galerkin methods on curved elements that are provably stable," *Applied Mathematics and Computation*, vol. 272, pp. 274–290, Jan. 2016.

[115] M. Bernacki and S. Piperno, "Stabilization of Kelvin-Helmholtz instabilities in 3d linearized Euler equations using a non-dissipative discontinuous Galerkin method," 2006.

[116] M. Ainsworth, P. Monk, and W. Muniz, "Dispersive and Dissipative Properties of Discontinuous Galerkin Finite Element Methods for the Second-Order Wave Equation," *Journal of Scientific Computing*, vol. 27, pp. 5–40, June 2006.

[117] G. Gabard and E. Brambley, "A full discrete dispersion analysis of time-domain simulations of acoustic liners with flow," *Journal of Computational Physics*, vol. 273, pp. 310–326, Sept. 2014.

[118] A. Michalke, "On the inviscid instability of the hyperbolic–tangent velocity profile," *Journal of Fluid Mechanics*, vol. 19, p. 543, Aug. 1964.

[119] A. Michalke, "On spatially growing disturbances in an inviscid shear layer," *Journal of Fluid Mechanics*, vol. 23, p. 521, Nov. 1965.

[120] W. Blumen, "Shear layer instability of an inviscid compressible fluid," *Journal of Fluid Mechanics*, vol. 40, no. 4, pp. 769–781, 1970.

[121] P. Huerre and P. A. Monkewitz, "Local and Global Instabilities in Spatially Developing Flows," *Annual Review of Fluid Mechanics*, vol. 22, pp. 473–537, Jan. 1990.

[122] M. Williamschen, G. Gabard, and H. Beriot, "Performance of the DGM for the Linearized Euler Equations With Non-Uniform Mean-Flow," in *21st AIAA/CEAS Aeroacoustics Conference*, p. 3277, 2015.

[123] M. Williamschen, G. Gabard, and H. Beriot, "A study of aliasing error in DGM solutions to turbofan exhaust noise problems," 2015.

[124] I. Amidror, "Scattered data interpolation methods for electronic imaging systems: a survey," *Journal of Electronic Imaging*, vol. 11, pp. 11 – 11 – 20, 2002.

[125] M. M. Gracia, B. Vanelderen, W. De Roeck, and W. Desmet, "Accurate interfacing schemes for the coupling of CFD data with high order DG methods for aeroacoustic propagation," *Proceedings of ISMA2014*, pp. 15–17, 2014.

[126] A. Nealen, "An as-short-as-possible introduction to the least squares, weighted least squares and moving least squares methods for scattered data approximation and interpolation," *URL: http://www. nealen. com/projects*, vol. 130, p. 150, 2004.

[127] S. R. Slattery, S. P. Hamilton, and T. M. Evans, "A Modified Moving Least Square Algorithm for Solution Transfer on a Spacer Grid Surface," Jan. 2015.

[128] S. Fleishman, D. Cohen-Or, and C. T. Silva, "Robust Moving Least-squares Fitting with Sharp Features," *ACM Trans. Graph.*, vol. 24, pp. 544–552, July 2005.

[129] F. Bassi and S. Rebay, "High-Order Accurate Discontinuous Finite Element Solution of the 2d Euler Equations," *Journal of Computational Physics*, vol. 138, no. 2, pp. 251 – 285, 1997.

[130] T. Colonius, S. K. Lele, and P. Moin, "The scattering of sound waves by a vortex: numerical simulations and analytical solutions," *Journal of Fluid Mechanics*, vol. 260, pp. 271–298, 1994.

[131] V. Clair and G. Gabard, "Numerical assessment of the scattering of acoustic waves by turbulent structures," American Institute of Aeronautics and Astronautics, June 2015.

[132] G. A. Dilts, "Moving-least-squares-particle hydrodynamics I. Consistency and stability," *International Journal for Numerical Methods in Engineering*, vol. 44, pp. 1115–1155, Mar. 1999.

[133] J. Behley, V. Steinhage, and A. B. Cremers, "Efficient radius neighbor search in three-dimensional point clouds," in *2015 IEEE International Conference on Robotics and Automation (ICRA)*, pp. 3625–3630, May 2015.

[134] P. G. Tucker, "Assessment of geometric multilevel convergence robustness and a wall distance method for flows with multiple internal boundaries," *Applied Mathematical Modelling*, vol. 22, no. 4–5, pp. 293 – 311, 1998.

[135] G. R. Joldes, H. A. Chowdhury, A. Wittek, B. Doyle, and K. Miller, "Modified moving least squares with polynomial bases for scattered data approximation," *Applied Mathematics and Computation*, vol. 266, pp. 893 – 902, 2015.

[136] B. Tester, F. Arnold, S. Caro, and S. Lidoine, "TURNEX: Turbomachinery Noise Radiation through the Engine Exhaust," *Publishable Final Activity Report, EU Project*, no. 516079, 2008.

[137] G. Gabard, "Noise Sources for Duct Acoustics Simulations: Broadband Noise and Tones," *AIAA Journal*, vol. 52, pp. 1994–2006, Sept. 2014.

[138] R. Arina, "Validation of a Discontinuous Galerkin Implementation of the Time-Domain Linearized Navier–Stokes Equations for Aeroacoustics," *Aerospace*, vol. 3, p. 7, Feb. 2016.

[139] R. M. Munt, "The interaction of sound with a subsonic jet issuing from a semi-infinite cylindrical pipe," *Journal of Fluid Mechanics*, vol. 83, p. 609, Dec. 1977.

[140] G. Gabard and R. J. Astley, "Theoretical model for sound radiation from annular jet pipes: far- and near-field solutions," *Journal of Fluid Mechanics*, vol. 549, p. 315, Feb. 2006.

[141] J. W. Cooley and J. W. Tukey, "An Algorithm for the Machine Calculation of Complex Fourier Series," *Mathematics of Computation*, vol. 19, no. 90, pp. 297–301, 1965.

[142] F. N. Fritsch and R. E. Carlson, "Monotone Piecewise Cubic Interpolation," *SIAM Journal on Numerical Analysis*, vol. 17, no. 2, pp. 238–246, 1980.

[143] M. J. Lighthill, "On Sound Generated Aerodynamically. II. Turbulence as a Source of Sound," *Proceedings of the Royal Society A: Mathematical, Physical and Engineering Sciences*, vol. 222, pp. 1–32, Feb. 1954.

[144] D. Casalino, F. Diozzi, R. Sannino, and A. Paonessa, "Aircraft noise reduction technologies: A bibliographic review," *Aerospace Science and Technology*, vol. 12, pp. 1–17, Jan. 2008.

[145] K. Zaman, J. Bridges, and D. Huff, "Evolution from 'tabs' to 'chevron technology' - a review," *International Journal of Aeroacoustics*, vol. 10, pp. 685–710, Oct. 2011.

[146] E. Nesbitt, V. Mengle, M. Czech, B. Callender, and R. Thomas, "Flight Test Results for Uniquely Tailored Propulsion-Airframe Aeroacoustic Chevrons: Community Noise," American Institute of Aeronautics and Astronautics, May 2006.

[147] J. Mabe, F. Calkins, and G. Butler, "Boeing's Variable Geometry Chevron, Morphing Aerostructure for Jet Noise Reduction," American Institute of Aeronautics and Astronautics, May 2006.

[148] M. J. Doty, B. S. Henderson, and K. W. Kinzie, "Turbulence Measurements of Separate-Flow Nozzles with Pylon Interaction Using Particle Image Velocimetry," *AIAA Journal*, vol. 45, pp. 1281–1289, June 2007.

[149] B. Callender, E. Gutmark, and S. Martens, "Near-Field Investigation of Chevron Nozzle Mechanisms," *AIAA Journal*, vol. 46, pp. 36–45, Jan. 2008.

[150] S. Birch, D. Lyubimov, V. Maslov, and A. Secundov, "Noise Predictions for Chevron Nozzle Flows," American Institute of Aeronautics and Astronautics, May 2006.

[151] H. Xia, P. G. Tucker, and S. Eastwood, "Large-eddy simulations of chevron jet flows with noise predictions," *International Journal of Heat and Fluid Flow*, vol. 30, pp. 1067–1079, Dec. 2009.

[152] X. Xu, J. He, X. Li, and F. Q. Hu, "3-D Jet Noise Prediction for Separate Flow Nozzles with Pylon Interaction," American Institute of Aeronautics and Astronautics, Jan. 2015.

[153] J. M. Tyler and T. G. Sofrin, "Axial Flow Compressor Noise Studies," in *SAE Technical Paper*, SAE International, 1962.

[154] S. Sinayoko, P. Joseph, and A. McAlpine, "Multimode radiation from an unflanged, semi-infinite circular duct with uniform flow," *The Journal of the Acoustical Society of America*, vol. 127, no. 4, pp. 2159–2168, 2010.

[155] S. Saini, J. Chang, and H. Jin, "Performance Evaluation of the Intel Sandy Bridge Based NASA Pleiades Using Scientific and Engineering Applications," in *High Performance Computing Systems. Performance Modeling, Benchmarking and Simulation* (S. A. Jarvis, S. A. Wright, and S. D. Hammond, eds.), vol. 8551, pp. 25–51, Cham: Springer International Publishing, 2014.

[156] A. McAlpine, M. J. Fisher, and B. J. Tester, ""Buzz-saw" noise: A comparison of measurement with prediction," *Journal of Sound and Vibration*, vol. 290, no. 3, pp. 1202 – 1233, 2006.

[157] G. Gabard, "Boundary layer effects on liners for aircraft engines," *Journal of Sound and Vibration*, vol. 381, pp. 30 – 47, 2016.

[158] P. J. Morris, "The scattering of sound from a spatially distributed axisymmetric cylindrical source by a circular cylinder," *The Journal of the Acoustical Society of America*, vol. 97, no. 5, p. 2651, 1995.

[159] S. W. Rienstra and A. Hirschberg, "An Introduction to Acoustics," Tech. Rep. revised and updated version of IWDE 92-06, Technische Universiteit Eindhoven, 2012.